Dissertation
submitted to the
Combined Faculties for the Natural Sciences and for Mathematics
of the Ruperto-Carola University of Heidelberg, Germany
for the degree of
Doctor of the Natural Sciences

Put forward by

Dipl.-Phys. Stephen Vogel
born in Karlsruhe

Oral examination: 4th February 2016

Developments at an Electrostatic Cryogenic Storage Ring for Electron-Cooled keV Energy Ion Beams

Stephen Vogel

Referees:

Prof. Dr. Andreas Wolf
Prof. Dr. André Schöning

Developments at an Electrostatic Cryogenic Storage Ring for Electron-Cooled keV Energy Ion Beams

This work is devoted to final setup activities and the commissioning of an electrostatic cryogenic storage ring (CSR) at the Max Planck Institute for Nuclear Physics (MPIK) in Heidelberg. The first cryogenic operation of CSR in 2015 has been documented and characterized using a set of non-destructive beam diagnostic tools developed within this work. These are (1) the current pick-up system for the determination of the current of the stored ion beam and its velocity, (2) a position pick-up system for measuring the transverse position of the ion beam center at six symmetric locations of the storage ring circumference, and (3) a SCHOTTKY pick-up system for the monitoring of coasting ion beams. Despite the requirements imposed by the cryogenic operation, the developed diagnostic system demonstrated its full functionality. First characterizations of the storage ring properties and the performance of the diagnostic system are presented. Based on previous work, an electron cooling system for CSR has been developed and largely realized. With the implementation into CSR in 2016, the electron cooler will enhance the storage ring into a unique experimental facility for electron-ion collision studies. With this CSR is on the track to become the first cryogenic storage ring featuring actively cooled ion beams.

Entwicklungen an einem elektrostatischem kryogenem Speicherring für elektronengekühlte Ionenstrahlen mit keV Energie

Diese Arbeit widmet sich abschließenden Aufbauarbeiten und der Inbetriebnahme eines elektrostatischen kryogenen Speicherringes (CSR) am Max-Planck-Institut für Kernphysik (MPIK) in Heidelberg. Der erste kryogene Betrieb des CSR im Jahr 2015 wurde dokumentiert und charakterisiert mittels einer Reihe von zerstörungsfreien Strahldiagnose-Elementen, die in dieser Arbeit entwickelt wurden. Diese sind (1) das Strom-Pickupsystem zur Bestimmung des Stroms eines gespeicherten Ionenstrahls und dessen Geschwindigkeit, (2) ein Positionsbestimmungssystem zum Messen des transversalen Ionenstrahlschwerpunktes an sechs symmetrischen Orten des Speicherringumfangs und (3) ein SCHOTTKY-Pickupsystem zur Beobachtung von Gleichstrom-Ionenstrahlen. Trotz der Anforderungen durch den kryogenen Betrieb hat das entwickelte Diagnosesystem seine volle Funktionalität demonstriert. Erste Charakterisierungen der Speicherringeigenschaften sowie die Leistungsfähigkeit des Strahldiagnosesystems werden vorgestellt. Basierend auf vorherigen Arbeiten wurde ein Elektronenkühlungssystem für den CSR entwickelt und zu großen Teilen realisiert. Mit dem Einbau in den CSR im Jahr 2016 wird der Elektronenkühler den Speicherring zu einer einzigartigen experimentellen Anlage für Elektronen-Ionen Kollisionsstudien verbessern. Somit ist der CSR auf dem Weg, zu dem ersten kryogenen Speicherring mit aktiv gekühlten Ionenstrahlen zu werden.

Contents

Chapter 1

Introduction

The knowledge in natural science is based on the interplay between experiments and theory. We can extend our understanding of nature only by probing the predictions of new theories or by initiating new ideas due to experimental discoveries. The typical approach especially for physicists is the study of isolated systems which can either be well characterized in a full theory or well controlled experimentally. Examples are the experimental discovery of the electron by Joseph J. Thomson in 1897 by deflecting 'cathode rays' in a magnetic field and measuring their charge [1] or the discovery of the atomic nucleus by Ernest Rutherford in 1911 by using α particles (from a radioactive source) and investigating their scattering behaviour when passing a thin gold foil [2]. More than a century later these experimental setups are easily comprehensible and realizable. Nowadays the experimental setups have become more technically advanced, and fundamental physics studies can address more complex composite systems, such as multi-electron atoms, and molecules. These studies concern the interaction of atoms and molecules with photons or their collisions with other particles such as electrons. These processes are more complex, but they also can reveal important details about the composition of the molecules, their internal dynamics, and the interactions in their environment. But how can we study such processes experimentally and how can we control or prepare the conditions of the interacting particles?

In order to study molecules close to, or ideally in their rovibrational ground state the ambient temperature of the experimental setup has to be lowered significantly below room temperature. This simplifies the analysis and interpretation of the experimental data, since only a few internal excitations have to be taken into account. At temperatures of $\sim 10\,\mathrm{K}$, most molecular ions can relax into or close to their rovibrational ground state, except for some ions with vanishing electric dipole moment. These low temperatures are also found in cosmic objects like dense interstellar clouds

[3]. Astrochemistry demands for experimental data on collisional cross sections under these conditions in order to model the gas-phase chemistry. Many of the relevant reactions involve simple and abundant collision partners, such as H_2 molecules, simple atoms such as H, and C, and electrons. To model the effect of these reactions, cross sections are compiled in databases like UMIST [4], which show that a smaller percentage of these reaction cross sections have been measured. An important example is the dissociative recombination of molecular ions with electrons, leading to molecular fragmentation. For relevant systems listed there, only $\sim 30\%$ of the cross sections for this process have been measured and in most experiments performed so far, the internal excitations of the molecules, in particular rotations, have been neglected. The ions of interest are mainly positively charged large molecules, but negative ions can also reveal information about their internal properties.

As in the experiments of THOMSON and RUTHERFORD, the easiest experimental approach is to use a beam of particles (either electrons or ions) and let them collide with a stationary target, counting the reaction products. Electrons can be easily extracted from a thermionic cathode by using electric fields, whereas ion beams can be formed from hot plasma sources, of which the ions are extracted and accelerated to high kinetic energies. By changing the stationary target to a region of two merged beams [5], where the beams have a common interaction path, the collision energy between interacting particles can be well-defined down to energies in the meV range, which is practically impossible with a beam impinging on a stationary target. Due to the high energies of the particles in the laboratory frame, the detection efficiency of collision products is also very high. Using magnetic or electrostatic deflection fields the product particles can be separated from their parent beams and both particle currents can be measured individually.

With the invention of ion storage rings in 1945 [6], which were initially designed for high energy physics [7], the use of stored charged particle beams became possible. While originally designed for elementary particles, the technique can also be used for composite particles like atomic and molecular ions. With stored beams of such ions, the spontaneous relaxation of their internal excited states and, with the presently available laser techniques, one may even think of more advanced control methods for their internal states during the beam storage. Simultaneously, the circulating ion beam can interact repeatedly with internal targets or merged beams increasing the measurement duty cycle. A crucial advantage is the possibility to manipulate the ion beam by phase space cooling reducing its momentum spread, divergence, and transverse beam profile. The cooling also counteracts heating processes in the ion beam due to gas or intrabeam scattering resulting in an enhanced beam lifetime. The established methods for phase space cooling for ions are stochastic, electron, or laser cooling. The first method, invented by S. VAN MEER in 1980 [8], is based on the measurement and correction of the ion beam trajectory by the use

of pick-up and kicker electrodes. The last method, first realized in 1993 [9], uses the optical pumping by lasers and isotropic re-emission of photons, which results in an effective cooling of the ions. Another very efficient method is electron cooling, which was invented by G. Budker in 1966 [10] and realized in 1974 [11]. It uses a velocity matched ($v_{\mathrm{el}} = v_{\mathrm{ion}}$), cold, i.e. nearly mono-energetic, electron beam, which is continuously renewed and merged with the hot ion beam. This setup also serves simultaneously as an experimental platform for studying various electron-ion reactions (e.g., dissociative recombination) by detecting their products. Due to their changed mass-to-charge ratio, the reaction products are separated from their parent beam in the bending fields of the storage rings and can easily be detected.

The interest in atomic and molecular physics in collisions between electrons and molecular ions first started with light molecules. With increasing understanding it went to more complex and heavier molecules. With magnetic storage rings like TSR [12, 13], ASTRID [14] or CRYRING [15], which were designed mainly for ion energies in the MeV region and for highly charged ions, the storage of heavy molecules is not feasible considering the limited bending radii of the employed dipole magnets for a given magnetic field. To overcome this limitation in ion mass, several electrostatic storage rings have been constructed and most of them went in operation in the last few years. The first pioneering device is ELISA [16] at the Århus University, Denmark, which has a racetrack layout formed by two 160° and four 10° cylindrical deflectors. Multiple other machines adopted this layout. These are the TMU E-Ring [17] at the Tokyo Metropolitan University in Tokyo, Japan, the ELASR [18] at the King Abdulaziz City for Sciences and Technology in Riyadh, Saudi Arabia, and the ESRING [19], which has been the first electrostatic storage ring with a merged electron target [20], at the KEK-High Energy Accelerator Research Organization in Tsukuba, Japan. But also totally new layouts of smaller size, like the Mini-Ring [21] at the Université Lyon, France, and the μE-ring [22] at the Tokyo Metropolitan University in Tokyo, Japan, or of bigger size, like the FLSR [23] at the Johann Wolfgang Goethe-Universität in Frankfurt, Germany, and SAPHIRA [24] at the Århus University, Denmark, have been realized. All of these devices are operated at room temperature conditions, except for the TMU E-Ring, which can partly be cooled to liquid nitrogen temperature. At the corresponding vacuum pressures, the storage lifetimes for ion energies in the keV range is limited by electron capture from the residual gas. By operating the whole apparatus at cryogenic temperatures of $\sim 10\,\mathrm{K}$, an increase of the storage lifetime by a few orders of magnitude can be gained, which is crucial to be able to investigate heavy low charged ion species. Up to now there are three such devices in their commissioning or at an early experimentally phase. DESIREE [25] at the Stockholm University, Sweden, has recently gone into operation completely and produced first mutual neutralization results [26]. RICE [27] at the RIKEN Advanced Science Institute in Saitama, Japan, has reported first beam storage. And finally, the CSR [28] at the Max-Planck-Institut

für Kernphysik (MPIK) in Heidelberg, Germany, underwent commissioning and its first experimental programme during the time frame of this work.

In the list of these devices, the CSR takes an unique place. It is specifically designed to serve as an experimental platform for various experiments on stored keV ion beams under cryogenic conditions. Its lattice is optimized for long, free, straight sections dedicated to experiments on neutral-ion collisions (in merged and crossed geometries), laser-ion interactions, and electron-ion collisions. For the operation of the storage ring itself, but also for the experimental setups with internal targets (merged electron, neutral, and laser beams), the ion beam has to be controlled and its properties must be analyzed. Both the ion beam size and its relative position with respect to the targets define the overlap in the collisional experiments and by this the interaction cross sections. Furthermore, the absolute collisional cross sections can only be determined with the knowledge of the number of stored and interacting particles. The ion energy defines the relative collision energy and the momentum spread of the ion beam is influencing the achievable energy resolution in the experiments. For some of the experiments it is also advantageous to have collisions with several short ion pulses rather than with a constant current of ions, so that the bunching of the stored ion beam is desired.

The work in hand is dedicated to the development and realization of important sub-systems of CSR and to their initial operation in the first cryogenic beamtime period of CSR. This first concerns the diagnostic system of CSR which allows the non-destructive detection of stored ion beams. With this system a variety of beam parameters such as the number of initial stored ions, the ion beam energy, the momentum spread, as well as the transverse position of the ion beam can be determined. Furthermore, the design of the CSR electron cooler has been finalized and the realization of this setup has been started. In the following chapter 2 the beam dynamics in ion storage rings and the principle of electron cooling are discussed, followed by the presentation of the CSR facility and an overview of its diagnostic tools. The diagnostic system based on capacitive pick-up electrodes, developed and realized in this work is then discussed in detail in chapter 3. In the subsequent chapter 4 the final design of the CSR electron cooler is presented, which has been elaborated in parallel during this work facing the technical and experimental requirements of the implementation of such a setup in the environment of CSR. With the completion of the construction of the CSR facility at the beginning of 2015 the commissioning has started. Some of the first results and characterizations are discussed in chapter 5.

Chapter 2

The Cryogenic Storage Ring

In this chapter we first summarize the fundamental beam dynamics in an ion storage ring, followed by a brief discussion on the principles of electron cooling. After this, the Cryogenic Storage Ring (CSR) is introduced and its most important properties with respect to the diagnostic system and the electron cooler are presented.

2.1 Beam dynamics in an ion storage ring

The movement of an ion can be manipulated either with electrical $\vec{\mathcal{E}}$ or magnetic fields $\vec{B}$, which is expressed in the LORENTZ force equation:

$$\vec{F}_{\mathrm{L}} = m\frac{\mathrm{d}^2\vec{r}}{\mathrm{d}t^2} = z\,e\,\vec{\mathcal{E}} + z\,e\,\vec{v}\times\vec{B}, \tag{2.1}$$

where m, $z\,e$, and $\vec{v}$ are the mass, the charge, and the velocity of the ion, respectively. We are concerned with low velocities $v/c_0 \lesssim 10^{-2}$ where we can use the non-relativistic approximation for most purposes throughout this thesis. By the usage of electrostatic or magnetic deflectors a closed ion trajectory can be created. In the deflecting field the LORENTZ force then counteracts the centripetal force, which requires

$$\left|\vec{F}_{\mathrm{L}}\right| = \frac{mv^2}{\rho_0}, \tag{2.2}$$

where ρ_0 is the curvature of the ion trajectory. Solving for the ion velocity v for both the electrical and magnetic part of the LORENTZ force independently reveals the advantage of electrostatic over magnetic storage rings. At a given bending radius ρ_0 the maximal velocity of the ion that can be reached for a given field

strength scales with $m^{-1/2}$ in the electrostatic case compared to m^{-1} in the magnetic case. Thus, higher velocities can be achieved, especially for ions of large mass. Furthermore, the bending radius for static electromagnetic fields scales with the ion energy in the electrostatic case, but with the ion momentum in the magnetic case. As a consequence, in a fully electrostatic ion storage facility all optical elements only have to be scaled linearly when the ion energy is changed. Additionally, this makes the usage of pilot beams possible, which are accelerated to a given energy for the adjustment of the storage ring. Then it can be switched to the ion species of interest with possibly different mass, but identical energy. For both magnetic and electrostatic storage rings, the basic description of the ion beam dynamics is the same, which is summarized in the following.

A modern circular accelerator is made of a sequence of ion-optical elements arranged within a single deflecting plane in an approximately circular manner, separated by field-free drift sections. The nowadays most common type of a strongly-focusing storage ring consists of several deflecting elements and a number of focusing quadrupoles. The former bend the particle trajectories into a closed loop, the latter prevent particle losses due to beam divergence or mutual repulsion of the particles. The ion trajectory which an *ideal particle* follows each turn is called *central orbit*. Within certain limits, particles may deviate from the ideal particle orbit in the phase space transverse to the main flight direction. Through the action of the focusing elements, these particles then perform *betatron oscillations* [29] around the central orbit. For the description of the beam dynamics it is convenient to construct a co-moving curved coordinate system with one longitudinal coordinate s, which is always tangential to the flight direction of the particle. The transverse coordinates are given relative to the central orbit by the horizontal x (here defined to be pointing to the outside) and vertical y coordinate (pointing upwards). Figure 2.1 displays this henceforth used coordinate convention. In the following sections the transverse and longitudinal beam dynamics are summarized. We here follow and summarize the discussion that can be found in many pertinent textbooks (e.g. [30] or the CERN Accelerator School reports [31]).

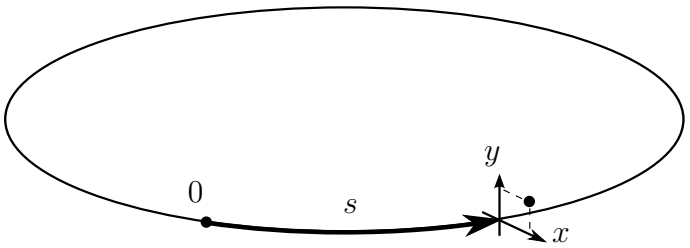

Figure 2.1: Co-moving coordinate system of a storage ring, modified from [30, fig. 6.1], and adapted to the sense of rotation of CSR.

2.1.1 Transverse beam dynamics

In linear approximation (valid for suitably small deviations from the ideal closed orbit) the transverse beam dynamics in a storage ring are given by HILL's equation [32]

$$\frac{\mathrm{d}^2x(s)}{\mathrm{d}s^2} + k_x(s)\,x(s) = \frac{1}{\rho_0(s)}\frac{\Delta p}{p_0}, \tag{2.3}$$

$$\frac{\mathrm{d}^2y(s)}{\mathrm{d}s^2} + k_y(s)\,y(s) = 0. \tag{2.4}$$

It is assumed that the bending of the trajectory is done only in the (x, s)-plane. Thus, the dispersive effects due to the momentum spread $\Delta p/p_0$ only affect the x-coordinate. $\rho_0(s)$ is the bending radius of the trajectory. The coefficients $k_{x,y}(s)$ are periodic functions $k_{x,y}(s + C_0) = k_{x,y}(s)$ of the s-coordinate and their period is the circumference C_0 of the storage ring. These coefficients describe the focusing and defocusing forces of the optical elements.

For a mono-energetic ion beam (i.e. $\Delta p/p_0 = 0$) both equations are identical in their structure and equal to the equation of a quasi-harmonic oscillator. The solutions[1] are sine-like oscillations, which are called *betatron oscillations* [29],

$$y(s) = a\sqrt{\beta_y(s)}\cos\left(\psi(s) + \psi_0\right), \tag{2.5}$$

with variable amplitude $a\sqrt{\beta_y(s)}$ and variable wave number $\mathrm{d}\psi(s)/\mathrm{d}s = 1/\beta_y(s)$. The integration constants a and ψ_0 define the betatron amplitude and the starting phase of an individual particle, respectively. The betatron function $\beta_y(s)$ is of central importance and determines the properties of the storage ring. It is one of the so-called *lattice functions* of the storage ring [33]

The working point of a storage ring

The number of betatron oscillations per revolution is called *tune* and is given by

$$Q_{x,y} = \frac{1}{2\pi}\oint \frac{\mathrm{d}s'}{\beta_{x,y}(s')}. \tag{2.6}$$

Integer tune values cause resonances and excite strong betatron oscillations. On these resonances the dipole field errors (and higher multipole field errors in general)

[1] The hereafter given formulae are also true for the horizontal coordinate x, if the beam is mono-energetic.

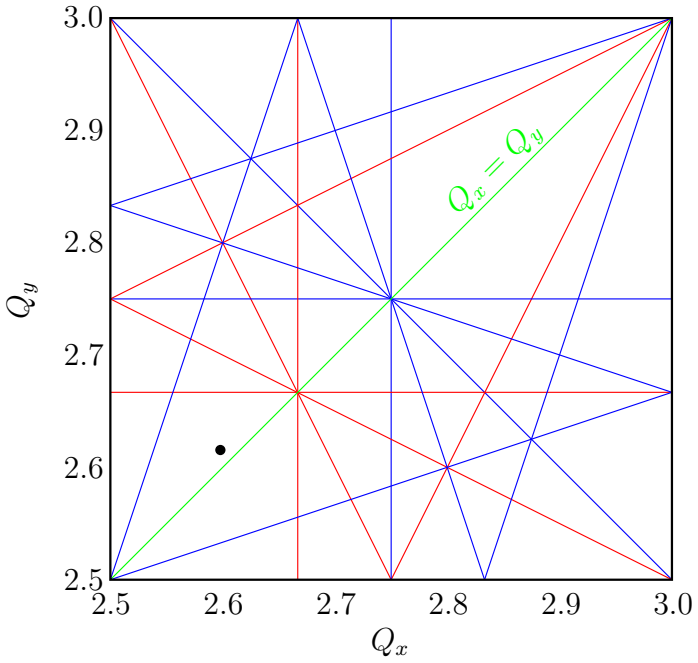

Figure 2.2: Working diagram of CSR. Black dot: intended working point of CSR, black (border) lines: first and second order resonances, red lines: third order resonances, blue lines: fourth order resonances. The green line indicates where $Q_x = Q_y$.

act on the ion in phase resulting in a kick of the ion trajectory. By this over many revolutions the ion beam is lost and storage becomes impossible. Besides integer resonances there are also resonances of higher order as well as coupled resonances possible which describe the cross-talk between the horizontal and transverse motion. The resonances can be summarized in the following equations

$$k = nQ_x \tag{2.7}$$
$$k = nQ_y \tag{2.8}$$
$$k = lQ_x + mQ_y, \quad n = |l| + |m| \,. \tag{2.9}$$

Here k, l, m, and n are integers and n characterizes the order of the resonance. The smaller the order the larger the strength of the resonances. The *working point* of a storage ring corresponds to a certain set of Q_x and Q_y and is adjusted to be as far as possible remote of strong resonances.

Figure 2.2 shows a typical working diagram. The straight lines correspond to first and second order (black border lines), third order (red), and fourth order (blue) resonances. The green line shows the line where $Q_x = Q_y$. At this line, energy is transferred between both transverse coordinates, which leads to a beating of the transverse betatron oscillations. Since these are unlikely to be in phase with multipole field errors (except for the intersections with the other resonance lines)

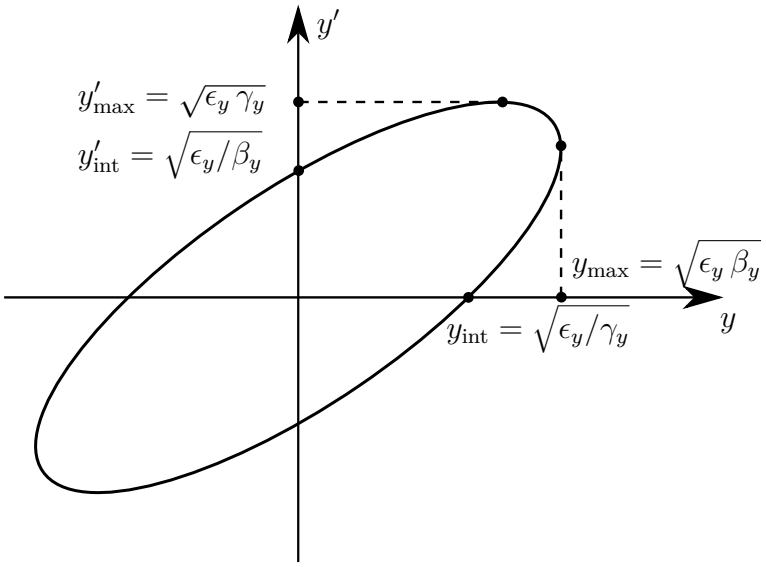

Figure 2.3: The phase space ellipse in the (y, y')-plane, modified from [30, fig. 6.2].

they are not harmful for the storage behaviour provided that the acceptances (which are defined below) in both coordinates are approximately the same (as it is the case for CSR). The black dot indicates the intended working point of CSR.

The emittance and acceptance

The mathematical structure of the solutions (2.5) leads to a constant of motion, which is the COURANT-SNYDER-invariant [33],

$$\gamma_y(s)\, y(s)^2 + 2\alpha_y(s)\, y(s)\, y'(s) + \beta_y(s)\, y'(s)^2 = \epsilon_y \tag{2.10}$$

which contains the related *lattice functions*

$$\alpha_y(s) = -\frac{1}{2}\beta'_y(s), \tag{2.11}$$

$$\gamma_y(s) = \frac{1 + \alpha_y^2(s)}{\beta_y(s)}, \tag{2.12}$$

depending on the betatron function $\beta_y(s)$. Equation (2.10) represents an ellipse in the phase space spanned by y and y', which is plotted in figure 2.3.

A particle with coordinates (y, y') moves in phase space on the circumference of an ellipse, which itself is changing its geometry with changing longitudinal coordinate s. The shape of the ellipse is defined by the lattice functions α_y, β_y, and γ_y. The enclosed area of the ellipse is a constant and is determined by the betatron amplitude

of the particle. The area of this ellipse is given by the *single-particle emittance* ϵ_y as $\epsilon_y \pi$. As depicted in figure 2.3 the maximal space deviation of a single particle is given by

$$y_{\max}(s) = \sqrt{\epsilon_y \, \beta_y(s)}, \tag{2.13}$$

and its maximal divergence by

$$y'_{\max}(s) = \sqrt{\epsilon_y \, \gamma_y(s)}. \tag{2.14}$$

Since an ion beam is an ensemble of individual particles, it is convenient to define also the *beam emittance* E_y. The individual particles of the beam are usually not filling the phase space homogeneously, but rather have a two-dimensional GAUSSian density distribution. The one-dimensional projections of this distribution onto the respective transverse coordinates represent the *beam profile*, which is an one-dimensional GAUSSian distribution. The beam emittance is defined using either one, two or three standard deviations σ_y of the beam profile

$$\sqrt{E_y^{(1\sigma)} \, \beta_y} = \sigma_y, \quad \sqrt{E_y^{(2\sigma)} \, \beta_y} = 2\sigma_y, \quad \sqrt{E_y^{(3\sigma)} \, \beta_y} = 3\sigma_y \tag{2.15}$$

representing 39.3 %, 86.5 % or 98.9 % of the beam intensity, if both transverse emittances are identical [30, pp. 153]. The beam envelope and the beam divergence are also defined by the equations (2.13) and (2.14) with the respective beam emittances.

The maximal beam envelope is limited by the walls of the vacuum chambers or other barriers and sets a limit for the maximal storable single-particle emittance. The *acceptance* A is defined as the maximal area of the phase space (divided by π), where ions still can be stored. It is a machine property of a storage ring and depends on the working point. There is a *geometrical acceptance* limited by mechanical apertures and a *dynamical acceptance*, which is limited by the quality of the deflecting and focusing fields of the ion optics. For CSR the dynamical acceptance has been simulated by single-particle tracking with the Opera-3D software package [34] at the standard operation mode to be $A_x = 120\,\text{mm mrad}$ (for $\epsilon_y \to 0$) and $A_y = 180\,\text{mm mrad}$ (for $\epsilon_x \to 0$) [35]. The corresponding maximal beam sizes in the center of a straight section are $x_{\max} = \pm 40\,\text{mm}$ and $y_{\max} = \pm 14\,\text{mm}$ [35], respectively. The limiting optical elements are the quadrupoles [35].

Dispersive effects

The fact that a realistic ion beam is not mono-energetic, as assumed so far, but rather has a momentum spread $\Delta p/p_0$, see equation 2.3, leads to several consequences, some of which will be discussed in the following.

A particle with positive momentum deviation $\Delta p > 0$ compared to the ideal particle is less affected by the deflecting fields and moves consequently at a larger orbit with a position deviation $x_D(s)$ with respect to the ideal orbit (with $\Delta p = 0$). The offset in position is characterized by the *dispersion*[2] $D(s)$, which is defined by [30, p. 264]

$$x_D(s) = D(s)\,\frac{\Delta p}{p_0}. \tag{2.16}$$

The orbit lengthening $\Delta C/C_0$ is (in linear approximation) characterized by the *momentum compaction factor* α_p [30, eq. 6.73]

$$\frac{\Delta C}{C_0} = \alpha_\mathrm{p}\,\frac{\Delta p}{p_0}. \tag{2.17}$$

The momentum compaction factor and the dispersion are directly linked via [30, eq. 6.74]

$$\alpha_\mathrm{p} = \frac{1}{C_0}\int_0^{C_0}\frac{D(s)}{\rho_0(s)}\mathrm{d}s. \tag{2.18}$$

Of course also the revolution frequency of a circulating ion depends on its momentum, which is characterized by the *phase slip factor*. It is defined (in linear approximation) by [30, eq. 6.67]

$$\frac{\Delta f}{f_0} = \eta\frac{\Delta p}{p_0}. \tag{2.19}$$

Since the revolution frequency $f = v/C$ depends on the velocity and the closed orbit circumference, which both depend on the momentum of the particle, it is

$$\frac{\Delta f}{f_0} = \frac{\Delta v}{v_0} - \frac{\Delta C}{C_0}. \tag{2.20}$$

Obviously, there is a connection between the phase slip factor and the momentum compaction factor, which we want to deduce in the following for the electrostatic case (in non-relativistic approximation).

If we consider a test particle with mass m and charge $z\,e$ in an electrical field of an electrical potential ϕ, its energy E is given by

$$E = \frac{m}{2}v^2(s) + z\,e\,\phi(s) = E_0 + \Delta E \tag{2.21}$$

with an energy deviation ΔE from the ideal particle, which has (due to $\phi(s) = \phi_0 \equiv 0$ on the ideal orbit) an energy $E_0 = \frac{m}{2}v_0^2$. Assuming only small velocity differences ($v \approx v_0$) and solving equation (2.21) for the velocity spread results in

$$\frac{\delta v}{v_0} = \frac{v(s) - v_0}{v_0} = \frac{\Delta E}{2E_0} - \frac{z\,e}{2E_0}\phi(s). \tag{2.22}$$

[2] In principle there is also a dispersion for the y coordinate, but if the bending of the ion trajectory is only in one plane (x, s), it is convenient to use $D(s)$ without the index x.

As long as the electrical potential $\phi(s)$ is constant for all coordinates the second term is zero and the velocity of the particle solely depends on its energy (as in the magnetic case). But since the potential in the electrostatic deflectors depends on the transverse particle position, it is non-zero. Assuming only a small transverse position offset $x(s)$, the electrical potential of the deflector can be approximated to change only linearly with x

$$\phi(s) \approx \phi_0 + x(s)\frac{\partial \phi}{\partial x} = \phi_0 + \frac{2E_0}{z\,e}\frac{x(s)}{\rho_0(s)} \tag{2.23}$$

Inserting this (with $\phi_0 \equiv 0$) in equation (2.22) gives

$$\frac{\delta v}{v_0} = \frac{\Delta E}{2E_0} - \frac{x(s)}{\rho_0(s)}. \tag{2.24}$$

The integrated change over one revolution is then

$$\frac{\Delta v}{v_0} = \frac{\Delta E}{2E_0} - \frac{1}{C_0}\int_0^{C_0}\frac{x(s)}{\rho_0(s)}\mathrm{d}s. \tag{2.25}$$

With $\Delta E/2E_0 = \Delta p/p_0$ and the definitions of the dispersion and the momentum compaction factor (equations (2.16) - (2.18)) and inserting equation (2.25) in (2.20) yields

$$\frac{\Delta f}{f_0} = (1 - 2\alpha_\mathrm{p})\frac{\Delta p}{p_0}. \tag{2.26}$$

Thus, the connection between the phase slip factor and the momentum compaction for an electrostatic storage ring (in non-relativistic approximation) is given by

$$\eta = 1 - 2\alpha_\mathrm{p}. \tag{2.27}$$

This relation stands in contrast to the case of magnetic storage rings, where the relation in the non-relativistic case is [30, p. 309]

$$\eta_\mathrm{magn} = 1 - \alpha_\mathrm{p}. \tag{2.28}$$

The difference is caused by the different influence of the electrostatic and magnetic fields onto the ion velocity. The absolute value of the velocity cannot be changed by magnetic fields, but only its direction, see equation (2.1). While in the electrostatic case also the absolute value of the velocity is changed by the electrical potential, see equation (2.22).

Matrix formalism and simulation software

Analog to geometrical optics it is possible to describe the motion of particles in magnetic and electrical fields using a matrix formalism. Herein each optical element

is represented by a single matrix. By multiplying the different matrices of drift sections, quadrupoles, and deflectors a single *transfer matrix* can be calculated. In the latter the influence of the ion optics for a complete revolution on a test particle is united.

Software packages based on linear equation solvers like the Methodical Accelerator Design code (MAD, [36]) are using this formalism to calculate the important properties of a storage ring. A limitation of this software is often the neglect of fringing fields and the simplification of the fields of some optical elements. Also the simulation of complicated ion beam optics, where it is not possible to derive the transfer matrix for, is difficult. For this, finite-element solver software, like Opera-3D [34], G4beamline [37] or SIMION [38] can be used. Here, the electrical and magnetic fields of some given geometry are calculated on a fine mesh in space by solving MAXWELL's equations via finite element analysis. Usage of tracking routines allows then the simulation of the movement of particles [39].

2.1.2 Longitudinal beam dynamics

The longitudinal structure of an ion beam can be separated into two cases. Either the beam is a *coasting* (or *direct current*) beam without any time structure or it is a *bunched* (or *chopped*) beam, which has a certain time structure. Bunching can be achieved by applying a time dependent voltage to a drift tube. In the simplest case the accelerating field results from the two gaps that separate the drift tube from the grounded surrounding on either sides. During bunching the accelerating voltage has to be applied continuously, otherwise the beam would lose its time structure and turn into a coasting beam (so-called *debunching*). For creating a quasi-constant bunching effect the applied voltage must be periodic with a frequency

$$f_\mathrm{b} = h \cdot f_0, \tag{2.29}$$

where f_0 is the revolution frequency and $h \in \mathbb{N}$ is the *harmonic number*.

The CSR drift tube with an electrode length L_0 has two gaps. To simplify the equation it is possible to convert the voltage at the two gaps to an effective voltage U_b of a single gap. Assuming a harmonic signal at $\omega_\mathrm{b} = 2\pi f_\mathrm{b}$ an ion with charge $z\,e$ by passing the drift tube gains the energy

$$\Delta E_{\text{two gaps}} = z\,e\,\hat{U}_\text{drift}\left[\cos\left(\phi + \omega_\mathrm{b}\,t_\mathrm{f}\right) - \cos\left(\phi - \omega_\mathrm{b}\,t_\mathrm{f}\right)\right], \tag{2.30}$$

where ϕ is the phase of the applied voltage with amplitude $\hat{U}_\text{drift}$ when the particle passes the center of the drift tube. $t_\mathrm{f} = L_0/(2v)$ is the flight time of the ion from one gap to the center of the drift tube. The negative sign in front of the second term is

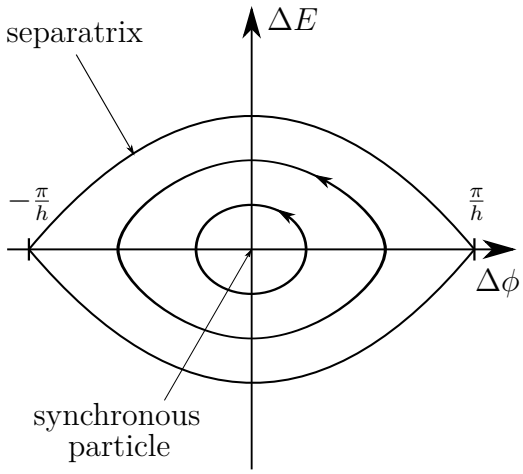

Figure 2.4: Energy deviation ΔE as a function of phase deviation $\Delta\phi$ for a synchronous phase of zero and positive phase slip factor, see equation (2.19).

due to the reversed electric field in the second gap. Simplifying equation (2.30) and setting $\Delta E_{\text{two gaps}} = z\,e\,\hat{U}_\text{b}\cos\phi$ gives the effective voltage for a single gap

$$\hat{U}_\text{b} = 2\,\hat{U}_\text{drift}\,\sin\left(h\pi\frac{L_0}{C_0}\right), \tag{2.31}$$

where C_0 is the circumference of the storage ring.

For describing the dynamics in a bunched ion beam it is convenient to consider a *synchronous particle* with revolution frequency f_s, which fulfills equation (2.29) with $f_0 = f_\text{s}$. It has a phase[3] ϕ_s and energy E_s. The other particles in the bunch have a phase difference $\Delta\phi = \phi - \phi_\text{s}$ and energy difference $\Delta E = E - E_\text{s}$ with respect to the synchronous particle. Due to the bunching the particles start to oscillate around the synchronous particle depending on their phase and energy difference. These *synchrotron oscillations* are phase and energy oscillations around the synchronous particle. Figure 2.4 schematically displays the energy deviation ΔE as a function of phase deviation $\Delta\phi$ assuming the accelerating field of equation (2.30) and time independent values of f_s and E_s. The border line between the stable and unstable area is the *separatrix*. It describes the largest possible phase differences and energy difference from the synchronous particle in which the bunched ions still oscillate within closed, stable longitudinal synchrotron-motion orbits. The stable area enclosed by the separatrix is called *bucket*. There are as many buckets as the harmonic number h, nevertheless not all of them have to be filled with ions necessarily.

For synchrotron oscillations with small amplitudes the equation of motion is the

[3]The circumference of the storage ring then corresponds to $\Delta\phi = 2\pi$.

equation of a harmonic oscillator [30],

$$\frac{\mathrm{d}^2}{\mathrm{d}t^2}\Delta\phi + \omega_{\mathrm{sync}}^2\,\Delta\phi = 0, \tag{2.32}$$

with

$$\omega_{\mathrm{sync}} = \omega_{\mathrm{s}}\sqrt{\frac{h\,\eta}{2\pi\,p_{\mathrm{s}}\,v_{\mathrm{s}}}z\,e\,\hat{U}_{\mathrm{b}}\,\cos\phi_{\mathrm{s}}}. \tag{2.33}$$

Here $f_{\mathrm{sync}} = \omega_{\mathrm{sync}}/2\pi$ is the *synchrotron frequency* and p_{s}, v_{s}, and ϕ_{s} are the revolution frequency, momentum, velocity, and phase of the synchronous particle, respectively. $z\,e$ is the ion's charge, h is the harmonic integer, and η is the phase slip factor defined in equation (2.19).

2.2 Electron cooling

Electron cooling [40] is a method for reducing the occupied phase space of stored ion beams in a storage ring. In absence of friction forces or diffusive momentum changes only the shape and orientation of the phase space ellipse can be changed, as is done by focusing and steering the ion beam. The area of the phase space ellipse, however, is constant as a direct consequence of LIOUVILLE's theorem, see equation (2.10). To overcome this limitation and to effectively compress the occupied phase space, a cold, dense, and velocity-matched electron beam is merged over some fraction of the circumference with the hot ion beam. The ions undergo RUTHERFORD scattering in the electron gas and thereby lose energy. The energy transferred in these multiple COULOMB interactions is taken by the electrons. The electrons are continuously renewed. As will be shown below, the energy loss of the ions undergoes a maximum and then becomes smaller as the velocity spread of the ion beam shrinks. The cooling process reaches its equilibrium once the average energy loss of the ions becomes equal to the energy gain by the diffusive heating.

The description of the collisions between ions and electrons is similar to the case of stopping of fast charged particles in matter. Simplifying the situation, we first consider the scattering of an ion at a free electron, neglecting the fact that there is a magnetic guiding field present. In the *binary collision model* [41] a single ion with positive charge $z\,e$ and velocity v_{i} encounters an electron at rest, see figure 2.5.

The momentum transfer from the ion to the electron can be calculated in lowest-order perturbative approximation (large b) to

$$\Delta p = \frac{1}{4\pi\varepsilon_0}\int_{-\infty}^{+\infty}\frac{ze^2}{x^2+b^2}\mathrm{d}t = \frac{2z\,e^2}{4\pi\varepsilon_0\,v_{\mathrm{i}}\,b}, \tag{2.34}$$

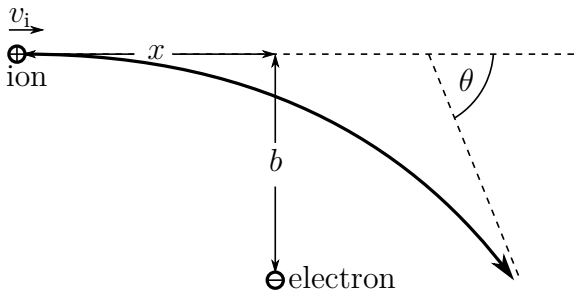

Figure 2.5: Geometry of the scattering of a positively charged ion at an electron.

with the impact parameter b. The energy transferred from the ion to the electron is correspondingly

$$\Delta E(b) = \frac{(\Delta p)^2}{2m_\mathrm{e}} = \frac{2z^2e^4}{(4\pi\varepsilon_0)^2\, m_\mathrm{e}\, b^2\, v_\mathrm{i}^2}. \tag{2.35}$$

Extending the model to the situation that the ion passes a homogeneously distributed electron gas with density n_e the energy loss per traveling distance $\mathrm{d}x$ is calculated via the integration over all possible impact parameters b

$$\frac{\mathrm{d}E}{\mathrm{d}x} = -2\pi \int_0^{+\infty} n_\mathrm{e}\, b\, \Delta E(b)\mathrm{d}b = -\frac{4\pi z^2 e^4 n_\mathrm{e}}{(4\pi\varepsilon_0)^2 m_\mathrm{e} v_\mathrm{i}^2} L_\mathrm{C}. \tag{2.36}$$

Here $L_\mathrm{C} = \int_{b_\mathrm{min}}^{b_\mathrm{max}} \mathrm{d}b/b = \ln(b_\mathrm{max}/b_\mathrm{min})$ is the COULOMB logarithm, which eliminates the divergence of the integral in equation (2.36) for $b \to 0$ and $b \to +\infty$ by introducing a lower and upper cut-of impact parameter b_min and b_max, respectively.

A head-on collision between ion and electron, beyond the perturbative approximation, results in a maximal momentum transfer given by $\Delta p_\mathrm{max} = 2m_\mathrm{e}v_\mathrm{i}$, which finally yields

$$b_\mathrm{min} = \frac{z\, e^2}{4\pi\varepsilon_0 m_\mathrm{e} v_\mathrm{i}^2} \tag{2.37}$$

within the perturbative model (equation (2.35)).

For the maximal impact parameter we can take in the case of the CSR electron cooler the DEBYE screening radius λ_D [42]

$$b_\mathrm{max} = \lambda_\mathrm{D} \equiv \sqrt{\frac{\varepsilon_0 k_\mathrm{B} T_\mathrm{e}}{n_\mathrm{e} e^2}}. \tag{2.38}$$

A. SHORNIKOV estimated for the COULOMB logarithm values of $L_\mathrm{C} = 2.4 - 4.5$ [43, tab. 3.1] for the CSR electron cooler.

The situation is generalized by taking the non-zero temperature of the electrons into account, which is represented by a velocity distribution $f(\vec{v}_\mathrm{e})$ with the electron

velocity $\vec{v}_\mathrm{e}$. Then the resulting cooling force, which is effectively a friction force experienced by the ions, is given by [41, p. 152]

$$\vec{F}_\mathrm{cool} = -\frac{4\pi z^2 e^4 n_\mathrm{e}}{(4\pi\varepsilon_0)^2 m_\mathrm{e}} L_\mathrm{C} \int \frac{\vec{v}_\mathrm{i} - \vec{v}_\mathrm{e}}{|\vec{v}_\mathrm{i} - \vec{v}_\mathrm{e}|^3} f(\vec{v}_\mathrm{e}) \mathrm{d}\vec{v}_\mathrm{e}. \tag{2.39}$$

The force vanishes, if the ion and electrons velocities are the same, and is maximal when the relative velocity $\vec{v}_\mathrm{i} - \vec{v}_\mathrm{e}$ reaches the thermal velocity spread of the electrons.

Through the electrostatic acceleration of the electron beam and the presence of the magnetic guiding field, the temperatures of the electrons are anisotropic. Thus, it is convenient to differentiate between a longitudinal $T_\parallel$ and transverse $T_\perp$ temperature, which are related to the longitudinal $\vec{v}_\parallel$ and transverse $\vec{v}_\perp$ electron velocities, respectively [44, p. 22]

$$k_\mathrm{B} T_\parallel = m_\mathrm{e} \left(\left\langle v_\parallel^2 \right\rangle - \left\langle v_\parallel \right\rangle^2 \right), \tag{2.40}$$

$$k_\mathrm{B} T_\perp = \frac{m_\mathrm{e}}{2} \left(\left\langle v_\perp^2 \right\rangle - \langle \vec{v}_\perp \rangle^2 \right), \tag{2.41}$$

where k_B is the Boltzmann constant, m_e is the electron mass and $\vec{v}_\parallel$, $\vec{v}_\perp$ are the longitudinal and transverse component of the electron velocity vector $\vec{v}_\mathrm{e}$ with respect to the electron beam axis. The additional factor 2 in equation (2.41) accounts for the two contributing degrees of freedom in the transverse coordinate. In the following we are considering a co-moving reference frame, where the average velocities are $\langle v_\parallel \rangle = 0$ and $\langle \vec{v}_\perp \rangle = 0$. In this frame the electron velocity distribution is represented by an anisotropic Maxwell-Boltzmann distribution

$$f(\vec{v}_\mathrm{e}) = \frac{m_\mathrm{e}^{3/2}}{(2\pi k_\mathrm{B})^{3/2} T_\parallel^{1/2} T_\perp} \exp\left(-\frac{m_\mathrm{e} v_\parallel^2}{2 k_\mathrm{B} T_\parallel} - \frac{m_\mathrm{e} v_\perp^2}{2 k_\mathrm{B} T_\perp} \right). \tag{2.42}$$

For several reasons the electron beam is guided by a longitudinal magnetic field, which are (i) the merging and demerging of electrons and ions, (ii) the reduction of the transverse electron temperature, (iii) the suppression of the kinetic energy relaxation (TLR, see below), and (iv) the prevention of blow-up of the electron beam due to its internal Coulomb repulsion. As a consequence of the presence of this magnetic field $\vec{B}$ the electrons are not entirely free but move on spiral trajectories around the magnetic field lines with a revolution frequency given by the *cyclotron frequency*

$$\omega_\mathrm{c} = \frac{eB}{m_\mathrm{e}}. \tag{2.43}$$

The radius of the spiral is denoted by the *cyclotron radius*

$$r_\mathrm{c} = \frac{m_\mathrm{e} v_\perp}{eB}, \tag{2.44}$$

and the longitudinal distance an electron travels per cyclotron spiral is given by the *cyclotron length*

$$\lambda_\mathrm{c} = 2\pi\frac{v_\parallel}{\omega_\mathrm{c}} = 2\pi\frac{m_\mathrm{e}v_\parallel}{eB}. \tag{2.45}$$

For the merging and demerging of the electron and ion beam the magnetic guiding field has necessarily curved regions, which give rise to gradients of the magnetic field. In order to adiabatically transport the electron beam and to avoid heating effects, the change of the magnetic field strength in longitudinal direction z must be much smaller then the total magnetic field over one cyclotron length λ_c [45]

$$\left|\frac{\mathrm{d}B}{\mathrm{d}z}\right| \ll \frac{B}{\lambda_\mathrm{c}}. \tag{2.46}$$

Fulfilling this criterion it is also possible to lower the transverse temperature of electron beams by so-called *adiabatic magnetic expansion* [46, 47]. The method is based on two adiabatic invariants, which are (i) the product of the squared beam radius and the magnetic induction $R^2B = \mathrm{const}$ [42, p. 17] and (ii) the ratio of the mean transverse energy and magnetic induction $\langle E_\perp\rangle / B = \mathrm{const}$ [48]. From the first invariant it follows that an electron beam increases its radius when traveling from a high initial magnetic field region B_i to a lower final magnetic field region B_f, by

$$R_f = \sqrt{\frac{B_i}{B_f}}R_i = \sqrt{\alpha}R_i. \tag{2.47}$$

Here $\alpha := B_i/B_f$ is the *magnetic expansion factor*. Accordingly, the electron density n_e is lowered by $1/\alpha$ simultaneously.

The second invariant has the consequence that the transverse temperature is reduced by the inverse of the expansion factor α:

$$k_\mathrm{B}T_{\perp,f} = \frac{k_\mathrm{B}T_{\perp,i}}{\alpha} = \frac{k_\mathrm{B}T_\mathrm{cath}}{\alpha}. \tag{2.48}$$

The initial temperatures $T_{\perp,i}$ and $T_{\parallel,i}$ of the electron beam are both determined by the cathode temperature T_cath, where the electrons are produced near thermal equilibrium and the velocity distribution before the beam formation can still be assumed isotropic.

Since the electrons are electrostatically accelerated by a voltage U_0 their longitudinal temperature is reduced in the co-moving reference frame. Using the kinematic transformation from the laboratory to the co-moving reference frame the final longitudinal temperature can be calculated to be [49, p. 42]

$$k_\mathrm{B}T_{\parallel,f} = \frac{(k_\mathrm{B}T_\mathrm{cath})^2}{2eU_0}. \tag{2.49}$$

The factor 2 in the denominator follows from a specific consideration regarding the anisotropy which is described in [49]. As the electron kinetic energy is conserved during the magnetic expansion, energy is shifted from the transverse degrees of freedom into the longitudinal one. The transferred energy is equal to $(1-\alpha^{-1})k_{\mathrm{B}}T_{\mathrm{cath}}$, as can be calculated from equation (2.48). But again, because of the transformation from the laboratory to the co-moving reference frame this energy contribution is reduced and the longitudinal temperature is given by [50]

$$k_{\mathrm{B}}T_{\parallel,f} = \left(\left(1+\left(1-\alpha^{-1}\right)^2\right)\frac{(k_{\mathrm{B}}T_{\mathrm{cath}})^2}{2eU_0} \approx \frac{(k_{\mathrm{B}}T_{\mathrm{cath}})^2}{eU_0}. \tag{2.50}$$

Since the desired magnetic expansion factor for the CSR electron cooler is $\alpha = 20$, the expression in round brackets can be approximated by 2.

Up to now we considered a simplified situation when treating the electron beam as an ideal gas of non-interacting free particles. But due to the COULOMB interaction among the electrons different plasma relaxation effects appear, which will be briefly discussed in the following. For more detailed discussions see [51–53].

The acceleration process of the electrons is highly anisotropic. The electron cloud, initially at rest, is elongated along the electron beam axis whereas the transverse coordinate is not affected. This leads to a changed potential energy of the interacting electrons, which directly after the acceleration is not minimized as in an equilibrium plasma. The excess of potential energy is then transferred into kinetic energy and contributes to the longitudinal temperature. The effect [51] is called *longitudinal-to-longitudinal relaxation* (LLR). Thus, another term must be added to equation (2.50), which depends on the density of the electrons n_{e} as [51, p. 46]

$$k_{\mathrm{B}}T_{\parallel,f} \approx \frac{(k_{\mathrm{B}}T_{\mathrm{cath}})^2}{eU_0} + C\frac{e^2}{4\pi\varepsilon_0}n_{\mathrm{e}}^{1/3}, \tag{2.51}$$

where C is a dimensionless parameter representing the degree of adiabaticity of the acceleration process. It is ~ 1.9 for a fast acceleration process [51].

Hence, the final achievable electron temperatures (see equation (2.51) and (2.48)) are basically defined by the cathode temperature T_{cath} of the electron source and the extractable electron density n_{e}. For the commonly used thermionic electron sources, where a filament is heated to high temperatures and the electrons are extracted electrostatically, the energy spread is of the order of $k_{\mathrm{B}}T_{\mathrm{cath}} \approx 100\,\mathrm{meV}$. Much lower temperatures can be achieved by the usage of semiconducting photocathodes, where the electrons are excited to the conducting band by a laser beam and extracted into the vacuum. With these devices typical cathode temperatures of $k_{\mathrm{B}}T_{\mathrm{cath}} \approx 10\,\mathrm{meV}$ can be realized when cooling the cathode to liquid nitrogen temperatures [54]. The typical electron densities are of the order of $10^6\,\mathrm{cm}^{-3}$ [55]. To maintain reasonably

high electron densities also at low cooling energies envisaged at CSR, as recently shown in [56], the *beam deceleration technique* will be applied at the CSR electron cooler. In section 4.1 this will be discussed in more detail.

When calculating the expected longitudinal and transverse temperatures with equations (2.51) and (2.48) for the cathode temperatures of the already existing cryogenic photocathode setup of the TSR electron target [55], which will be used for CSR electron cooler, one gets longitudinal temperatures of some tens of μeV and transverse temperatures of $\sim 1\,\mathrm{meV}$. This inequality gives rise to the *transverse-to-longitudinal relaxation* (TLR). In a non-magnetized electron beam this would lead to a thermal equilibrium by equalizing all temperatures. However, in a magnetic field with a certain strength this relaxation process can be effectively suppressed. Already at a minimum magnetic induction of $B_{\mathrm{min}}^{\mathrm{TLR}} \approx 20 - 50\,\mathrm{G}$ this effect can be neglected for the CSR electron cooler [43, p. 41].

Also the space-charge (SC) of the electron beam itself gives rise to a velocity spread of the electrons, even in a longitudinal magnetic guiding field. The almost constant electron density creates a radially outwards pointing electrostatic field. In combination with the axial magnetic field the electrons perform a drift motion around the electron beam axis. The minimal required magnetic induction, where the transverse divergence is still prevented, is given by the BRILLOUIN field $B_{\mathrm{min}}^{\mathrm{SC}} = \sqrt{2 n_{\mathrm{e}} m_{\mathrm{e}} / \varepsilon_0}$ [57, p. 6]. In case for the CSR electron cooler one calculates for the highest reasonable electron densities of $n_{\mathrm{e}} = 1 \times 10^8\,\mathrm{cm}^{-3}$ (compare [43, fig. 3.16]) a value of $B_{\mathrm{min}}^{\mathrm{SC}} \approx 45\,\mathrm{G}$.

Finally we are now able to estimate the *cooling time*, which is the exponential time constant after which an ion beam is phase space cooled, from the cooling force given by equation (2.39). The cooling time τ_{cool} is defined via $F_{\mathrm{cool}} = -m_{\mathrm{i}} v_{\mathrm{i}} / \tau_{\mathrm{cool}}$, where m_{i}, v_{i} are the mass and velocity of the ion beam, respectively. The electron velocity distribution is given by equation (2.42) and the expected longitudinal and transverse temperatures by the equations (2.51) and (2.49). This estimation has already been done for the CSR electron cooler in detail in [43, fig. 3.20], which is based on experimental measurements of the electron densities achievable by the *beam deceleration technique* [56, chap. 3] and therefore it will not be redone here. Nevertheless for rough estimations of the cooling time the 'time of relaxation' is very useful, which an electron-ion plasma with different temperatures for electrons and ions needs to equalize its temperature [42, p. 135]

$$\tau_{\mathrm{cool}} = \frac{3(4\pi\varepsilon_0)^2 m_{\mathrm{e}}}{8\sqrt{2\pi} e^4} \frac{m_{\mathrm{i}}}{z^2} \frac{1}{n_{\mathrm{e}} L_{\mathrm{C}}} \left(\frac{k_{\mathrm{B}} T_{\mathrm{i}}}{m_{\mathrm{i}}} + \frac{k_{\mathrm{B}} T_{\mathrm{e}}}{m_{\mathrm{e}}} \right)^{3/2} . \tag{2.52}$$

Since the thermal velocity spreads of the ions is much smaller than these of the electrons the first term in round brackets is negligible. Neglecting also the dependencies

of the COULOMB logarithm $L_C(n_e, T_e, Z, v_i)$ then equation (2.52) essentially scales like

$$\tau_{cool} \propto \frac{m_i}{z^2} \frac{T_e^{3/2}}{n_e}. \tag{2.53}$$

Here the main challenge of electron cooling at low energies gets obvious. For molecular heavy ions the charge-to-mass ratio becomes relatively small, since most molecules can typically not be produced with higher charge states than $z = 1$ without breaking their chemical bonds. Thus, in order to reach short cooling times compared to the ion storage time it is crucial to create as cold as possible electron temperatures T_e and to maintain as high as possible electron densities n_e.

2.3 The CSR facility

The Cryogenic Storage Ring [28, 58] is an electrostatic ion storage ring which can be cooled down to cryogenic temperatures of $\sim 10\,K$. Figure 2.6 shows a schematic overview of CSR. CSR has a quadratic layout consisting of four straight sections and four 90° corners. The ring lattice is optimized for long free straight sections (A-D) dedicated to experiments. The electrostatic optical elements are altogether placed in the corners, consisting of two pairs of quadrupoles (3), two cylindrical 6° deflectors (2), and two cylindrical 39° deflectors (1). This arrangement allows a neutral particle detector (12) following a straight section to have a collecting angle of ±1° with respect to the middle of a straight section. It also allows a single turn injection scheme by fast switching of one of the 6° deflectors (so-called *kicker electrodes* (4)).

The circumference of the storage ring is 35.12 m, of which each straight section has 2.6 m length. The vacuum system, discussed in detail in the subsequent sections 2.4 and 2.5, consists of an inner ion beam vacuum pipe embedded in a larger outer vacuum system with rectangular cross section. The outer vacuum chamber has large openings allowing good access on the internal structure. For the cryogenic operation there are in addition two radiation shields embracing the inner vacuum pipe. The cryogenic concept of the storage ring is also discussed in detail in the subsequent section.

There are several diagnostic tools (label (5) to (12)) installed, which will be discussed later in section 2.6. Especially the final development and the realization of the capacitive pick-up electrode system, consisting of the current (6), SCHOTTKY (7), and the position pick-ups (8), are discussed in detail in chapter 3. One of the straight sections (C) is specifically dedicated to the ion beam diagnostic system.

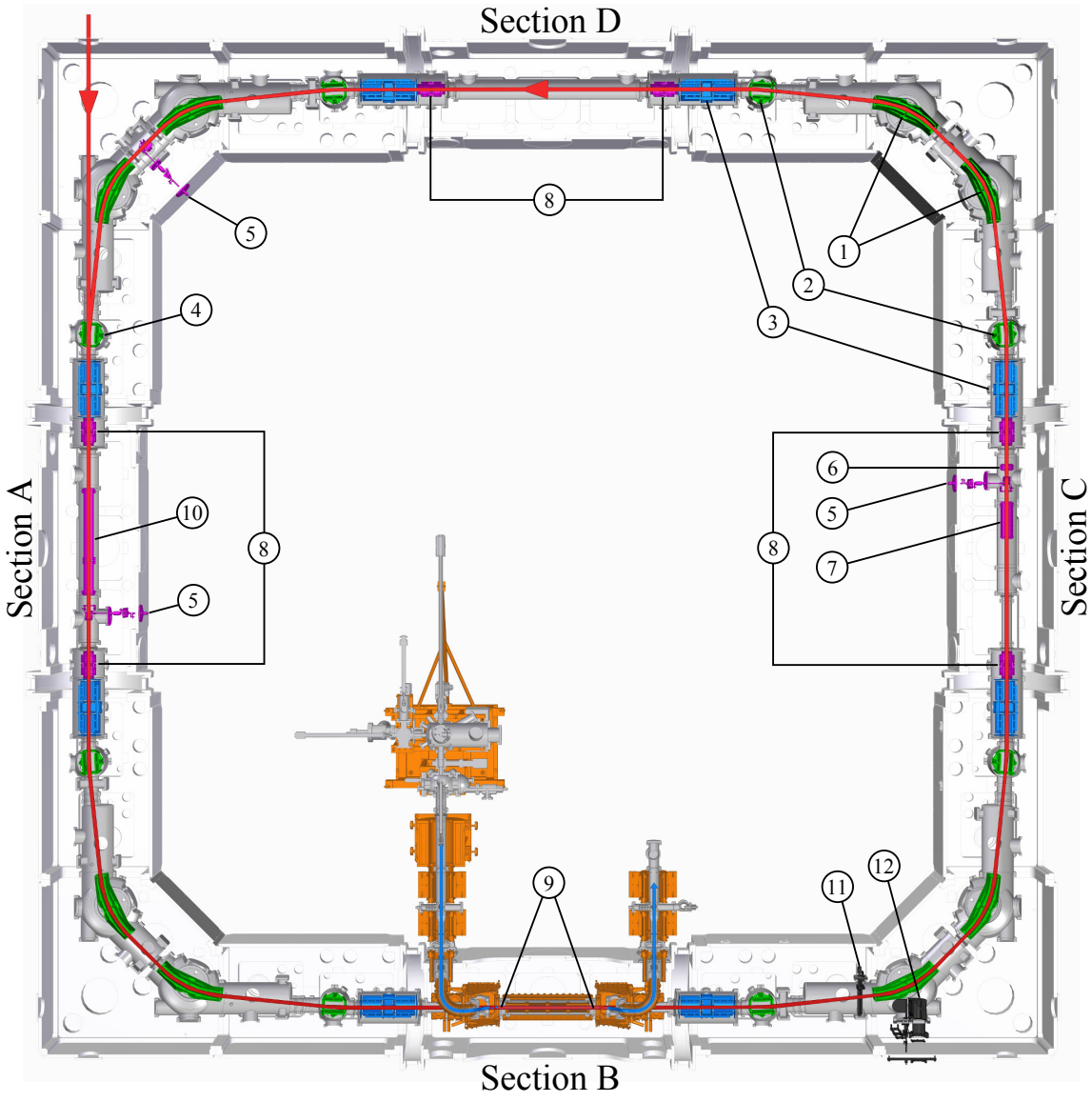

Figure 2.6: Schematic overview of CSR with the (red line) ion beam trajectory, (1) 39° deflectors, (2) 6° deflectors, (3) quadrupole dublets, (4) injection kicker, (5) first-turn diagnostics (beam profile monitors), (6) current pick-up, (7) SCHOTTKY pick-up, (8) position pick-ups, (9) wire scanners (10) rf system, and detectors for (11) charged and (12) neutral products. The straight sections are dedicated to the (Section A) co-linear neutral target, (Section B) electron cooler/target, (Section C) beam diagnostics, and (Section D) reaction microscope.

The remaining straight sections are dedicated to the experimental platforms for electron-ion, neutral-ion, and photon-ion studies. In section (B) the future electron cooler (coloured orange) will be installed, which also will serve as the merged beam

electron target for the ion beam. The developments towards the finalized device are presented in chapter 4. The reaction products of ion-electron collisions will be detected by several detectors following the straight section (B). There is one neutral particle imaging detector (12), which was developed and realized as described in [59], and one counting detector for charged reaction products (11), which was developed and realized as described in [60, 61]. In future, adapted versions of the latter detector will also be installed at other positions.

In section (A) the stored ion beam will interact with a merged neutral beam, which will be created in the injection beam line by photodetachment of anions. The reaction products will be detected in a similar manner as discussed for the electron target. For more details on this setup see [62]. The interaction of stored ions with an atomic or molecular gas jet or with a laser beam in crossed beam geometry will be studied in the 'reaction microscope' [63], which will be installed in section (D). In this setup all reaction products (electrons and ions) will be detectable in coincidence.

Another important component of the CSR facility is the ion production. The positive and negative ions will be produced by several kinds of ion sources, which will be installed on an electrostatic high voltage platform. In order to enable electron cooling of relatively heavy molecules, the high voltage platform and the electrostatic ion optics of the storage ring itself are designed for ion energies up to 300 keV per charge unit. This still involves a challenging demand on the electron cooler design, since the electron beam must be relatively slow and still maintain a good beam quality and sufficient electron density. This will be discussed in section 4.1 in more detail.

The ion beams are electrostatically accelerated to kinetic energies up to 300 keV per charge unit and then guided through a, mainly electrostatic, transfer beamline into CSR. Dipole magnets integrated into the transfer beamline can be used for mass selection of the injected ion beam. Also these can be exchanged by electrostatic dipole deflectors in the future in order to have a complete electrostatic ion storage facility providing the advantages discussed in section 2.1. The design of the transfer beamline is discussed in [62].

For the first cryogenic beamtime of CSR (see chapter 5) the high voltage platform was limited to 90 keV and the available ion sources were a PENNING and a Cs-sputter ion source producing positive and negative ions, respectively. The electron cooler was not yet installed. A laser interaction setup was applied in Section B and used in connection with the single-particle detectors described.

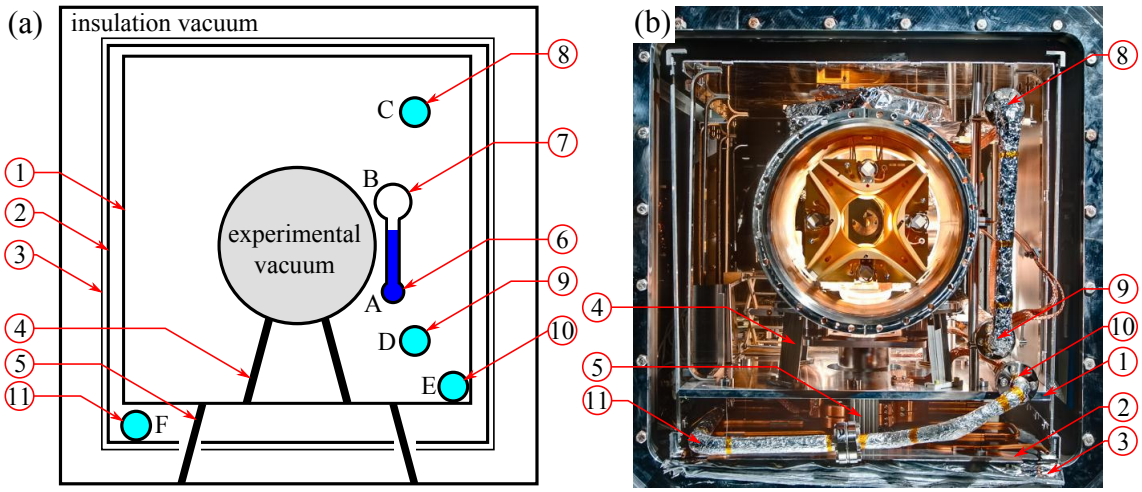

Figure 2.7: A cross section of CSR shown (a) schematically and as a (b) photograph, with (1) the inner radiation shield (40 K shield), (2) outer radiation shield (80 K shield), (3) multilayer insulation, (4+5) titanium posts, (6) 2 K-He-supply, (7) 2 K-He-return, (8) first 5 K-He-turn, (9) second 5 K-He-turn, (10) 40 K-He-turn, and (11) 80 K-He-turn. A-F: The six ring tubes of the cryogenic helium refrigeration system in the sequence of flow.

2.4 Cryogenic operation

Extremely high vacuum (XHV) is a need for long storage times of slow beams of heavy molecules and clusters. CSR is designed to achieve a rest gas pressure of the order of 10^{-13} mbar (room temperature equivalent) in cryogenic operation. This corresponds to approximately 2000 particles per cm^3. Large copper surfaces cooled to the temperature of liquid helium act as cryo condensation pumps for H_2, the main residual gas component under these conditions. In a previous study [64] this pumping scheme was investigated at a ~ 3 m long prototype setup of similar cryostat cross section. Pressures of $< 10^{-13}$ mbar could be demonstrated at ~ 10 K temperature.

At CSR there are five cryocondensation pumps per corner and two per straight section, summing up to 28 pumping units distributed over the circumference of the ring. The beam pipe (*experimental vacuum*) itself is cooled to ~ 10 K, also serving as a huge cryo-adsorption-pump. Additionally, the cooling of the beam pipe has the advantage of a very weak black-body radiation field stored ions are interacting with. This allows stored ions, with non-vanishing electric dipole moment, to reach their rovibrational ground state and imitates interstellar conditions, as discussed in chapter 1. In order to reach these low temperatures over the whole ring, CSR has a cryostat design as shown by figure 2.7 in a schematic cross section. The coldest

part including the cryocondensation pumps has been constructed to operate with superfluid helium of 2 K temperature.

The experimental vacuum chamber is mounted inside a larger additional vacuum chamber, which is mainly pumped by turbo-molecular pumps. This *insulation vacuum* has a pressure of the order of 10^{-6} mbar preventing heat transport by convection of gases. Two radiation shields of which the outer one (80 K shield) is additionally wrapped in multilayer insulation (MLI) [65, 66] lower the room temperature blackbody radiation onto the experimental vacuum chambers. For compensating the poor thermal conductance of the stainless steel vacuum chambers close to liquid He temperature they are additionally wrapped in thin oxygen free copper foil. To minimize the thermal conduction input the experimental vacuum chambers are supported by thermally insulating titanium posts. The inner chambers are mounted by these onto the inner radiation shield (40 K shield), which itself is mounted by similar posts onto the room temperature outer vacuum chamber.

The cooling power for CSR is supplied by a commercial Linde helium refrigerator system [67]. It delivers a cooling power of 20 W at 2 K superfluid helium and additional 600 W at 80 K gaseous helium [28]. The helium is distributed in the ring in two independent pipe systems. The liquid helium pipe system is connected to all cryocondensation pumps and experimental vacuum chambers in one circuit. The helium vaporizes and is being returned to the refrigerator. The circuit for the gaseous helium consists in a total of four turns around the ring. The helium gas has initially 5 K and cools in its first two turns the cryogenic amplifiers of the diagnostic system (see chapter 3) and additional charcoal cryopumps for a room temperature operation of the storage ring (see section 2.5). In the last two turns (40 K and 80 K pipes) the helium is used to cool both thermal radiation shields one after the other, compare to the label A-F in figure 2.7 indicating the sequence of flow.

The ion beam optics have a high demand on the exact positioning of the elements to allow storage of an ion beam. In order to ensure that the deflectors and quadrupoles do not move by the thermal shrinking in the cooldown of CSR to cryogenic temperatures, they are individually supported directly on concrete foundations using a combination of poor thermally conducting fiberglass (G-10) and thin-walled stainless steel cylinders [68]. Bellows between these supports and the experimental vacuum chambers allow independent movement of the vacuum chambers and shields with respect to the ion beam optics. The mechanical construction has been described in detail in an earlier publication [28].

2.5 Room temperature operation

CSR can also operate at room temperature for several reasons. In principle this allows experiments on stored ion beams also at intermediate temperatures between room temperature and cryogenic temperatures. A more technical aspect is the better initial vacuum conditions prior to the cooldown of CSR, lowering the gas load during the cryogenic operation. Moreover, the commissioning of the electron cooler is facilitated, since only the superconducting coils of the electron cooler have to be cooled down to cryogenic temperatures.

To achieve ultrahigh vacuum (UHV) conditions also in absence of cryopumping, all beam guiding vacuum chambers of CSR are equipped with resistive heating elements for bakeout to 250 °C. The experimental vacuum is pumped with ion getter pumps (Varian StarCell), 16 non-evaporating getter pumps (NEG, SAES ST 707 strips), and 6 charcoal cryopumps. The inner stages of the cryopumps are coated with charcoal and are connected to the first 5 K-He line (loop C). Their shields are connected to the second turn (loop D). For room temperature operation of CSR the helium refrigerator system provides cooling for the cryopumps, the diagnostic system (see chapter 3), and the electron cooler (see chapter 4). During bakeout the chambers are heated to 250°C and the NEG-pumps are activated at 450°C. An additional water circuit system inside CSR is mounted to the 80 K shield preventing the non bakeable multilayer insulation from damaging.

The baking procedure of the entire ring was performed in 2015. After activation of the NEG pumps and cooldown to room temperature a pressure of $\sim 1.5 \times 10^{-10}$ mbar was reached.

2.6 Overview of the diagnostic tools of CSR

For monitoring and for measuring the properties of a stored ion beam, CSR is equipped with a full set of diagnostic tools. For the initial adjustment of the ion beam orbit there are three beam profile monitors (also called beam viewers or first-turn diagnostics) installed in CSR (label (5) in figure 2.6). The first beam profile monitor is positioned directly on the injection line, the second after half a turn, and the last after almost one completed turn. They are based on rotatable converter electrodes, which are hit by the incident ion beam. Secondary electrons are created there and accelerated to a multi-channel plate (MCP), which is backed by a phosphorous screen. The electrons are multiplied by the MCP and give rise to light emission. By observing the screen with a camera from the outside of the vacuum the beam

profile can be measured. At the given low ion energies of CSR, this leads to the destruction of the ion beam. The beam profile monitors are not suitable for the detection of a stored ion beam. An important role is played by non-destructive electronic diagnostics, described in the following.

After the injection and storage of an ion beam the first important tool for the detection and proof of storage is the current pick-up (label (6) in figure 2.6). It is based on the charging effect of the electrode by a passing ion beam. By the switching of the kicker electrodes (4) a time structure is imprinted onto the injected ion beam. This modulation of the stored ion beam can be detected for the first hundreds or thousands of revolutions. Furthermore, by calibration of the amplification system the number of injected and stored particles can be measured. With the knowledge of the circumference of the storage ring the ion energy can also be calculated from the measured revolution frequency. The design of this pick-up will be discussed in detail in section 3.3 and measurements performed during the CSR commissioning are presented in chapter 5.

After the time structure of the ion beam due to its injection has decayed, a continuous (DC) beam remains stored in CSR. On such a beam, still fluctuations from the SCHOTTKY noise [69, 70] are measurable. From statistical density fluctuations of the stored ions a noise signal arises at the harmonics of the revolution frequency of the stored ions. The SCHOTTKY pick-up (label (7) in figure 2.6) is specifically designed for detecting these small signals. With the frequency spectrum of this noise, it is possible to monitor the momentum spread of the initially injected ion beam and, once the electron beam cooler will be installed, especially the change in momentum spread during electron cooling. It is also an important tool for adjusting the electron cooler and ensuring the velocity matching of electrons and ions. This pick-up will be discussed in section 3.5 and respective measurements are presented in section 5.6.

As a further diagnostic tool, CSR has six position pick-ups (label (8) in figure 2.6) that can locate the center of charge of the stored ion beam in the transverse plane. They are installed at both sides of each straight section (except for the electron cooler section). They can measure both transverse coordinates x and y and are based on the charging effect of their electrodes by a bunched ion beam that passes through them. The closed orbit can be monitored in real time and can be adapted to the needs of the experiments, e.g. changing the overlap or angle of neutral beam and stored beam or with the gas jet target. These pick-ups are discussed in section 3.4 and measurements are presented in section 5.5.

Because of spatial constraints the electron cooler section itself will be equipped with wire scanners (label (9) in figure 2.6) instead of electronic position pick-ups. They are used for detecting both the electron and ion beam. From their special shape

both transverse coordinates are extractable and the overlap of both beams can be ensured.

For manipulating the longitudinal structure of the ion beam CSR has a drift tube (also called rf system, label (10) in figure 2.6) in the injection straight section (A). In order to avoid cross talk of the bunching signal onto the current or SCHOTTKY pick-ups it is on purpose installed on the opposite side of the ring as compared to the diagnostic section (C). By the usage of the rf system the ion beam can be actively bunched and also de- or accelerated. The bunching is either necessary for the ion beam position pick-up system or the needs of experiments, where a series of short ion bunches may be preferred rather than a coasting beam. The design of the rf system is discussed in section 3.8 and bunching measurements are presented in section 5.3.

Also the single-particle detectors for charged (called COMPACT detector, label (11) in figure 2.6) [60, 61] and neutral products (called NICE detector, label (12) in figure 2.6) [59] can be used for diagnostics of the stored ion beam. Both are reliable tools for measuring the ion beam lifetime and also the longitudinal structure of the stored ion beam. Additionally, the NICE detector can be used for the measurement of the transverse beam profile detecting and imaging the neutralized particles originating from collisions of the ion beam with rest gas molecules or electrons or from the photo-detachment by a laser.

Later addition of a Cryogenic Current Comparator (CCC) [71–74] is planned, which will be used for the measurement of the ion beam intensity of bunched and coasting ion beams. This device has a similar working principle as dc-transformers, but it is based on the measurement of the magnetic field of a circulating ion beam using SQUIDs (Superconducting QUantum Interference Device).

The realization of the diagnostic system described in this work departs from the previous work of F. LAUX [75]. He developed the cryogenic pre-amplifier for the use in CSR, which is now implemented for all three pick-up systems. He also tested the concept of using only a single amplifier per position pick-up coordinate by applying cryogenic electrical relays. Basic conceptional design studies were performed by F. LAUX for the pick-up electrodes and for the screening boxes containing the cryogenic electronics. The here presented work has realized the final design and setup of all non-destructive diagnostic elements and found solutions for many detailed requirements, such as transmission of small electrical signals and cryogenic compatibility. The following chapter 3 describes the final design and the setup of the entire non-destructive diagnostic system, consisting of the current, SCHOTTKY, and position pick-ups and their respective signal amplification systems. The measurements performed during the commissioning of CSR are presented then in chapter 5.

Chapter 3

The Diagnostic System of CSR

In this chapter the development and realization of the electronic diagnostic system of CSR is described. After the discussion of the challenges and requirements of this system, first a brief overview of the entire diagnostic system is given in order to guide the reader through this setup. Then the individual pick-ups (current, position, and SCHOTTKY) with their respective working principles, the characteristics regarding their pick-up electrodes and their individual measuring electronics are presented. Since the amplification system of all three sub-systems is similar it is discussed entirely after the description of the sub-systems also pointing out the differences between the individual systems. At the end of this chapter the cryogenic realization and the rf system are described.

3.1 Challenges and requirements

For realizing the CSR diagnostic system a number of physical and technical aspects have to be taken into account, the most important of which are briefly discussed here.

Sensitivity

A main criterion is the required sensitivity of the electronic pick-ups and, hence, the intensity of the ion beams that can be stored in CSR. For this the space charge limit must be estimated. Because of their space charge the ions in stored beams experience a defocusing force, by which the tune and consequently the working

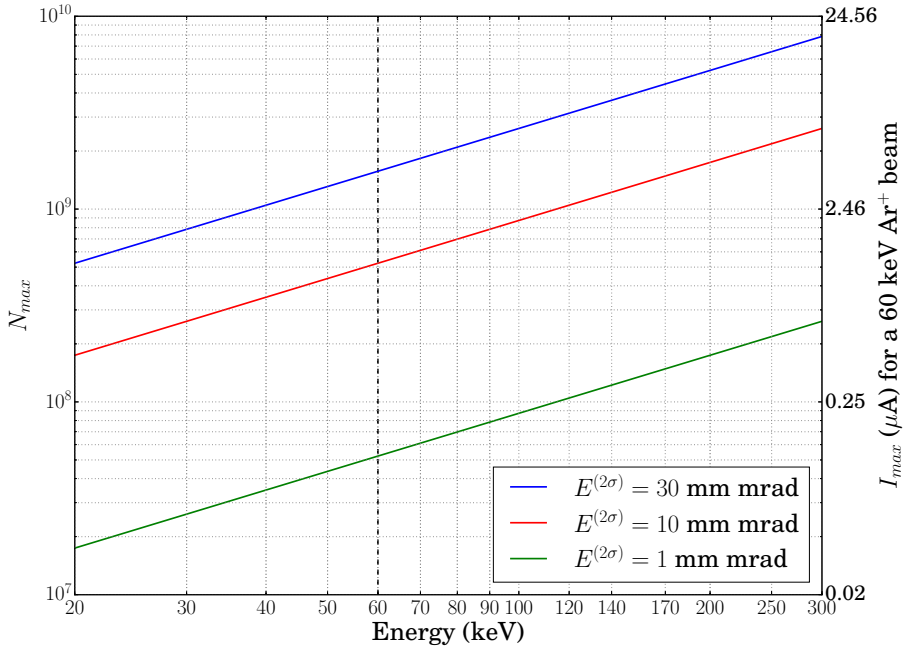

Figure 3.1: The incoherent space charge limit of CSR for the maximum tune shift of $|\Delta Q| = 0.1$ at various 2σ-emittances $E^{(2\sigma)}$ as a function of beam energy. The left ordinate shows the maximal number of storable ions, whereas the right one shows the maximal ion beam current of an $^{40}Ar^+$ beam with 60 keV (energy marked with the black dashed line). The emittances are discussed in the text.

point of the storage ring is changed. Above a certain value ΔQ for this tune change resonances may be crossed and the ion beam is lost. The maximal number of storable ions N_{max} can be estimated by the *incoherent tune shift* [76]

$$N_{\mathrm{max}} = \frac{2\pi}{r_{\mathrm{p}}} \frac{A}{z^2} \beta^2 E^{(2\sigma)} \left(-\Delta Q\right) \tag{3.1}$$

with the classical proton radius $r_{\mathrm{p}} = e^2/(4\pi\varepsilon_0 m_{\mathrm{p}} c_0^2)$, the mass number A, and charge state z of the ion beam, the velocity in units of the speed of light $\beta = v/c_0$ and the 2σ-emittance of the ion beam $E^{(2\sigma)}$.

The maximal number of singly charged ions of mass A and with $z = 1$ scales as $N_{\mathrm{max}} \propto A\,\beta^2$ and, hence, proportional to the beam energy. Thus, the calculated N_{max} applies for all singly charged particles with the same energy. The maximal allowed tune shift at which a resonance is crossed can be estimated from figure 2.2 with $\Delta Q = -0.1$. Depending on the emittance of the ion beam there can be calculated a different maximal number, which is shown in figure 3.1 for various 2σ-emittances of CSR as a function of the relevant ion energies.

The highest possible emittance can be estimated from the simulated dynamical acceptances of $A_x = 120\,\mathrm{mm\,mrad}$ (for $\epsilon_y \to 0$) and $A_y = 180\,\mathrm{mm\,mrad}$ (for $\epsilon_x \to 0$) [35] (see section 2.1.1). Assuming a symmetric ion beam with equal transverse emittances $E_x = E_y$ filling the acceptance by 3σ gives for the 3σ-emittance $E^{(3\sigma)} = A_x/2 = 60\,\mathrm{mm\,mrad}$. Hence the maximal 2σ-emittance amounts to $E^{(2\sigma)} = 4/9 \cdot E^{(3\sigma)} \approx 30\,\mathrm{mm\,mrad}$, which is shown as a blue line in figure 3.1. The lowest emittance (green line) has been set to 1 mm mrad demonstrating the case which should be reached in future with an operational electron cooler. The true emittance may be even lower. The 10 mm mrad (red line) is a rough estimate of the emittance $E^{(2\sigma)}$ of the ion beams actually used during the commissioning beamtime.

Since the maximal ion beam current $I = N\,z\,e\,v/C_0$ depends also on the velocity v of the ion beam it differs for the different ion species. For this reason the maximal beam current at the space charge limit is shown only for the case of an $^{40}Ar^{+}$ beam with 60 keV (right ordinate in figure 3.1 corresponding to the vertical black dashed line). An $^{40}Ar^{+}$ ion beam has been mainly used for the measurements discussed in chapter 5. Thus, the expected maximal number of storable ions was $0.5 - 1.6 \times 10^9$ corresponding to a current of $1.3 - 3.9\,\mu$A for the cases of $E^{(3\sigma)} = 10 - 30\,\mathrm{mm\,mrad}$, respectively.

Frequency range

The relevant ion energies of CSR reach from 20 to 300 keV, which defines the frequency range where the diagnostic system has to be sensitive. The fastest singly charged ion is a proton with 300 keV energy circulating with a revolution frequency of $f_{\mathrm{rev}} = 216\,\mathrm{kHz}$. Also higher frequencies up to 1 MHz must be reached in order to be able to measure higher harmonics of the revolution frequencies. The lower frequency limit can be defined by f_{rev} for a singly charged ion of 20 keV energy and an atomic mass of $A \approx 200$, which calculates to a revolution frequency of approximately 4 kHz.

Cryogenic Operation

One of the most crucial technical aspects is the compatibility of the diagnostic system with both operation modes of CSR. On the one hand a most sensitive system is desired on the other hand for the signal connections the heat input on the cryogenic cooling machine has to be considered. While another limitation is that bakeout at 250 °C should be possible for all elements of CSR. Here a practical solution mainly with respect to the cryogenic amplification system had to be developed.

3.2 Overview of the diagnostic section

Before we discuss the individual pick-up systems in detail an overview of the entire setup is given in this section. Most parts of the diagnostic system are situated in the diagnostic straight section (section (C) in figure 2.6), which will be considered in detail. Position pick-ups of the same design are distributed over further locations along the ring circumference.

In figure 3.2 half of the diagnostic section is depicted schematically viewed from the inside of the storage ring. Shown is the outer frame of the insulation vacuum chamber (8), in which the actual ion beam pipe (4) is embedded. The ion beam is shown as a red arrow. The pick-up electrodes of the three sub-systems are mounted inside of the ion beam vacuum system. These are the (1) current pick-up, whose electrode is coloured magenta, (2) the position pick-up, and the (3) SCHOTTKY pick-up, whose electrode is coloured orange. The remaining five position pick-ups are at different but symmetric locations of the storage ring (label (8) in figure 2.6).

Each of the sub-systems has its own amplification chain (coloured dashed lines and triangles representing the individual amplifiers) for transmitting the induced signals to the outside of the storage ring. Although the individual pick-up systems have their own requirements, their amplification systems are very similar to each other. Each amplification system is based on a (5) cryogenic pre-amplifier (discussed in detail in section 3.6.1) and a room temperature (6) main amplifier (discussed in section 3.6.5). The cryogenic and the room temperature amplifiers are identical among each other, respectively, except for the current pick-up which has a different room-temperature main amplifier, discussed in section 3.3.3 specifically. The main differences of the sub-systems are in the cryogenic signal connection schemes of the respective electrodes, which will be discussed in detail in section 3.6.2. This modular scheme with partly identical components has been chosen on purpose to facilitate the manufacturing of the individual components, since in total 14 amplification chains had to be realized (one current, one SCHOTTKY, and 12 position pick-ups consisting of one amplifier chain per coordinate and location in the ring).

Each individual pre-amplifier, together with other cryogenic electronics which will be discussed later in section 3.6 in detail, is placed inside a screening box, which is attached inside the insulation vacuum to the (7) coldest gaseous helium line of the CSR refrigerator system (5 K-He line, loop C in figure 2.7). The main amplifiers are located at the atmospheric side directly at the insulation vacuum feedthrough.

The structure of the following sections is as follows. The basic theory of the operation principle of capacitive pick-ups is the same for all of the individual sub-systems. Only the procedure how the signals are interpreted and used to extract various

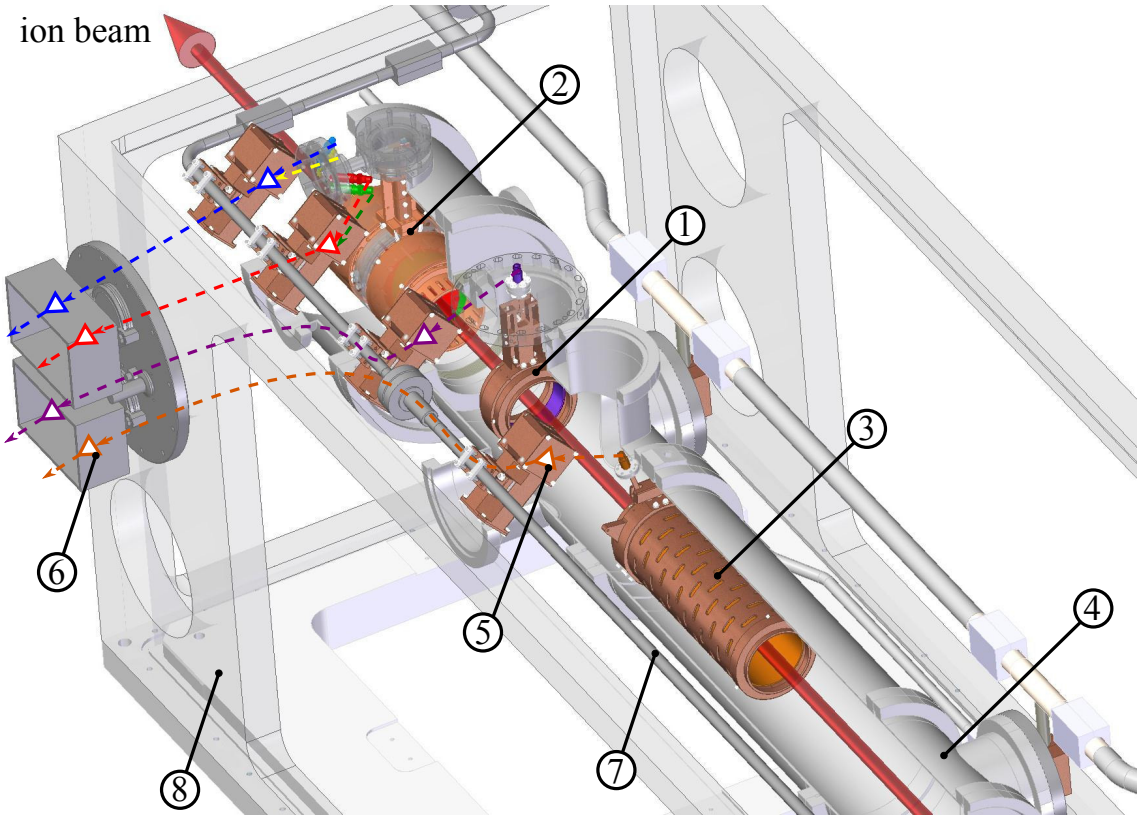

Figure 3.2: Schematic overview of part of the diagnostic section (section (C) in figure 2.6) viewed from the inside of the storage ring. Shown are the pick-up electrodes of the (1) current, (2) position, and (3) SCHOTTKY pick-ups, which are mounted inside of the (4) experimental vacuum chamber (ion beam pipe). With coloured dashed lines their respective amplification systems are indicated, consisting of (5) cryogenic pre-amplifiers and (6) room temperature main amplifiers. The former are mounted to the (7) first gaseous helium line (first 5 K-He line, compare figure 2.7) and the latter are outside of the (8) CSR insulation vacuum chamber connected directly to the vacuum feedthrough.

information about the ion beam differs. For this reason first the current pick-up is discussed in the subsequent section 3.3 with focus on the optimal design of the pick-up electrode and the measuring electronics for extracting the ion beam current. In a similar manner then the position pick-ups, section 3.4, and the SCHOTTKY pick-up, section 3.5, with all their individual characteristics are discussed. After that, finally, the individual components of the amplification chain of all three sub-systems are described altogether in section 3.6. Also the differences of the amplification systems are discussed. The chapter closes then with a discussion of the cryogenic realization of the entire diagnostic system, section 3.7, and the presentation of the rf system, section 3.8, which is used for manipulating the time structure of the ion beam.

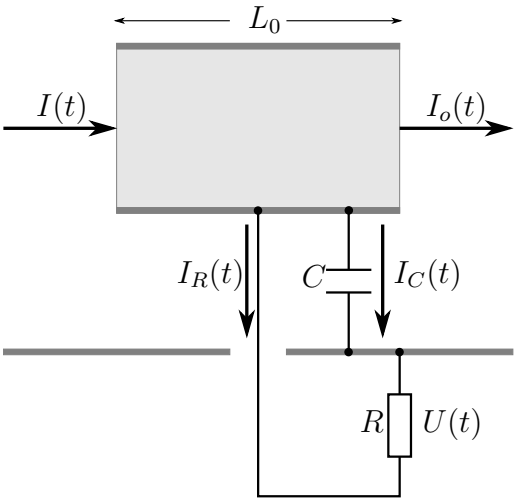

Figure 3.3: The principle of the current pick-up. Fulfilling KIRCHHOFF's junction rule the ingoing ion beam current $I(t)$ is equal to the sum of outgoing ion beam current $I_o(t) = I(t - \Delta t)$ and outgoing currents $I_R(t) + I_C(t)$.

3.3 The beam current pick-up

3.3.1 Theory of operation

A capacitive pick-up is in the simplest case a hollow tube oriented coaxial to the ion beam. Once an ion passes the pick-up its charge creates a mirror charge on the inner wall of the tube. By measuring this induced charge one has a non-destructive measurement principle of an ion beam.

Figure 3.3 shows this schematically. The pick-up with length L_0 is located in a grounded vacuum chamber and has a capacity C. An additional attached high-OHMic amplifier with input resistance R amplifies the arising signals. Fulfilling KIRCHHOFF's junction rule the ingoing ion beam current $I(t)$ is equal to the outgoing ion beam current $I_o(t) = I(t-\Delta t)$, where $\Delta t = L_0/v$ is the time an ion with velocity v needs for passing the pick-up. Additionally there are currents outgoing charging the capacitor $I_C(t)$ and resistor $I_R(t)$. Thus, it is

$$I(t) - I(t - \Delta t) = I_R(t) + I_C(t). \tag{3.2}$$

A TAYLOR series of the left hand side of this equation gives

$$\dot{I}(t)\,\Delta t + \mathcal{O}[\ddot{I}(t)\,(\Delta t)^2] = I_R(t) + I_C(t). \tag{3.3}$$

For ion bunches longer than the pick-up length it is justified to neglect the higher order terms. Using in addition the relations $I_R(t) = U(t)/R$ and $I_C(t) = C\,\dot{U}(t)$ the equation simplifies to

$$\frac{L_0}{v}\dot{I}(t) = \frac{1}{R}U(t) + C\dot{U}(t). \tag{3.4}$$

The solution of this differential equation can be found using the ansatz $I(t) = I_0 \exp(i\omega t)$ and $U(t) = U_0 \exp(i\omega t)$

$$i\omega\frac{L_0}{v}I_0 = \left(\frac{1}{R} + i\omega C\right)U_0. \tag{3.5}$$

For frequencies relevant for CSR (4-220 kHz) and capacities of a few hundreds of pF the use of high-OHMic amplifiers (5 MΩ) allows the assumption $R \gg 1/\omega C$. Thus, equation (3.5) writes to

$$U(t) = \frac{L_0}{C\,v}I(t). \tag{3.6}$$

The induced signal is proportional to inverse ion beam velocity $1/v$, accordingly, the system gets more sensitive for slow ion beams. By the time integration over the revolution time T_0 the total number N of ions stored in the storage ring can be calculated

$$N = \frac{C}{z\,e}\frac{C_0}{L_0}\frac{1}{T_0}\int_0^{T_0} U(t)\,\mathrm{d}t, \tag{3.7}$$

where C_0 is the circumference of the storage ring.

3.3.2 The pick-up electrode

Unless the bunches in the ring are very short ($\lesssim T_0 L_0/C_0$), the voltage at the input impedance of the amplifier is proportional to the ratio of pick-up length to the total capacity of the pick-up $U \propto L_0/C$ (see equation (3.6)). Therefore it is preferable to have a pick-up length as long as possible and a capacity as low as possible at the same time. However, this is contradictory. As a compromise the length of the current pick-up electrode is set to 30 mm [75], which corresponds to 10^{-3} of the circumference of CSR. In order not to reduce the geometrical acceptance of the storage ring the aperture of the pick-up is set to 100 mm in diameter [75].

Figure 3.4 shows a (a) CAD-model and (b) photograph of the mounted pick-up electrode. It is manufactured from oxygen free copper (OFC 99.95) completely, assuring good thermal and electric conductivity. The electrode is imbedded in a grounding screen and is mounted to it using sapphires (mono-crystalline Al_2O_3) for electric insulation and maintaining good thermal conductance. The signal wire is insulated with ceramic (amorphous Al_2O_3) tubes and connects the electrode with

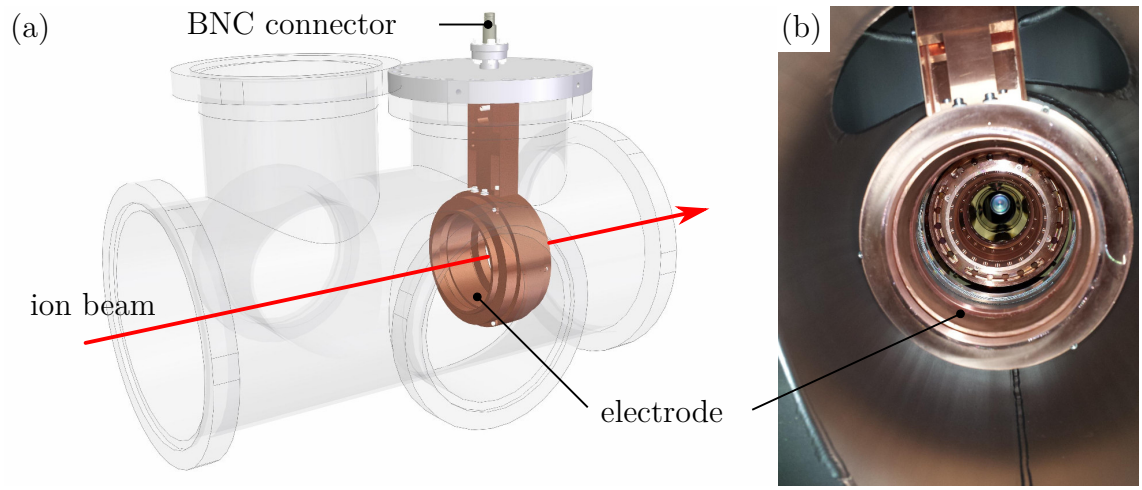

Figure 3.4: The current pick-up electrode as a (a) CAD-model and (b) photograph mounted in CSR. The electrode has a length of 30 mm and aperture diameter of 100 mm.

a BNC-connector via clamped connections. The pick-up electrode has been aligned to the optical axis defined by the quadrupoles during the final construction of the storage ring. Since the pick-up is not sensitive for the transverse position of the ion beam, in contrast to the position pick-ups, the alignment does not have to fulfill special requirements.

The capacities of both the electrode with BNC-connector on the one side and the cryogenic amplifier (which will be discussed in section 3.6.1) with connection cable on the other side were measured independently. The measurements were done using a LC' circuit with inductance L and capacity C' and determining its resonance frequencies without and with test capacity C_{test} (electrode or amplifier). The resonance frequencies for such a circuit are

$$f_{C'} = \frac{1}{2\pi\sqrt{LC'}}, \tag{3.8}$$

$$f_{C'+C_{\text{test}}} = \frac{1}{2\pi\sqrt{L(C'+C_{\text{test}})}}. \tag{3.9}$$

Solving these equations for the test capacity gives

$$C_{\text{test}} = \frac{1}{4\pi^2 L}\left(\frac{1}{f^2_{C'+C_{\text{test}}}} - \frac{1}{f^2_{C'}}\right). \tag{3.10}$$

The inductance L was determined by connecting five reference capacitors, whose capacitances were determined with a LCR-meter (ESI 252 Impedance Meter) to

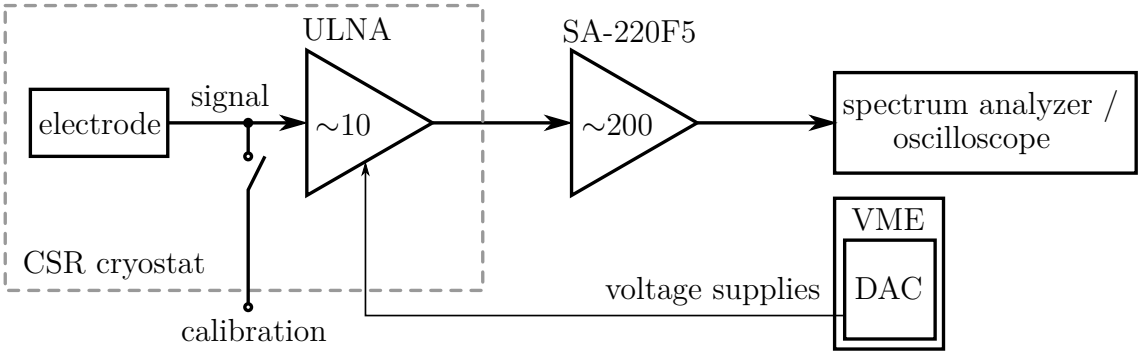

Figure 3.5: Measuring electronics of the current pick-up system. The induced signal of the pick-up electrode is pre-amplified by a high-OHMic pre-amplifier (ULNA) discussed in detail in section 3.6.1. The main amplification is done outside of the CSR cryostat at room temperature with a commercial high-OHMic amplifier (SA-220F5). The signals are recorded either with a spectrum analyzer or an oscilloscope. The voltage supplies of the cryogenic electronics (gate and drain bias-voltage as well as the voltages for the cryogenic relay) are provided by a digital-to-analog converter (DAC). For the determination of the entire amplification a calibration signal can be switched directly onto the input of the pre-amplifier. The cryogenic signal connection circuit is discussed in section 3.6.2 and the electrical circuit is shown in figure 3.19.a.

$\pm 0.5\,\mathrm{pF}$. From resonance frequency measurements with $\pm 50\,\mathrm{Hz}$ accuracy the capacity of the current pick-up electrode with BNC-connector was determined as $C_{\mathrm{electrode}} = 61.4(9)\,\mathrm{pF}$ and the total capacity of the entire system $C_{\mathrm{total}} = 97.3(13)\,\mathrm{pF}$ at room temperature.

3.3.3 The measuring electronics

The measuring electronics for the current pick-up is shown schematically in figure 3.5. The induced signal is amplified by a cryogenic high-OHMic pre-amplifier by an amplification factor of ~ 10, which will be discussed in section 3.6. The main amplification is done at room temperature outside of the CSR cryostat by a commercial amplifier discussed below. The voltage supply of the cryogenic amplifier (drain and gate bias voltage) are provided by a VMEbus (Versa Module Europa-bus) Digital-to-analog converter (DAC) module, which itself is remote controlled by a computer. The amplified signal can then either be fed into a spectrum analyzer or an oscilloscope.

For precise ion beam current measurements the total gain of the entire system has to be known. Therefore a calibration signal can be applied directly onto the input of

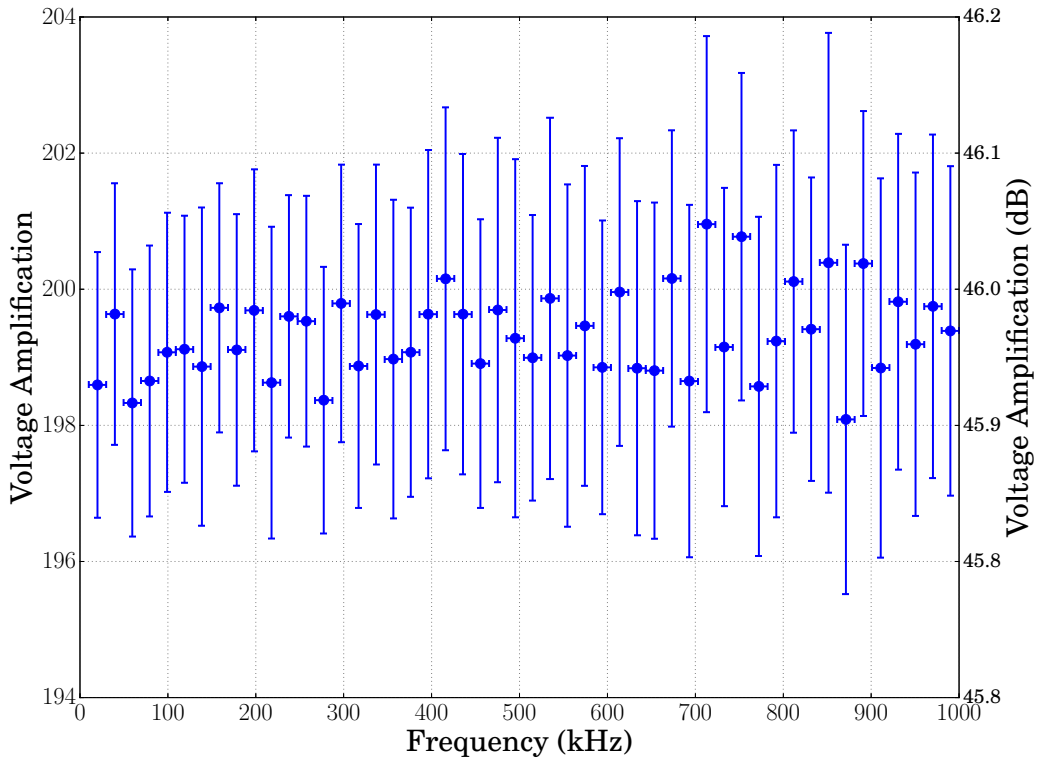

Figure 3.6: Measured voltage gain of the amplifier NF-SA-220F5 with a 50 Ω termination resistance at the frequency range relevant for CSR.

the cryogenic pre-amplifier by switching a cryogenic relay (see section 3.6.2 for the detailed signal connection scheme), which also is controlled by the DAC-module.

The main amplifier for the current pick-up is a commercial low noise FET (Field Effect Transistor) amplifier SA-220F5 (NF Corporation) with a high OHMic input resistance of $1\,\mathrm{M\Omega} \pm 5\%$, a nominal input voltage noise density $e_n = 0.5\,\mathrm{nV}/\sqrt{\mathrm{Hz}}$, input noise current density $i_n = 200\,\mathrm{fA}/\sqrt{\mathrm{Hz}}$, and nominal voltage gain of 46.0(5) dB at a 50 Ω termination and a frequency of 1 MHz [77], which corresponds to a nominal voltage amplification of 200(12). A measurement of the voltage gain in the frequency range relevant for CSR is shown in figure 3.6. It shows an almost constant voltage gain over these frequencies with a mean value of 199(2), which is needed for the non-distortion of the ion beam signals.

Before we discuss the details of the cryogenic amplification system (see section 3.6) in more detail, first in the following two sections the characteristics of the position and the SCHOTTKY pick-ups are discussed.

3.4 The position pick-ups

The position pick-ups[1] are a standard tool in accelerator and storage devices for measuring the transverse center of the beam [78, 79]. Their function is also based on the principle of capacitive pick-ups (see section 3.3.1). By cutting a hollow tube diagonally one gets two position sensitive electrodes, which are charged by the passing ion beam. An amplifier on each of the electrode measures the ion beam current signal depending on the relative position to the electrode. From these signals the actual ion beam position can be calculated. On the basis of the studies of F. Laux [75] it has been decided that the CSR position pick-ups have no conventional measuring scheme but using only one amplifier and connecting both electrodes via a relay to the same amplifier chain. The advantage of this scheme is, that the amplification of the individual amplifiers does not have to be known, but it relies on cryogenic reliably working relays.

3.4.1 Theory of operation

In figure 3.7 the principle of the position pick-ups is shown. The electrodes are diagonally cut and have a total length L_{PU} and radius r. Due to the manufacturing process of the electrodes there is a short extension e necessary. Both electrodes have a capacity C_1 and C_2 to the grounded vacuum chamber and a coupling capacity C_{coupling} among each other. Two relays connect one of the electrodes to the Ohmic resistance R and the other electrode to ground (red) or vice versa (green).

Depending on the position x the ion beam induces the voltages $U_{x,1}(t)$ and $U_{x,2}(t)$. In order to have a position measurement independent of the ion beam current it is convenient to normalize the difference to the sum of these signals. By using two sets of electrodes 90°-rotated to each other both positions x and y can be determined from the measured voltage drops via

$$x = k_x(x,y)\frac{U_{x,1} - U_{x,2}}{U_{x,1} + U_{x,2}}, \tag{3.11}$$

$$y = k_y(x,y)\frac{U_{y,1} - U_{y,2}}{U_{y,1} + U_{y,2}}, \tag{3.12}$$

with the scaling functions $k_x(x,y)$ and $k_y(x,y)$. For diagonally cut electrodes the scaling functions become a constant factor [79] and the equations (3.11) and (3.12)

[1] Also called beam position monitors (BPM). But this is avoided in this thesis, because of the ambiguity of beam profile monitors (first turn diagnostics).

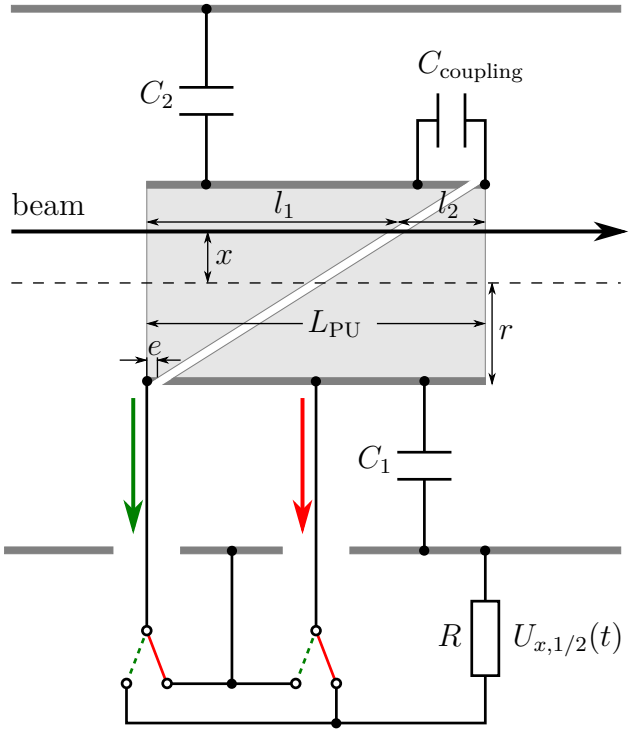

Figure 3.7: The principle of the position pick-ups. Using a relay both pick-up electrodes are connected to one resistance R creating a voltage drop $U_{x,1}(t)$ for electrode 1 and $U_{x,2}(t)$ for electrode 2, respectively.

become linear

$$x = k\frac{U_{x,1} - U_{x,2}}{U_{x,1} + U_{x,2}}, \tag{3.13}$$

$$y = k\frac{U_{y,1} - U_{y,2}}{U_{y,1} + U_{y,2}}, \tag{3.14}$$

with the constant scaling factor for both transverse coordinates

$$k \equiv k_x(x, y) = k_y(x, y). \tag{3.15}$$

3.4.2 The scaling factor

Analog to equation (3.4) KIRCHOFF's junction rule determines the currents of both electrodes. Assuming an identical capacity of both electrodes $C = C_{1,2} + C_{\text{coupling}}$ one derives the following equations[2] (see also figure 3.7)

$$\frac{l_1}{v}\dot{I} = C\dot{U}_{x,1} + \frac{U_{x,1}}{R}, \tag{3.16}$$

[2]The derivation of the equations is done for coordinate x, but is also true for coordinate y.

$$\frac{l_2}{v}\dot{I} = C\dot{U}_{x,2} + \frac{U_{x,2}}{R}. \tag{3.17}$$

Using an amplifier with high input resistance ($R \to \infty$) and low capacity ($\ll C$) the last terms can be neglected. Dividing then the difference (3.16) - (3.17) through the sum (3.16) + (3.17) yields

$$\frac{l_1 - l_2}{L_{\mathrm{PU}}} = \frac{U_{x,1} - U_{x,2}}{U_{x,1} + U_{x,2}}. \tag{3.18}$$

By geometric considerations one can find for the length difference

$$l_1 - l_2 = \frac{x}{rL_{\mathrm{PU}}}(L_{\mathrm{PU}} - 2e). \tag{3.19}$$

Inserting this relation in equation (3.18) and solving for x gives

$$x = \frac{r}{1 - 2e/L_{\mathrm{PU}}}\frac{U_{x,1} - U_{x,2}}{U_{x,1} + U_{x,2}}. \tag{3.20}$$

Thus, the scaling factor is

$$k = \frac{r}{1 - 2e/L_{\mathrm{PU}}} \tag{3.21}$$

solely depending on geometric parameters of the pick-up electrode with radius r, length L_{PU} and extension e (see figure 3.7). F. Laux [75, p. 48] verified that equation (3.21) describes the scaling factor of pick-ups with quadratic aperture very well, but it underestimates pick-ups with round aperture by roughly 10 %.

3.4.3 The pick-up electrode

As for the case of the current pick-up (see section 3.3.2) the signal at the position pick-up electrode arising from the ion beam is proportional to the ratio of effective pick-up length and its capacity $U \propto L_{\mathrm{eff}}/C$ (see equation (3.6)). Additionally the total length of the whole pick-up limits the free space available for experiments, because there are two position pick-ups per linear section (except of the electron cooler section). Therefore the length of one set of electrodes is set to 60 mm. The total length is 288 mm including two sets of electrode pairs for both transverse coordinates and three grounded extension tubes reducing field distortions at the edges [80]. The aperture is set to 100 mm in diameter not reducing the storage ring's acceptance. These dimensions are identical with the prototype tested by F. Laux [75]. The design of the realized pick-ups differs from the prototype in some not that important details and the mounting principle in the vacuum chamber.

Figure 3.8 shows a (a) CAD-model and (b) photograph of one of the position pick-ups mounted in CSR. Except of some smaller parts it is manufactured from oxygen free

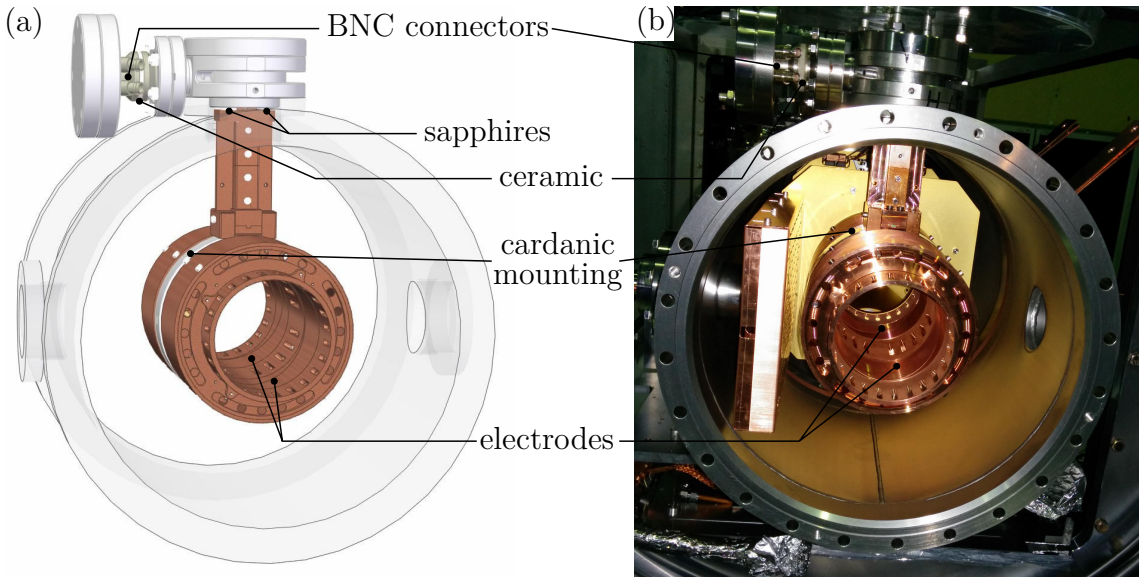

Figure 3.8: The position pick-up electrode as a (a) CAD-model and (b) photograph mounted in CSR. The total length of the pickup is 288 mm, the electrode lengths are 60 mm and the aperture diameter is 100 mm.

copper (OFC 99.95) completely assuring good electric and thermal conductivity. The actual electrodes are embedded in a grounded shielding. Because of possible cross-talk of the rf system (see section 3.8), all position pick-up are mounted electrically insulating to the experimental vacuum chamber using sapphires (mono-crystalline Al_2O_3) and ceramics (amorphous Al_2O_3). The sapphires allow good thermal contact for cooling the relative massive position pick-up via the experimental vacuum chamber. The electrodes are connected to BNC-connectors using OF-copper wires, which are insulated with ceramic tubes. A CARDANIC-like suspension allows proper alignment to the ion beam axis using glass targets and TAYLOR-HOBSON-telescopes. The alignment of all pick-ups has been performed at room temperature conditions prior of closing the experimental vacuum. The accuracy for the transverse offset has been bellow 0.5 mm.

During cryogenic operation of the storage ring the closed orbit defined by the center of quadrupoles lowers due to shrinkage of the used materials (G-10, stainless steel, and aluminium). Assuming the expected temperature distribution (see section 2.4) and thermal expansion coefficients for the materials [81, pp 572–573] a rough estimation is a 1.43(11) mm lowered closed orbit with respect to room temperature operation. The denoted error arises from the unknown temperature gradients of the transitions. It is calculated via the extreme cases, where the transitions are either at highest or lowest possible temperature. A similar estimation for the center of the position pick-ups (materials: titanium, aluminium, stainless steel, and copper) gives

a 0.86(5) mm lowering with respect to the room temperature closed orbit. Thus, in total it can be expected, that during cryogenic operation the center of the position pick-ups lies 0.57(16) mm above the closed orbit (cryogenic). In fact the lowering of the electrostatic elements has been measured during cooldown of the first completed corner of the storage ring. The value is given in [82, p. 93] to 0.69(16) mm. But at this time the ion optical support structures have not yet been anchored at the two thermal shields. This could have led to higher temperatures of the supports and therefore to a smaller lowering in comparison to the above given estimation.

3.4.4 Scaling factor measurement

The scaling factor of a position pick-up is the proportionality factor which connects the measured signals to the actual ion beam center (see equation (3.13) and (3.14)). It is purely determined by the geometry of the pick-up electrodes (equation (3.21)). Hence it can be measured in a test setup simulating an ion beam by the use of a wire. A similar measuring scheme was used as applied by F. Laux for determining the scaling factor of the position pick-up prototype [75, sec. 4.3.2].

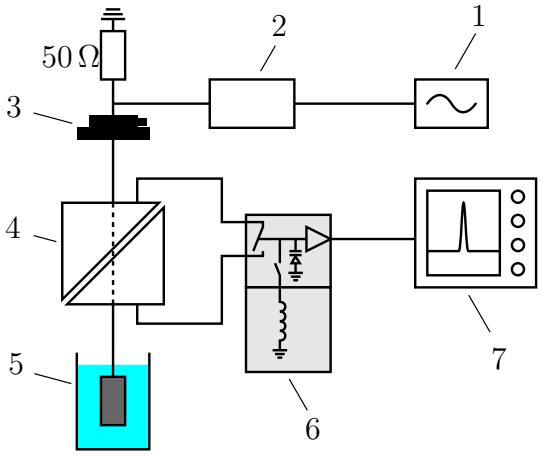

Figure 3.9: Scheme for scaling factor measurement: (1) function generator (2) optical fiber (3) manual translation stage for x and y (4) position pick-up (5) damping weight in water basin (6) amplifier box with relay, inductance, and capacitive diode, and a (7) spectrum analyzer.

Figure 3.9 shows the scheme of the wire measurement. A function generator (1) creates a rf signal at a wire, which is spanned through the position pick-up (4). The signal is decoupled using an optical fiber (2) reducing cross-talk. The wire can be moved transversely using a (x, y)-translation stage (3), whereby a weight in a water basin (5) damps the mechanical oscillations of the wire after changing its position.

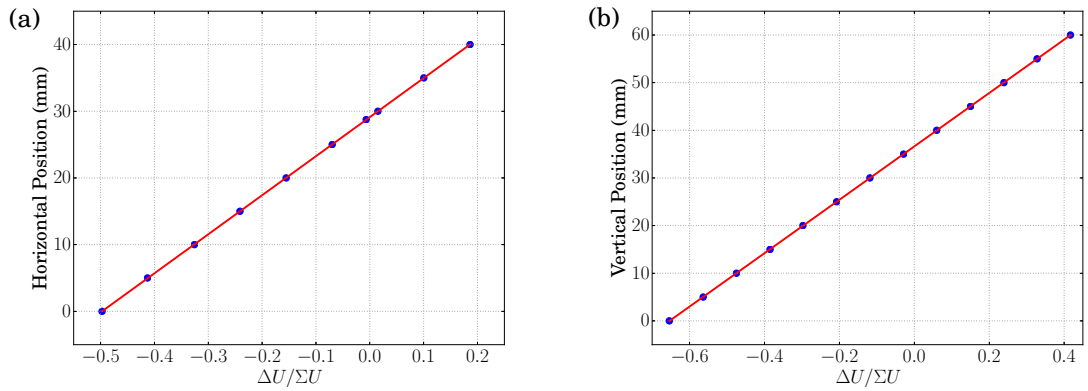

Figure 3.10: Plot of measured (a) horizontal and (b) vertical position versus the difference of voltages over their sum.

The pick-up electrodes are connected to one of the so-called *amplifier boxes* (see section 3.6.4), which contains essentially the ultra-low noise amplifier (ULNA) and a relay for connecting one of the electrodes to the input of the amplifier and grounding the other electrode simultaneously or vice versa (in figure 3.9 the grounding relay of the electrode is omitted for the sake of clarity). Additionally there are a voltage controlled capacitive diode and a switchable inductance for adjusting the capacity differences between the two pick-up electrodes. The output of the amplifier is read out by a spectrum analyzer (7).

Figure 3.10 shows the measured (a) horizontal and (b) vertical position versus the measured ratio of voltage difference and voltage sum. By fitting linear functions to the measured data the scaling factors for both coordinates can be extracted to

$$k_x = 58.53(5)\,\text{mm}, \tag{3.22}$$

$$k_y = 56.04(2)\,\text{mm}. \tag{3.23}$$

The denoted statistical errors are calculated by the method of least squares and are below 0.1 %. For an ideal position pick-up with perfect alignment and identical electrodes, the scaling factors for both positions should be the same. However, the obvious deviation of the scaling factors for the x and y coordinate cannot be explained by the statistical errors. In fact this indicates a systematical error in the measurement. Possible explanations could be a misalignment of the pick-up with respect to the wire or the internal relative positions of the electrodes themselves. For this reason the averaged scaling factor for the CSR position pick-ups is afflicted with a systematically uncertainty of roughly 2.2 % (neglecting the small statistical error of the measurement)

$$k = (57.29 \pm 1.25)\,\text{mm}. \tag{3.24}$$

The scaling factor of the prototype, which has a slightly different geometry, has been determined to $k_{\text{prototype}} = 56.9(1)\,\text{mm}$ [75, tab. 4.2] and lies within the systematic uncertainty. Using the equation (3.21) and considering the manufacturing tolerances the scaling factor can be calculated to $k_{\text{geometric}} = 54.6(2)\,\text{mm}$. Also this is consistent to the experimentally determined scaling factor taking the 10 % correction for round apertures into account [75, p. 48]. The relative shrinkage of copper due to cooldown to 10 K is roughly 3×10^{-3} [83]. Thus, the expected change of the scaling factor due to cooldown of the storage ring is also $\sim 0.3\,\%$ (see equation (3.21)).

3.4.5 Influence of the ion beam lifetime

Although the beam lifetimes of ion species in CSR are expected to be relative long (from several minutes to a few hours), the decreasing beam intensity has an influence on the position measurement, if the electrodes are measured one after the other. Assuming a beam on the closed orbit ($x = 0$) with lifetime τ and a time $\Delta t > 0$ between two measurements the measured voltages at two electrodes are $U_1 = U_0$ and $U_2 = U_0\, e^{-\Delta t/\tau}$. This causes an error in the position measurement of

$$x = k\frac{U_1 - U_2}{U_1 + U_2} = k\frac{1 - e^{-\Delta t/\tau}}{1 + e^{-\Delta t/\tau}} \neq 0. \tag{3.25}$$

By measuring the first electrode and the second electrode followed by the first electrode again after a constant measuring time Δt one can calculate two positions x_1 and x_2. The average of these two is

$$\bar{x} = \frac{x_1 + x_2}{2} = \frac{1}{2}\left(k\frac{1 - e^{-\Delta t/\tau}}{1 + e^{-\Delta t/\tau}} + k\frac{e^{-\Delta t/\tau} - 1}{e^{-\Delta t/\tau} + 1}\right) = 0 \tag{3.26}$$

and independent of the beam lifetime τ. Thus, by averaging two consecutive position measurements with constant measuring time Δt the beam lifetime cancels out for the position determination.

3.4.6 The measuring electronics

In total there are six position pick-ups consisting of two pairs of electrodes for both transverse coordinates. Each pair of electrodes is connected to one amplifier chain, of which one is schematically shown in figure 3.11. The main advantage of the use of this unconventional measurement scheme is, that it is not necessary to know the exact amplification of the whole system (see equations (3.13) and (3.14)), because the amplification cancels out.

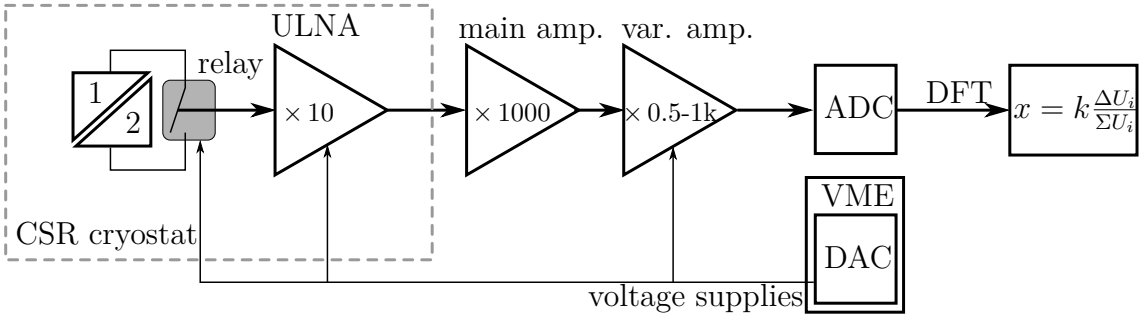

Figure 3.11: The measuring electronics of the position pick-ups at the example of one coordinate of one position pick-up. For simplification the relay, which grounds the not used electrode as well as the parallel circuit with voltage controlled capacitive diode and the inductance are omitted. These are discussed in section 3.6.2 and the electrical circuit is shown in figure 3.19.b. The induced signals are fed into the cryogenic pre-amplifier (ULNA, discussed in section 3.6.1), then transmitted to the outside of the vacuum and amplified by the room temperature main amplifier (discussed in section 3.6.5) and a variable gain amplifier. The amplified signal is recorded by a fast analog-to-digital converter (ADC) and the position is calculated via a computer software. All voltage supplies (relays, gate and drain bias voltage of the ULNA as well as the amplification set value of the variable gain amplifier) are provided by a digital-to-analog converter (DAC).

However, in the case of a capacity difference between the electrodes this scheme leads to a faulty position measurement. Already a capacity difference of $\Delta C = 1\,\mathrm{pF}$ causes a position determination error of $\Delta x \approx 0.5\,\mathrm{mm}$ (using equation (3.6) and typical values for the position pick-up). Therefore there are voltage controlled capacitive diodes parallel to the electrode capacity installed (not shown in figure 3.11) to correct for a possible capacity difference. The electrical circuit will be discussed in section 3.6.2. By switching a parallel inductance and using a calibration signal the resonance frequencies can be adjusted and a capacity difference can be compensated.

Both electrodes of one coordinate are connected to a signle cryogenic pre-amplifier (ULNA), which will be discussed in section 3.6.1. The not used electrode is simultaneously grounded via an additional relay (not shown in figure 3.11). The cryogenic signal connection circuit will be discussed in detail in section 3.6.2 and the electrical circuit is shown in figure 3.19.b. The main amplification is done outside of the CSR cryostat by in-house built room temperature high-OHMic amplifiers, discussed in section 3.6.5. For optimal digitizing with an analog-to-digital converter (ADC) the signal strength is adapted to the ADC input level by an additional variable gain amplifier. The digitized signals are transformed in their FOURIER spectrum with a discrete FOURIER transformation (DFT) algorithm. Finally a controlling and mea-

suring software[3] calculates the averaged (i.e. beam lifetime independent, see section 3.4.5) ion beam position of both transverse coordinates and all position pick-ups in real time. All voltage supplies for the cryogenic relays, the gate, and drain bias voltages of the pre-amplifiers as well as the amplification set value of the variable gain amplifiers are provided by digital-to-analog converter (DAC) VME-modules.

Before we discuss the amplification system in detail in section 3.6 first the characteristics of the SCHOTTKY pick-up will be presented in the following section.

3.5 The SCHOTTKY pick-up

In contrast to the above already discussed current and position pick-ups the SCHOTTKY pick-up is designed for analyzing coasting beams. It uses the fact, that the ion beam consists of a large, but still finite, number of individual particles. These create the so-called SCHOTTKY noise[4] due to statistical fluctuations of the individual charges. The subsequent section summarizes the theory of SCHOTTKY signals (for a more detailed discussion see e.g. [70, 84]), followed by the description of the pick-up electrode and presentation of the measuring electronics.

3.5.1 Theory of SCHOTTKY signals

In figure 3.12 a SCHOTTKY pick-up is schematically shown. The ion beam current $I_{\mathrm{in}}(t)$ goes into the pick-up and leaves it again $I_{\mathrm{out}}(t) = I_{\mathrm{in}}(t-\Delta t)$ after a flight time Δt. Simultaneously it gives rise to a signal current $I(t)$ creating a voltage drop at the amplifier impedance $Z(\omega)$ consisting either of LCR-circuit for resonant signal amplification (or RC-circuit for the non-resonant case).

A single particle i stored in a storage ring with charge $z\,e$ results in a current representing a sequence of δ-pulses at each harmonic of the revolution time T. Hence the in- and outgoing currents are given by

$$I_{\mathrm{in},\,i}(t) = z\,e \sum_h \delta(t - hT), \tag{3.27}$$

$$I_{\mathrm{out},\,i}(t) = z\,e \sum_h \delta(t - hT + \Delta t). \tag{3.28}$$

The summation index h corresponds to the harmonic number. Because these signals are periodic one can calculate the FOURIER-series only taking positive ('physically

[3] The software has been mainly developed by R. EPKING.

[4] Also known as *shot noise*. Discovered by W. SCHOTTKY in 1918 [69].

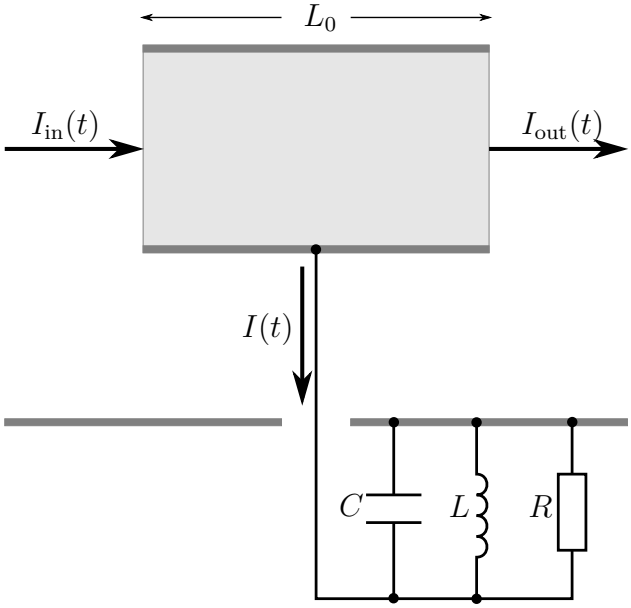

Figure 3.12: The principle of the SCHOTTKY pick-up.

meaningful') frequencies into account

$$I_{\mathrm{in},\,i}(t) = \frac{z\,e}{T} + \frac{2z\,e}{T}\sum_{h=1}^{\infty}\cos\left(h\omega_0 t\right), \tag{3.29}$$

$$I_{\mathrm{out},\,i}(t) = \frac{z\,e}{T} + \frac{2z\,e}{T}\sum_{h=1}^{\infty}\left[\cos\left(h\omega_0\Delta t\right)\cos\left(h\omega_0 t\right) - \sin\left(h\omega_0\Delta t\right)\sin\left(h\omega_0 t\right)\right], \tag{3.30}$$

with $\omega_0 = 2\pi/T$. The signal current $I_i(t) = I_{\mathrm{in},\,i}(t) - I_{\mathrm{out},\,i}(t)$ flowing into the impedance $Z(\omega)$ for one ion is then given by

$$I_i(t) = \frac{2z\,e}{T}\sum_{h=1}^{\infty}\left[\left(1-\cos\left(h\omega_0\Delta t\right)\right)\cos\left(h\omega_0 t\right) + \sin\left(h\omega_0\Delta t\right)\sin\left(h\omega_0 t\right)\right]. \tag{3.31}$$

The spectral components of this current are

$$\hat{I}_{i,\,h} = \frac{2z\,e}{T}\sqrt{\left(1-\cos\left(h\omega_0\Delta t\right)\right)^2 + \sin^2\left(h\omega_0\Delta t\right)}, \tag{3.32}$$

$$= \frac{2\sqrt{2}z\,e}{T}\sqrt{1-\cos\left(h\omega_0\Delta t\right)}. \tag{3.33}$$

The voltage drop at the impedance $Z(\omega)$ is then

$$\hat{U}_{i,\,h} = \frac{2\sqrt{2}z\,e}{T}Z(h\omega_0)\sqrt{1-\cos\left(h\omega_0\Delta t\right)}. \tag{3.34}$$

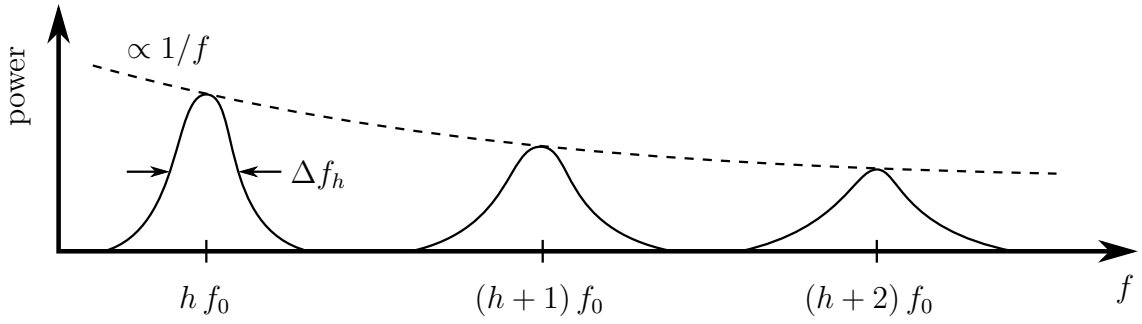

Figure 3.13: SCHOTTKY bands in power spectrum.

Obviously this signal has maxima and zero points at harmonics fulfilling

$$h_{\max} = \frac{(2k+1)\pi}{\omega_0 \Delta t} \text{ and} \tag{3.35}$$

$$h_{\text{zero}} = \frac{2m\,\pi}{\omega_0 \Delta t}, \tag{3.36}$$

with $k, m \in \mathbb{N}_0$, respectively.

Calculating the SCHOTTKY noise power caused by N ions, which can be defined by

$$P(h\omega_0) = \left(\sum_{i=1}^{N} \hat{U}_{i,\,h}(h\omega_0)\, \cos\phi_i \right)^2, \tag{3.37}$$

where ϕ_i is the phase[5] of the ion i. Assuming a statistical homogenous distributed ion beam the phase term simplifies to $(\sum \cos\phi_i)^2 = N/2$. Since the voltage drop, equation 3.34, is for all ions the same, the SCHOTTKY power scales linearly with the number of stored particles

$$P(h\omega_0) = \frac{N}{2} \hat{U}_i^2(h\omega_0). \tag{3.38}$$

A realistic beam with N particles is not perfectly mono-energetic, but the ions have an energy distribution, which leads to a distribution of frequencies. Thus, the ideal lines in the spectrum discussed above are changed to so-called SCHOTTKY-bands centered around multiples of the revolution frequency f_0 of an ideal particle. In figure 3.13 a power spectrum for a GAUSSian energy distribution is schematically shown. Because the power within on SCHOTTKY-band is constant, the width of the lines become broader $\Delta f_h = h \cdot \Delta f_0$ and their heights decrease with increasing harmonic number h. According to equation (2.19) this frequency spread Δf_0 is linked via the slip factor η to the momentum spread $\Delta p/p_0$ of the ion beam.

[5] In the equations (3.29) and (3.30) the arbitrary phases ϕ_i were omitted for sake of clarity.

3.5.2 The pick-up electrode

According to equation (3.36) the SCHOTTKY signal has zero points at harmonics, which are multiples of the ratio of storage ring circumference and pick-up length C_0/L_0. For this reason the length of the pick-up electrode must not be too short. As in the previous section discussed, a passing ion creates mirror charges on the SCHOTTKY pick-up electrode. These mirror charges have a distribution, which can be estimated by a GAUSSian profile with a width $\sigma_{\mathrm{rms}} = R/\sqrt{2}$, where R is the aperture radius of the pick-up [85]. Thus, in order to fully cover the influenced mirror charge representing the true ion beam charge the length of the pickup should be much longer than its radius $L_0 \gg R$. A good criterion is a length corresponding to $L_0 > 6\sigma_{\mathrm{rms}}$. By a defined aperture diameter of 100 mm this gives a minimum length of ~ 210 mm. Due to the first given argument the final pick-up length is set to $L_0 = 350$ mm [75], which corresponds to roughly one percent of the circumference of the storage ring $L_0/C_0 \approx 0.01$.

Thus, there are expected zero points at each $\sim 100^{\mathrm{th}}$ harmonics. In figure 3.14 the voltage drop (see equation (3.34)) of a singly charged ion as a function of the harmonic number is depicted. The impedance $Z(\omega)$ for the non-resonant case is equal to the impedance of a parallel RC-circuit

$$Z_{\text{non-res}} = \frac{1}{\sqrt{(2\pi h f_0 C)^2 + \frac{1}{R^2}}} \tag{3.39}$$

where f_0 is the revolution frequency of the stored ion, C is the total capacity of the SCHOTTKY pick-up and amplifier and R is the input resistance of the amplifier. For the calculation a capacity of $C = 452.5$ pF (equal to the total capacity of electrode and amplifier, which is determined at room temperature resonantly, similar to section 3.3.2) and an input resistance of the amplifier of $R = 5\,\mathrm{M}\Omega$ are used, which will be discussed later in section 3.6. From the plot it can be seen, that for the measurement of optimal SCHOTTKY signals as small as possible harmonics ($h \lesssim 25$) should be used.

Figure 3.15 shows a (a) CAD-model and (b) photograph of the SCHOTTKY pick-up mounted in its vacuum chamber. Except of some smaller parts it is manufactured from oxygen free copper (OFC 99.95) completely assuring good electric and thermal conductivities. The electrode is mounted via sapphires (mono-crystalline Al_2O_3) to a grounded shielding, which itself is mounted to the vacuum chamber. The signal wire is insulated with ceramic (amorphous Al_2O_3) tubes and connects the electrode with a BNC-connector via clamped connections.

Similar to the current pick-up the SCHOTTKY pick-up is directly mounted to the vacuum chamber without any adjustment possibilities, for what reason during the

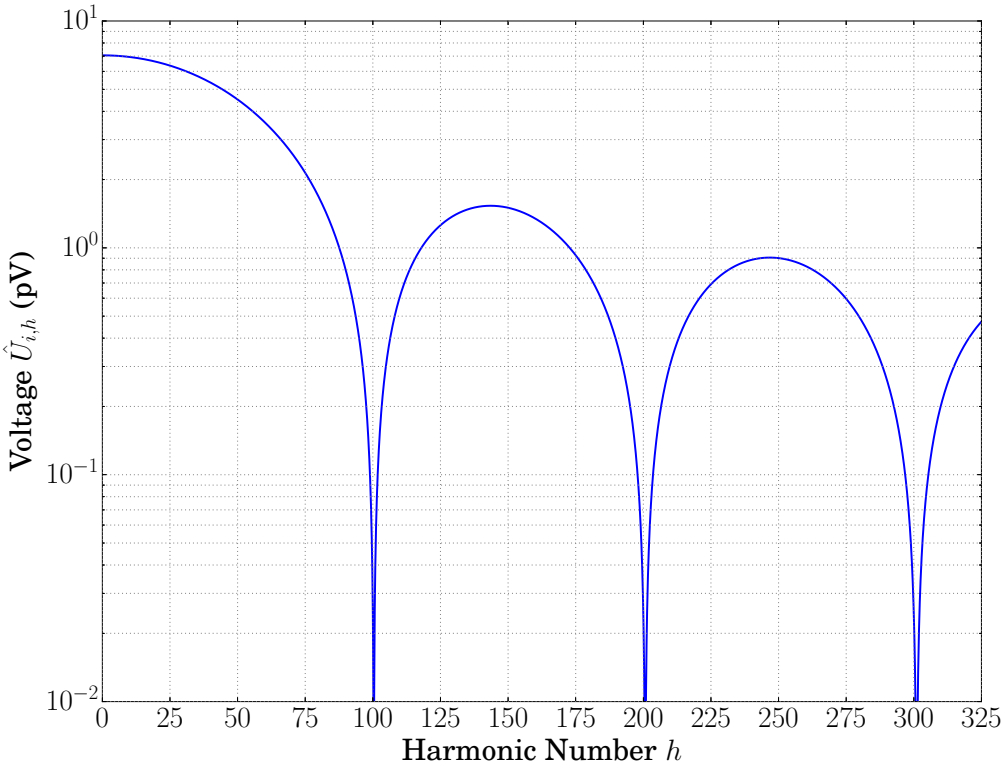

Figure 3.14: The expected voltage spectrum of a singly charged ion at the SCHOTTKY pick-up as a function of the harmonic number for non-resonant amplification.

final construction of the diagnostic section (section (C) in figure 2.6) the pick-up electrode together with the vacuum chamber were adjusted to the ion optical axis defined by the quadrupoles. But also here there is no position sensitivity, wherefore there is no special requirement for the alignment.

3.5.3 The measuring electronics

The measuring electronics of the SCHOTTKY pick-up is shown in figure 3.16 schematically. The SCHOTTKY signal is directly fed into the cryogenic pre-amplifier (ULNA, voltage gain ~ 10), which will be discussed in section 3.6.1. The main amplification is done outside of the CSR cryostat with a room temperature main amplifier (voltage gain ~ 1000), discussed in section 3.6.5. The amplified signal is then recorded with a spectrum analyzer.

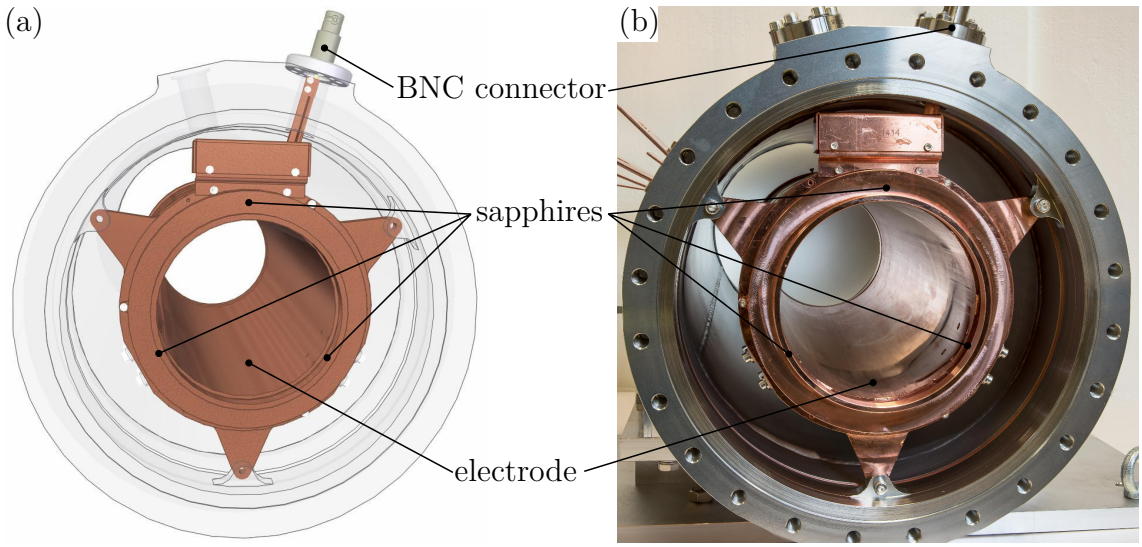

Figure 3.15: The SCHOTTKY pick-up electrode as a (a) CAD-model and (b) photograph mounted in its CSR vacuum chamber. The electrode has a length of 350 mm and aperture diameter of 100 mm.

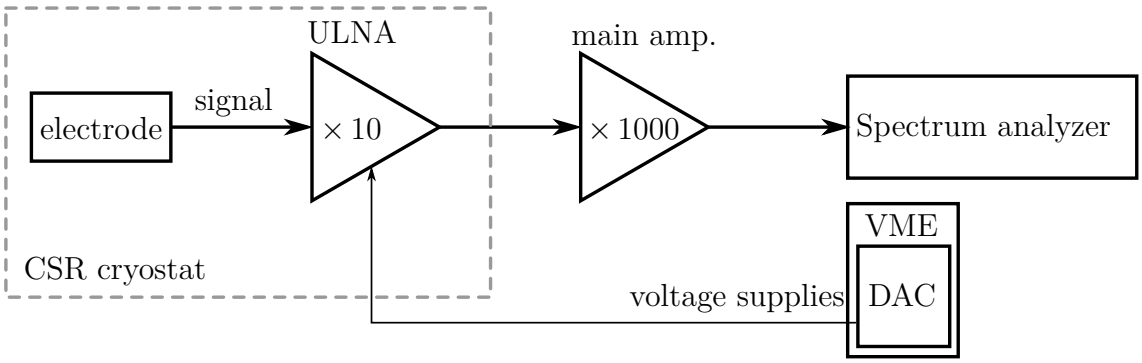

Figure 3.16: The measuring electronics of the SCHOTTKY pick-up. The induced signals are fed into the cryogenic pre-amplifier (ULNA), discussed in section 3.6.1. The main amplification is done outside of the CSR cryostat with a high-OHMic room temperature amplifier, discussed in section 3.6.5. The cryogenic connection scheme is depicted simplified, but it will be discussed in section 3.6.2 and the electrical circuit is shown in figure 3.19.c). The voltage supplies of the cryogenic pre-amplifier (gain and drain bias voltages) are provided by a digital-to-analog converter (DAC).

In contrast to the current and the position pick-ups the SCHOTTKY pick-up has also the option for resonant signal amplification, by switching an inductance parallel to the input impedance of the cryogenic pre-amplifier (not shown in figure 3.16). The cryogenic signal connection scheme is discussed in section 3.6.2 and the electronic circuit is shown in figure 3.19.c in detail. The resonant operation of the SCHOTTKY

pick-up and its realization is discussed in detail in section 3.6.6. The voltage supplies of the cryogenic electronics (gain and drain bias voltages of the ULNA as well as the relay voltages) are provided by a VME digital-to-analog converter (DAC) module.

3.6 The amplification system of the diagnostics

As already pointed out in the section 3.3.1, the voltage of a passing ion at a parallel-connected resistance (which corresponds to the input resistance of the pre-amplifier) to the pick-up electrode is proportional to the inverse of the total capacity (of the electrode, cable, and pre-amplifier) $U \propto 1/C$, see equation (3.7). Therefore it is advantageous to have an amplifier as close as possible to the pick-up electrode, even though the amplification may be relatively small. By this also the influence of external noise sources onto the signal line is reduced. For these reasons the amplification system of the CSR diagnostics is split into two parts. A cryogenic pre-amplifier, as close as possible to the pick-up electrode, and a main amplifier outside of the CSR cryostat at room temperature. For the connection between both amplifiers a compromise between good signal transmission, low heat input, and practicability for the operation modes of CSR had to be found. In the subsequent sections first the cryogenic amplifier and its cryogenic electronics are discussed, followed by the presentation of the main amplifier, the considerations for the connection between the amplifiers, and estimations for the expected thermal loads.

3.6.1 The cryogenic pre-amplifiers

The heart piece of the signal amplification is the cryogenic pre-amplifier. It has been initially developed by S. Sturm [86] for measuring the axial frequency of a stored ion in a Penning-trap and has been adapted by F. Laux together with S. Sturm for the needs of the CSR diagnostics [75]. The schematic layout of the so-called ultra-low noise amplifier (ULNA) is depicted in figure 3.17.

Two parallel field effect transistors (FET) NE25139 (NEC) form the input stage of the amplifier for the purpose of noise reduction. The second amplification stage of a third transistor 3SK124 (NEC) forms a so-called 'cascode'[6], which has several advantages for the amplification properties. The input impedance of the amplifier is increased and the drain voltage of the first transistor is stabilized by what the feedback of the output onto the input of the first transistor is reduced, which is called the Miller-effect [87]. A last transistor stage (3SK124) serves as an imped-

[6]The first transistor is operating as a common source and the second as a common gate.

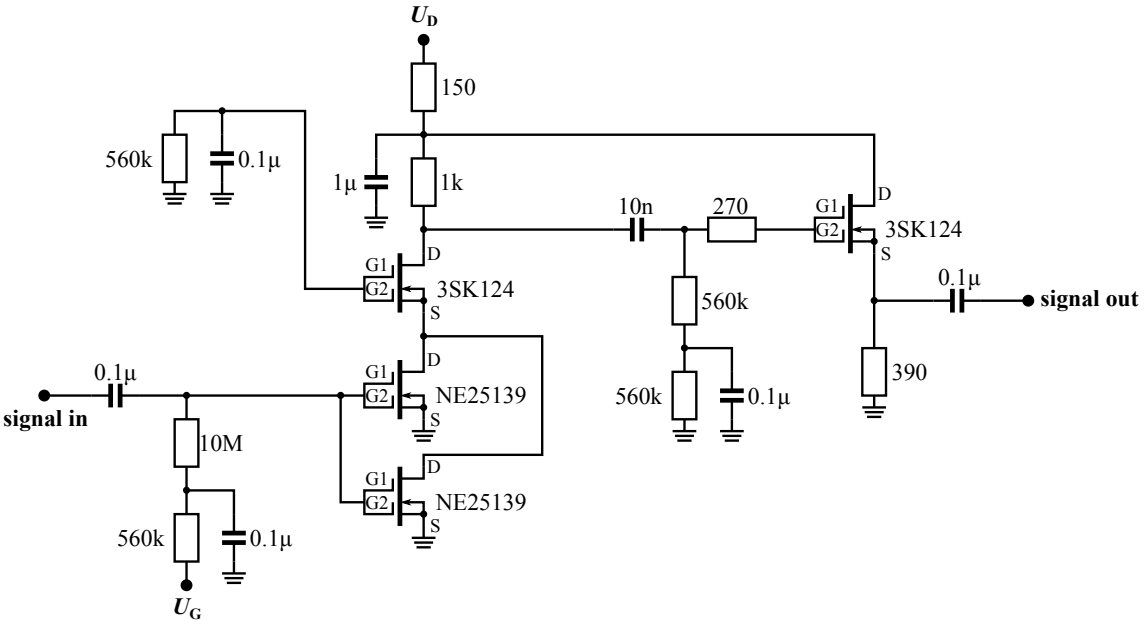

Figure 3.17: Schematic layout of the ultra-low noise amplifier (ULNA) [75].

ance converter and adaption to 50 Ω of the transmission line. For a more detailed discussion on the design considerations see [86, sec. 4.3.3].

Both FET types are based on Gallium Arsenide (GaAs), which is still working under cryogenic conditions down to 4 K in contrast to silicon based devices [88]. The amplifier is biased by the gate U_G and drain voltage U_D, which are filtered on the board. The gates of the 3SK124 are not biased. Deviating from the former design [75, p. 134] the input resistance has been changed from 100 MΩ to 10 MΩ. The reason for this in on the one hand the loading time constants of the capacitive diodes and on the other hand the discharging time constants of the pick-up electrodes, which should be both of the order of a few milliseconds. Both aspects are discussed in the subsequent section and the electrical circuit is shown in figure 3.19.

Figure 3.18 shows the voltage gain of the ULNA (at the example of the current pick-up) as a function of the bias voltage of the gate U_G at a fixed frequency of $f = 1$ MHz (left panel) and as a function of the frequency at a fixed working point of $U_G = -0.6$ V (right panel). The measurement is performed in a test cryostat, which reaches a temperature of 20 K. The bias voltage of the drain is $U_D = 5$ V producing a power consumption of ~ 20 mW. The voltage gain has been measured for both termination resistances of (blue) 1 MΩ and (red) 50 Ω with the network analyzer Bode 100 (OMICRON Lab). Due to the capacitive out-coupling capacity of 0.1 μF (see figure 3.17) frequencies below ~ 100 kHz are damped in the case of a termination resistance of 50 Ω. The optimal working point lays approximately at

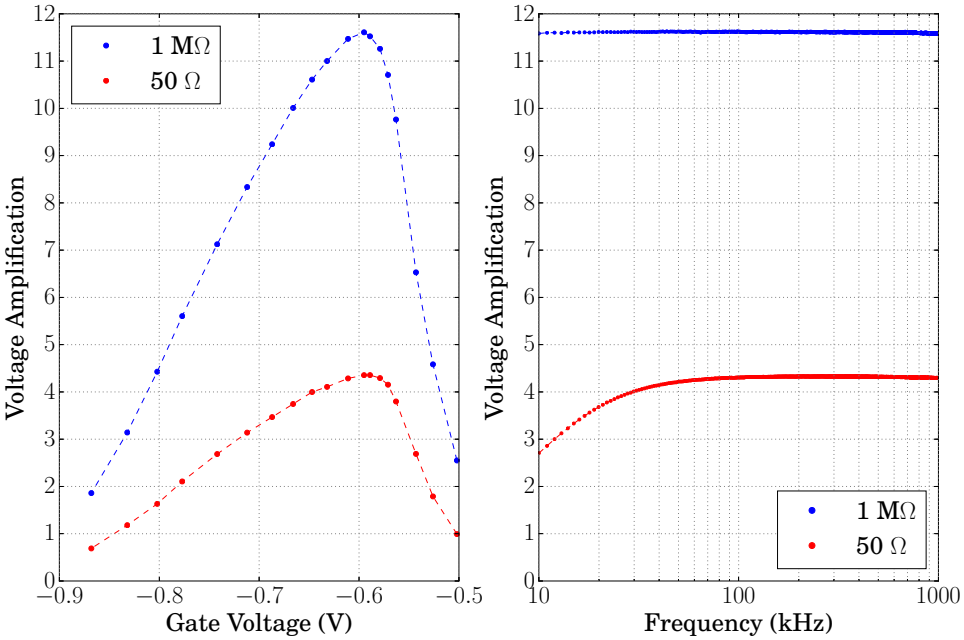

Figure 3.18: Voltage gain of the current pick-up ULNA as a (left) function of the gate voltage at $f = 1\,\mathrm{MHz}$ and (right) function of the frequency at $U_\mathrm{G} = -0.6\,\mathrm{V}$. The drain voltage is $U_\mathrm{D} = 5\,\mathrm{V}$ and the temperature is 20 K. The termination resistances of the amplifier for the measurements are (blue) $1\,\mathrm{M\Omega}$ and (red) $50\,\Omega$.

$U_\mathrm{G} = -0.6\,\mathrm{V}$ reaching a voltage amplification of 11.6 and 4.4, respectively. Due to the non identical electronic components the voltage gains of the other ULNAs (position and SCHOTTKY pick-ups) have a variation between $8.5-12.5$ and $3.3-5.3$ for the termination resistances of $1\,\mathrm{M\Omega}$ and $50\,\Omega$, respectively. Also their optimal bias voltages of the gate are varying between $-0.47\,\mathrm{V}$ and $-0.62\,\mathrm{V}$. Since the working points of the amplifier depend also on the actual operation temperature the gate voltage U_G can be set variably with a digital-to-analog module. The drain voltage is fixed to 5 V.

The input related voltage noise density and current noise density has already been measured in former works using the same amplifier [86, 89] and for frequencies higher than the cutoff frequency of $\sim 400\,\mathrm{kHz}$ are $e_n \approx 0.4 - 0.7\,\mathrm{nV}/\sqrt{\mathrm{Hz}}$ and $i_n \approx 1-4\,\mathrm{fA}/\sqrt{\mathrm{Hz}}$, respectively. Due to the $1/f$-noise (also called flicker noise) behaviour typical for semi-conductor devices [90] the voltage noise density is increasing with decreasing frequency. For the frequencies relevant for CSR the voltage noise density is, thus, $e_n \lesssim 1\,\mathrm{nV}/\sqrt{\mathrm{Hz}}$. For the current noise density also F. LAUX has given a conservative estimation of $i_n = 10\,\mathrm{fA}/\sqrt{\mathrm{Hz}}$ [75, p. 106].

The board material is a PTFE (Polytetrafluoroethylene) copper laminate (Taconic), which has a low dielectric permittivity. The layout was milled with a CNC-machine (Computerized Numerical Control) without using drilling water but ethanol. For good grounding the upper and bottom side of the board are connected by thin silver rods, which are soldered in former drilled holes. All electrical components are surface mountable devices (SMD) in order to avoid parasitic reactances. The resistors are of thin-film type (Susumu and Yageo) and the capacitors are for low values high-Q type (Johanson Technologies) and for high values of ECHU type (Panasonic).

3.6.2 Cryogenic signal connection schemes

As already pointed out in the previous section 3.4 a crucial ingredient for the position pick-up system is a reliable working cryogenic relay. But also for the calibration of the current pick-up and the switching between non-resonant and resonant operation of the SCHOTTKY pick-up relays are needed.

Despite of the studies and tests of different relay types [75, sec. 4.3.3] and the recommendation of F. LAUX for the relay CRR05-1A (Meder), this relay turned out to be not reliable for the use in CSR. During the first realization of the relay circuit board with this relay type half of the used relays failed working after some cooling cycles. In most cases the internal connection to the coil broke, but only when cooled by a cold head under vacuum. This failure did not occur, when cooled in liquid nitrogen. Therefore another more reliable relay type had to be found.

The RF180-12[7] (Teledyne Relays) [91] is a hermetic sealed, magnetic latching, and double change-over (DPDT - double pole double throw) relay. In contrast to the CRR05-1A it has also the advantage to only need short pulses for switching, which reduces the power dissipation practically to zero. And due to its DPDT design only few relays per pick-up are needed. Tests under cryogenic conditions reveal, that operation times (time between beginning of switching pulse and end of contact bouncing) of $\lesssim 3\,\mathrm{ms}$ can be reached using switching pulse amplitudes of $3-5\,\mathrm{V}$ and switching pulse lengths of $1-2\,\mathrm{ms}$ (under cryogenic conditions). Whereas under room temperature conditions amplitudes of $10\,\mathrm{V}$ are needed due the the higher OHMic resistance of the switching coil. So far only one out of ~ 30 used relays has failed operation.

The actual realization of the relay circuit board, which connects the pick-up electrode with the input of the cryogenic amplifier (ULNA), is depicted in figure 3.19 for the (a) current, (b) position, and (c) SCHOTTKY pick-up.

[7] On the recommendation of STEFAN STAHL, stahl-electronics.com.

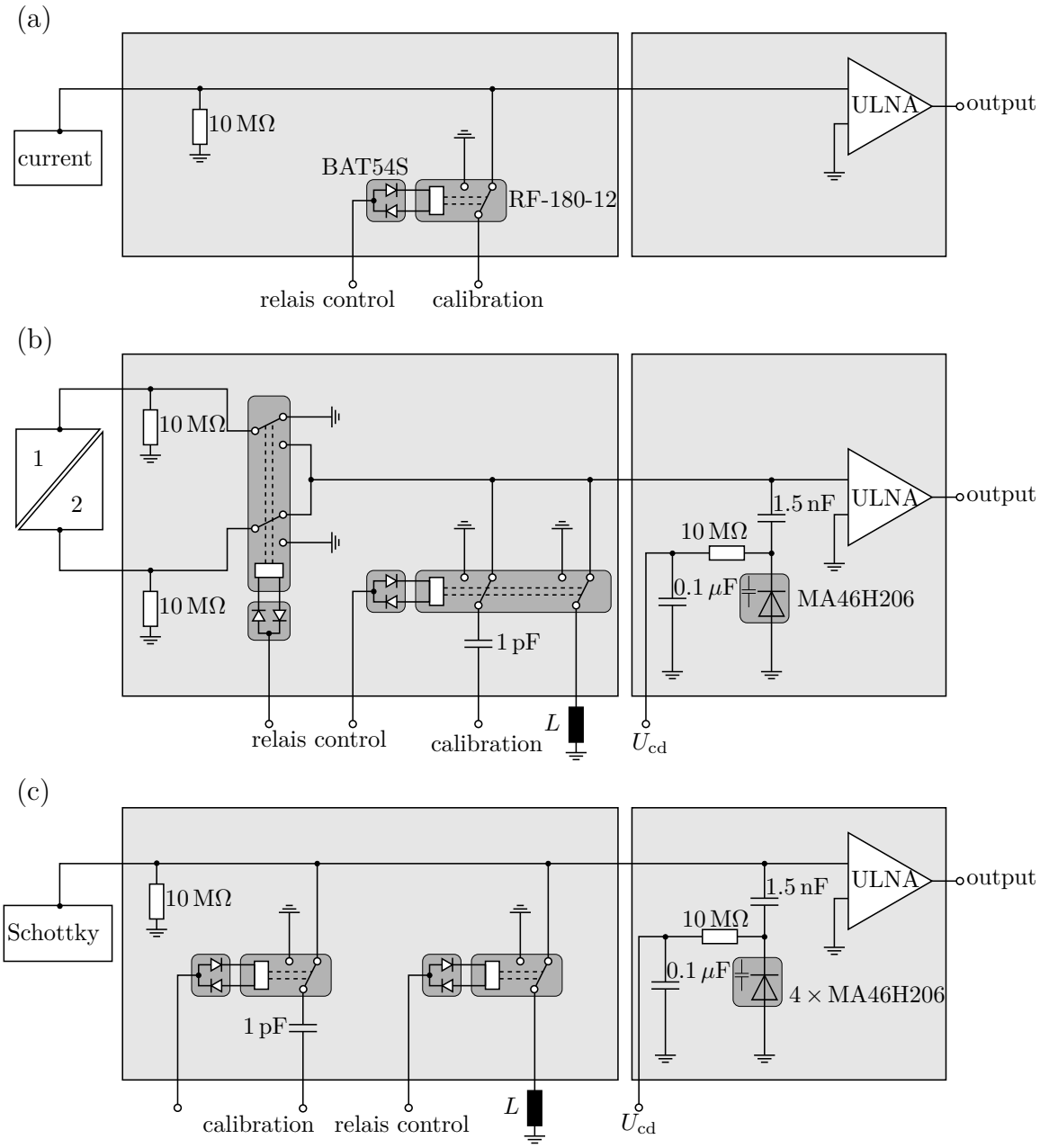

Figure 3.19: Schematic layout of the cryogenic electronics for (a) current, (b) position, and (c) SCHOTTKY pick-up. For the sake of clarity the SCHOTTKY diode (BAT54S) and the relay (RF-180-12) is only labeled in (a).

All electrodes are grounded via an OHMic resistance of 10 MΩ for discharging the electrodes, when the diagnostic system is not in use. Thus, depending on the capacity of the pick-up electrode the discharging time constants are between $1 - 5$ ms, which is sufficiently short compared to the expected revolution frequencies of the

stored ion beams. Nevertheless the input resistance of the ULNA is lowered by this by half (to 5 MΩ). In principle a better solution could be the replacement of the resistance by an additional relay albeit this would need to be most reliable.

In the case of the current pick-up (a) there is no need for a capacity matching but for the determination of the absolute voltage gain (compare section 3.3.3) a calibration signal can be switched directly onto the input of the ULNA. In order to save signal lines the relay is controlled via a bipolar signal, which is fed into a SCHOTTKY diode BAT54S (Philips Semiconductors).

In the case of the position pick-ups (b) a relay is switching between two related electrodes, whereby one of the electrodes is grounded simultaneously (compare section 3.3.2). For the capacity matching of both electrodes there is one voltage controlled, GaAs-based capacitive diode MA46H206 (M/A-COM) [92] installed parallel to the electrode capacity. The capacity can be varied between $6 - 32\,\mathrm{pF}$ by applying a dc-voltage of $10 - 0\,\mathrm{V}$. In order to enable a fast measuring scheme the charging time constants of the capacities should be at least in the millisecond range. The bottle neck in this case is the capacity of 1.5 nF, which is necessary for the ac-coupling and for optimal capacity tuning should be larger than the capacity of the diode (as discussed in [75, sec. 4.3.4.5]). The resistance of 10 MΩ and the capacity of $0.1\,\mu\mathrm{F}$ form a filter for the applied dc-voltage (U_{cd}). Finally this limits the charging time constant to $\tau \approx 10\,\mathrm{M\Omega} \cdot 1.5\,\mathrm{nF} = 15\,\mathrm{ms}$ accepting an additional reduction of the input resistance of the ULNA. The second ingredient of the capacity matching is formed by an additional relay, which switches an inductance ($L \sim 840\,\mu\mathrm{H}$) parallel to the electrode capacity forming a LCR-circuit. By the ac-coupling (1 pF) of a calibration signal the resonance frequencies of both electrodes can be matched avoiding a systematic measurement error in the beam position determination (compare section 3.4.6). The resonant measuring scheme of the position pick-up system is not yet realized and is postponed to a possible future upgrade. The necessary change would be the adaption of the tunable resonance frequencies to a frequency range of approximately $360 - 460\,\mathrm{kHz}$ [75, fig. 4.35] by changing the inductance and the number of capacity diodes.

For the SCHOTTKY pick-up (c) an optional resonant operation is realized. In total there are four capacity diodes and a switchable inductance ($L = 434\,\mu\mathrm{H}$) installed parallel to the electrode capacity. The tunable resonance frequency range allows the resonant measuring scheme of almost all ion species storable in CSR (see section 3.6.6). In addition to that, there is also the possibility to couple a calibration signal onto the input of the amplifier (independently of the inductance) for the adjustment of the resonance frequency.

3.6.3 High-Q resonator layout

Both, for the resonant operation of the SCHOTTKY pick-up and the capacity matching of the position pick-ups inductances are needed. The combination of a coil in its conductive housing is called hereafter resonator.

A formalism for the optimal high-Q resonator design for helical coils is discussed in [93]. Herein a given value for the resonator housing diameter defines the geometry of an ideal resonator and its coaxial helical coil:

$$D_{\mathrm{R}} = 65\,\mathrm{mm} \tag{3.40}$$
$$L_{\mathrm{R}} = 1.325\,D_{\mathrm{R}} \approx 90\,\mathrm{mm} \tag{3.41}$$
$$d_{\mathrm{c}} = 0.550\,D_{\mathrm{R}} \approx 36\,\mathrm{mm} \tag{3.42}$$
$$l_{\mathrm{c}} = 0.825\,D_{\mathrm{R}} \approx 54\,\mathrm{mm} \tag{3.43}$$

where D_{R} and L_{R} are the inner diameter and length of the resonator housing, respectively, and d_{c} and l_{c} are the inner diameter and length of the helical coil, respectively.

Each two neighboring windings give rise for a capacity. The sum of all these parasitic capacities is the self-capacity of the coil, which should be as small as possible. Because of dimension constraints a two layered coil has to be wound, where the self-capacity can be reduced by so-called *interleaved winding* [94]. Here the coil is not wound layer by layer, but in (total 5) cells consisting of two layers of 26 windings each, whereas the last cell has partly less windings. For lowering the self-capacity further the two layers are separated by $\sim 1\,\mathrm{mm}$ of PTFE tape. The windings of the resonator coils for the position pick-ups are even values in the range of $234 - 248$. The resonator coil for the SCHOTTKY pick-up has in total 145 windings (in 3 cells).

The coils are wound using a PFA[8] insulated copper wire (IEC-TFCP-010, Newport Electronics) with a diameter of 0.25 mm and an insulation thickness of 0.08 mm. The coil body is a PTFE cylinder with the above given dimensions. The resonator housing consists of oxygen free copper (OFC 99.95) assuring good electric and thermal conductivities.

In an OHMic conductor ac-currents create eddy currents, which eliminate currents in its interior and only allow currents in a small effective area at its surface (skin effect [95]). The characteristic skin depth δ denotes the length, where the current has dropped to $1/e$. It scales with the square root of the specific resistance of the conductor and the inverse of the rf frequency $\delta \propto \sqrt{\rho/f}$. For this reason the inner surface of the resonator housing is polished and kept clean in order to reduce the effective surface area and minimizing the losses due to the resonator resistance.

[8] Perfluoroalkoxy alkane has similar properties than polytetrafluroethylene (PTFE).

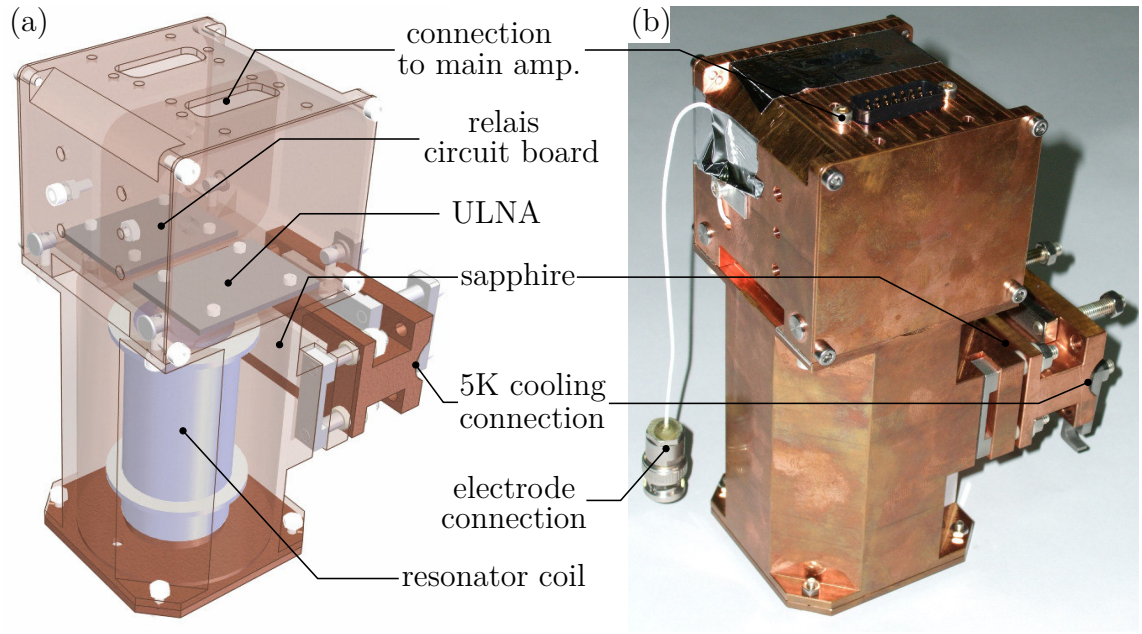

Figure 3.20: The cryogenic amplifier box of the current pick-up as a (a) CAD-model and (b) photograph. Note that the current pick-up has actually no resonator coil installed, but the position and SCHOTTKY pick-ups.

3.6.4 Hardware layout of the cryogenic amplifiers

All electronic components (cryogenic amplifier, relays circuit board, and resonator) discussed in the three previous sections 3.6.1 to 3.6.3 are installed in the so-called cryogenic amplifier box. In figure 3.20 the current pick-up amplifier box is exemplary shown as a (a) CAD-model and (b) photograph. It is an oxygen free copper box shielding the electronics from external noise, assuring a good thermal cooling of the electronics and being a practical solution for fast access and possible replacement.

The boxes are mounted directly to the first turn of the gaseous He line of the CSR refrigerator system (see section 2.4) inside of the insulation vacuum. The sapphires are used for electrical decoupling avoiding grounding loops of the electronics, but simultaneously assuring good thermal conduction. In figure 3.21 the (a) cryogenic amplifier and (b) relays circuit board of a position pick-up is shown installed inside its cryogenic amplifier box. The cryogenic amplifiers are connected to the electrodes via $\sim 0.2\,\mathrm{m}$ long commercial miniature coaxial cables STC-50A-36T (Vishay) with BNC-connectors. The connections to the main amplifiers (discussed in section 3.6.5) is done via a Sub-D15 interface and an in-house built cable (discussed in section 3.7).

After the full assembly of the electronics each amplifier box has been tested under cryogenic conditions in a test setup assuring the functionality and characterizing the

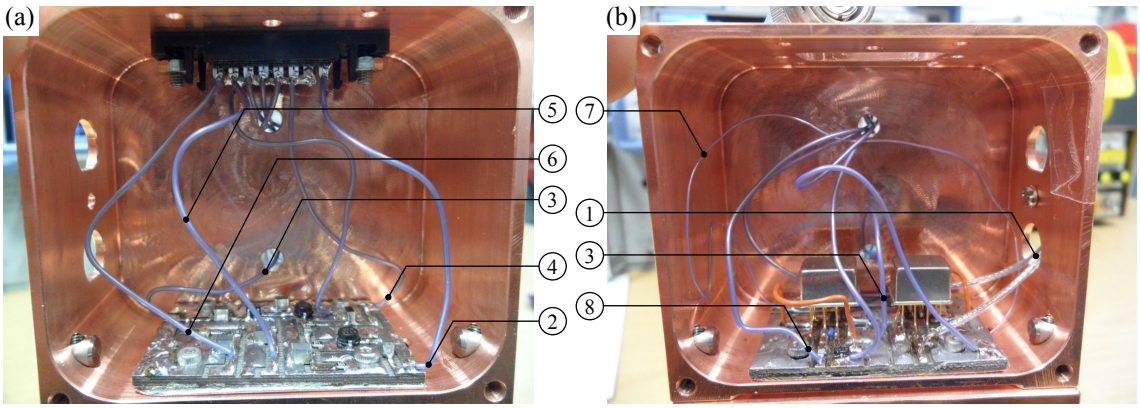

Figure 3.21: The (a) cryogenic amplifier and (b) relays circuit board inside the cryogenic amplifier box of one of the position pick-ups, with (1) input and (2) output of the cryogenic amplifier, (3) connection between ULNA and relays circuit board, the (4) drain, (5) gate, and (6) capacitive diode bias voltages, and the (7) connection to resonator coil and (8) calibration signal.

amplification properties. Prior to the installation into CSR the amplifier boxes are wrapped additionally in ten layers of multilayer insulation in order to reduce the radiation heat input onto the helium cooling circuit during the room temperature operation of CSR.

3.6.5 Room temperature amplifier system

The main amplifiers are in-house built[9] low noise room temperature amplifiers. Solely the current pick-up main amplifier is a commercial amplifier, discussed already in section 3.3.3. The reason for this is discussed below. Due to the characteristic damping at low frequencies ($\lesssim 100\,\mathrm{kHz}$ at $50\,\Omega$ termination) of the cryogenic amplifier (see section 3.6.1 and figure 3.18) the main amplifier has been designed with a high OHMic input resistance of $1\,\mathrm{M}\Omega$. Especially for the commissioning phase of CSR (see section 5) it has been important to be sensitive for low frequencies corresponding to low revolution frequencies at low ion beam energies. In a later operation stage of CSR the high OHMic main amplifiers may be replaced by $50\,\Omega$ adapted amplifiers for best noise reduction.

The layout of the main amplifier is depicted in the appendix A.2. The measured voltage gains as a function of frequency of the 13 used amplifiers (12 for the position and one for the SCHOTTKY pick-up) are shown in figure 3.22. The voltage gain reaches $\sim 60\,\mathrm{dB}$ for frequencies between $100 - 1000\,\mathrm{kHz}$. Roughly at $4\,\mathrm{kHz}$ is the

[9]The amplifier has been designed by VOLKER WIEDER of the MPIK electronics shop.

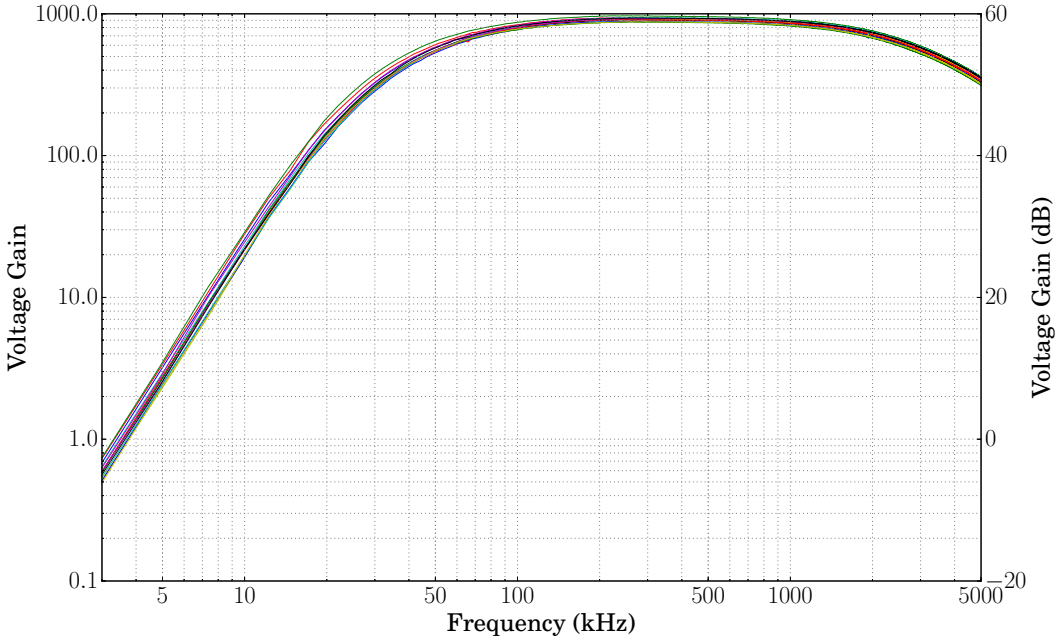

Figure 3.22: Measured voltage gain as a function of frequency of the room temperature main amplifiers.

edge of effective amplification. Both lower frequencies and the higher frequencies ($\gtrsim 10\,\mathrm{MHz}$) are actively damped in order to suppress external noise.

Due to the non constant amplification of the main amplifier the signals (in time domain) are distorted. For the position pick-ups and the SCHOTTKY pick-up this is not problematic, since here the signals of only a small frequency span are being measured and analyzed. But for the current pick-up the signals are recorded directly in time domain with an oscilloscope in order to integrate the signals occurring from the ion bunches (see section 5.2). Therefore the main amplifier of the current pick-up is a commercial low noise amplifier with an input resistance of $1\,\mathrm{M}\Omega$ (see section 3.3.3), which has a constant amplification over the relevant frequency range (see figure 3.6).

3.6.6 The resonant SCHOTTKY measurement system

The SCHOTTKY pick-up system is realized with the option of resonant operation in order to achieve highest sensitivities as will be discussed in this section.

The impedance of a parallel LCR-circuit is given by [96]

$$Z(\omega) = \frac{1}{i\omega C - \frac{i}{\omega L} + \frac{1}{R}}. \tag{3.44}$$

At the resonance frequency

$$f_{\mathrm{res}} = \frac{1}{2\pi\sqrt{L\,C}} \tag{3.45}$$

the imaginary part in equation (3.44) cancels and the effective resistance of the tuned circuit can be expressed as [97]

$$R_{\mathrm{p}} = 2\pi f_{\mathrm{res}} L\,Q, \tag{3.46}$$

where Q is the so-called *quality factor*, which is defined as the ratio of electromagnetic energy stored in the circuit W over the loss per cycle N [94]

$$Q = \omega_{\mathrm{res}} \frac{W}{N}. \tag{3.47}$$

The stored energy is equal to $W = {}^1\!/_2 LI^2$, whereas the losses can be expressed as $N = {}^1\!/_2 R_{\mathrm{loss}} I^2$, which results in

$$Q = \omega_{\mathrm{res}} \frac{L}{R_{\mathrm{loss}}}. \tag{3.48}$$

The losses summarized in R_{loss} are due to OHMic resistances in the wire of the coil R_{coil}, losses in the resonator housing $R_{\mathrm{resonator}}$, and dielectric losses $R_{\mathrm{dielectric}}$ [98]

$$R_{\mathrm{loss}} = R_{\mathrm{coil}} + R_{\mathrm{resonator}} + R_{\mathrm{dielectric}}. \tag{3.49}$$

In [99, sec. 4.1.4] each contribution is derived already in detail and therefore will only be summarized here briefly in the following three equations. The losses in the coil taking the skin effect and the proximity effect[10] into account are

$$R_{\mathrm{coil}} = \frac{1}{\sqrt{1 - d_{\mathrm{wire}}^2/a^2}} \frac{\rho\, l_{\mathrm{wire}}}{\pi d_{\mathrm{wire}}} \sqrt{\frac{\pi f_{\mathrm{res}}\,\mu}{\rho}}, \tag{3.50}$$

where d_{wire} and l_{wire} are the diameter and length of the wire, a is the distance between two wire centers and ρ is the specific resistance of the wire. The last factor is equal to the inverse skin depth δ with the magnetic permeability $\mu = \mu_r \mu_0$.

The losses in the resonator are due to induced currents in the resonator material and can be derived using the transformer equation

$$R_{\mathrm{resonator}} = \frac{\rho\,\pi D_{\mathrm{R}}}{L_{\mathrm{R}}} \sqrt{\frac{\pi f_{\mathrm{res}}\,\mu}{\rho}} \left(\frac{d_{\mathrm{c}}}{D_{\mathrm{R}}}\right)^2 n^2, \tag{3.51}$$

[10] Two neighboring windings with ac-currents influence each other in a similar manner as for the intrinsic skin effect, resulting in an increase of the resistance by a factor $1/\sqrt{1 - d_{\mathrm{wire}}^2/a^2}$ [94].

where D_R is the inner diameter and L_R the length of the resonator housing and d_c is the diameter and n the number of windings of the helical coil.

The dielectric losses are due to changes in the polarization in the insulation material and its non-zero resistance. It can be expressed as

$$R_\mathrm{dielectric} = 0.15\, l_\mathrm{c}\, \omega^3 L^2 C_s \tan\phi, \tag{3.52}$$

where l_c is the length, L is the inductance, C_s the self-capacity of the coil, and $\tan\phi$ the dielectric loss tangent. But due to the low loss tangents of PTFE at cryogenic temperatures can the contribution of dielectric losses be neglected for a resonator coil with the here given dimensions similar to [99, sec. 4.1.8].

Experimentally the quality factor can be measured over the determination of the $-3\,\mathrm{dB}$ width of the resonance in a power spectrum

$$Q = \frac{f_\mathrm{res}}{\Delta f_{3\ \mathrm{dB}}}. \tag{3.53}$$

In resonant operation the signal but also the noise is boosted by the factor Q. Consequently the signal-to-noise ratio (SNR) is only amplified by a small fraction of Q. As derived in [75, eq. 4.96] the effective gain is given by

$$\mathrm{SNR}_\mathrm{gain} = Q \sqrt{\frac{e_n^2 \Delta f}{(4 k_\mathrm{B} T R_\mathrm{p} + i_n^2 R_\mathrm{p}^2 + e_n^2)\Delta f}}, \tag{3.54}$$

where e_n and i_n are the input related voltage and current noise densities of the amplifier, respectively, Δf the measurement resolution band width, k_B the BOLTZMANN constant, T the temperature, and R_p the effective resistance, given by equation (3.46).

Important for the SCHOTTKY pick-up is the possibility to match the resonance frequency to, at least, one harmonic of the revolution frequency of not one ion beam, but optimally of all storable ion beams. In figure 3.23 a calculation of the measurement frequency (upper panel) with corresponding harmonic number (lower panel), where the SCHOTTKY frequency is close to 400 kHz, are shown as a function of the mass of a singly charged ion beam with energies of (blue) 300 keV and (red) 20 keV, respectively.

Starting from the relative high electrode capacity of $C_\mathrm{electrode} = 229.6(8)\,\mathrm{pF}$ (resonant measurement at room temperature, similar to section 3.3.2) and with the capacity range per capacitive diode for a given frequency range the number of capacity diodes and the value of the inductance are fixed. After manufacturing of test coils and varying the number of capacity diodes the final setup of the SCHOTTKY pick-up has four parallel capacity diodes and a resonator with an inductance

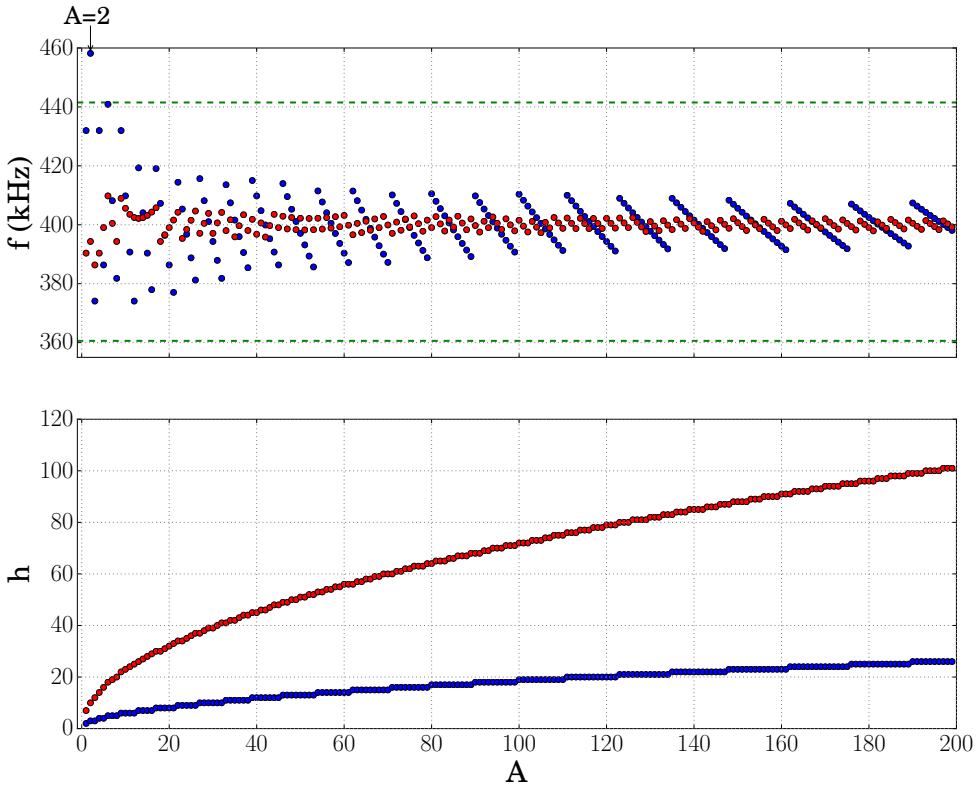

Figure 3.23: Calculation of the (upper panel) measurement frequency and (lower panel) harmonic number for SCHOTTKY frequencies close to 400 kHz as a function of ion mass of a singly charged ion beam with (blue) 300 keV and (red) 20 keV, respectively. The green dashed lines corresponds to the tuning range of the SCHOTTKY pick-up under cryogenic conditions.

of $L = 433.8(11)\,\mu$H allowing a frequency tuning between $360.6 - 441.5$ kHz (under cryogenic conditions). These limits are also shown in figure 3.23 as green dashed horizontal lines. Consequently except for the mass of $A = 2$ (e.g. H_2^+ or D^+ ion beam with 300 keV energy) the SCHOTTKY pick-up can be operated for all ion masses resonantly.

Figure 3.24 shows the measured resonance frequencies as a function of the bias voltage at the capacitive diodes for (blue) cryogenic and (red) room temperature operation. The shape of the curves is caused by the characteristic non-linear capacity dependence of the capacitive diodes [92]. Mainly due to the shrinkage of the resonator coil and the electrode the shift of the frequency to higher values with decreasing temperature can be understood qualitatively. According to equation (3.45) the resonance frequency scales with $f_{\mathrm{res}} \propto 1/\sqrt{L\,C}$. Assuming a solenoidal coil

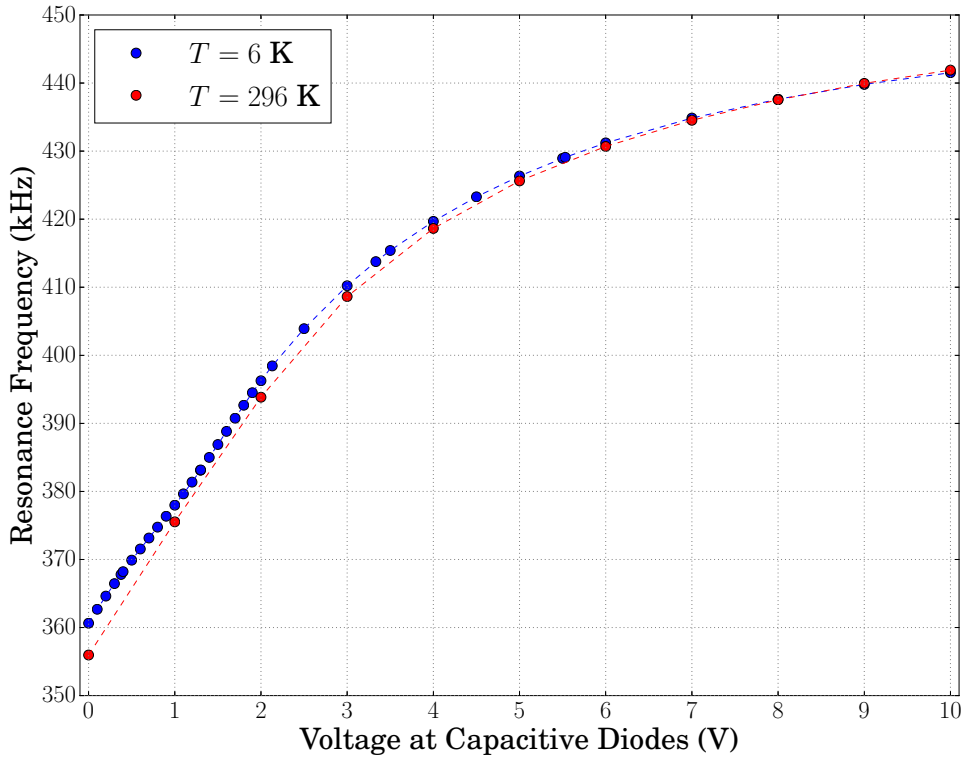

Figure 3.24: Measured resonance frequencies as a function of the bias voltage at the capacitive diodes for (blue) cryogenic and (red) room temperature operation.

for the resonator coil with radius r and length l the inductance is proportional to $L \propto r^2/l$, which decreases with decreasing temperature. Approximating the total capacity by a parallel plate capacitor with radius r and distance d of the plates the capacity is given by $C \propto r^2/d$, which also decreases with decreasing temperature. Thus, the resonance frequency increases with decreasing temperature.

Figure 3.25 shows the measured quality factor as a function of the bias voltage at the capacitive diodes at a temperature of $T = 6\,\mathrm{K}$. The measurement has been performed during the cryogenic commission phase of CSR (see section 5). But due to bad luck the cryogenic amplifier failed operation, before any other measurement regarding the resonant SCHOTTKY pick-up could be performed.

With the equation (3.48) the quality factor can be calculated using for the loss resistance the equations (3.49) to (3.51) and neglecting dielectric losses. Unfortunately the specific resistance of the used coil wire is not specified for cryogenic conditions. Therefore it is assumed to be the widely used standard electrolytic-

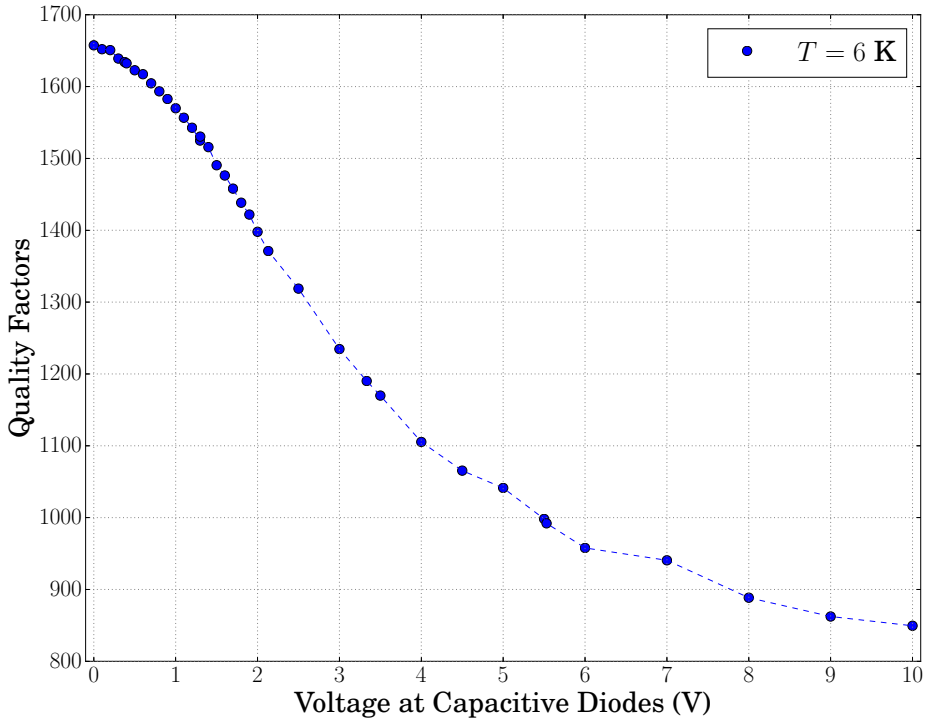

Figure 3.25: Measured quality factor as a function of the bias voltage at the capacitive diodes at a temperature of $T = 6\,\mathrm{K}$.

tough-pitch (ETP) copper with a specific resistance of $\rho_{293\,\mathrm{K}} = 1.7 \times 10^{-8}\,\Omega\mathrm{m}$ and a residual-resistance ratio (RRR) of typically $\mathrm{RRR} = \rho_{293\,\mathrm{K}}/\rho_{4\,\mathrm{K}} \sim 100$ [81, p. 543]. With the geometrical dimensions from section 3.6.3, the (room temperature) inductance $L = 433.8\,\mu\mathrm{H}$ and a resonance frequency of $f_{\mathrm{res}} = 360\,\mathrm{kHz}$ one calculates a quality factor of $Q \approx 1700$ assuming a $\mathrm{RRR} = 120$. This is in good agreement with the measured data. Nevertheless there is obviously a decrease in the quality factor with increasing bias voltage at the capacitive diodes, which could be caused by a non constant but decreasing quality factor of the capacitive diodes (This is not specified by the manufacturer). The decrease has also been observed in [75, fig. 4.50] but with quality factors of $Q_{\mathrm{Laux}} \approx 500$ (with $L_{\mathrm{Laux}} = 1160\,\mu\mathrm{H}$ and $f_{\mathrm{res,\,Laux}} = 434\,\mathrm{kHz}$) and less pronounced. But although the inductance (of the actual SCHOTTKY pick-up) is smaller by a factor of ~ 2.7, at the same resonance frequency the achieved quality factor is higher by a factor of ~ 1.8 indicating a smaller loss resistance.

In figure 3.26 the calculated gain in signal-to-noise ratio by resonant amplification using equation (3.54) is shown. For this calculation a temperature of 6 K, an input related voltage noise density $e_n = 0.5\,\mathrm{nV}/\sqrt{\mathrm{Hz}}$ of the ULNA (see section 3.6.1)

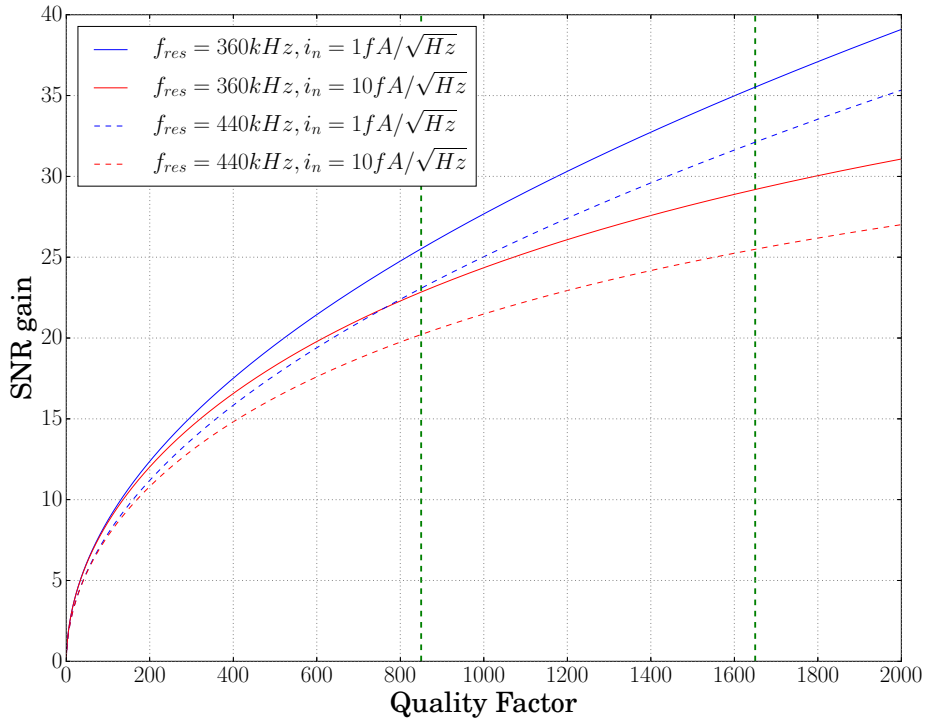

Figure 3.26: Calculated gain of signal-to-noise ratio (SNR) by resonant amplification at a temperature of $T = 6\,\mathrm{K}$. The green dashed vertical lines correspond to the quality factor range taken from figure 3.25.

and an inductance of $L = 433.8\,\mu\mathrm{H}$ has been assumed. The input related current noise density of the ULNA is either (blue) $i_n = 1\,\mathrm{fA}/\sqrt{\mathrm{Hz}}$ or (red) $i_n = 10\,\mathrm{fA}/\sqrt{\mathrm{Hz}}$ (compare section 3.6.1) and the resonance frequencies are either (solid lines) $f_{\mathrm{res}} = 360\,\mathrm{kHz}$ or (dashed lines) $f_{\mathrm{res}} = 440\,\mathrm{kHz}$. Thus, the expected gain in SNR due to resonant amplification for the SCHOTTKY pick-up is between $20 - 35$ depending on the true current noise density.

3.7 Cryogenic realization

One of the most demanding challenges regarding the CSR diagnostic has been the compatibility of the entire system with the environment and the different operation modes of CSR. Since the experimental vacuum chambers of CSR are baked at $\sim 250\,^{\circ}\mathrm{C}$ for the room temperature operation mode (see section 2.5) the in-vacuum parts of the electronics (meaning the cryogenic amplifier boxes as well as the con-

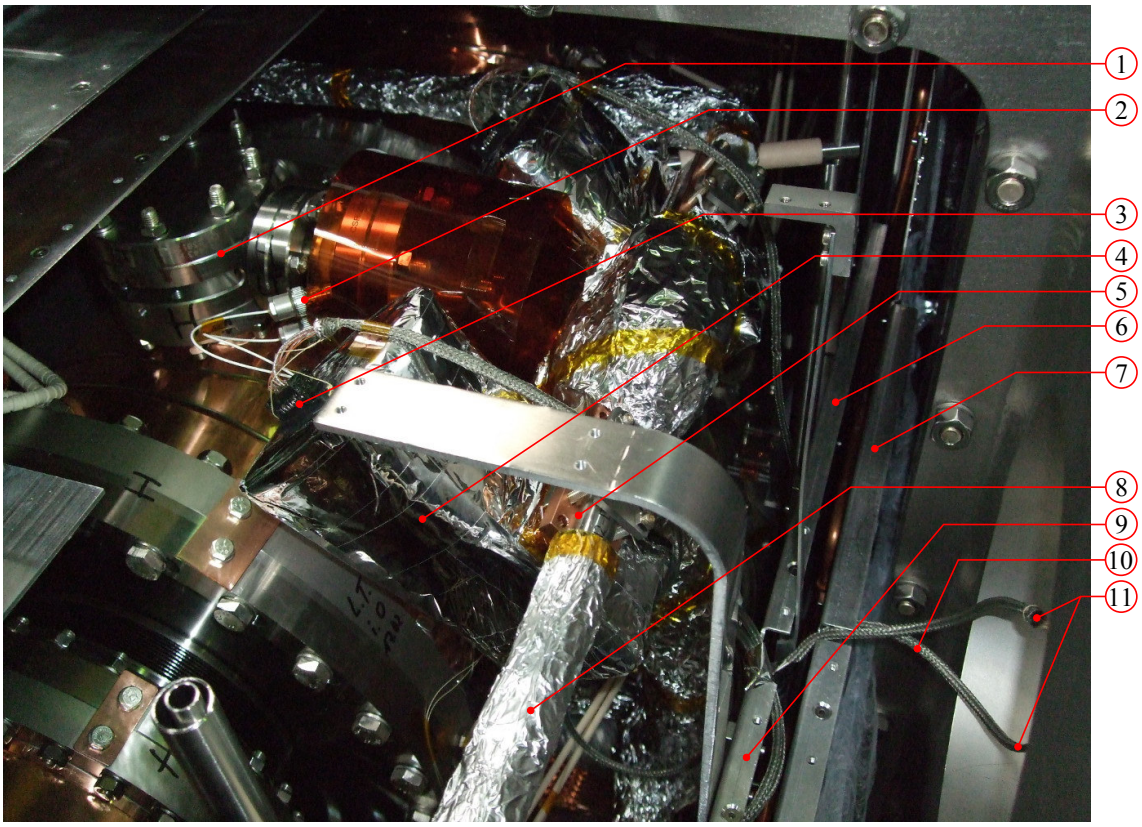

Figure 3.27: Photograph of installed amplifier electronics in CSR at the entrance of the injection straight section with (1) position pick-up, (2) BNC connections between electrodes and cryogenic amplifier, (3) Sub-D15 connection between cryogenic and main amplifier, (4) cryogenic amplifier box, (5) cooling connection between cryogenic amplifier and 5 K He-line, (6) inner radiation shield, (7) outer radiation shield, (8) first turn of 5 K He-line, (9) anchoring point of inter-amplifier connection cable at inner radiation shield, (10) inter-amplifier connection cable, and (11) Sub-D25 connection between cryogenic and main amplifiers.

nection cables between cryogenic electronics and room temperature main amplifiers) have to be easily accessible and removable. For this reason the thermal radiation shields and the multilayer insulation of CSR have dedicated openings in the relevant straight sections in order not to need to dismount the whole shield structure as a preparation for the bakeout of CSR. In figure 3.27 a photograph of the installed amplifier electronics in CSR is shown for the case of the position pick-up 1 (entrance of the first straight section (A), see also figure 2.6).

Another demand is the maximal allowed heat input of the diagnostic system onto the refrigeration system of CSR. In the case of cryogenic operation mode of CSR this is uncritical, since the heat input arises mainly from the thermal conduction

from room temperature (11) onto the first 5 K He-line (8) via the connection cables (10) between cryogenic and room temperature amplifiers. Thus, these cables are as long as practically reasonable (approximately $\sim 1.5\,\mathrm{m}$) and are thermally anchored in between (after $\sim 0.3\,\mathrm{m}$) at the inner radiation shields (9).

This cable consists of six twisted pairs of PFA insulated copper wires (IEC-TFCP-005, Newport Electronics) with 0.13 mm diameter for the controlling voltages of the electronics and two coax cables (GVLZ081, GVL Cryoengineering) for the output signal of the ULNA and the calibration signal (the current pick-up calibration cable is a $\sim 1.5\,\mathrm{m}$ long coaxial cable STC-50A-36T, Vishay). These cables are in the inside of a copper braid screen (with $8 \times 40 = 320$ copper wires with $90\,\mu\mathrm{m}$ diameter each). The heat input through these cables can be estimated using the thermal conductivity of copper (with RRR = 50) under cryogenic conditions $\lambda_{\mathrm{Cu50}}(T)$ [100, 101], see also appendix A.1, and the equation for thermal conduction [81, sec. 2.2]

$$\dot{Q}_{\mathrm{cond}} = \frac{A}{L} \int_{T_{\mathrm{cold}}}^{T_{\mathrm{hot}}} \lambda(T) \mathrm{d}T, \tag{3.55}$$

where A is the cross sectional area and L the length of a solid bar with temperatures T_{cold} and T_{hot} at its ends. In table 3.1 a conservative calculation of the heat input contributions is summarized for cryogenic and room temperature operation of CSR.

The heat input by radiation in an environment with temperature T_{hot} can be calculated with the Stefan-Boltzmann law [102, p. 58]

$$\dot{Q}_{\mathrm{rad}} = \sigma e A \left(T_{\mathrm{hot}}^4 - T_{\mathrm{cold}}^4 \right), \tag{3.56}$$

where σ is the Stefan-Boltzmann constant and e the total emissivity of the cold surface with area A and temperature T_{cold}.

In the case of the room temperature operation mode of CSR the main contribution is due to the thermal radiation onto the cryogenic parts of the electronics (mainly the cryogenic amplifier boxes), which in total have an area of $\sim 1\,\mathrm{m}^2$. Using equation (3.56) and a conservative value for the emissivity of copper of $e = 0.018$ [102, tab. 5.8] the maximal heat input by radiation of 8.3 W can be calculated. This can be lowered using 10 layers of multilayer insulation (Coolcat 2 NW, RUAG Space GmbH), which has a total heat transmission of $1.5\,\mathrm{W/m}^2$ from room temperature to 4 K [65].

The contribution of electrical dissipated power is due to the cryogenic amplifiers and has been measured to be $\sim 20\,\mathrm{mW}$ per amplifier (see section 3.6.1).

The calculated total heat contributions can be well accepted and are within the budget estimated for the CSR refrigerator system (see section 2.4).

Table 3.1: Thermal power calculations for the CSR diagnostics.

	Cryogenic Operation		**RT Operation**
Contribution	**5K He-line**	**40K He-line**	**5K He-line**
Signal Wires to Electrodes	–	–	3.0 W
Signal Wires to Main Amplifier	0.13 W	–	0.4 W
Cable Screening	–	11.4 W	–
Thermal Radiation	$\lesssim$ 0.003 W	–	1.5 – 8.3 W
Electrical Components	0.3 W	–	0.3 W
Total	**0.5 W**	**11.4 W**	**5.2–12.0 W**

3.8 The rf system

For the manipulation of the ion beam and creating short ion bunches CSR is equipped with a drift tube called rf system, which is discussed in this section. The bunching of the ion beam is also the prerequisite for the position pick-up system (discussed in section 3.4), since the detection of the ion beam relies on a time structured ion beam.

The rf system consists of two drift tubes with lengths of 340 mm and 736 mm, respectively. The aperture diameter is 100 mm. The two electrode design is advantageous for the experiments with merged neutral beams [62]. Here the relative collision energy will be either varied by varying the ion source potential of the negative ion platform (which corresponds to a variation of the energy of the neutrals) or by the variation of the stored ions' energy. For the latter a dc voltage at both electrodes of the rf system will be applied. As a result the overlap region of neutral and stored ion beam can be as large as the effective length of the rf system 1086 mm (with gap).

Figure 3.28 shows the rf system as a (a) CAD-model and (b) photograph mounted in its CSR vacuum chamber. The principal design is similar to the SCHOTTKY pick-up electrode (see section 3.5.2). The materials and the mounting principle is the same except for the electrical feedthroughs, which are high voltage single copper pin feedthroughs (W-HV10S-CE-CU24, Vacom) designed for 10 kV. The electrical breakdown strength has been measured under vacuum conditions of the order of 10^{-6} mbar and room temperature to be $\pm$1800 V versus ground. For the bunching of an ion beam only voltages up to 100 V are necessary. The connection in the insulation vacuum are done with kapton-insulated manganin ($Cu_{84}Mn_4Ni_{12}$) wires of 250 μm in diameter and $\sim$ 2 m length (312-KAP-MAN-025, Allectra).

For the bunching of a stored ion beam only the shorter electrode (L_0 = 340 mm) of the rf system is used, whereas the other is grounded. The effective rf voltage

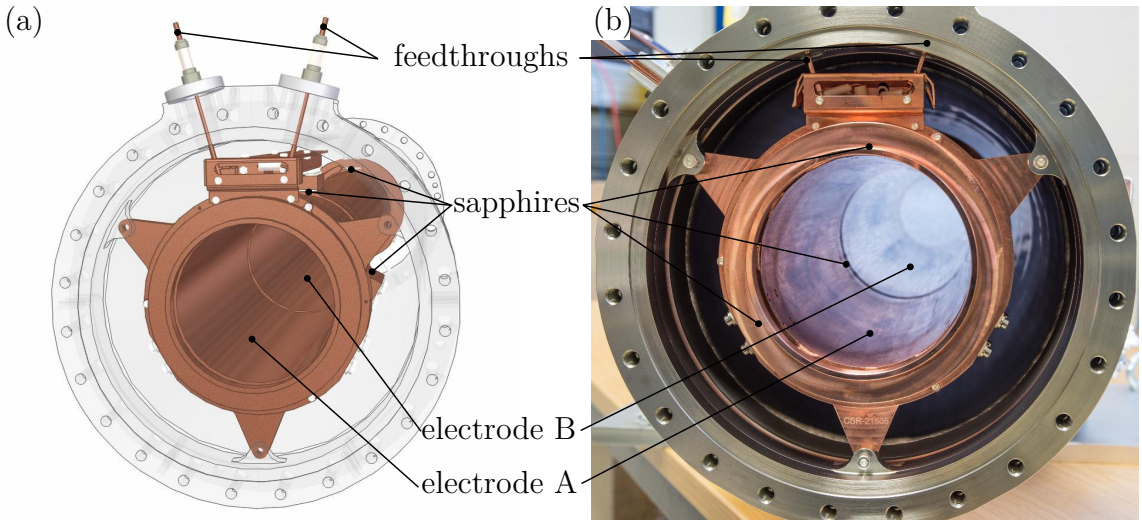

Figure 3.28: The rf system as a (a) CAD-model and (b) photograph mounted in its CSR vacuum chamber. The length of the electrodes A and B are 340 mm and 736 mm, respectively, and the aperture diameter is 100 mm.

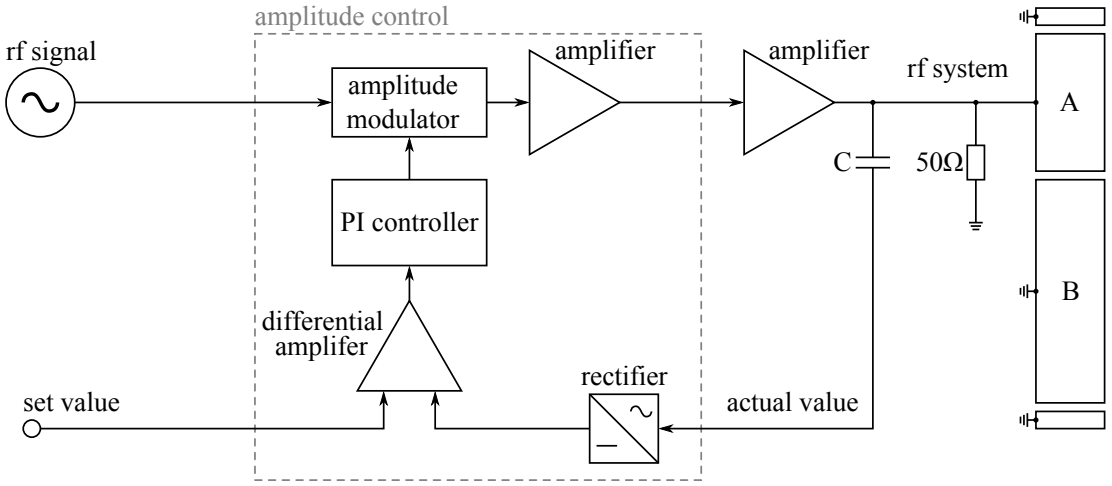

Figure 3.29: Schematic layout of the amplitude regulation system of the rf system.

(see equation (2.31)) depends on $\hat{U}_\mathrm{b} \propto \sin(h\pi L_0/C_0)$, where h is the harmonic number and C_0 is the circumference of the storage ring. Thus, bunching can not be performed near multiples of the $\sim 100^{\mathrm{th}}$ harmonic of the revolution frequency.

For reducing the influence of external noise the amplitude of the bunching signal is actively regulated. In figure 3.29 the schematic layout of the regulation system is shown. It is based on the amplitude modulation of the rf signal by an active feedback loop of the actual value and comparison with the set value.

3.9 Summary

In this chapter the basic principles, realization, and measuring electronics of each individual pick-up system has been presented in detail. Special importance has lain on the amplification system, which consists of cryogenic pre-amplifiers and room temperature amplifiers. The design has been chosen to be as similar as possible to be suited for all of the different kind of pick-ups. Also the technical aspects regarding the heat load on various CSR temperature stages, the different CSR operation modes, and the signal transmission quality has been taken into account in the final design and realization of the diagnostic system.

The measurements performed with the diagnostic system during the commissioning of CSR are presented in chapter 5.

Chapter 4

The CSR electron cooler

In this chapter the CSR electron cooler will be discussed. First the challenges and the requirements of such a new device are emphasized. This is followed by a detailed presentation of the final design of the three different main components of the electron cooler, which are the electron beam production section, the cryogenic merging and interaction sections, and the electron beam collection section. Special focus in the design lies on the adiabatic electron beam transport but also the technical aspects of a cryostat compatible design. At the end of this chapter the realization of key components of the cryogenic section and the setup of the outer beamlines are discussed. The chapter closes by a review of the present status of the entire electron cooler project and its outlook.

4.1 Challenges and requirements

Electron energies

The principle of electron cooling is the merging of a cold, dense and velocity-matched electron beam with a hot ion beam. Therefore the electrons have to be accelerated to an energy E_e which depends on the ratio of electron and ion mass $m_\mathrm{e}/m_\mathrm{i}$ and the ion energy E_i

$$E_\mathrm{e} = \frac{m_\mathrm{e}}{m_\mathrm{i}} E_\mathrm{i}. \tag{4.1}$$

The fastest ion storable in CSR is a proton with 300 keV energy, which corresponds to an electron energy of 163 eV. However, for most heavy molecules (with the same energy) much lower electron energies are needed and at an ion mass of $\sim 160\,u$ the electron energy reaches down to ~ 1 eV.

Cooling time and beam storage time

On top of that, the cooling time constant, equation (2.52), must be significantly shorter than the ion beam storage time. One aspect of CSR are the long storage times at extremely low vacuum, expected to be in the range of 1000 s. On the other hand, as already discussed in section 2.2, the cooling times can be kept short enough by using as cold as possible electron sources and high electron densities.

Cold electron source

Commonly used thermionic electron sources with typical energy spreads of the order of 100 meV are not ideally suited for this purpose. To obtain lower energy spreads the use of the photoemitted electrons originating from cryogenically cooled GaAs photocathodes irradiated by a near-infrared laser were proposed in 1988 [103] and realized in the following years.

In this work, a GaAs semiconductor crystal is covered with a monolayer-thin film of Cs and O, reaching a state of *effective negative electron affinity* (NEA) [104] where the thermalized electrons can be extracted from the crystal surface. The cathode is driven preferably in the so-called *space charge limited mode*, in which due to high laser intensities and low extraction voltages the extracted electrons accumulate in front of the cathode forming a space charge and partly screening the cathode surface from the extraction potential. This effect stabilizes the extraction current and compensates for laser intensity or temperature fluctuations [55].

The photocathode electron source for the CSR electron cooler will be the one developed for the electron target setup at the magnetic Test Storage Ring (TSR) [53, 55, 105]. It has been continuously improved in its performance and proven its reliability for several years at electron kinetic energies between $\sim$ 31 eV and a few keV. However, electron energy spreads of $\sim$ 10 meV for photocathodes cooled down to liquid nitrogen temperature have been demonstrated [54] and the setup features an in vacuo photocathode preparation and renewing setup allowing an almost uninterruptible operation.

When operating the photocathode in the space charge limited mode, the maximal extractable current I depends only on the applied extraction voltage U_{ext} and follows the Child-Langmuir law [41]

$$I = p\, U_{\mathrm{ext}}^{3/2}, \tag{4.2}$$

where the perveance p is a parameter depending solely on the gun geometry and is typically of the order of $1\,\mu\mathrm{A\,V}^{-3/2}$. Thus, for low electron kinetic energies of a few

eV also the electron density is limited. To soften this limitation the electrons will not be produced directly with their final kinetic energy but with higher energy and decelerated then to the desired kinetic energy, which is the so-called *beam deceleration technique*. By this method a substantial enhancement of the electron density (up to $2 \times 10^5\,\mathrm{cm}^{-3}$) at these low kinetic energies (of $\sim 1\,\mathrm{eV}$) has been demonstrated at the TSR electron target [56].

Magnetic guiding field

Another main feature of electron coolers is the longitudinal magnetic guiding field, which performs several functions as discussed in section 2.2 already. Most important is the guidance of the electron beam and the possibility to merge and demerge the electron and ion beam due to the much lower mass of the electrons. Typically, high energy electron coolers have an U- or S-shaped layout and the merging is done with toroids.

The merging scheme of the CSR electron cooler is unconventional. It deviates from standard schemes, where toroids consisting of discrete racetrack coils are used to merge the electron and ion beams. At the low ion velocities in CSR, the inhomogeneous toroidal field especially for lighter ions causes distortions of the ion trajectory which cannot be corrected by simple dipole compensation coils [106]. For this reason H. Fadil et al. [106] proposed a toroidal-free merging scheme, which A. Shornikov [43] developed further to a point where it became basically compatible with a mechanical design. Although the ions have a much higher mass than the electrons their trajectory is slightly influenced by the merging coils. Therefore the ion trajectories are corrected by two sets of correction dipole coils in front of and after the cooler section.

The presence of the magnetic field also allows the magnetic expansion of the electron beam to lower its transverse temperature, as discussed in section 2.2. However for both, the magnetic expansion and the merging region the changes of the magnetic field have to fulfill the adiabaticity criterion stated by equation (2.46). At the same time the field must have a certain minimal strength in order to suppress the various heating effects like TLR and the blow-up due to the Coulomb repulsion. As seen in section 2.2, they can be neglected for minimal magnetic inductions of $B_{\min} \approx 50\,\mathrm{G}$.

The low kinetic energy of the electrons allows to use rather moderate magnetic fields in order to avoid transverse heating effects. For the highest desired electron energy of 1 keV A. Shornikov estimated for the main guiding field a minimal strength of the magnetic induction (of 215 G) [43, p. 52]. For this reason in the final design the nominal field was set to 250 G.

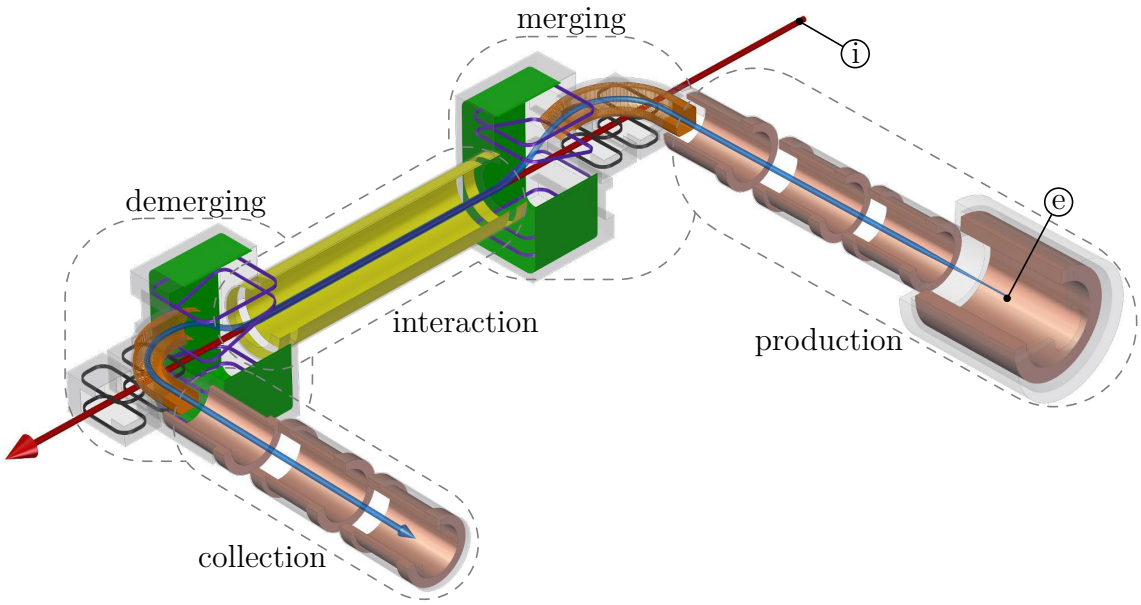

Figure 4.1: Schematic drawing of the magnetic guiding field of the CSR electron cooler. The electron beam (e) is formed in the production section, merged with the ion beam (i), and after the interaction is demerged and collected in the collection section.

Overview of the CSR electron cooler

Figure 4.1 shows a schematic overview of the final magnetic guiding field of the CSR electron cooler. The electron beam (e) is produced by the photocathode in a high-field solenoid (2500 G), then magnetically expanded ($\alpha_1 = 10$) and guided by low-field solenoids (250 G) into the cryogenic region. Here the electron beam is merged with the ion beam (i) after a simultaneous second magnetic expansion ($\alpha_2 = 2$). In the interaction region (125 G) the ion and electron beams are collinear. In a similar manner the electron beam is then demerged (and magnetically compressed), guided to the outside of the CSR cryostat and collected by an analyzing FARADAY cup setup. The ion beam trajectory is corrected by two pairs of correction coils (coloured black) situated before and after the merging regions.

The magnetic system outside of the CSR cryostat (production and collection region) are built from water cooled copper coils. In contrast, the merging and interaction regions are inside of the CSR cryostat and will be realized as high temperature superconductors (HTS) coils only (except for small steering coils inside the longitudinal solenoids).

The basis of the here presented design is formed by the former work by A. SHOR-

NIKOV [43] on the feasibility of the CSR electron cooler. He explored the creation of low-energy electron beams with sufficient high densities for electron cooling at CSR. This was demonstrated by using the electron target of the TSR, whose electron source is a photocathode setup, which will be used for the CSR electron cooler. Furthermore, he developed the layout of the cryogenic magnetic guiding system of the CSR electron cooler, which will be situated inside of the CSR cryostat. This design was compatible with the requirements regarding the vacuum and cryostat layout. First conceptional mechanical design studies of the cryogenic region has been started. In order to provide sufficient cooling power for the HTS coils he developed a cooling system independently of the helium refrigerator system of CSR. This system uses only small amounts of neon at low pressures and was successfully commissioned during his work achieving cooling powers up to 30 W at $\sim$ 30 K. Also a prototype coil using HTS was successfully tested with this cooling system demonstrating the conceptional feasibility of the CSR electron cooler.

During the design of the entire electron beam line, fulfillment of the adiabatically electron transport was tested using the FEA software package Opera-3D [34]. However, the layout of the beamline also depends on other factors, like spatial constraints imposed by the already existing CSR insulation vacuum chamber and beam lines, or mechanical feasibility issues of the electron cooler vacuum and magnet system. The final layout of the full electron cooler system presented here is the result of several design iterations, during which both, the quality of the electron beam and the technical requirements related to the CSR vacuum system and cryostat had to be kept in mind. An ultrahigh vacuum of the order of 10^{-11} mbar, in the photocathode region is particularly important for the long time operation of these electron sources [55].

In the subsequent sections the final mechanical design of each individual region is presented in detail following the trajectory of the electrons from their production (section 4.2) over the merging and interaction with the ion beam (section 4.3) to their collection (section 4.4). At the end of this chapter the performed work towards the setup of the electron cooler will be discussed (section 4.5).

4.2 The electron beam production section

In the simplest and optimal case the electron beam production region consists of a continuous arrangement of magnetic guiding fields. It uses a closed system of two solenoidal coils differing in magnetic inductions in order to allow the magnetic expansion. But this scheme could not be realized for the CSR electron cooler, since for different reasons regarding the vacuum system the solenoidal structure has to be

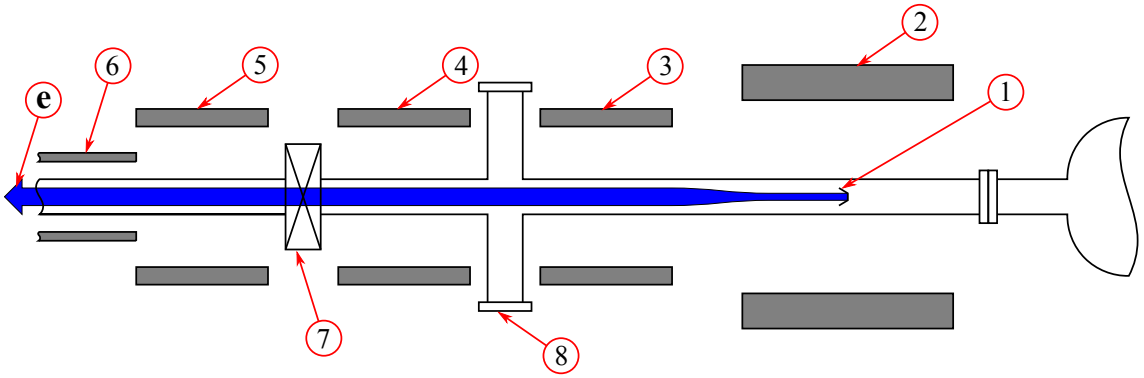

Figure 4.2: Schematically drawing of the electron beam production section. The (e) electron beam is produced by the (1) photocathode, which is in the center of a (2) high-field magnet. The electron beam is then guided and simultaneously expanded by the transition to the low-field region, which is split into three individual (3 – 5) solenoids. The beam is guided into the CSR cryostat and enters the (6) cryogenic magnetic guiding system. The interruptions of the room temperature low-field guiding field are necessary for the vacuum system, which requires gaps for a (7) bakeable gate valve and (8) pumping units.

interrupted.

Figure 4.2 visualizes the electron beam production region as a simplified schematic drawing. Both a bakeable gate valve (7) for separating the CSR from the outer vacuum system and vacuum pumps (8) must be included in the magnetic structure. On the other hand, the required field strength is rather low, as discussed in section 4.1. This facilitates the coil layout substantially. It was also possible to design a transition of the guiding field from room temperature (5) to cryogenic conditions (6). The low-field solenoid (5) can be fitted into a vacuum side flange of 250 mm nominal diameter in order to form the transition to the magnetic guiding field inside the cryogenic system.

4.2.1 Field simulation

The simulation of the combined magnetic design has been performed with FEA software package Opera-3D [34]. In figure 4.3a the simulated magnetic induction (a) and its longitudinal derivative (b) along the magnetic symmetry axis are depicted as functions of the longitudinal coordinate z. The origin $z = 0$ corresponds to the center of the high-field magnet and the position of the photocathode surface. The nominal magnetic inductions are scaled to 2500 G and 250 G for the high and low-field region, respectively.

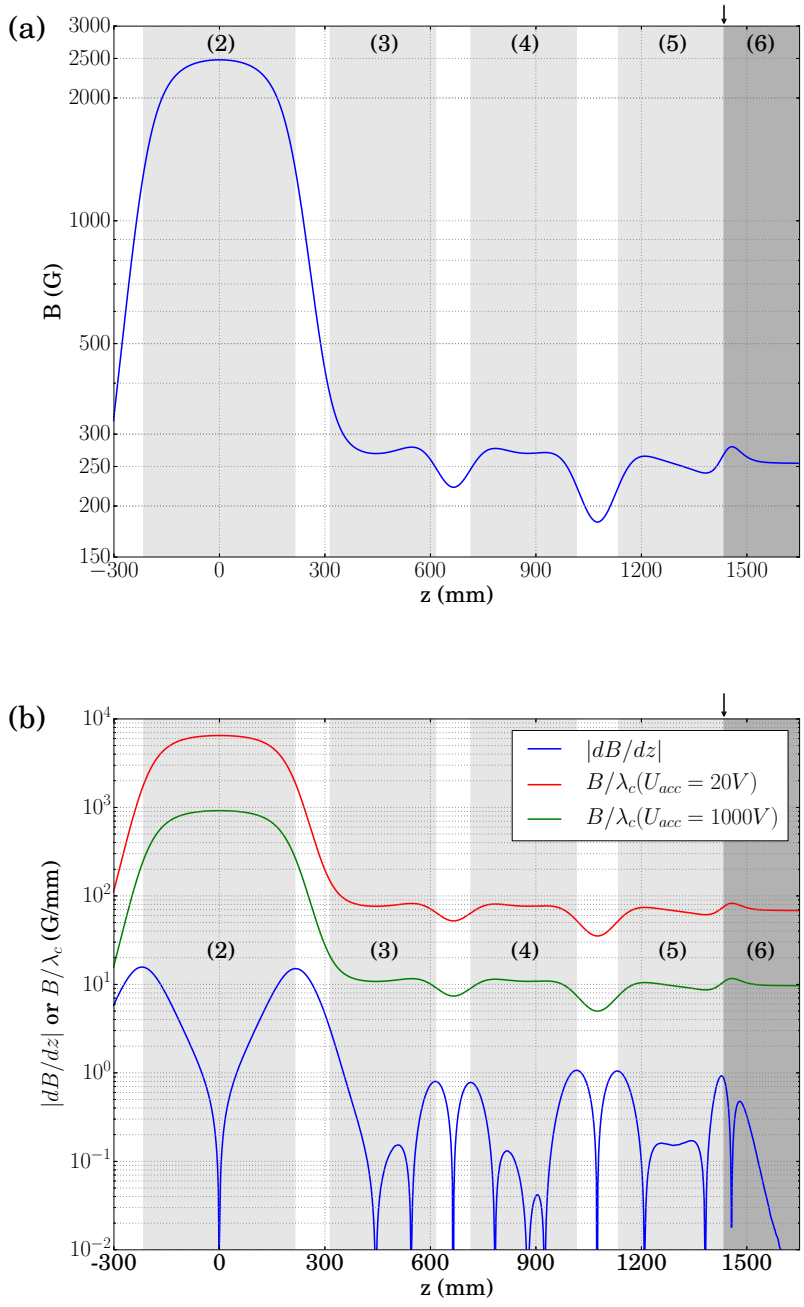

Figure 4.3: The (a) simulated magnetic induction and the (b) calculated derivative together with the ratio of the magnetic induction B and cyclotron length λ_c for two different electron acceleration voltages as a function of the longitudinal coordinate z along the axis of the magnetic fields. The gray shaded areas correspond to the different solenoids and the labeling is according to figure 4.2. The arrow marks the transition from the room temperature to the cryogenic toroid.

The dimensions of the coils correspond to the actual realized design and will be discussed in subsequent section. The gray shaded areas correspond to the interiors of the different solenoids, which are labeled according to figure 4.2. The arrow marks the transition from the room temperature to the cryogenic magnet system.

In order to verify the adiabaticity of the design, the derivative is calculated and shown in figure 4.3b together with the ratio of magnetic induction and cyclotron length B/λ_c which must be much lager than $|\mathrm{d}B/\mathrm{d}z|$ according to equation (2.46). The parameter B/λ_c is shown for a high electron kinetic energy of 1 kV and a low kinetic energy of 20 V. These are the extreme cases for the desired energy range of the beam transport. The higher limit allows to reach also high collision energies of a few 100 eV in the co-moving reference frame of the merged beam. The lower limit corresponds to the transport of the electrons into the interaction region before they are further decelerated if required. The adiabaticity criterion is in all regions well fulfilled by roughly one order of magnitude for high and even better for low electron energies.

In order to verify the adiabatic electron transport electron tracking has been performed with the software package. For this purpose the electrons were started from the center of the high-field solenoid ($z = 0$, corresponding to the photocathode position) with electron kinetic energies ranging up to 1 keV. Also transverse starting offsets up to a radius of 1.5 mm (corresponding to the effective emitting photocathode surface due to the PIERCE electrode aperture) have been investigated. For each starting point the flight direction of the electrons has been set parallel to the magnetic induction simulating a zero starting transverse energy. After passing all low-field solenoids the resulting transverse energy has been calculated at various points over a distance of 200 mm in the middle of the cryogenic solenoid (which in this model was a straight solenoid with 900 mm length but with the true racetrack profile). By calculating the mean transverse kinetic energy over this distance the phase of the cyclotron phase cancels (the longest cyclotron length corresponds to 1 keV electron energy and is in a field of 250 G amounts to roughly 27 mm). For all starting positions and electron kinetic energies the resulting transverse component has been in average far below $\sim 50\,\mu$eV. Thus, it is concluded that no transverse heating occurs.

4.2.2 Mechanical design

Based on the field simulations discussed in the previous section both the magnetic guiding field structure and the vacuum system has been designed. The realized mechanical design is shown in figure 4.4 as a schematic drawing. The guiding field is formed by a high-field solenoid (2) and a total of three low-field solenoids (3 –

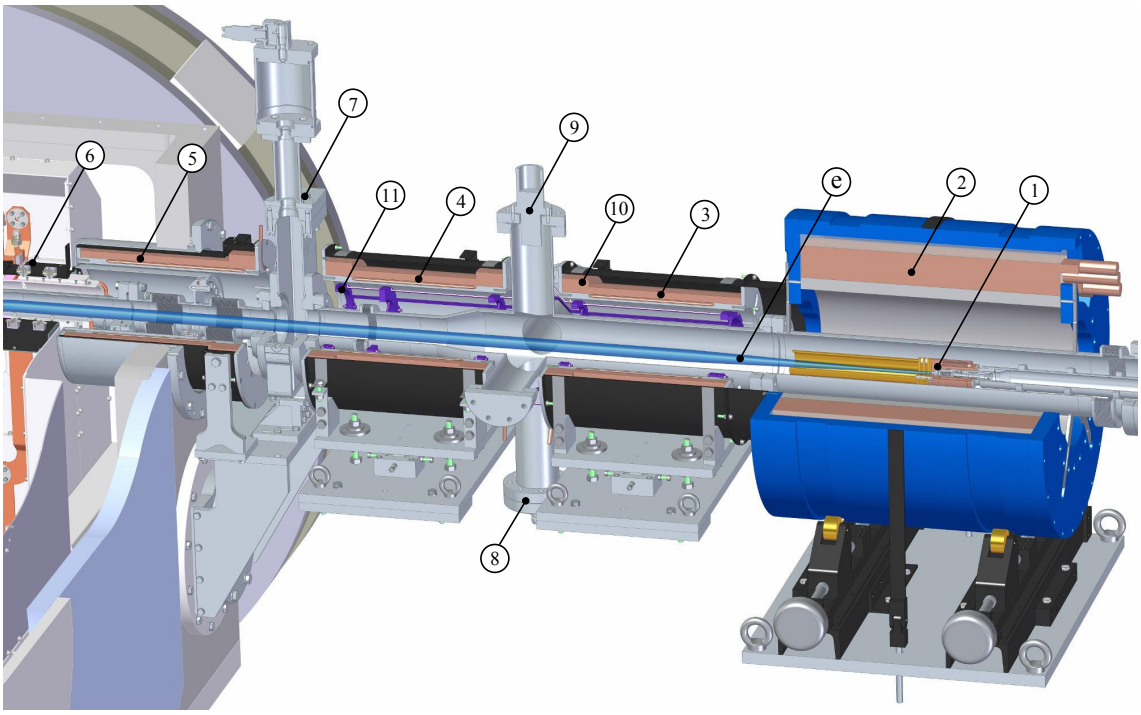

Figure 4.4: Mechanically design of the electron beam production section with (e) the electron beam, (1) the photocathode gun, (2) the high-field solenoid, (3 – 5) the low-field solenoids with (10) additional ring coils at their ends, (6) the cryogenic toroid, (7) a full-metal gate valve, (8) a NEG-pump, (9) a vacuum gauge, and (11) steering coils.

5). The gaps are chosen to be 100 mm for both the magnetic expansion region and between the first two low-field coils (3+4), while it is set to 120 mm between the next low-field coils (4+5) in order to accommodate a bakeable gate valve as a connection of the XHV and UHV vacuum systems. In order to reduce the effect of the gaps and to ensure the adiabaticity of the magnetic field, additional ring coils (10) are added to the ends of the low-field solenoids resulting in a more homogeneous field in the solenoid gaps. These were already included in the presented field simulations.

The high-field magnet (2) is a water cooled copper solenoid (recovered from TSR) with 430 mm length and 150 mm inner winding diameter. Its outside iron yoke (blue coloured parts) is 25 mm thick. In the center, where the photocathode (1) is positioned, it reaches magnetic inductions of 2500 G at approximately 775 A. It was characterized by a field measurement at the photocathode position before its installation. Iron end plates with 200 mm diameter holes were installed to obtain realistic conditions. The measured magnetic induction versus electrical current relation is

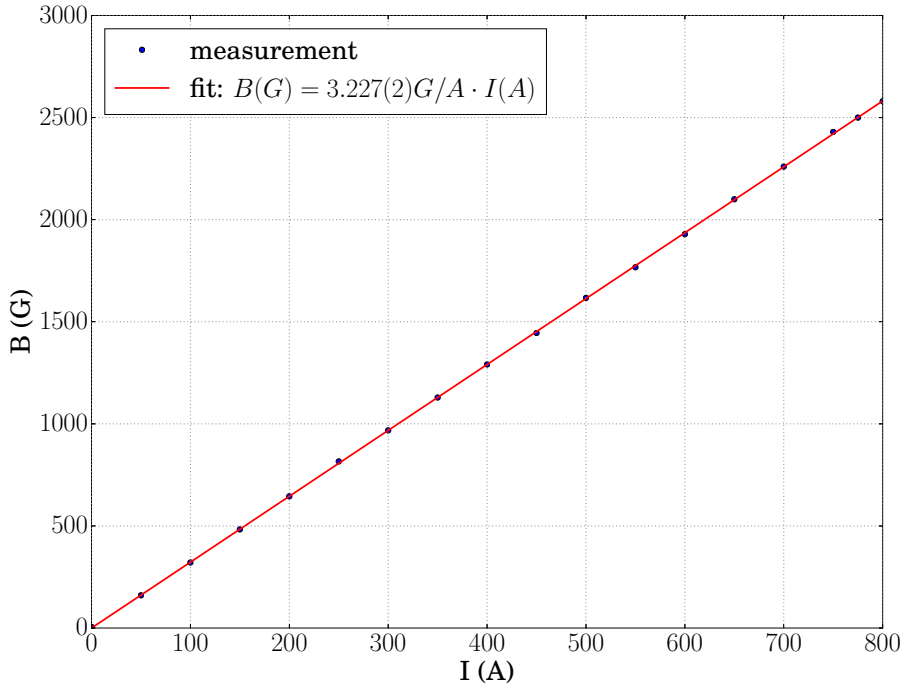

Figure 4.5: Magnetic induction as a function of the current of the high-field solenoid.

shown in figure 4.5. The linear fit of the measurement gives:

$$B(\mathrm{G}) = 3.227(2)\,\mathrm{G/A} \cdot I(\mathrm{A}) \tag{4.3}$$

Each low-field solenoid (3 – 5) is 300 mm long and its main body has in total 460 windings (in 4 layers) and the additional stacks at its ends with 50 mm length are 68 windings each (also in 4 layers). The inner winding diameter is 190 mm. An aluminum cylindrical body serves as support structure for the windings and has an embedded water cooling circuit. The iron screens (carbon steel, 1.0330, DC01) of the low-field solenoids (black coloured parts) have a thickness of 2 mm and provide the return path for the magnetic flux. The low-field solenoids were wound by 2.5 mm diameter enamelled copper wire and have been designed to reach magnetic inductions up to 250 G at approximately 13.5 A.

Additionally, in the first two low-field solenoids (3+4), transverse steering coils (11, coloured magenta) are integrated in order to correct small electron trajectory deviations. They consist of two pairs of HELMHOLTZ-like coils for the horizontal and vertical direction. Their transverse 'radius' is ~ 65 mm and their length is 660 mm. They are wound from 0.8 mm thick enamelled copper wire and each coil has 20 windings. Field simulations reveal that for a longitudinal magnetic guiding field

of 250 G a beam displacement of ±25 mm can be achieved by a steering current of roughly ±5 A.

4.2.3 Vacuum system

The vacuum system of the electron production region, which is also depicted in figure 4.4, consists of a commercial (8) NEG-pump with $\sim$ 600 l/s pumping speed for H_2 (GP 100 MK5, SAES) and a (9) vacuum gauge (IONIVAC IE 514, Oerlikon Leybold). Directly attached is the gun chamber of the photocathode setup (not shown in the figure), which is equipped with an additional ion getter pump with $\sim$ 60 l/s pumping speed for N_2 and Ar and an in-house built NEG module [105]. In order to achieve extremely high vacuum conditions the whole vacuum system is equipped with heating elements and is wrapped in thermal insulating material to be able to bake the system up to 250 °C and to reach vacua of the order of 10^{-11} mbar. For safety reasons, like in case of a vacuum collapse, and to have an independent vacuum system the outer vacuum can be separated from the CSR experimental vacuum by a pneumatically driven (7) full-metal gate valve (CF63, VAT).

4.3 The merging and interaction sections

In this section the cryogenic region of the CSR electron cooler is discussed. It can be split into three functional regions, of which two are mirror images of each other and are performing the merging and demerging of the electron and ion beams. And the third is the interaction region, where both beams are collinear. These tasks are accomplished by the magnetic guiding field, which is schematically depicted in figure 4.6 and is discussed in its caption.

The magnetic guiding field is an important but not the only aspect, which needs to be considered for a functioning electron cooler. Just as necessary is the vacuum system and especially for the CSR electron cooler the cryogenic layout. In the final development and the mechanical realization all these aspects were incorporated, which are discussed in detail in the subsequent sections.

First the advanced field simulations (section 4.3.1) are presented, followed by the discussion of the mechanical design (section 4.3.2), magnetic system (section 4.3.3), vacuum system (section 4.3.4), and the cryogenic layout (section 4.3.5). At the end the cryogenic cooling powers and expected thermal loads for the entire CSR electron cooler are estimated (section 4.3.6).

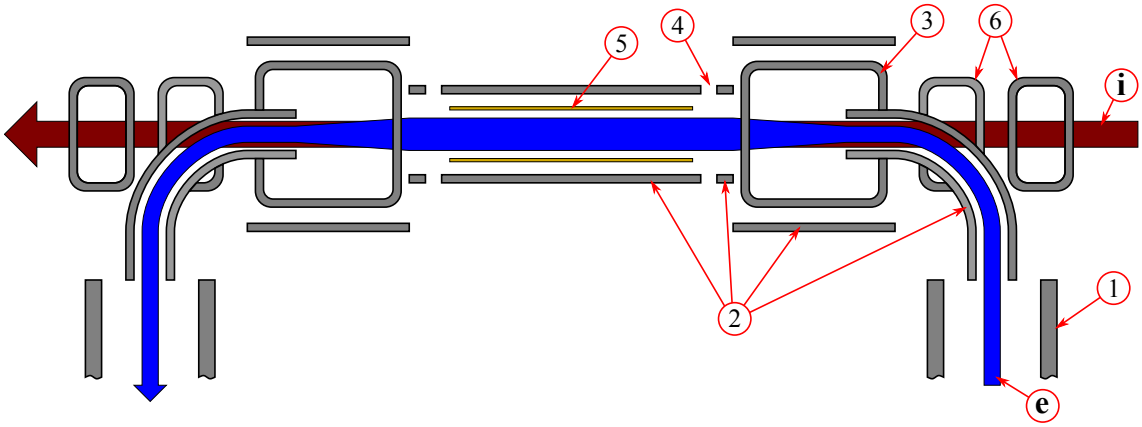

Figure 4.6: Schematically drawing of the merging and interaction regions viewed from the top. For a three dimensional view see also figure 4.1. The (e) electron beam enters the merging region guided by the last room temperature (1) low-field solenoid, which reaches into the CSR cryostat. In the cryogenic region the magnetic guiding field is provided by (2) longitudinal oriented solenoid-like HTS coils. The electrons are bend horizontally by a toroid and then vertically merged with the (i) ion beam by a combination of longitudinal solenoids and vertically oriented (3) dipole racetrack coils. During the merging the nominal longitudinal guiding field strength is reduced from initially 250 G (in the toroid) to 125 G (in the interaction solenoid). The magnetic structure has (4) small gaps giving access to the homogenous solenoid region, where both beams are collinear. Wire scanners installed at these locations will allow the measurements of the transverse positions of both beams. The interaction region features a (5) drift tube defining the kinetic energy of the electrons. The distortions of the ion beam trajectory, caused by the merging fields, can be corrected by two pairs of (6) compensation dipole coils in front of and after the merging regions.

4.3.1 Field simulations

The magnetic design conceived in previous work (see section 4.1) was further developed regarding small adaptations and changes due to space constraints encountered during the mechanical design. Moreover, the existing magnetic guiding field models were corrected with respect to the conductor geometry, which was initially designed for resistive coils with higher conductor cross sections, but lower current densities. These were changed to the actual HTS geometries with smaller cross sections but higher current densities. The initial model simulated only one half of the cryogenic region of the electron cooler, which is reasonable since the cooler is mirror symmetric. This was achieved by introducing a symmetry plane with corresponding boundary conditions. However, the new model was created without any symmetry plane avoiding possible artifacts especially in the center of the interaction section.

Less severe introduced changes were the shortening of the interaction solenoid of 944 mm (former value was 1060 mm), including gaps in iron screens and adapting the iron screens of the interaction solenoid. Also additional transverse steering coils in the merging and interaction region were implemented together with a drift tube in the latter.

The shortening of the interaction solenoid has been necessary in order to achieve a coaxial centering of the electrons in the insulation vacuum with respect to the existing side flange of the cryostat vacuum chamber. Therefore the 'good field' region A. SHORNIKOV defined in his work [43, sec. 3.4.5] was recalculated using the new model.

The total effective cooling length (corresponding to the length of the 'good field') is defined by the following criterion: The ratio of transverse and longitudinal magnetic induction $B_\perp/B_\parallel$ must be locally smaller than the divergence of the electron beam caused by its temperature

$$\frac{B_\perp}{B_\parallel} \leq \sqrt{\frac{k_\mathrm{B} T_{\mathrm{e},\perp}}{E_{\mathrm{e,\,kin}}}} \approx 1.8\,\mathrm{mrad} \tag{4.4}$$

assuming a transverse energy spread of the electrons of 0.5 meV (including the magnetic expansion of 20) and an electron energy of 163 eV (for high cooling energies), compare section 4.1.

The second criterion defines the average field quality, for which the magnetic field angle averaged over the effective cooling length

$$\gamma = \frac{1}{L}\int_0^L \frac{B_\perp}{B_\parallel}\mathrm{d}l, \tag{4.5}$$

must be smaller than 1 mrad within the electron beam cross section, where $B_\perp = \sqrt{B_x^2 + B_y^2}$.

In figure 4.7a the calculated averaged field angle is shown together with the expected electron beam cross section with a radius of 6.7 mm (assuming a magnetic expansion of 20, black dashed circle). The first criterion, stated by equation (4.4), defines the effective cooling length of $L = 700\,\mathrm{mm}$. Surprisingly this is the same length calculated in the previous work by A. SHORNIKOV [43, sec. 3.4.5], even though the interaction solenoid has been shortened by 116 mm. Furthermore, the simulated averaged divergence within the electron beam cross section is lower than 0.35 mrad (compared to 1 mrad). This is most likely a consequence of the improved field model, which does not has a symmetry plane in the middle of the interaction solenoid anymore and therefore no artificial boundary conditions in the investigated region.

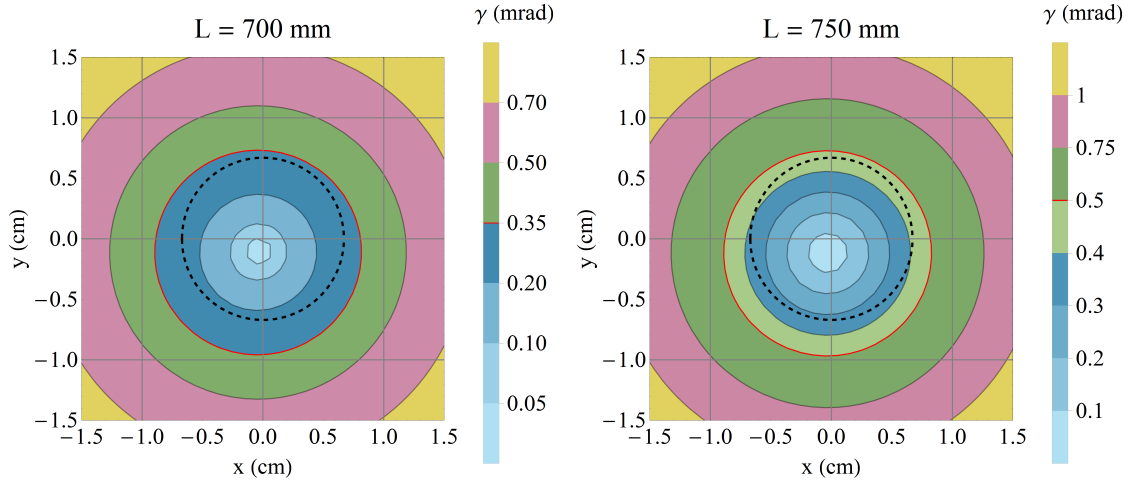

(a) Good field region for high cooling energy. (b) Good field region for low cooling energy.

Figure 4.7: The averaged magnetic field angle γ, given by equation 4.5, in the plane perpendicular to the ion beam. The black dashed circle corresponds to an electron beam radius of 6.7 mm in the interaction region (for a magnetic expansion of 20).

Nevertheless, for lower cooling energies (see figure 4.7b), where a local divergence of 3 mrad could be acceptable [43, sec. 3.4.5], the effective cooling length is only $L = 750\,\text{mm}$ (compared to 800 mm). But also here the average field angle in the cross section of the electron beam is less than 0.5 mrad.

Finally the ratio of the cooling length and the storage ring circumference is still ~ 50, which in [43, sec. 3.4.2] has been used for estimating the expected cooling lifetime of the CSR electron cooler. Thus, they are assumed to be still valid.

4.3.2 Mechanical design

Merging region

The final mechanical design[1] of the merging region is shown in figure 4.8. The electron beam (e) enters the CSR cryostat guided by the last room temperature solenoid (1). It is then guided by a 110 mm long solenoidal extension of the toroid (2a), then bend by a 90° toroid in the horizontal plane (2b) and finally bend downwards by an 30° extension of same toroid (2c), which has a lower winding density. The ac-

[1]The mechanical design work of the cryogenic region of the electron cooler has been done by the MPIK design office and especially by T. Weber.

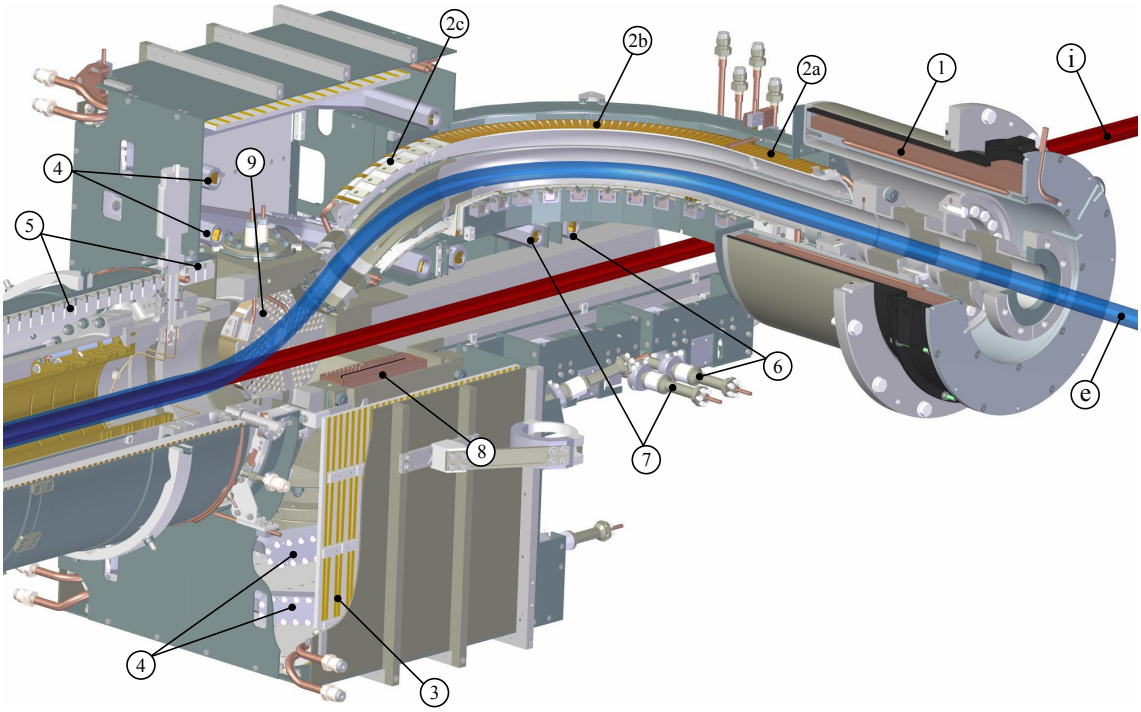

Figure 4.8: Mechanical design of the electron and ion beam merging section with the (e) electron and (i) ion beam, (1) the last low-field guiding magnet, the toroid, consisting of (2a) a solenoidal extension, (2b) the horizontal 90° bend, and (2c) a vertical 30° bending, (3) the longitudinal merging solenoid, (4) four vertical merging coils, (5) the interaction solenoid, (6-7) two pairs of ion beam compensation coils, (8) a charcoal cryopump, and (9) a NEG-pump.

tual merging with the ion beam (i) is performed by a combination of a rectangular shaped longitudinal solenoid (3) and in total four racetrack coils (4), which create a vertical dipole field. The guiding field strength is simultaneously decreased by a factor of 2 during the merging. After the merging both beams enter the interaction region, where the electrons are guided by the interaction solenoid (5).

The distortion of the ion beam trajectory caused by the merging fields can be compensated by two pairs of dipole correction coils (6-7) in front of and following the electron cooler section. The outer coils (6, Comp1) create a field in the same direction and field integral as the vertical merging coils (4, MV). The field of the inner correction coils (7, Comp2) goes in the opposite direction but has twice the field integral.

Both in the 90° part of the toroid and in the merging region (not shown in the figure) for both transverse directions steering coils will be installed. These are necessary for small adjustments of the electron trajectory, but also for the correction of the

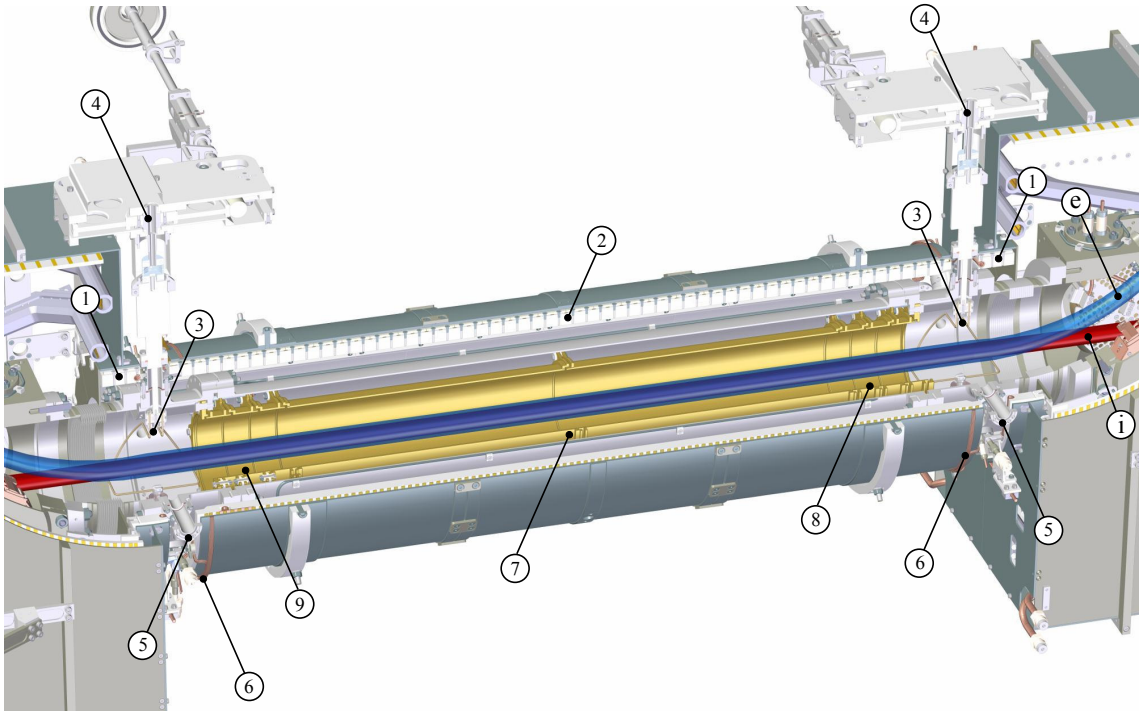

Figure 4.9: Mechanical design of the electron and ion beam interaction section with the (e) electron and (i) ion beam, the interaction solenoid, which is split in (1) two 47 mm and (2) one 944 mm long parts, providing two 34 mm wide gaps for electrical feedthroughs, (3) two wire scanners with (4) their rotational stages, and (5) two crossed laser beam viewports, (6) the transverse steering coils, and (7-9) drift tube consisting of different electrodes.

electron energy dependent toroidal drift caused by the field gradient in the toroidal section [43, 52]. The steering coils will be discussed in the subsequent section.

Interaction region

Figure 4.9 shows the mechanical design of the interaction region. It is the common beamline for the electron (e) and ion (i) beams. The interaction solenoid is split in a 944 mm long (2) and two 47 mm long (1) parts in order to create 34 mm wide gaps at the outer ends of the interaction section. The gaps give access to the homogeneous solenoid region by various vacuum feedthroughs.

Most importantly, measurement of the transverse positions and current distributions of both beams is foreseen by rotating wire scanners (3). Also shown are the rotational stages (4) of the wire scanners, which consists mainly of a cryogenic worm gear with

a transmission of 1 : 360 (inner axis : outer axis). The special shape of the wire scanners allows the determination of both transverse coordinates. For more details especially on the readout and signal processing see [107].

In the horizontal direction of the magnet gap, two optical-grade sapphire viewports (5) will be installed in order to allow also crossed laser beam experiments on the cooled ion beam.

Over the length of the interaction solenoid (2) for both transverse coordinates steering coils (6) are integrated, which will be discussed in the subsequent section.

The interaction region is equipped with a 870 mm long drift tube in order to define the kinetic energy of the electrons. It consists of gold-plated copper tubes with an aperture of 100 mm and is split in two 333 mm long (7) and six 30 mm long electrodes (8-9) and has 3 mm long grounded end caps. The gaps between the electrodes are 2 mm ensuring break down strength for voltages up to several kV. The electrical feedthroughs are placed in the 34 mm wide gaps in the interaction solenoid. The last three electrodes (9) are also vertically cut into two pieces each in order to serve as clearing electrodes for possibly trapped ions in the space charge potential of the electron beam. The total length of the drift tube is designed as long as technically possible (achieving the longest possible effective cooling length) and a smooth potential transition can be formed with the different electrodes.

4.3.3 Magnetic system

The realized total number of turns of the HTS coils and their expected electrical currents for a guiding field of 250 G (in the toroid and 125 G in the interaction solenoid) are listed in table 4.1. This design allows to use only 4 power supplies for all HTS magnets, i.e. all longitudinal guiding magnets (solenoids and toroids) are in series, as well as the vertical merging coils (MV), the outer (Comp1), and the inner compensator coils (Comp2), respectively. This lowers the heat input through the necessary copper leads, but also financial costs. However, hereby the possibility to adjust the magnetic guiding field is restricted, for what reason in various regions smaller, resistive copper coils (steering coils) are installed. The fractional parts of the last three coils in the table are accounting for the non-perfect winding of these coils, which has been technically impossible to realize as integer values.

The steering coils create a transverse magnetic field which is much smaller than the longitudinal guiding field. The superposition of both fields, however, shifts the electron beam trajectory and the beam can be steered. In table 4.2 all cryogenic steering coils are listed with their number, maximal ampere-turns, and offset, as

Table 4.1: Number of turns n and nominal current I of the cryogenic coils for a magnetic induction of 250 G in the toroid (and 125 G in the interaction solenoid). The labels are according to figure 4.8. The coils (4,6,7) have fractional number of windings since it has been technically impossible to realize integer values, i.e. some fraction of the winding circumference is missing.

Coil	**Label**	**Type**	n	I/A
Toroid	(2a)+(2b)+(2c)	HTS	$30 + 84 + 14 = 128$	76
Merging Solenoid	(3)	HTS	32	76
Interaction Solenoid	(5)	HTS	$112 + 2 \times 6 = 124$	76
Merging Vertical (MV)	(4)	HTS	12.7	60
Compensator 1 (Comp1)	(6)	HTS	20.2	68
Compensator 2 (Comp2)	(7)	HTS	32.2	69

Table 4.2: The steering coils of the cryogenic region for a magnetic guiding field of 250 G (in the toroid) with their number (#), ampere-turns (AT) per coil, the maximal displacement of the electron beam, number of windings n, length per turn l_{turn}, and electrical current I. All steering coils are manufactured of enamelled copper wire of 0.8 mm thickness.

Steerer	#	**AT per coil**	**Displacement**	n	l_{turn}/m	I/A
Toroid-X + Y	8	30	drift comp.	9	0.5	3.4
Merging-X	4	150	±10 mm	20	0.3	7.5
Merging-Y	4	100	±10 mm	20	1.2	5.0
Interaction-X + Y	4	20	±15 mm	9	3.0	2.2

well as the number of windings, the length per turn, and electrical current. The steering coils installed in the cryogenic region of the electron cooler are inside of the toroids (90° parts only), in the merging region and in the interaction solenoid for both transverse directions. In the toroid as well as in the interaction solenoid their cross sections are HELMHOLTZ-like with a 'radius' of ~ 50 mm and ~ 100 mm, respectively. Their average lengths are ~ 320 mm and 950 mm, respectively. They are imbedded in the aluminum supports of the HTS coils and are thermally coupled to the neon cooling system.

In the merging region there are horizontal steering coils (Merging-X) consisting of two loops of 240 mm diameter and 240 mm distance of each other. They create a horizontal dipole field and are positioned with respect to the center of the longitudinal merging solenoid. The vertical steering coils (Merging-Y) are following the inner profile of the two tilted vertical merging coils (4, in figure 4.8). Both merging steering coils are also coupled to the neon cooling system.

All steering coils will be manufactured of enamelled copper wire of 0.8 mm thickness. The denoted ampere-turns and respective maximal beam displacements listed in table 4.2 have been simulated with the field model of the electron cooler for a magnetic guiding field of 250 G (in the toroid and 125 G in the interaction solenoid). The data of the toroid steerers are taken from [43, tab. 4.1] and are scaled to the mentioned guiding field.

4.3.4 Vacuum system

The experimental vacuum system of the cryogenic region is shown in figure 4.10 schematically. For the sake of clarity only one half of the cooler is shown, because the setup is mirror-symmetric.

Since the transitions from room temperature to the cryogenic region are cause of the most gas load in the cryogenic cooler section, all necessary vacuum pumps are directly attached to the merging vacuum chambers. The pumps are two cryocondensation pumps (1), which consist of enlarged copper surfaces cooled by the 2 K-He cooling circuit of CSR (2). In the cryogenic operation mode of CSR these pumps and the vacuum chambers itself, which are also coupled to the same cooling circuit and reach hereby temperatures of ~ 10 K, are sufficient for the pumping of the whole system.

However, for the room temperature operation mode of CSR there are additional pumps installed. These are two NEG modules (3) consisting of 1.5 m long and 30 mm wide getter strips (St707, SAES) each resulting in an estimated pumping speed of $\sim$ 1200 l/s in total [108]. For the activation of the NEG material the strips are heated to temperatures up to 450 °C (locally) by applying high electrical currents. For additional pumping there are two bakeable charcoal cryopumps[2] (4) with an active area of $2 \times 70\,\mathrm{cm}^2 = 140\,\mathrm{cm}^2$ resulting in an estimated pumping speed of $\sim$ 1200 l/s in total [108]. The inner stage (active area) of the cryopump is coupled to the first 5 K-He (5) and the outer stage (thermal radiation shield) to the second 5 K-He (6) cooling circuit of CSR, respectively.

All vacuum chambers are equipped with resistive heating elements (7) for a bake-out of the experimental vacuum chambers up to 250 °C. In order to protect the superconducting coils all vacuum chambers are wrapped in bakeable multilayer insulation (Coolcat 2 NF, RUAG Space GmbH and special Alu/glass MLI, DeMaCo). In the region of the NEG modules even higher temperatures are expected for what reason special multilayer insulation withstanding temperatures up to 350 °C is in-

[2]The coating is done by the group of C. Day at the ITEP-department of the Karlsruher Institut für Technologie (KIT).

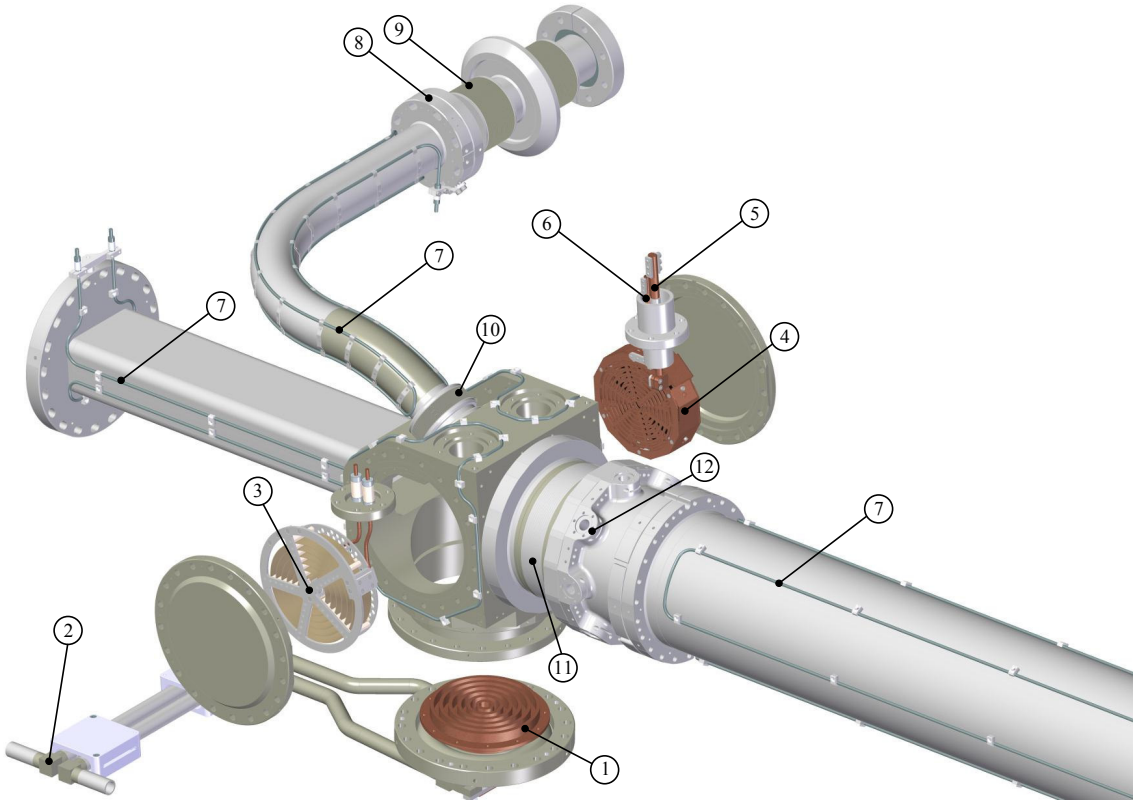

Figure 4.10: Mechanical design of the cryogenic vacuum system with (1) the cryocondensation pumping unit, which is connected to the 2 K-He cooling circuit of CSR, (3) the NEG-pump, (4) the charcoal cryopump, which thermal stages are connected to the (5) first and (6) second 5 K-He cooling circuit, (7) resistive heating elements for the vacuum chambers, (8) the thermal anchoring point of the toroidal vacuum chamber, which is decoupled with bellows from the (9) room temperature and (10) cryogenic vacuum parts, (11) a bellow decoupling the merging from the interaction region, and (12) the vacuum chamber with eight ports for electrical feedthroughs, wire scanners and laser viewports.

stalled (Coolcat 2 LOX, RUAG Space GmbH). The toroidal chamber serves as the temperature transition region being thermally coupled (8) to the shield temperature stage of the electron cooler and which, hence, absorbs the main thermal radiation load from room temperature. Edge-welded bellows to room temperature (9) and to the cryogenic 10 K region (10) act as a thermal and mechanical decoupling. Since the thermal shrinkage of the whole cooler section of 2.6 m length is ~ 7.8 mm both merging regions are decoupled from the interaction region by two additional edge-welded bellows (11). In the interaction region the electrical feedthroughs for the drift tube, the wire scanners, and laser viewports are installed (12), which coincide with the 34 mm wide gaps in the magnetic structure discussed above.

4.3.5 Cryogenic layout

The cryogenic concept of the CSR electron cooler is visualized in figure 4.11 at the schematic cross section of the cooler. Since the superconducting magnets need to be cooled to cryogenic temperatures for both operation modes of CSR the scheme deviates significantly from the cryogenic concept of CSR (compare section 2.4 and figure 2.7).

Both merging section and the interaction section are supported independently. A main base plate (1), which is based on thermal insulating titanium posts (2) with as small as mechanically possible cross sections, forms the support for all other structures. It holds the experimental vacuum chambers via additional titanium posts (3), the iron screens of the magnets (13) as well as the thermal radiation shield of the cooler section (6). The experimental vacuum chambers are coupled to the 2 K-He cooling circuit of CSR (4) and both are wrapped in bakeable multilayer insulation (5) for the protection of the enclosing superconductors (16). The thermal radiation shield (6) creates a ~ 80 K environment in order to reduce the heat input on the superconductors (16) and the experimental vacuum chambers. It encloses the whole cryogenic part of the cooler section and also in the transition to the corners of CSR. It only has openings for the electron and ion beam vacuum chambers.

In order to lower the thermal radiation contribution on the shield itself it is additionally wrapped in 30-40 layers of non-bakeable multilayer insulation (7) Coolcat 2 NW (RUAG Space GmbH). Depending on the operation mode of CSR the shield and the base plate are connected via a thermal bridge (8) to different cooling circuits of CSR. In the case of cryogenic operation of CSR it is coupled to the 80 K-He cooling circuit (9) whereas for the room temperature CSR operation to the second 5 K-He cooling circuit (10).

The first turn of the 5 K-He cooling circuit (11) is only connected to the inner stages of the cryopumps. The 40 K-He cooling circuit of CSR (12) is not used at all. The iron screens (13) are thermally decoupled via insulating stainless steel posts (14) and mounted to the base plate. The screens itself support the superconductors (16) via also thermally insulating stainless steel or PTFE pieces (15). The superconductors are wound onto aluminum support bodies (17), which are either filled with neon and the superconductors are immersed in the cooling medium (in the case of MV, Comp1 and Comp2) or the neon cooling circuit is embedded in the aluminum bodies (in the case of the toroids and the longitudinal solenoids).

All superconducting magnets are connected in series by stainless steel tubes (18) with VCR couplings (Swagelok) and forming one closed circuit with the neon cooling

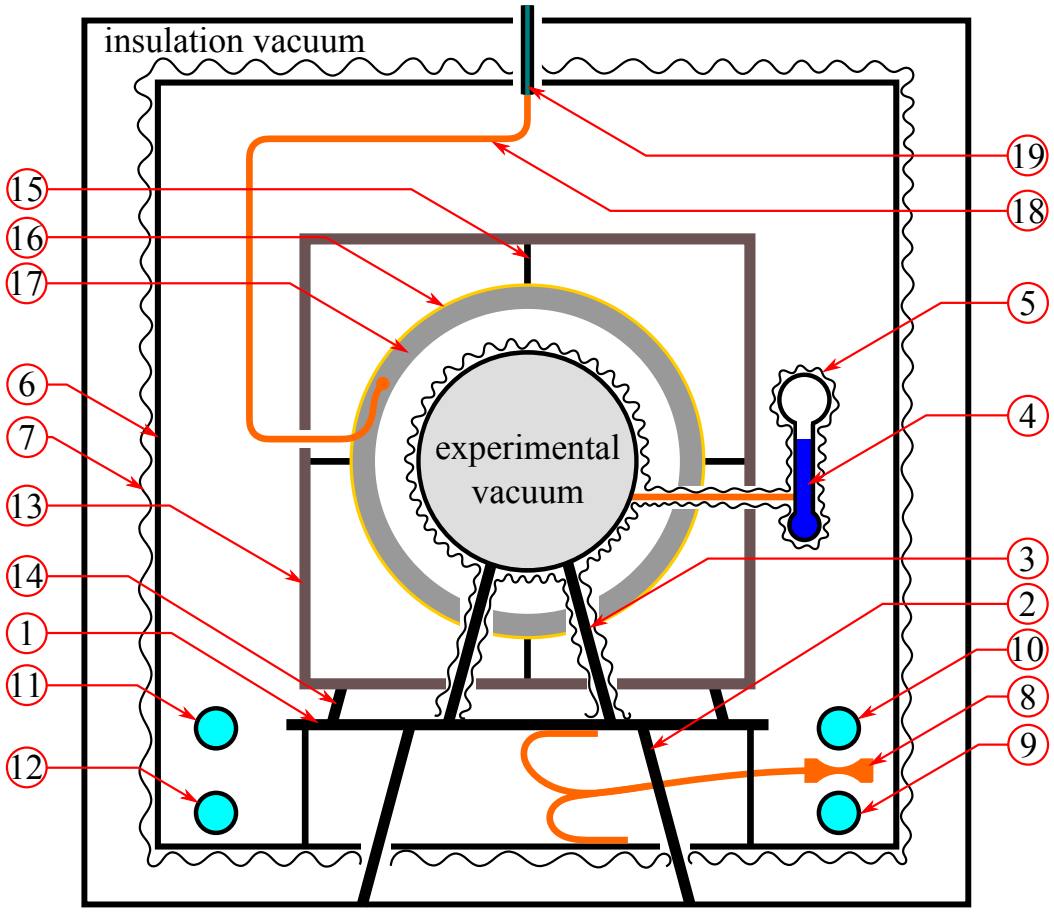

Figure 4.11: Cryogenic concept of the CSR electron cooler. The mechanical main structure forms a (1) base plate, which is supported by thermally insulating (2) titanium posts. Via (3) additional titanium posts it supports the beam guiding vacuum chambers, which are connected to the (4) 2 K-He cooling circuit of CSR. All these parts are wrapped in (5) bakeable multilayer insulation. The base plate also holds the thermal (6) radiation shield, which is additionally wrapped in (7) non-bakeable multilayer insulation. Both the base plate and the thermal radiation shield are connected via a (8) thermal bridge to either the (9) 80 K-He (for the cryogenic CSR operation) or the (10) second 5 K-He (for the room temperature CSR operation) cooling circuit. The (11) first 5 K-He turn is only connected to the inner stage of the cryopump and the (12) 40 K-He turn is not used at all. In addition, the base plate supports the (13) iron screens via thermally insulating (14) stainless steel parts. The iron screens itself hold via (15) thermally insulating posts (stainless steel or PTFE) the (16) superconducting coils, which are wound onto (17) aluminum bodies. The aluminum support bodies are either filled with neon (MV, Comp1+2) or the neon cooling circuit is embedded (toroids and solenoids). These structures are altogether connected via (18) tubes and are part of the (19) neon cooling system, which is mounted on top of the electron cooler cryostat.

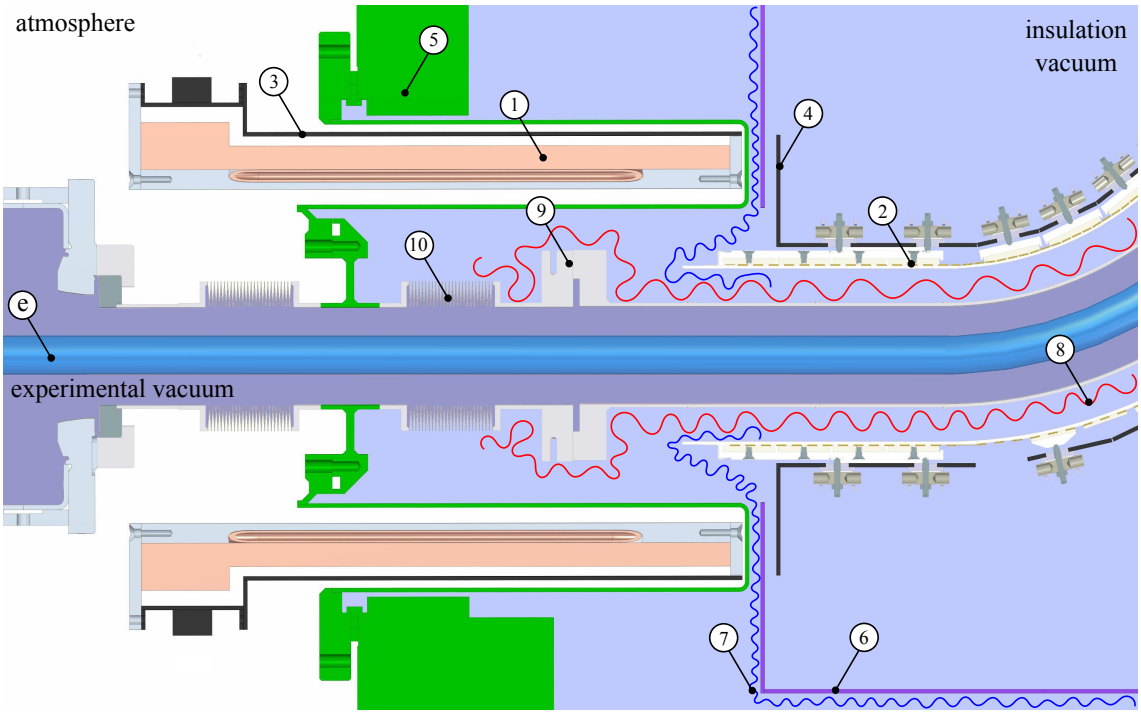

Figure 4.12: Schematic drawing of the transition from the room temperature to the cryogenic region with (e) the electron beam, (1) the room temperature guiding solenoid and (2) the cryogenic toroid, with (3 – 4) their respective iron screens, (5) the insulation vacuum chamber, (6) the thermal radiation shield, (7) the non-bakeable and (8) bakeable multilayer insulation, (9) the thermal anchoring point of the toroidal vacuum chamber, and (10) the decoupling bellow between the room temperature and cryogenic region.

system (19), which is installed on top of the electron cooler cryostat. The latter consists mainly of a commercial closed-cycle pressurized helium cold head, a heat exchanger and circulating pumps at the room temperature side of the system. The cooling system has been developed, constructed, commissioned, and described in [43, 109] and an additional automatic controlling and stabilizing system has been developed and realized as reported in [110].

The transition from room temperature to the cryogenic region

One of the most crucial regions with respect to the cryogenic concept is the transition from the room temperature section to the cryogenic region, which is shown in figure 4.12 schematically.

Since the magnetic guiding field for the electron beam (e) changes from the room temperature solenoid (1) to the cryogenic operating HTS toroid (2), the latter is almost directly exposed to the room temperature thermal radiation without the protecting thermal radiation shield (6). Also the iron screens of both (3+4) need to have a gap of 14 mm to give space for the thermal shield, support structures of the vacuum chambers and electrical connections. At the same time the insulation vacuum chamber (5) must be closed and therefore enfolds the room temperature solenoid. In order to reduce the thermal radiation contribution onto the neon cooling system and especially the HTS toroid the outer non-bakeable multilayer insulation (7), which covers the radiation shield, also enfolds the toroid.

Furthermore, the toroid must be protected against too high temperatures during the bakeout of the experimental vacuum chambers by bakeable multilayer insulation (8), which covers the toroidal vacuum chambers and is extended up to the edge-welded bellow (10). The bellow also thermally decouples the room temperature part from the cryogenic part in normal operation. In order to form a heat sink and to have an additional temperature transition to the cryogenic 10 K region the front part of the toroidal vacuum chamber (9) is thermally anchored to the 80 K temperature stage of the electron cooler.

4.3.6 Cryogenic cooling powers and thermal load

During the design of the cryogenic region (merging and interaction region) of the CSR electron cooler one important aspect is the cryostat compatible design. As discussed in the previous section the cooler consists of several different temperature stages, which has to be cooled separately. Since the available cooling power is limited, thermal power calculations had to be performed in order to estimate the actual thermal load and to optimize the different structures, which are necessary to mechanically design the electron cooler.

The superconducting coils are cooled by the neon cooling system, which has been designed, developed, and commissioned by A. Shornikov. In [43] it has been shown, that the neon cooling system can deliver $25 - 30$ W of cooling power (at approximately the condensation point of neon, which is ~ 30 K).

For reducing the thermal load onto the HTS coils the shield of the electron cooler must be held at roughly 80 K. Additionally this temperature stage is needed for thermal anchoring of the electrical connections, which carry partly high electrical currents and are therefore relatively thick. The cooling power of the 80 K temperature stage of the electron cooler is provided by the CSR helium refrigerator system (compare section 2.4). In former thermal power calculations of the entire CSR for

the electron cooler cooling powers of 100 W and 250 W for the cryogenic and room temperature CSR operation, respectively, were reserved.

The thermal power calculations of the electron cooler are listed in table 4.3 for the neon cooling system and in table 4.4 for the 80 K temperature stage of the electron cooler, respectively. There are three main contributions, which are electrical power, thermal conduction and thermal radiation, which are discussed in the following.

Electrical power

The electrical contribution is caused by the dissipated electrical power:

$$\dot{Q}_{\mathrm{elec}} = \frac{l}{A}\rho(T)\, I^2, \tag{4.6}$$

with the length l and cross section A of the respective conductor, the temperature dependent specific electrical resistance $\rho(T)$, and the applied electrical current I.

For the calculation of the electrical power contributions the electrical resistance of the used materials has to be known. Mattiessen's rule describes the temperature dependence of the electrical resistivity [81, eq. 6.9]:

$$\rho(T) \cong \rho_{\mathrm{res}} + \rho_{\mathrm{i}}(T) \tag{4.7}$$

The first term accounts for the residual resistance ρ_{res} caused by impurities in the conducting material and the second term accounts for the temperature dependent phonon contributions, which is called the intrinsic resistance ρ_{i}.

If the residual resistance of the material is unknown, it can be approximated by $\rho_{\mathrm{res}} = \rho_{\mathrm{i}}(T = 293\,\mathrm{K})/(\mathrm{RRR} - 1)$ [81, eq. 6.11]. The residual resistance ratio (RRR) is a quality factor of the material and is defined as the ratio $\rho_{\mathrm{RT}}/\rho_{4\,\mathrm{K}}$.

All electrical consumers of the electron cooler (excluding HTS) consist of copper wire but with different length, cross section and current. The intrinsic electrical resistances $\rho_{\mathrm{i}}(T)$ of copper are taken from [111, tab. 2] and a copper with RRR = 50 is assumed, which is a good approximation for standardly used copper wires.

For the 'steerer coils' and the 'HTS to HTS connections' a temperature of 40 K has been assumed. For the latter also the power contributions for 80 K are given, denoted with b, since the thermal coupling of these connections to the neon system is not assumed to be well. In case for of the superconducting magnets special care has to be taken in the dimensioning of the connections going to the room temperature feedthroughs.

Table 4.3: Thermal power estimations for the neon cooling system of the CSR electron cooler. For the parameter definitions see the corresponding equations (4.6), (3.55), and (3.56).

Electrical power	**Type**	#	I/A	l/m	A/mm^2	P/W
HTS connections to terminals 80 to 40 K	Solenoids	2	76	2.24	25	1.45
	Comp1	2	68	2.50	25	1.30
	Comp2	2	69	2.46	25	1.32
	MV	2	60	2.83	25	1.15
HTS to HTS connections	Solenoids	1	76	4.0	25	0.52[a] - 2.28[b]
	Comp1	1	68	4.0	25	0.42[a] - 1.83[b]
	Comp2	1	69	4.0	25	0.43[a] - 1.88[b]
	MV	1	60	6.0	25	0.48[a] - 2.14[b]
Steerer coils	Toroids	8	3.4	9×0.5	0.5	0.46
	Merging-X	4	7.5	20×0.3	0.5	1.58
	Merging-Y	4	5.0	20×1.2	0.5	2.68
	Interaction	4	2.2	9×3.0	0.5	0.58
Steerer leads 80 to 40 K	Toroids	8	3.4	1.0	0.5	0.26
	Merging-X	4	7.5	1.0	0.5	0.63
	Merging-Y	4	5.0	1.0	0.5	0.28
	Interaction	4	2.2	1.0	0.5	0.05

Heat conduction	**Type**	#	$\lambda(T)$	L/m	A/mm^2	P/W
HTS connections to terminals 80 to 30 K	Solenoids	2	Cu	2.24	25	0.95
	Comp1	2	Cu	2.50	25	0.85
	Comp2	2	Cu	2.46	25	0.86
	MV	2	Cu	2.83	25	0.75
HTS supports	Toroids	54	SS	0.008	7.1	0.10
	Merging	32	PTFE	0.015	24.0	0.55
	Interaction	8	SS	0.014	12.6	0.07
	Rest	8	SS	0.025	156	0.45
Steerer leads	All	20	Cu	1.0	0.5	0.43
T. Sensors	All	100	Ag	3.5	0.1	0.10

Thermal radiation	**Comments**	A/m^2	P/W
from 80K	environment	2.0	4.66
from 300K	through MLI of the XHV chambers	2.0	5.00[c]

Total Power		
	Cryogenic CSR operation	**23.4 - 29.7**
	Room temperature CSR operation	**28.4[d] - 34.7[d]**

[a] 40 K for the HTS-HTS connections

[b] 80 K for the HTS-HTS connections

[c] Occurs in the case of room temperature operation.

[d] This includes the contributions marked with c.

Table 4.4: Thermal power estimations for the 80 K temperature stage of the CSR electron cooler. For the parameter definitions see the corresponding equations (4.6), (3.55), and (3.56).

Electrical power	**Type**	#	I/A	l/m	A/mm^2	P/W
HTS connections to terminals 300 to 80 K	Solenoids	2	76	1.15	25	6.16
	Comp1	2	68	1.29	25	5.53
	Comp2	2	69	1.27	25	5.61
	MV	2	60	1.46	25	4.87
Steerer leads 300 to 80 K	Toroids	8	3.4	0.5	0.5	0.83
	Merging-X	4	7.5	0.5	0.5	2.59
	Merging-Y	4	5.0	0.5	0.5	1.15
	Interaction	4	2.2	0.5	0.5	0.22

Heat conduction	**Type**	#	$\lambda(T)$	L/m	A/mm^2	P/W
HTS connections to terminals 300 to 80 K	Solenoids	2	Cu	1.15	25	3.92
	Comp1	2	Cu	1.29	25	3.51
	Comp2	2	Cu	1.27	25	3.56
	MV	2	Cu	1.46	25	3.10
Steerer leads	All	20	Cu	0.5	0.5	1.19
T. Sensors	All	100	Ag	1.5	0.1	0.50
Shield supports	All	12 - 20	Ti	0.125	36.0	4.20[a] - 7.00[b]
Supports of XHV chambers	Merging	8 - 16	Ti	0.125	36.0	2.80[a,c] - 5.60[b,c]
	Interaction	4	SS	0.067	75.0	3.16[c]

Thermal radiation	**Comments**	A/m^2	P/W
through MLI	of the radiation shield	14.0	14.00
of MLI seams	of 30 m length	–	5.10
of MLI holes	two holes with 75 mm diameter	0.0045	16.22

Total Power	**Cryogenic CSR operation**	**82.3 - 85.1**
	Room temperature CSR operation	**88.2[d] - 93.8[d]**

[a]Single titanium supports

[b]Double titanium supports

[c]Occurs in the case of room temperature operation.

[d]This includes the contributions marked with c.

In order to lower the thermal heat input onto the neon system the connections are thermally anchored in between at a terminal at the 80 K temperature stage.

For high current connections there must be taken a compromise of electrical dissipated power in the cable and the thermal conducting contribution on the cryogenic temperature stage. For a given temperature difference there is an optimum ratio of length l to cross section A for a given electrical current I, which minimizes the total

power consumption [81]. Thus, for a given copper wire cross section of $A = 25\,\mathrm{mm}^2$ the optimal length results in $l_{300\,\mathrm{K}\to80\,\mathrm{K}} = 87.5\,\mathrm{m}/I[\mathrm{A}]$ and $l_{80\,\mathrm{K}\to30\,\mathrm{K}} = 170\,\mathrm{m}/I[\mathrm{A}]$ for the different temperature differences [81, sec. 4.9].

The calculated lengths are also listed in the respective tables. For the power calculation of these connections as well as for the steerer leads a linear temperature gradient over the lead length has been assumed, i.e. going from 300 K to 80 K (see table 4.4) and from 80 K to 40 K (see table 4.3). For a conservative estimation a higher temperature of the neon system has been assumed on purpose (actually it should be around the condensation point of neon $\sim 30\,\mathrm{K}$).

Heat conduction

For the calculation of the thermal conduction contributions, equation (3.55), the material dependent thermal conductivities $\lambda(T)$ are taken into account. These are taken from [100] and are listed in the appendix A.1. The used materials are copper (Cu), stainless steel (SS), titanium (Ti), silver (Ag), and polytetrafluroethylene (PTFE). For these calculations temperatures ranging from 300 K to 80 K (see table 4.4) and from 80 K to 30 K (see table 4.3) are used. In the contribution of the 'shield supports' additional values are given, marked with b, since the actual number of titanium posts is not yet fixed and are depending on the actual mechanical load capacity of the posts. The contributions of the 'supports of the XHV chambers' are only valid for the room temperature CSR operation, when the experimental vacuum chambers are not cooled. These are marked with c.

Thermal radiation

The thermal radiation is calculated using equation (3.56). The contribution for the neon system is originating from the 80 K environment of the shield and with a total surface of $2\,\mathrm{m}^2$ consisting of the HTS coils, steering coils and the neon tubing system. But also here during the room temperature CSR operation the magnets are exposed to the thermal radiation of the experimental vacuum chambers. The multilayer insulation lowers the heat input, but the true contribution is difficult to calculate, since different combinations and thicknesses will be used depending on the respective space limitations.

The manufacturer gives 'recommended' heat fluxes of $4 - 5\,\mathrm{W}/\mathrm{m}^2$ for the Coolcat 2 LOX [112] and $1.9 - 2.5\,\mathrm{W}/\mathrm{m}^2$ for the Coolcat 2 NF [113] (each for 20 layers). The first type is only used for small areas near the NEG-modules and it is planned to additionally use the second type as the outer layers. Thus, for the calculation an

average value of $2.5\,\mathrm{W/m^2}$ has been used. But this also demonstrates the importance of the properly attachment of the multi layer insulation during the construction of the cryogenic setup. The value given in the table (marked with c)) is a conservative estimation with a surface area of $2\,\mathrm{m^2}$ of the experimental vacuum chambers.

In case of the thermal radiation shield the multilayer insulation Coolcat 2 NW is used, which also covers the thermal shields of CSR. The manufacturer gives heat fluxes of $0.79 - 0.65\,\mathrm{W/m^2}$ for 20 or 40 layers, respectively [65]. In the calculation $1\,\mathrm{W/m^2}$ with a total shield surface of $14\,\mathrm{m^2}$ is used. For the seams in the multilayer insulation a value of $0.17\,\mathrm{W/m}$ is given for a similar application in [114] and has also been used for the thermal power estimations of CSR [115]. The necessary holes in the thermal shield structure for the entrance and exit of the electron beam are the major contributions and are calculated as black-bodies, i.e. all thermal radiation is absorbed.

Summary of the thermal power calculations

These calculations have been performed in order to ensure the operation of the CSR electron cooler and to optimize the support structures of the different temperature stages, but also the dimensioning of the various current leads. The total calculated powers of the neon cooling system are expected to be in the worst case 30 W or 35 W (depending on the CSR operation mode). Since in these calculations it has been assumed, that all steering coils are in maximal operation, which will be realistically not the case, the consumed power of the neon system is expected to be up to a value of 6.5 W (total electrical contribution of the steering coils) lower. This is well compatible with the provided cooling power of the neon cooling system of $25 - 30\,\mathrm{W}$ reported in [43].

In case of the 80 K temperature stage of the electron cooler the calculations are below $\lesssim 100\,\mathrm{W}$, which is compatible with the reserved cooling power of 100 W and 250 W for the cryogenic and room temperature CSR operation, respectively. In fact, the latter could actually cause problems with the neon cooling system, since the thermal shield could be cooled below the freezing point of neon around 25 K. For this reason the cooling power during the room temperature operation of CSR must potentially be reduced, when operating the electron cooler.

The largest potential for savings in the thermal load is in the inter HTS connections, which were assumed in this estimation to be manufactured from ordinary copper (RRR = 50). These connections could alternatively be realized with high-purity copper or even with high temperature superconductors. Whatever the case may be, the good thermal coupling of these connections is crucial as demonstrated in the

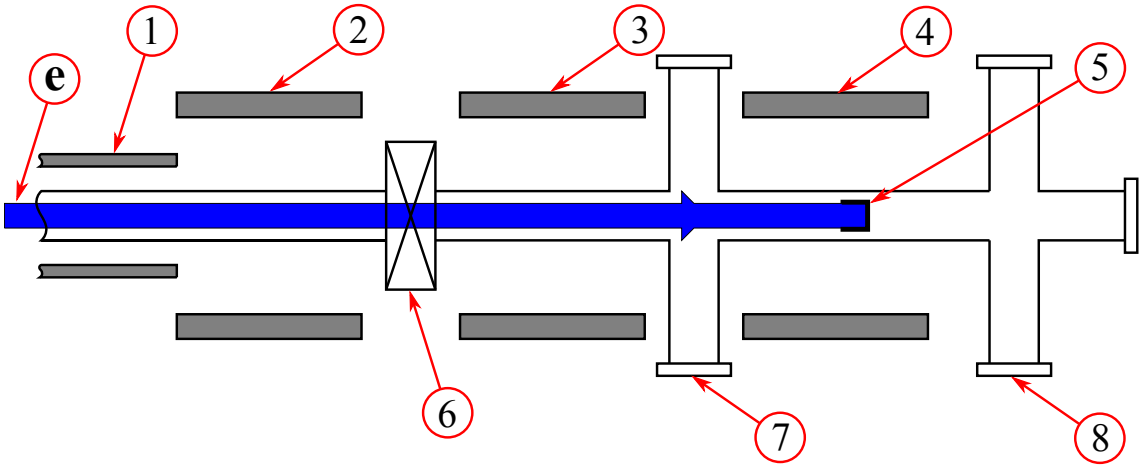

Figure 4.13: Schematically drawing of the electron beam collector section. The (e) electron beam enters the region magnetically guided by the (1) cryogenic toroid. The room temperature guiding field is provided by three individual (2 – 4) solenoids. The electron beam is collected by (5) the electron collector. The interruptions of the room temperature low-field guiding field are necessary for the vacuum system, which requires gaps for a (6) bakeable gate valve and (7+8) pumping units.

worst case scenario.

Based on the here presented work regarding the mechanical design of the magnetic and vacuum system as well as the cryogenic layout and the thermal power calculations, the manufacturing of all parts of the CSR electron cooler in the mechanical workshop of the MPIK has been started. Some of the cryogenic coils as well as the entire room temperature beamline could be already setup during the time frame of this work. The construction of these will be presented in section 4.5, but after the discussion of the electron beam collection region in the subsequent section 4.4.

4.4 The collector section

In the mirror-symmetric part of the merging region, discussed in the previous section 4.3, the electron and ion beam are demerged again and the electron beam enters the collector section. As depicted in figure 4.13 is the beam transport region a copy of the corresponding part of the beam production section, which has been discussed in section 4.2. The high-field electron gun part is, however, replaced by an analyzing cup setup with additional pumping facilities.

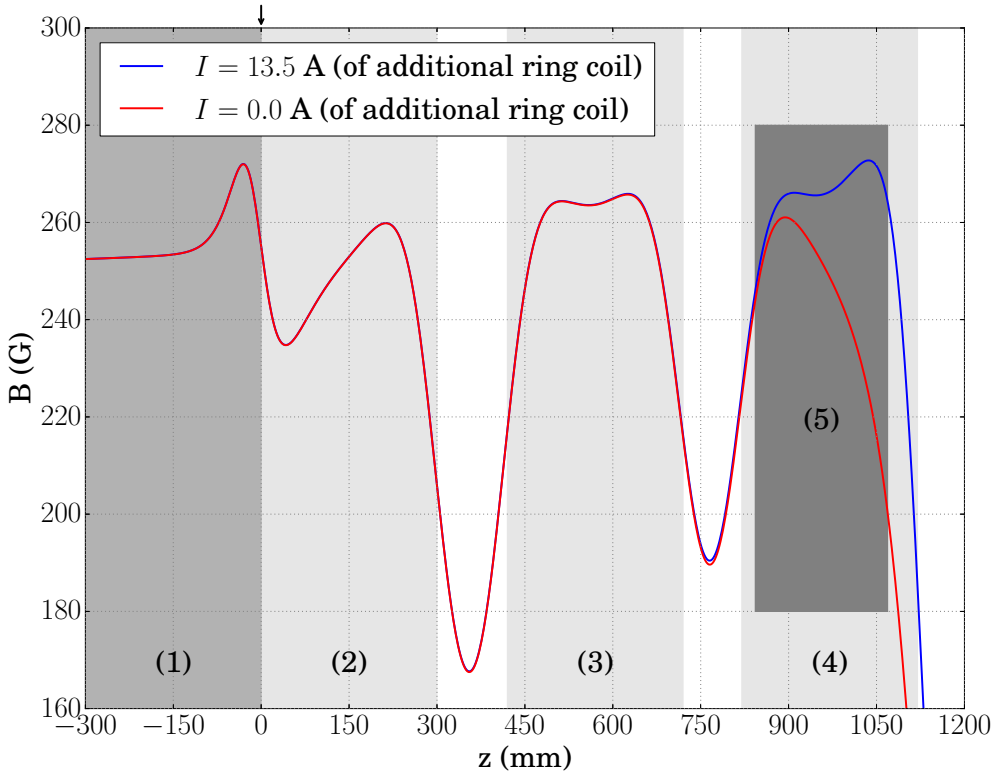

Figure 4.14: The simulated magnetic induction as a function of the longitudinal coordinate z along the axis of the magnetic fields. The gray shaded areas correspond to the different solenoids (1 – 4) and the collector (5). The labeling is according to figure 4.13. The arrow marks the transition from the room temperature to the cryogenic toroid

4.4.1 Field simulation

Even though the magnetic guiding field of the collector beamline design is very similar to the electron beam production region, also for this section a field simulation with the FEA software package Opera-3D [34] has been performed. The respective lengths are the same. The deviation is in the design of the last guiding magnet, which should form a homogeneous magnetic field in order to be able to measure both the electron beam profile for a constant expansion and the electron beam temperature. For these reasons there is an additional ring coil (to the end of this solenoid) introduced and the iron screen closes to the center of the solenoid with only an opening for the vacuum chamber.

Figure 4.14 shows the simulated magnetic induction along the optical axis as a

function of the longitudinal coordinate z for a nominal magnetic induction of 250 G (this corresponds to a current of $\sim$ 13.5 A). The origin corresponds to the transition from the cryogenic to the room temperature region, also marked with an arrow. The guiding magnets as well as the collector are visualized with gray shaded areas and labeled according to figure 4.13, which will be discussed in detail in the subsequent section.

The effect of the additional ring coil is visualized by the two simulations, wherein the coil is either powered with a current of 13.5 A (blue line) or it is not (red line). The first case is realized, if all magnets are powered in series. However, in the electron collector (5) region there should be a homogeneous magnetic field, which can be achieved by independently powering and fine tuning of the additional ring coil.

Since the region, where the electron beam is magnetically guided, corresponds to the electron beam production section, for this section there is no heating of the electron beam expected, see section 4.2.

4.4.2 Mechanical design

Figure 4.15 shows the realized mechanical design of this section schematically. The electron beam (e) is guided by the cryogenic toroid (1) to the outside of the CSR cryostat. The outer guiding field is provided by room temperature water cooled copper solenoids (2 – 4), which again have additional windings (11+12) at their ends in order to compensate the missing solenoidal parts in the gaps. Also here steering coils (13) over the length of two solenoids (3+4) are installed.

The electron beam is analyzed with the collector (5, coloured orange), which consists of a 'main' FARADAY cup for the electron current measurement, a retarding field 'analyzer' cup for the measurement of the electron beam profile and temperature and a WIEN filter for the suppression of back scattered electrons that could otherwise reach and damage the photocathode. The collector has been designed, constructed, and described in detail in [107].

4.4.3 Vacuum system

The vacuum system of the collector section has similar requirements as the electron beam production section (see section 4.2). A pneumatically driven (6) full-metal gate valve (CF63, VAT) separates this section from the experimental vacuum of CSR. The vacuum is established by two commercial actively-heated NEG-pumps

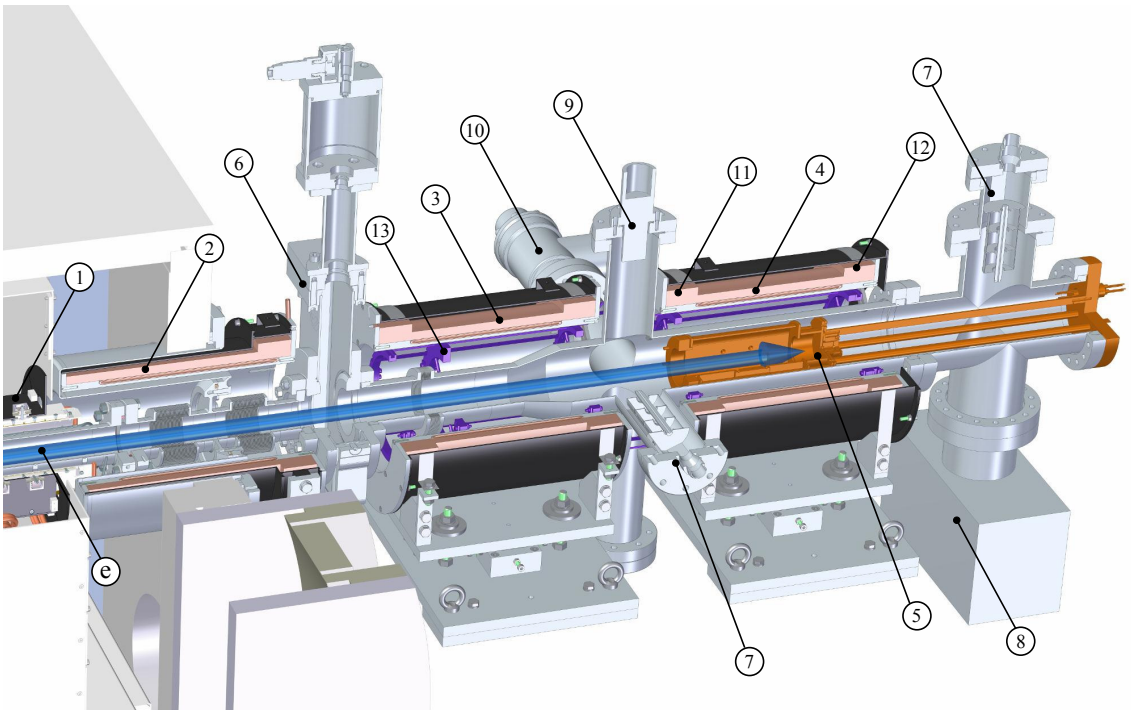

Figure 4.15: Mechanical design of the electron beam collector section with (e) the electron beam, (1) the cryogenic toroid, (2 – 4) the room temperature copper solenoids with (11+12) additional ring coils at their ends, (13) transverse steering coils, (5) the electron collector, (6) a full-metal gate valve, (7) two NEG-pumps, (8) an ion-getter pump, (9) a vacuum gauge, and (10) a full-metal angle valve.

(7) with a $\sim$ 600 l/s pumping speed for H_2 each (GP 100 MK5, SAES) and one ion-getter pump (8) with $\sim$ 60 l/s pumping speed for N_2 and Ar each (VacIon Plus 75 StarCell, Agilent Varian). The vacuum is monitored by a vacuum gauge (9) IONIVAC IE 514 (Oerlikon Leybold) and can be pre-pumped using a full-metal angle valve (10, CF63, VAT) and a turbomolecular pump. All vacuum chambers are equipped with heating elements and are wrapped in thermal insulation for the bakeout at 250 °C. A vacuum of the order of 10^{-11} mbar is envisaged.

4.5 Setup of the CSR electron cooler

Due to the construction of CSR itself and the limited capacity of the MPIK workshop, it has not been possible to construct the CSR and the electron cooler in parallel. But nevertheless, some important parts of the cryogenic region and the entire room temperature electron beamlines could be setup during this work and

will be presented in the following two sections in detail.

4.5.1 The HTS compensation and vertical merging coils

Coil design

The superconducting coils inside of the cryogenic region of the electron cooler are separated into two classes based on their current density and the cooling principle of the HTS wires. The first are relative low current density coils, which are creating the main guiding field and are oriented longitudinal to the electron beam trajectory. For this reason they are wound in two layers onto aluminum support bodies, which are conductively cooled by the imbedded neon cooling system. For good thermal contact the HTS wire is pressed onto these aluminum bodies using PTFE spacers. To this class of coils belong the two toroids, the two longitudinal merging solenoids and the interaction solenoid together with its two short extension solenoids.

The second class are high density coils and are therefore built in such a way, that the HTS wire is immersed in the cooling neon medium. This is achieved by hollow aluminum bodies containing the HTS wire but also the cooling medium. Thus, they are effectively part of the neon cooling system and must be leak tight against the insulation vacuum system of CSR. Their conceptional design is based on the prototype HTS coil, which has been designed, constructed, and successfully tested as reported in [43].

In figure 4.16 two exemplary versions of the ion beam trajectory compensation coils (Comp1+2) and of the vertical merging coils (MV) are shown schematically. PTFE spacers (3), situated in the corners within the aluminum body (2), keep the HTS wire (1) in place. The HTS wire is soldered to electrical copper contacts (4) using indium as solder. The contacts (5) are connected with copper leads of 25 mm^2 cross section with the insulation vacuum feedthroughs. Ceramics (6) serve as electrical insulation from the aluminum bodies and the copper contacts have conical sealing surfaces (7), which are sealed using 0.5 mm thick indium wire. The aluminum corner flanges (8) of the aluminum bodies are sealed with 1.0 mm thick indium wire, whereas the sealings (9) to the stainless steel parts of the electrical feedthroughs have smaller dimensions in order to reduce the effect of the difference in the thermal shrinkage of aluminum and stainless steel. These sealings are also done with 0.5 mm thick indium wire. Ensuring a constant flow of neon in the whole aluminum body a PTFE plug (10) serves as the prevention of a short circuit for the neon. It is placed directly in between the in- and outlet of the cooling circuit (11). All superconducting coils are in series forming one closed cooling circuit. For this system commercial VCR

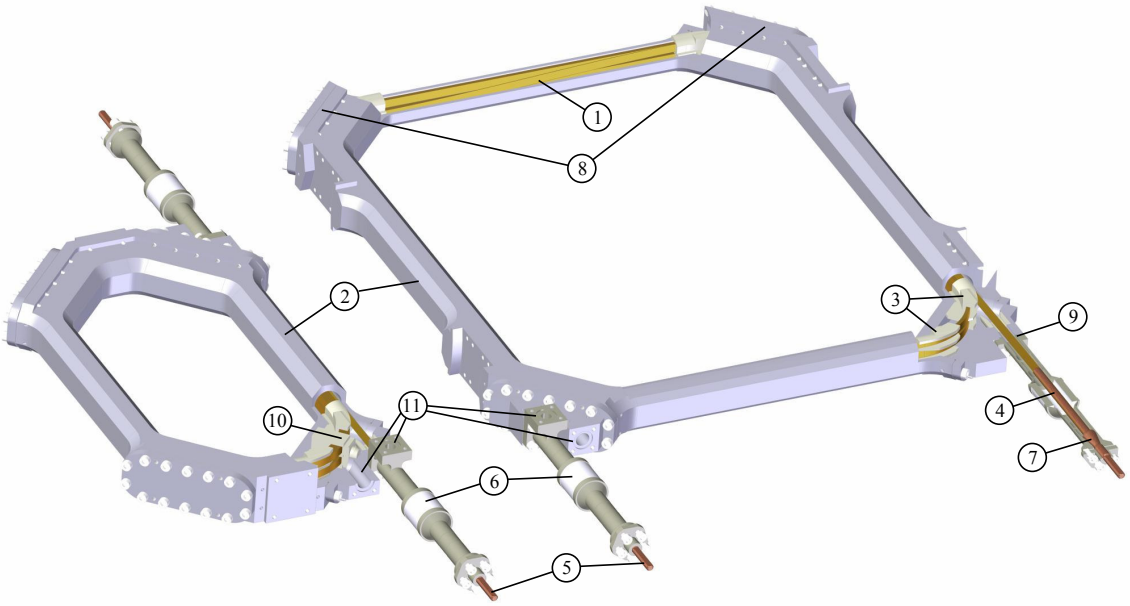

Figure 4.16: Schematic drawing of the high density HTS coils. The left is one of the ion beam compensation coils (Comp1+2) and the right one of the vertical merging coils (MV), respectively. The labels mark the (1) superconducting wire, (2) the aluminum bodies, (3) the PTFE support pieces of the HTS wire, (4-5) the electrical copper contact, (6) the ceramic electrical insulation, (7) the conical sealing, the indium sealings of the (8) corner flanges and (9) the electrical feedthroughs, (10) a PTFE plug preventing the neon short circuit, and (11) the in- and outlets for the neon.

couplings (Swagelog) with stainless steel gaskets are used. The transition to the aluminum bodies are of similar kind as the electrical feedthroughs and are sealed with 0.5 mm thick indium wire.

Setup of the coils

Even though the new design has changed in comparison to the prototype coil regarding the overall smaller dimensions, the HTS wire support and the optimized short circuit prevention of the neon flow, the general soldering and sealing procedure stayed basically the same as discussed in [43, sec 4.1.5]. Nevertheless, one crucial difference is the sealing principle of the conical sealing of the electrical feedthrough. In [43] for this type Apiezon H has been used and leak tightness has been demonstrated

during the operation and testing of the prototype with the neon cooling system. The proof of leak tightness has been the non detection of neon in the insulation vacuum monitored by a mass spectrometer. However, during the manufacturing of the final 16 coils (4 × Comp1, 4 × Comp2 and 8 × MV) a new faster testing procedure for the leak tightness has been developed and applied due to the high number of coils.

Testing

Special importance lies in the leak tightness of the coils during the cryogenic operation. For this purpose a cryostat setup has been set up, which is based on a modified cryo pump cold head (RPK800, Leybold Heraeus). The completed coil is mounted to the inner stage of the cold head and cooled to $\sim 20\,\mathrm{K}$. The inner neon system has been closed and formed an independent vacuum system, in which from the outside of the cryostat gaseous helium could be let in. A commercial helium leak detector connected to the insulation vacuum of the test cryostat detected helium leak rates down to $2 \times 10^{-11}\,\mathrm{mbar\,l/s}$. The pressures in the insulation vacuum were of the order of $10^{-7}\,\mathrm{mbar}$ during the tests under cryogenic conditions. With this test setup at least each of the compensation coils (Comp1+2) could be tested for leak tightness. The vertical merging coils (MV) do not fit into the setup and therefore has not been tested for leak tightness. When testing the first manufactured coil, which had the conical sealings done with Apiezon H, there were no helium leaks detected at room temperature, but after one cooling cycle and even larger leaks after more cycles. For this reason all conical sealings has been done with 0.5 mm thick indium wire, which turned out to be leak tight after up to 5 cooling cycles and therefore expected to be leak tight at all. As an additional result the VCR couplings (Swagelog, 1/4-inch) with stainless steel gaskets has been tested simultaneously and demonstrated their reliability even after consecutively opening and closing of the couplings. In order to test even the leak tightness of the coils after the bakeout of the experimental vacuum, during which some of these coils could reach temperatures up to $50 - 80\,^{\circ}\mathrm{C}$, one of the coils has been heated in a vacuum oven up to $90\,^{\circ}\mathrm{C}$ and maintained the leak tightness.

Also the quality of the soldering joints and the functionality of the superconductors has been tested for all 16 manufactured coils. The coils are manufactured depending on their type with different number of windings (see table 4.1). The HTS wire used is the second generation copper laminated Amperium Wire (Type 8501, YBCO-based, American Superconductor Corporation), which has a kapton insulation and is specified for critical currents up to 100 A at liquid nitrogen temperature (77 K). The cross section of the wire is $4.8 \times 0.22\,\mathrm{mm}^2$ (with kapton insulation) and it has a minimum double bend diameter of 30 mm [116]. Each completed coil has been immersed in liquid nitrogen and the resistance of the coil has been measured with

Table 4.5: Results of the critical current measurement of the compensation (Comp1+2) and vertical merging coils (MV) at liquid nitrogen temperature.

Coil	n	$I_c/\mathbf{A}$	$R/\mu\Omega$	**Coil**	n	$I_c/\mathbf{A}$	$R/\mu\Omega$
Comp1-1	20.2	86	26.7	MV1	12.7	98	20.4
Comp1-2	20.2	90	23.3	MV2	12.7	94	38.3
Comp1-3	20.2	90	21.1	MV3	12.7	94	39.4
Comp1-4	20.2	90	22.2	MV4	12.7	96	20.8
Comp2-1	32.2	80	23.8	MV5	12.7	96	30.2
Comp2-2	32.2	80	22.5	MV6	12.7	94	21.3
Comp2-3	32.2	80	20.0	MV7	12.7	94	17.0
Comp2-4	32.2	80	20.0	MV8	12.7	96	31.3

a four wire configuration using two copper cables with $25\,\mathrm{mm}^2$ cross section for the current leads and two additional voltage contacts connected with a digital volt meter. The results of these measurements are shown in table 4.5. The current at the respective coils has been increased in steps of 2 A and the denoted critical current I_c is defined as the last step before the resistance increases significantly compared to the average[3]. Comparing these results to table 4.1 and to the highest desired current of $\lesssim 70\,\mathrm{A}$ for these coils this demonstrates the accomplishment of the specifications. In fact, even higher critical currents (up to a factor of ~ 5 [81, fig. 10.20]) will be achieved increasing the safety margin, when cooling to liquid neon temperatures of $\sim 30\,\mathrm{K}$. The residual measured OHMic resistance is originating most likely from the OHMic contact resistances, since the soldering joint is expected to be of the order of $\sim 100\,\mathrm{nA}$ [117]. The contact resistances of one one-square-inch copper-copper junction is $1 - 67\,\mu\Omega$ at 77 K [118]. In total there are four copper-copper contacts in the here performed critical current measurements.

Summary

The 16 manufactured coils have been successfully tested for leak tightness and full electrical functionality. Also their withstanding of temperatures up to 90 °C in the presence of the indium sealings has been verified. All coils fulfill the desired specifications and are ready to be built into the cryogenic section of the CSR electron cooler.

[3]Usually this current corresponds to $\sim 70\%$ of the true critical current [81], which is actually defined as the transition point between superconductivity and normal conductivity of the material.

4.5.2 Cathode and collector section

During this work it was possible to manufacture and construct the complete outer room temperature electron beamline consisting of the photocathode setup (of the former electron target of TSR), the electron beam production section and the collector section.

In figure 4.17 a photograph of this setup is shown. The magnetic guiding and the vacuum systems of both sections are mounted and have been aligned using laser pointers. In the final mounting in CSR the alignment will be done with telescopes and glass targets achieving higher alignment accuracies. Both vacuum systems together with the gun chamber of the photocathode setup have been successfully baked at $\sim 250\,^{\circ}\mathrm{C}$ reaching final vacuum pressures of 4×10^{-11} mbar and 3×10^{-11} mbar in the electron beam production and collection section, respectively.

Magnetic field measurements

Prior to the mounting of the vacuum system also the magnetic field of the whole electron beam production region and especially the magnetic induction to current relation of the high-field magnet have been measured in place using a three axis HALL probe (THM7025, Metrolab). The latter measurement has been already discussed in section 4.2 and forms the important basis for the determination and adjustment of the true magnetic expansion, of which the transverse electron beam temperature can be estimated (see section 2.2).

The measurement of the magnetic inductions on the optical axis are shown in figure 4.18 for the high-field solenoid powered by 775 A only (blue markers), the low-field solenoids powered by 13.5 A only (red markers), and altogether (green markers). It can be compared to the design in figure 4.3a. As for this figure, the origin corresponds to the center of the high-field solenoid (2). Note that obviously there is no contribution of the toroid. The simulations are (A) those of figure 4.3a but without the toroid and its iron screens. The simulation (B) in addition takes into account that the low-field solenoids (3–4) were shortened on each side by 3 mm corresponding to two windings missing per layer (compare section 4.2). It can be seen that the simulations within the solenoids match the measurement very well, but there are discrepancies in the solenoidal gaps (for simulation A) of -12% and -7% in the gaps between the solenoids (3+4) and (4+5), respectively. The discrepancies can be partly explained by the simulation B and the fact, that the manufactured solenoids are non ideal in comparison to the homogeneously filled current cross sections assumed in the simulations. Nevertheless, the adiabaticity criterion, equation (2.46), has been verified also for the measurement.

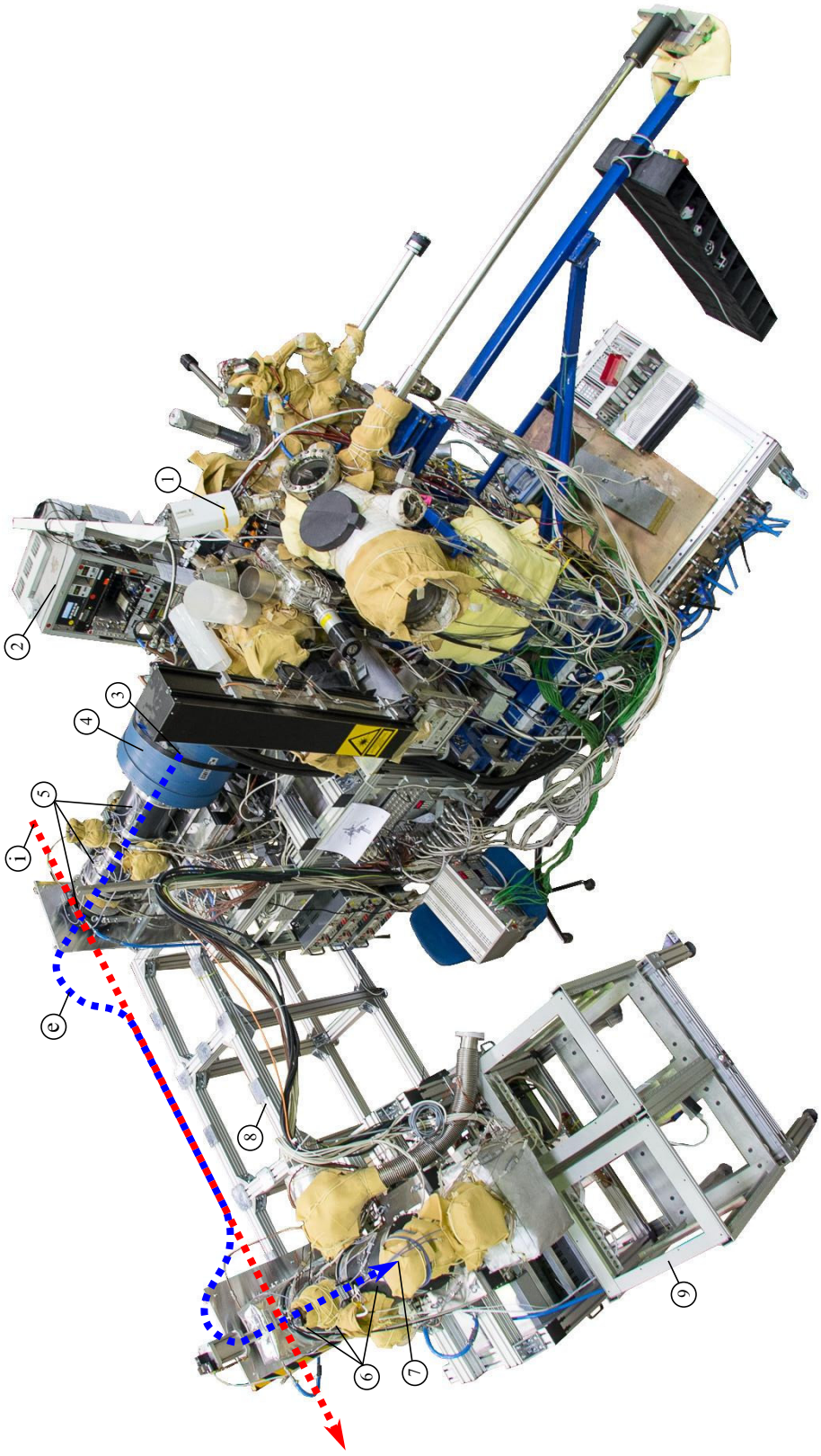

Figure 4.17: Photograph of the room temperature section of the CSR electron cooler setup with the (1) photocathode preparation setup and (2) its electronics, (3) the photocathode gun, (4) the high-field solenoid, the three low-field solenoids of the (5) production and (6) collector region, (7) the electron collector, (8) the temporary support structure for the cryogenic region, and the (9) high voltage cage. The trajectories of the (e) electron and (i) ion beam are shown additionally as an overlay.

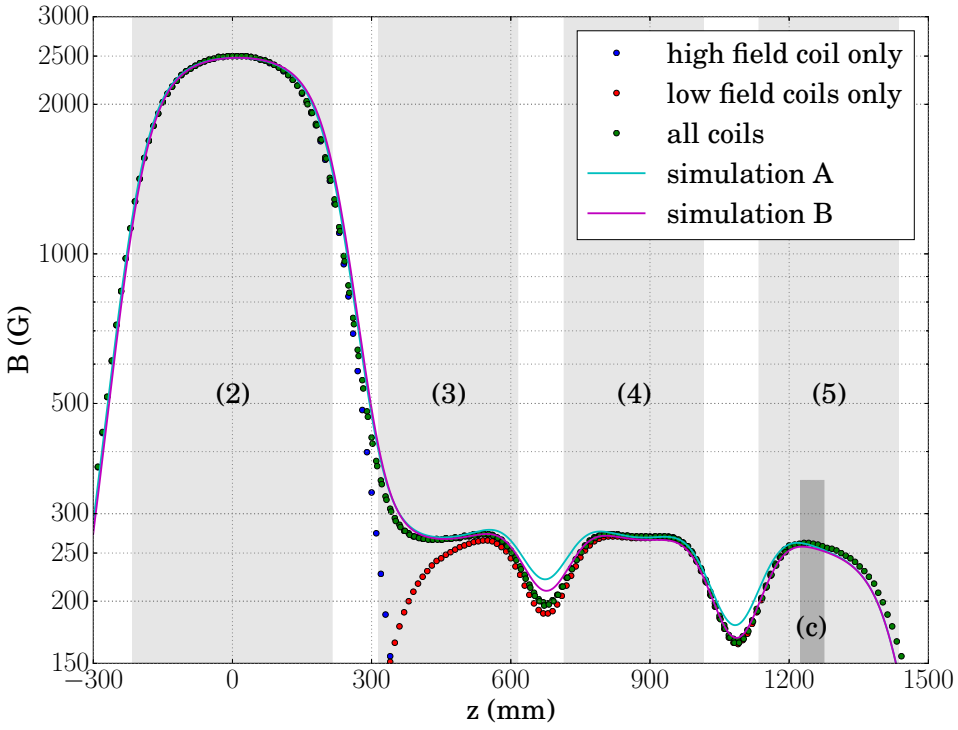

Figure 4.18: The measured (markers) and simulated (solid lines) magnetic induction as a function of the longitudinal coordinate z on axis of the magnetic fields. The gray shaded areas correspond to the different solenoids and the labeling is according to figure 4.2. The label (c) indicates the collector position used for the beam profile measurements discussed below in the text.

Photocathode electron beam operation and beam profiles

After the successful bakeout of the electron beam production region also the photocathode setup has been taken into operation as will be discussed here.

For this purpose during the setting up of this section an additional electron beam collector (not the final one, but a simplified version of it) has been installed at approximately in the center (label (c) in figure 4.18) of the last low-field room temperature solenoid (5). The position corresponds to the region of smallest magnetic field divergence as verified by the simulation (not shown here). The used collector setup will be discussed below.

The measurement scheme is depicted in figure 4.19 (not to scale). The photoelectron gun consists of the photocathode (1) and several electrodes. These are the Pierce

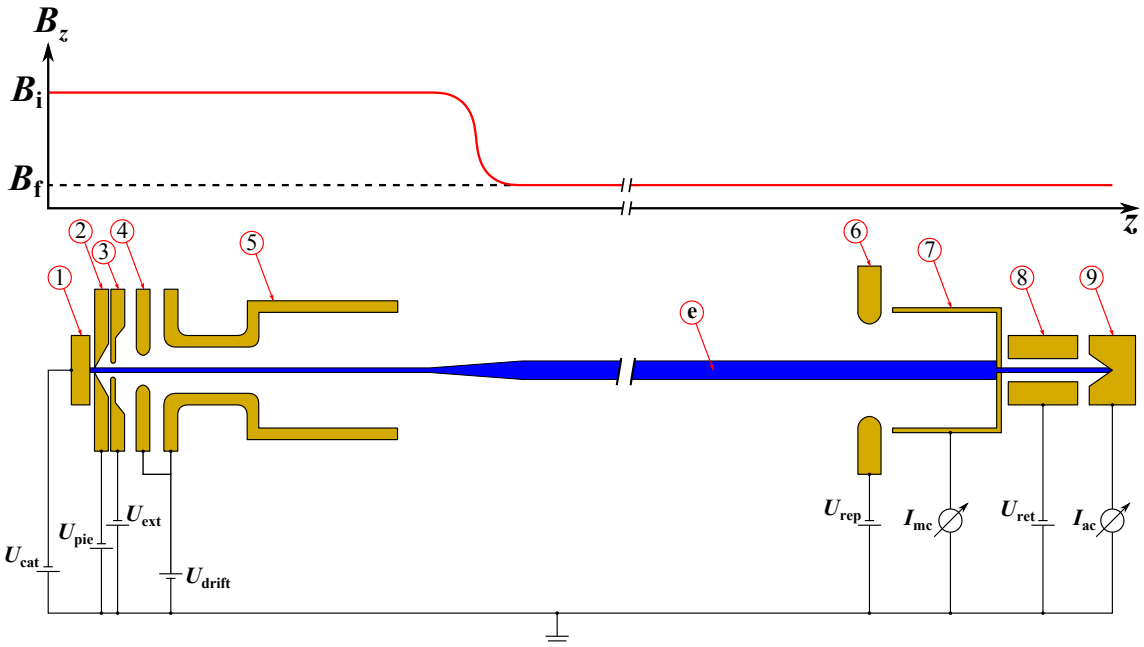

Figure 4.19: Measurement scheme for the electron beam profile measurements (not to scale). For explanations see text.

shield (2), the extraction electrode (3), and two drift electrodes (4+5), which were electrical connected with each other for this experiment. The photoelectron gun is discussed in detail in [55, sec. 3.2]. The respective denoted potentials are for the photocathode $U_{\mathrm{cat}} = -30\,\mathrm{V}$, the PIERCE shield $U_{\mathrm{pie}} = -27.2\,\mathrm{V}$, the extraction $U_{\mathrm{ext}} = -10\,\mathrm{V}$, and the drift electrodes $U_{\mathrm{drift}} = +7.1\,\mathrm{V}$, respectively.

The electron beam (e) is formed by the photoexcited electrons (by an infrared laser), which are extracted and accelerated by the difference potential $U_{\mathrm{acc}} = U_{\mathrm{ext}} - U_{\mathrm{cat}} = 20\,\mathrm{V}$. The PIERCE shield potential is slightly positive with respect to the cathode potential in order to form an uniform electron beam profile [52, sec. 5.1.1]. The positive drift electrode potential prevents positive ions from drifting towards the cathode and damage its surface [55, sec. 3.1.1]. The photocathode has been operated in the space charge limited mode by using high laser intensities.

After the acceleration of the electrons they drift towards the collector guided by the longitudinal magnetic field with strength B_z. The magnetic field strength is depicted as a function of the longitudinal coordinate z in the upper part of figure 4.19. The expansion factor $\alpha = B_{\mathrm{i}}/B_{\mathrm{f}}$ has been varied in the following experiments between $\alpha = 1, 4, 9$ with $B_{\mathrm{f}} = 250\,\mathrm{G}$.

The collector consists of a main FARADAY cup (7), which measures the total electron beam current I_{mc}. In order to capture all secondary electrons there is a repeller

electrode (6) in front of the main cup, which creates a barrier for the electrons by the potential $U_{\mathrm{rep}} = -20\,\mathrm{V}$. A $\sim 0.5\,\mathrm{mm}$ wide pin hole in the main cup allows a small fraction of the electrons to be collected by an additional analyzer cup (9), which measures the current I_{ac}. The retarding electrodes (8) were biased by $U_{\mathrm{ret}} = -4.5\,\mathrm{V}$. Using the retarding electrodes an additional barrier can be created for the electrons in order to analyze their longitudinal energy distribution [52, 105], which has not been done in this experiment.

However, this setup has been used to determine the beam profile as a function of the expansion factor. For this purpose the transverse steering coils of this section (label (11) in figure 4.4) have been used to steer the electron beam over the pin hole of the main cup.

The absolute calibration of transverse dimensions has been performed by sweeping the electron beam over the entire aperture of the collector setup. Since the entrance aperture of the repeller electrode is known to be 20 mm, the steering currents can be calibrated. For this dedicated measurement the repeller potential has been set to 0 V. The experimental calibration factors for the electron beam positions are found to be $k_x = 5.77\,\mathrm{mm/A}$ and $k_y = 5.68\,\mathrm{mm/A}$. These are in agreement with the simulated calibration factor of $k^{\mathrm{sim}} = 5\,\mathrm{mm/A}$, which has been simulated with a simplified steering coil geometry.

The measured electron beam profiles for the magnetic expansion factors of $\alpha = 1, 4, 9$ (with $B_{\mathrm{i}} = 250, 1000, 2250\,\mathrm{G}$ and $B_{\mathrm{f}} = 250\,\mathrm{G}$) are depicted in figure 4.20. The black dashed line visualizes the theoretically expected beam profile widths defined by the PIERCE shield aperture diameter of 3 mm and the respective expansion factors, compare equation (2.47).

As can be seen from the non-expanded beam profile (a), the electron beam profile is homogeneously round and has the expected width. However, there is a slight misalignment obvious, since the beam is not at the origin. This can be caused by a mismatch of cathode center and high-field solenoid axis or of collector center and low-field solenoid axis or most likely a combination of both. The alignment has been performed as accurate as possible with a laser pointer. However, the transverse offset between cathode center and magnetic field axis is estimated to be within 2 mm. The collector alignment is much worse, since it was directly mounted to the vacuum chamber, and is expected to be up to 10 mm. As a consequence of the misalignment in the electron gun magnet, the centers of the electron beam profiles for higher expansion factors move to higher transverse coordinates. Whereas the beam profile for the non-expanded beam is homogeneously round, the beam profiles for higher expansion factors become of elliptical shape. Its major axis still fills the expected beam radius, whereas the minor axis is oriented almost along the beam shift (indicated by the black dots, which correspond to the centers of the respective

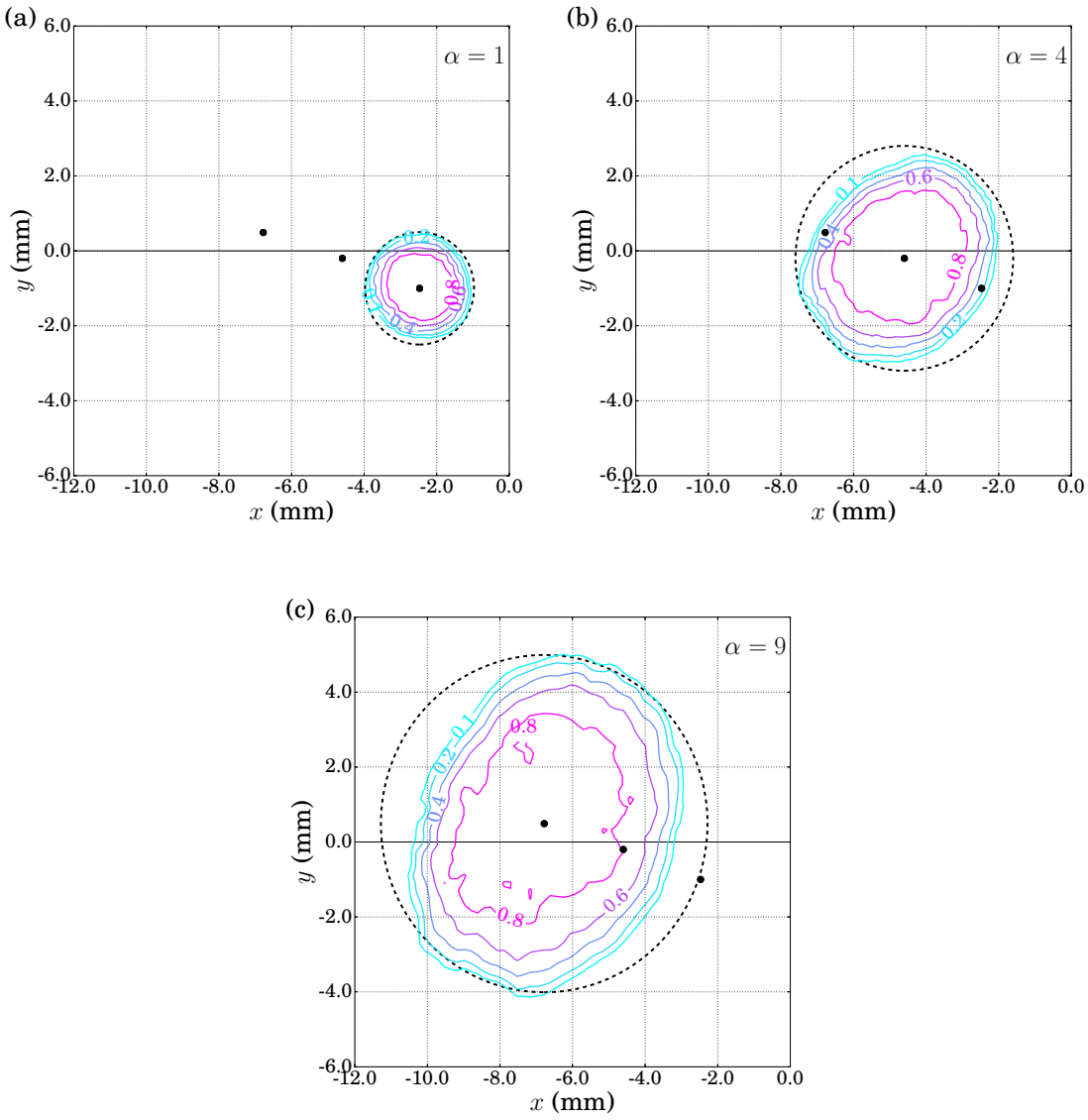

Figure 4.20: Measured beam profiles of an electron beam with 20 eV energy and electron current of 40 μA for three different magnetic expansion factors $\alpha = 1, 4, 9$. The denoted contours show the relative current with respect to the measured maximum of the profile. The black dashed circles indicate the theoretically expected electron beam profile widths. The black dots mark the centers of the respective beam profiles.

beam profiles). The elliptical shape could also be caused by the misalignment of the photocathode to the magnetic field axis.

During the setting up of this section the effort regarding the alignment of the individual elements has not been of high importance, since for the implementation of the electron cooler in CSR it has to be redone completely. In the final adjustment of the electron cooler in CSR much higher alignment accuracies have to be achieved. However, the measurements of the beam profiles might be used for the fine adjustment of the photocathode electron gun to the magnetic guiding field axis.

4.6 Status and outlook

In this chapter the final design of the complete CSR electron cooler setup has been discussed in detail. Special focus in the design has been on the compatibility with an adiabatic electron beam transport, but also on the technical aspects imposed by the environment of CSR regarding the ultra-high vacuum and cryogenic temperatures. The expected thermal loads for the different temperature stages of the electron cooler have been estimated. These helped to optimize the mechanical design as well as to ensure the thermal loads to be within the available cooling powers of the individual cooling systems. Based on this presented work the manufacturing process of all electron cooler parts has been started and is meanwhile essentially completed.

Already 16 out of the total 23 superconducting magnets of the cryogenic region could be completely assembled and tested. The accomplishment of their specifications for a successful electron cooler operation has been demonstrated.

In addition, the outer room temperature electron beamlines of the electron cooler setup have been designed, constructed and set up successfully. Both vacuum systems have been baked and achieved the envisaged vacuum pressures of the order of 10^{-11} mbar, which are well suited for a successful photocathode operation. The magnetic field in the electron beam production region has been measured and compared to simulations. The field fulfills the requirements of an adiabatic electron transport. The photocathode setup has been taken into operation and first electron beams were created in order to test the steering coils as well as the magnetic expansion of the beam.

The assembly of the cryogenic section is presently ongoing and its mounting inside the CSR will start in 2016.

Chapter 5

The commissioning of CSR

In spring 2015 the experimental vacuum chambers of CSR were baked at temperatures of $200 - 250\,^{\circ}\mathrm{C}$ for two weeks reaching finally pressures of $2 \times 10^{-10}\,\mathrm{mbar}$ at room temperature. Following this, the complete CSR was cooled down for the first time reaching temperatures of $\sim 4\,\mathrm{K}$ after 18 days of cooling. During the following months the properties and the performance of the electrostatic storage ring were tested with several different ion species including Ar^+, C^-, O^-, OH^-, CH^+, C_2^-, Co_2^-, Ag_2^- and Co_3^- at beam energies of $60 - 90\,\mathrm{keV}$.

Since the electron cooler has not yet been implemented in CSR, a merged laser beam setup has been installed for the commissioning phase in that section, in order to perform photodetachment and fragmentation studies. In particular, dedicated experiments on OH^- and CH^+ had the aim to study the internal temperature of these molecules, which should cool rotationally in the lowered black-body radiation field of CSR due to their relatively high dipole moment.

In this chapter the characterization of the storage ring properties and measurements regarding the beam parameters with the diagnostic system of CSR (see chapter 3) are presented. Special emphasis is put on the ion beam detection and its intensity, but also on the transverse position of the closed orbit and the ion beam lifetime. Also, different working points and their properties are studied regarding their applicability for the future electron cooler. At the end a summary of the most important commissioning results will be given.

5.1 Basic adjustment of the storage ring

The most fundamental adjustment of a new electrostatic storage ring is the setting of the electrostatic potentials, which depend on the ion beam energy as discussed in section 2.1. The symmetry of the storage ring allows to combine individual subgroups, which for CSR are two classes of deflectors and the quadrupoles consisting of two singlets. Arbitrarily the singlets closer to the straight sections are defined as family 1 and the singlets closer to the corners of the ring as family 2. All electrodes of one family are connected to two bipolar high voltage power supplies, whereby the horizontal and vertical electrodes have opposite electrical potentials. Thus, in total there are only eight electrical potentials, which need to be defined. These are the outer and inner electrodes of the respective deflectors (39° and 6°) and the four quadrupole family potentials. The deflection fields can be easily calculated for a given nominal energy in order to achieve a closed ion beam trajectory. However, the quadrupoles define the working point of the storage ring and consequently the ion beam dynamics.

An electrostatic quadrupole is characterized by its effective length L_{eff} and its quadrupole strength K, which is given by [30, eq. 5.53]:

$$K = \frac{z\,e}{E_0\,R_0^2}U, \tag{5.1}$$

where $z\,e$ and E_0 are the charge and the kinetic energy of the stored ion, respectively, U is the applied electrical potential, and $R_0 = 0.05\,\text{m}$ is its aperture radius, meaning the shortest distance from one of its poles to the center of the quadrupole. Since the electrical potential of a realistic quadrupole is not limited to the interior of its geometrical electrode length $L_0 = 0.2\,\text{m}$, but extends to the outside, it is convenient to define an effective length L_{eff}. This is defined as the length of a rectangular potential approximating the smoothed electrostatic potential of the realistic quadrupole, but with the same quadrupole strength, see [30, sec. 3.1.4]. For the first basic adjustments of the working point a former simulated effective quadrupole length of $L_{\text{eff}}^{\text{sim}} = 0.212\,\text{m}$ [35] was used. However, one of the tasks of the commissioning was the experimental determination of the quadrupole lengths, which will be discussed in section 5.7.1.

The CSR quadrupoles are designed for a maximum voltage of 10 kV limiting the possible quadrupole strengths at $K_{\text{max}} = \pm 13.33\,\text{m}^{-2}$ for a singly charged ion beam with an energy of 300 keV.

Figure 5.1 shows a MAD8 simulation [36] (assuming an effective quadrupole length of $L_{\text{eff}}^{\text{sim}} = 0.212\,\text{m}$) for this region of interest. There are plotted the possible quadrupole

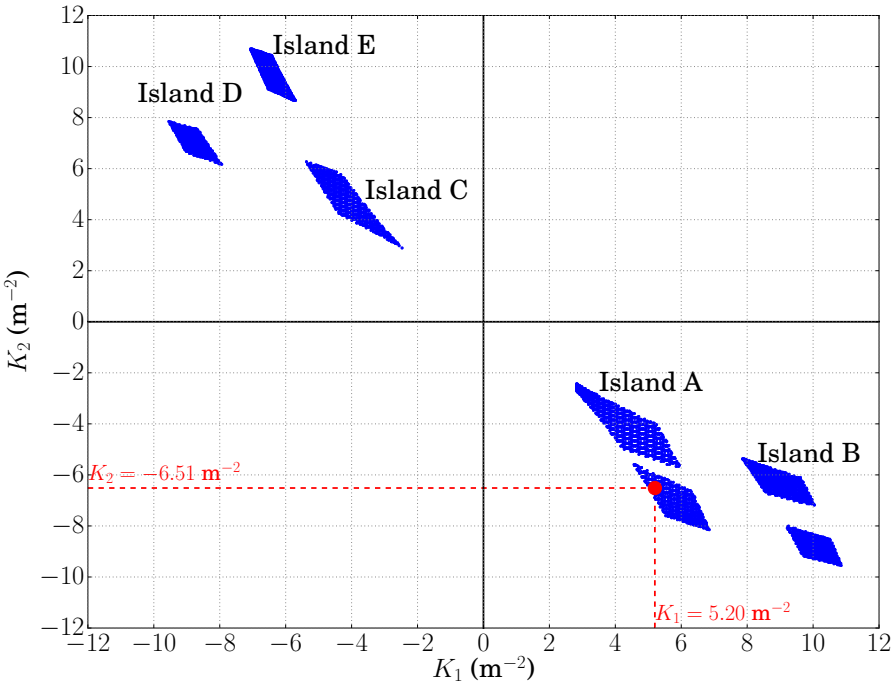

Figure 5.1: Stability diagram of CSR simulated with the MAD software (assuming an effective quadrupole length of $L_{\mathrm{eff}}^{\mathrm{sim}} = 0.212\,\mathrm{m}$). The red point ($K_1 = 5.20\,\mathrm{m}^{-2}$, $K_2 = -6.51\,\mathrm{m}^{-2}$) marks the working point for the commissioning of CSR, which is discussed in the text.

strengths[1] of both families allowing storage of ion beams (blue dots). In total there are five *islands of stability*, two in quadrant four (lower right) and three in quadrant two (upper left). Basically at all of these islands storage is possible, but there are different arguments confining the choice.

A simple technical argument is the avoidance of high voltages because of the electrical breakdown strength. Also, it is advisable to have an alternating order of focusing and defocusing elements in the storage ring. Due to the horizontally focusing bending elements (39° and 6° deflectors) the quadrupole family 2 should be horizontally defocusing and the family 1 horizontally focusing. This argument confines the choice to quadrant 4. However, even more important are the machine parameters which are defined by the working point. The working point should have a big acceptance allowing the storage of high intensities, increasing the lifetime, and reducing the influence of closed orbit shifts due to field imperfections or alignment inaccuracies.

[1]Definition: A positive (negative) quadrupole strength denotes a horizontal focusing (defocusing) and vertical defocusing (focusing).

For the same reasons the betatron amplitudes should be as small as possible. Especially for the future electron cooler, also the dispersion in the straight sections should be as small as possible to facilitate the adjustment of the electron cooler. In addition, the resonances and the effects due to the incoherent tune shift have to be considered in the choice of the working point, as discussed already in sections 2.1.1 and 3.1.

For these reasons the working point for the commissioning has been set to $K_1 = 5.20\,\mathrm{m}^{-2}$, $K_2 = -6.51\,\mathrm{m}^{-2}$, marked in figure 5.1 as a red point. Former simulation studies regarding the beam properties converged to this working point [35] fulfilling the above mentioned criteria. However, part of the tasks of the commissioning was the verification and the measurement of important machine parameters at this and other working points, which will be discussed in section 5.7.

With the ion beam optics set to their nominal set values immediate storage cannot necessarily be expected. For both, the fine tuning of the storage ring, but also of the transfer beamline, the most helpful tools are the destructive beam profile monitors, of which some are installed in the transfer beamline at various locations as well as in CSR. Their basic principle and their locations in CSR are discussed in section 2.6.

Nevertheless, since these tools destroy the ion beam, they cannot be used for the proof of successful storage of an ion beam. Here, the developed non-destructive ion beam diagnostics are crucial, as will be discussed in the subsequent sections. The first pilot beam was an $^{40}Ar^{+}$ beam with 60 keV energy produced by a Penning ion source.

5.2 Ion beam intensity measurement

Not only the principle of the ion beam current pick-up is simple, but also its importance and necessity for the operation of the storage ring is beyond dispute. The advantage of this device is its simplicity, robustness and the intuitively understandable signals. For these reasons the proof of the first stored ion beam in CSR has been recorded with the current pick-up.

First ion beam storage

Figure 5.2 shows the first turn (left panel) and the first stored ion beam (right panel) in CSR recorded on the 17$^{\mathrm{th}}$ March 2014. In order to create short pulses with lengths comparable to the circumference of the storage ring the ion beam has

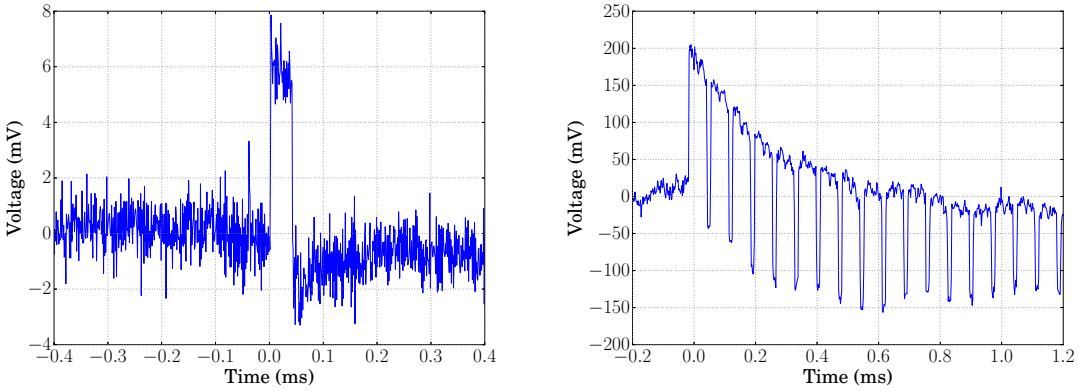

Figure 5.2: Current pick-up signals of the (left panel) first turn and (right panel) first stored ion beam ($^{40}Ar^{+}$ with 50 keV energy) in CSR.

been chopped with a fast switched electrostatic deflector ('chopper') located in the transfer beamline, which connects the high voltage platform and CSR.

The $\sim 50\,\mu$s long pulse in the left panel corresponds to one turn of the ion bunch. For the closing of the ion beam trajectory the 'kicker electrodes' (one of the 6° deflectors of CSR, see figure 2.6) are ramped quickly from zero to the desired high voltage. After minor adjustments of the electrostatic deflector potentials of the storage ring the ion beam trajectory is closed completely resulting in the typical spectrum shown on the right panel. Each pulse corresponds to one revolution of the circulating ion bunch. Apart from the simple proof of storing particles in a storage ring, important quantitative beam parameters can be deduced from these signals, which are the revolution frequency and from this the particle energy as well as the number of initially stored ions.

Baseline shift

First of all we need to comment on the obvious baseline shift which is visible in figure 5.2. This is no effect of external noise but rather a charging effect of the electrode capacity. In order to understand this effect numerical simulations of the occurring signals have been performed. In the derivation of the voltage signals at the input resistance of the cryogenic amplifier originating from the mirror charges of the ion beam, a differential equation has been formulated, see equation (3.4). This equation has been solved numerically for a sequence of current pulses with a current I_0. The total capacity C has been fixed to the measured value and the input resistance of the amplifier R is a free parameter.

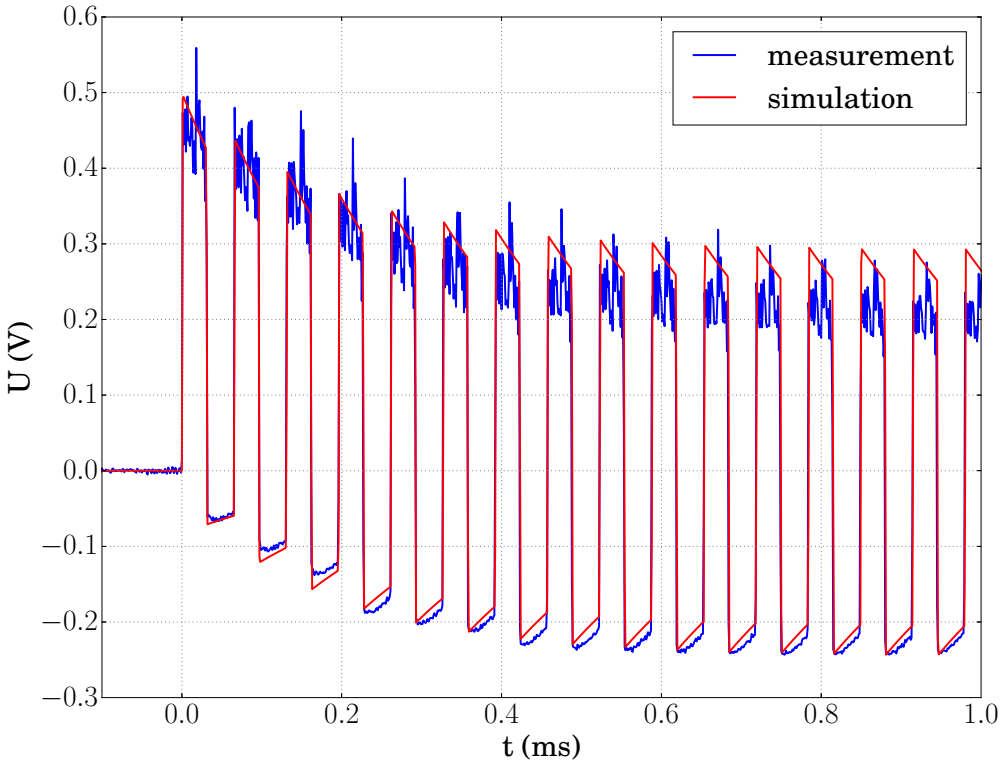

Figure 5.3: Measurement (blue line) of a current pick-up signal of an $^{40}Ar^{+}$ with 60 keV energy and a simulation (red line) of this signal.

Figure 5.3 shows a typical measured (blue line) current signal of a circulating ion beam ($^{40}Ar^{+}$ with 60 keV energy). In addition the simulation (red line) of a signal with $I_0 = 410\,\text{nA}$ is shown. The best agreement of simulated and measured signal is achieved for a total capacity of $C = 96.0\,\text{pF}$ and a resistance of $R = 2\,\text{M}\Omega$. For larger R the baseline minimum shifts to longer times and for smaller values to shorter times. The simulated capacity corresponds to the actual assumed total capacity of the current pick-up at cryogenic conditions, as discussed below, whereas the simulated resistance is by a factor of ~ 2.5 too small (nominal 5 MΩ). Additional measurements and corresponding simulations (not shown here) with the SCHOTTKY pick-up had revealed a similar result, i.e. for the correct capacity a resistance of $\sim 1\,\text{M}\Omega$.

The discrepancy might be caused by the simplified differential equation, which neglects the in-coupling capacity ($0.1\,\mu\text{F}$) of the cryogenic amplifier (see figure 3.17), but also the influence of the field effect transistor itself. However, the baseline shift can be explained by this model qualitatively and, thus, it is justified to correct the

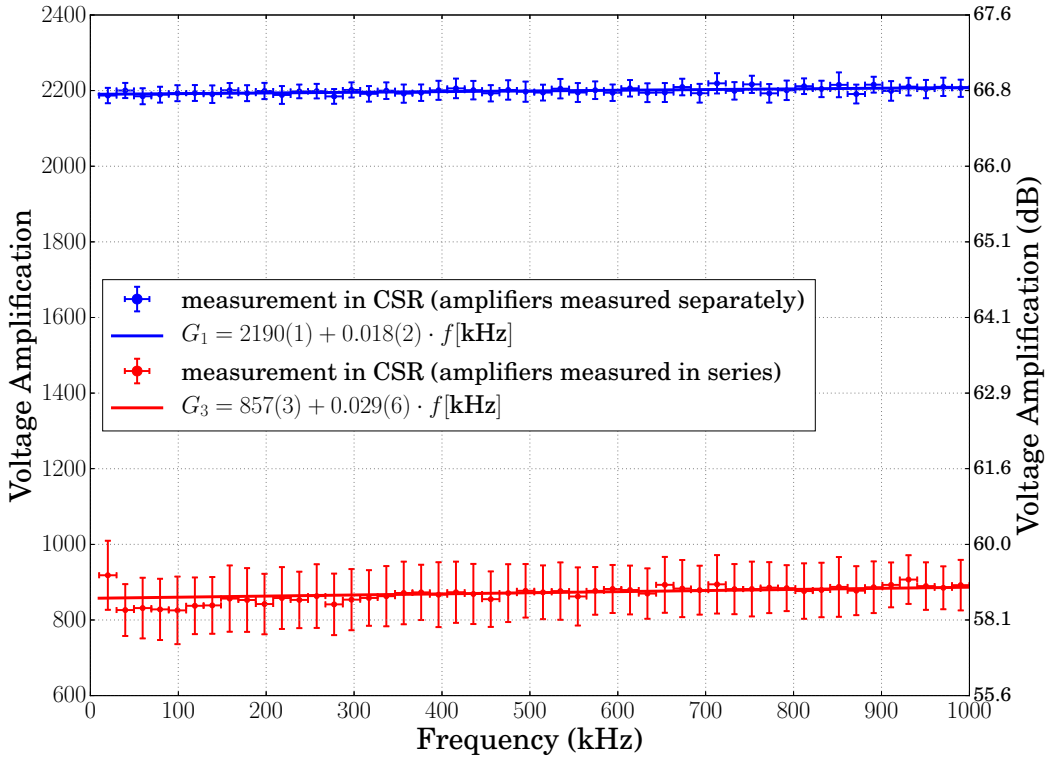

Figure 5.4: Total signal amplification of the current pick-up system when both amplifiers measured (blue markers) separately and (red markers) in series.

baseline shift and integrate the pulses in order to deduce the number of stored ions.

Gain of the amplification system

For the quantitative measurement of the stored ion number the gain of the entire amplification system of the current pick-up has to be known. The gain is also a function of the frequency and ideally should be constant over the frequency range of interest, since the observed signals are typically rectangular pulses, which are otherwise distorted. The influence of the higher harmonics becomes less prominent for rectangular pulses with pulse lengths of half the circumference of the storage ring, since in this case the agreement with a sine function is optimal.

Figure 5.4 shows the measured total amplification of the current pick-up (ULNA and NF-SA-220F) at the frequency range relevant for CSR. In blue is shown the multiplied amplification of both amplifiers when they are measured separately, and

in red is shown the measurement when they are in series. The cryogenic amplifier of the current pick-up has a switchable signal line ($\sim 1.5\,\mathrm{m}$ long coaxial cable STC-50A-36T, Vishay), which directly connects the input of the amplifier with the insulation vacuum feedthrough, compare figure 3.19. For both measurement the network analyzer Bode 100 (OMICRON Lab) was used.

In the first measurement the $50\,\Omega$ termination resistance for the calibration input signal was placed directly at the insulation vacuum feedthrough and the cryogenic amplifier was terminated with a $1\,\mathrm{M}\Omega \pm 2\%$ resistance (corresponding to the input resistance of $1\,\mathrm{M}\Omega \pm 5\%$ of the main amplifier NF-SA-220F), which can be internally set in the network analyzer. The main amplifier has been characterized in the same manner, but with an amplifier termination of $50\,\Omega$ (corresponding to the input resistance of the oscilloscope). For the second measurement both amplifiers were measured in series with the termination resistance of $50\,\Omega$ at the main amplifier.

Surprisingly, both measurements are not consistent. This in no saturation effect of the amplifier, which has been verified by varying the input signal strength. Most likely this is a temperature dependent effect of the transmission line, which connects the cryogenic with the main amplifier, because of the two following arguments. Firstly, both measurements are consistent when both amplifiers are at room temperature. And secondly, from measurements where only the cryogenic amplifier is measured it is known that the input signal strength is not damped, so that the effect should lie in the output side of the cryogenic amplifier.

The statistical uncertainty of both measurements is very good as can be seen from the linear fits and as desired there is also only a small frequency dependency of the gain in the relevant frequency range. The results hence are

$$G_{\mathrm{separately}} = 2190(1) + 0.018(2) \cdot f_0[\mathrm{kHz}] \tag{5.2}$$

$$G_{\mathrm{series}} = 857(3) + 0.029(6) \cdot f_0[\mathrm{kHz}]. \tag{5.3}$$

In summary the actual amplification of the current pick-up is uncertain and it appears appropriate to assign a large systematic error to it. However, at this point it is more likely that the series measurement represents the true conditions, even though the reason for the discrepancy is not yet fully understood. It will be required to clarify this behaviour in the future beamtimes.

Determination of the ion number

With equation (3.7) the total number N on the storage ring circumference can be determined. Also taking the gain G of the amplification system into account yields

$$N = \frac{C}{z\,e}\frac{C_0}{L_0}\frac{1}{G\,T_0}\int_0^{T_0} U(t)\,\mathrm{d}t. \tag{5.4}$$

Herein is C the total capacity of the current pick-up, z the charge state of the ion, e the elementary charge, C_0 the ring circumference, L_0 the electrode length of the pick-up, G the total amplification factor, T_0 the revolution time of the ion beam and $\int_0^{T_0} U(t)\,\mathrm{d}t$ the integrated voltage signal over one revolution.

The total capacity has been measured resonantly at room temperature, see section 3.3.2, but due to the cooldown to $\sim 6\,\mathrm{K}$ a change of the capacity is expected. From the measurement of the resonance frequencies of the SCHOTTKY pick-up at cryogenic conditions, see section 3.6.6 and especially figure 3.24, this change can be roughly estimated. Comparing the resonance frequencies for zero voltage at the capacitive diodes and assuming the total change is caused by the change of the capacity only ($f \propto C^{-1/2}$ and $L = \mathrm{const}$), the expected maximal change for the current pick-up capacity can then be estimated by

$$\frac{\Delta f}{f} = \frac{\partial f}{\partial C}\frac{\Delta C}{f} = -\frac{C^{-3/2}}{2}\frac{\Delta C}{C^{-1/2}} = -\frac{1}{2}\frac{\Delta C}{C} \tag{5.5}$$

$$\Rightarrow \Delta C = -2C\frac{\Delta f}{f} = -2\cdot 97.3\,\mathrm{pF}\frac{360635.9 - 355962.3}{355962.3} = -2.6\,\mathrm{pF}. \tag{5.6}$$

Adding the shift $\Delta C = (-1.3 \pm 1.3)\,\mathrm{pF}$ to the room temperature capacity measurement of $(97.3 \pm 1.3)\,\mathrm{pF}$, the total capacity of the current pick-up at cryogenic conditions is consequently given by

$$C = (97.3 \pm 1.3)\,\mathrm{pF} - (1.3 \pm 1.3)\,\mathrm{pF} \tag{5.7}$$

$$= (96.0 \pm 2.6)\,\mathrm{pF}. \tag{5.8}$$

The circumference of the storage ring is constructively given by 35.12 m (corresponding to the ideal closed orbit). Neglecting the influence of the betatron oscillations on the circumference its error can be estimated by the geometrical minimal and maximal allowed circumference

$$C_0 = (35.12 \pm 0.22)\,\mathrm{m}. \tag{5.9}$$

The error of the length of the pick-up electrode is mainly given by the manufacturing tolerances

$$L_0 = (30.0 \pm 0.2)\,\mathrm{mm}. \tag{5.10}$$

A conservative propagation of the errors by adding the absolute values of the individual errors gives

$$\Delta N = \left|\frac{\partial N}{\partial C}\Delta C\right| + \left|\frac{\partial N}{\partial C_0}\Delta C_0\right| + \left|\frac{\partial N}{\partial L_0}\Delta L_0\right| \tag{5.11}$$

$$= (19.0 + 4.4 + 4.7)\frac{10^9}{\mathrm{V}}\,\frac{1}{z\,G\,T_0}\int_0^{T_0} U(t)\,\mathrm{d}t. \tag{5.12}$$

And finally, the number of stored ions can be calculated via the following equation

$$N = F\,\frac{1}{z\,G\,T_0}\int_0^{T_0} U(t)\,\mathrm{d}t, \tag{5.13}$$

where $F = (701 \pm 28)\cdot 10^9/V$ is a geometrical coefficient taking the above mentioned error contributions into account. Thus, by integration of the pulses and the determination of the revolution time from the recorded signals and using equation (5.13) together with the measured gain of the amplification system (see equation (5.2) or (5.3)) the number of stored ions can be deduced. For this reason the current pick-up signals have been recorded throughout the commissioning phase of CSR routinely.

Because of the unavoidable momentum spread of an ion beam this method of non-destructive diagnostic has its limit, since the initially injected rectangular shaped ion pulse starts to spread longitudinally up to the point when only a coasting beam is left (typically after less than a second). For this reason the direct current pick-up signals (i.e. voltage versus time spectrum) can only be used for the first few revolutions in order to determine the initially stored number of ions. Accordingly, for the planned experiments with merged electron or neutral beams, long-time non-destructive beam diagnostics is desired.

5.3 Long-time ion beam detection using rf bunching

In order to detect the ion beam for longer time periods the longitudinal structure of an ion beam can be actively manipulated using the rf system, see section 2.1.2 and 3.8. By applying a rf signal on the drift tube electrode the coasting ion beam develops into a sequence of discrete ion pulses (bunches) corresponding in their number along the ring circumference to the harmonic number which is used for the bunching. In order to effectively capture most of the ions in the bucket the amplitude $\hat{U}$ of the applied rf signal must have a certain value. Since the ions are accelerated during the bunching process, also the amplitude should not be applied instantly,

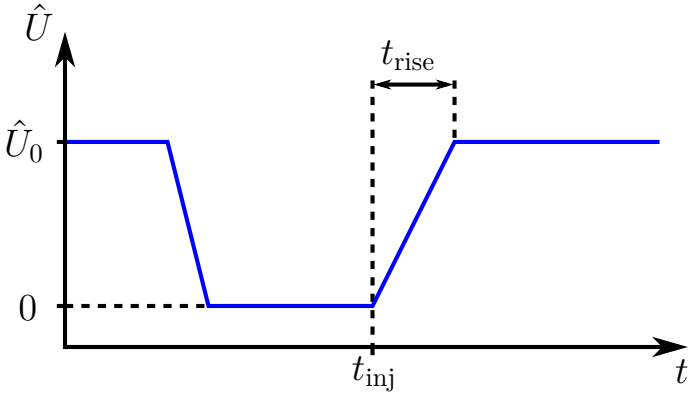

Figure 5.5: Timing scheme for the rf bunching.

but rather be ramped up to its full value over a certain 'rise time' t_{rise}. If the rise time is too short, ions could be accelerated too fast and lost as a consequence.

Figure 5.5 schematically illustrates the used timing scheme. The amplitude $\hat{U}_{\mathrm{drift}}$ applied at the drift tube is modulated by a control voltage $\hat{U}$, which is varied between zero and a certain amplitude $\hat{U}_0$. Prior to the injection (typically a few ms before) the amplitude is lowered to zero and then synchronously with the ion beam injection t_{inj} ramped over t_{rise} to the value $\hat{U}_0$ again. The control signal for the amplitude regulation of the rf system is created using an arbitrary waveform generator (DS340, Stanford Research Systems), compare figure 3.29. The actual rf frequency f_{rf} is provided by a DDS-card (Direct Digital Synthesis card) and is set to a harmonic frequency of the ion beam revolution frequency $f_{\mathrm{rf}} = h\, f_{\mathrm{rev}}$.

In order to reach high rf signal amplitudes the amplitude regulation system is equipped with internal amplifiers. Therefore the calibration of the actual applied voltage amplitude at the drift tube $\hat{U}_{\mathrm{drift}}$ has been measured as a function of the voltage amplitude of the control value $\hat{U}_0$ (provided by the arbitrary waveform generator). The DDS-card frequency has been set to $f_{\mathrm{rf}} = 229.816\,\mathrm{kHz}$, which corresponds to the 15^{th} harmonic of the revolution frequency of an $^{40}Ar^{+}$ ion beam with 60 keV energy. The drift tube voltage amplitude has been measured with an oscilloscope at the $50\,\Omega$ termination of the amplitude regulation system, compare figure 3.29. Figure 5.6 shows the measurement (blue markers) together with a linear fit (red straight line), which results in

$$\hat{U}_{\mathrm{drift}}(\hat{U}_0) = 10.1(1)\,\hat{U}_0[\mathrm{V}] + 0.64(5)\,\mathrm{V}. \tag{5.14}$$

The dependency is linear except for small values near zero set value voltage. For this reason the design of the amplitude control is being presently changed in order to optimize this behaviour in the future.

With the drift tube voltages $\hat{U}_{\mathrm{drift}}$ and equation (2.31) the effective voltage $\hat{U}_{\mathrm{b}}$ can

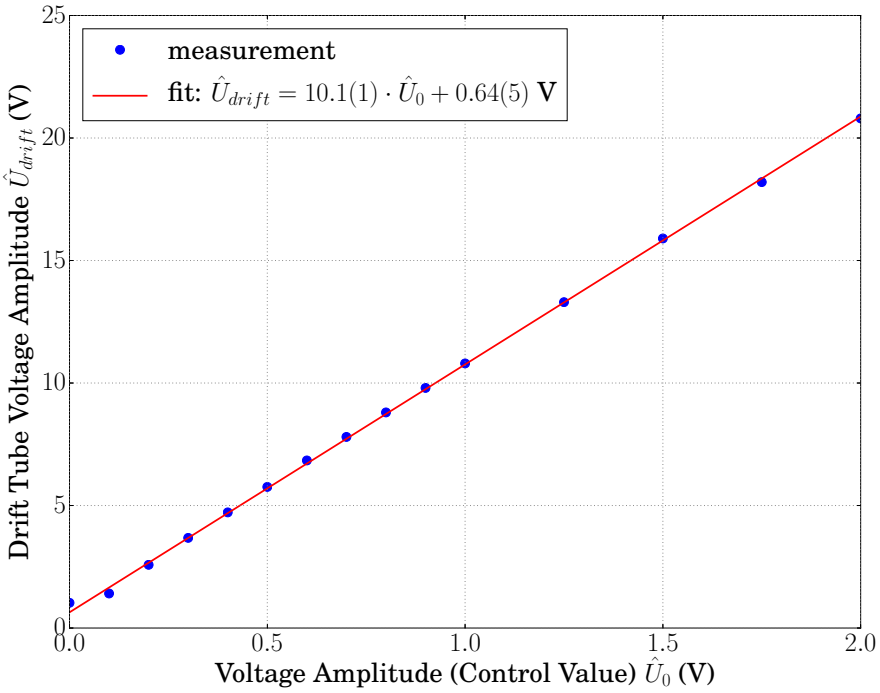

Figure 5.6: Calibration of the drift tube voltage.

be calculated, which is necessary for the description of the bunching process. In order to verify this experimentally synchrotron oscillations can be excited and their frequency can be measured. If the synchrotron oscillations are excited, sidebands are formed near the harmonics of the revolution frequency. The difference frequency of the sideband and the revolution frequency corresponds to the synchrotron frequency. According to equation (2.33) the synchrotron frequency depends on various parameters, which can be varied experimentally.

For the excitation of the synchrotron oscillations only some part of the initial longitudinal phase space is filled. By the usage of the electrostatic chopper (in the transfer beamline) an ion pulse of $\sim 95\,\%$ of the storage ring circumference is injected and stored. Simultaneously with the injection the amplitude of the rf signal is ramped as discussed above. The used parameters for this measurement are $f_{\mathrm{rf}} = 229.816\,\mathrm{kHz}$, $h = 15$, $t_{\mathrm{rise}} = 3\,\mathrm{ms}$ and $\hat{U}_0 = 0.1 - 2.0\,\mathrm{V}$ corresponding to $\hat{U}_{\mathrm{drift}} = 1.41 - 20.80\,\mathrm{V}$. The ion beam signal induced on the current pick-up is recorded with a spectrum analyzer (FSV, Rhode & Schwarz) with a resolution band width of 10 Hz and a sweep time of 500 ms (corresponding to ~ 7700 ion beam revolutions). For each setting of $\hat{U}_{\mathrm{drift}}$ in total 20 consecutive injections are averaged.

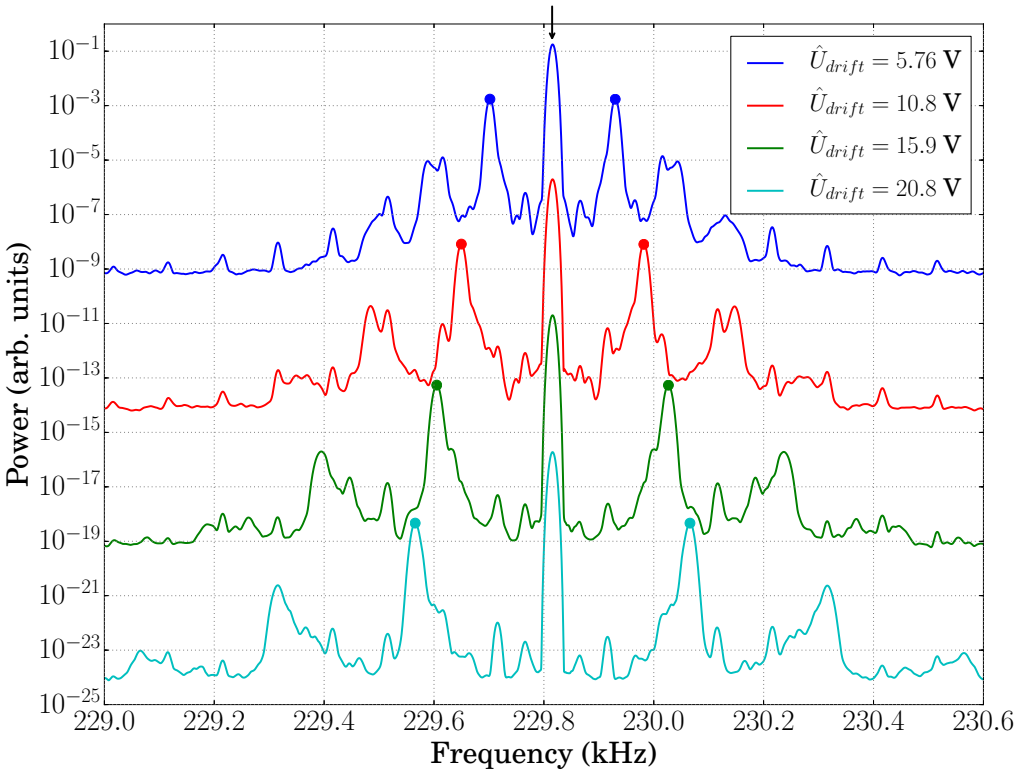

Figure 5.7: Synchrotron sidebands near the 15$^{\text{th}}$ harmonic of an $^{40}Ar^{+}$ beam with 60 keV energy.

Some of the recorded spectra are shown in figure 5.7. The 15$^{\text{th}}$ harmonic of the revolution frequency (of an $^{40}Ar^{+}$ beam with 60 keV energy) is marked with a black arrow. Coloured markers show the synchrotron sidebands, which are further analyzed. The higher order sidebands are neglected in the analysis due to their double peak structure.

Figure 5.8 shows the square of the measured synchrotron frequencies as a function of the measured applied drift tube voltage amplitudes. Each data point is the average of two analyzed synchrotron sidebands per spectrum, compare figure 5.7. The data is fitted with a polynomial function of second order (red line) and gives as an experimental result

$$f^2_{\text{sync, exp}} = 2001(27)\,\hat{U}_{\text{drift}}\,\text{Hz}^2/\text{V} + 50(2)\,\hat{U}^2_{\text{drift}}\,\text{Hz}^2/\text{V}^2. \tag{5.15}$$

Calculating the square of the synchrotron frequency using the equation (2.33) and

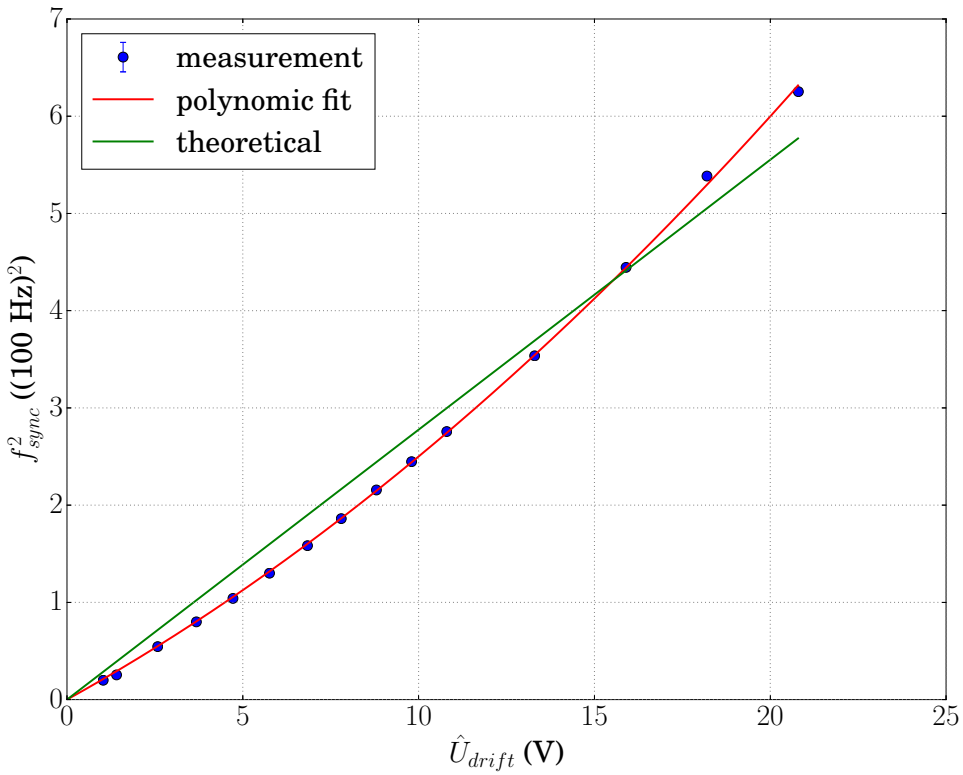

Figure 5.8: The measured square of the synchrotron frequency f_{sync} versus the measured drift tube voltage amplitude $\hat{U}_{\mathrm{drift}}$.

inserting equation (2.31) results in (also shown in the figure as a green line)

$$f^2_{\mathrm{sync,\,theo}} = \frac{h\,\eta}{\pi\,C_0^2}\frac{e}{m}\hat{U}_{\mathrm{drift}}\,\sin\left(h\,\pi\frac{L_0}{C_0}\right) \tag{5.16}$$

$$= 2776(71)\,\hat{U}_{\mathrm{drift}}\,\mathrm{Hz}^2/\mathrm{V}. \tag{5.17}$$

Herein $h = 15$ is the harmonic number, $\eta = 0.674(4)$ the measured phase slip factor, which will be discussed in section 5.7.4, $C_0 = 35.12(22)\,\mathrm{m}$ the circumference of the storage ring, e the elementary charge, $m = 39.948\,u$ the atomic mass of argon and $L_0 = 340.0(5)\,\mathrm{mm}$ the drift tube length.

The deviation cannot be explained by the denoted errors, which are in the experimental case the estimated fitting errors and for the theoretical case calculated by the propagation of the individual errors. The signal cable connecting the vacuum feedthrough with the rf system has an OHMic resistance of $\sim 17.5\,\Omega$, whereas the the impedance of the drift tube capacity is $\sim 1.8\,\mathrm{k}\Omega$. Thus, the true applied drift tube voltage is only 1 % smaller than the measured voltage outside of the cryostat.

This effect anyway changes only the slope of the linear curve. The origin of the non-linear dependence between f_{sync}^2 and $\hat{U}_{\mathrm{drift}}$ cannot be explained at this point.

5.4 Sensitivity limit of the current pick-up

With rf bunching also the sensitivity of the current pick-up can be increased in order to detect low intensity ion beams. For this purpose the ion beam is bunched and observed with a spectrum analyzer at a fixed frequency set to the bunching frequency. The calibration of the power level of the bunched ion beam is done with the initial injected ion number deduced from the current pick-up measurements in the time domain as shown in the following.

For optimal ion number determination the injected ion beam is chopped in a pulse of $\sim 50\,\%$ storage ring circumference and stored in CSR. Simultaneously with the injection of the ion pulse the rf bunching is started with a drift tube voltage of $\hat{U}_0 = 0.7\,\mathrm{V}$ (corresponding to $\hat{U}_{\mathrm{drift}} = 7.8\,\mathrm{V}$) and rise time of the rf amplitude of 20 ms. The bunching frequency is set to $f_{\mathrm{rf}} = 229.816\,\mathrm{kHz}$ corresponding to the 15^{th} harmonic of the revolution frequency of the $^{40}\mathrm{Ar}^+$ beam with 60 keV energy.

The current pick-up signals are recorded with an oscilloscope (DSO-X 2024A, Keysight Technologies) and with a spectrum analyzer (FSV, Rhode & Schwarz) at the fixed center frequency equal to f_{rf} and a resolution bandwidth of 1 kHz. For each of these measurements 32 consecutive injections are averaged. The ion beam intensity is varied with a variable aperture on the the ion source high voltage platform.

Figure 5.9 shows the baseline shift corrected (compare section 5.2) oscilloscope spectra of the first 7 revolutions of the ion beam. The noise peak at time zero is caused by the switching of the kicker electrodes.

Over a larger time scale, figure 5.10 shows the corresponding power level measured at the spectrum analyzer during the onset of the rf bunching. The timing is such that at time zero the ion beam is injected and the rf bunching ramp is started. At 20 ms (corresponding to ~ 300 ion beam revolutions) the full rf bunching voltage is applied at the drift tube.

A strong coherent peak rises when the ion beam is injected. This peak decays with time because of debunching due to the momentum spread of the ion beam. During the onset of bunching two structures appear. The first one (at ~ 6 ms) could be caused by the starting bunching process or by density waves, when the ends of the initial ion pulse start to merge with each other. After roughly 10 ms a clear signal

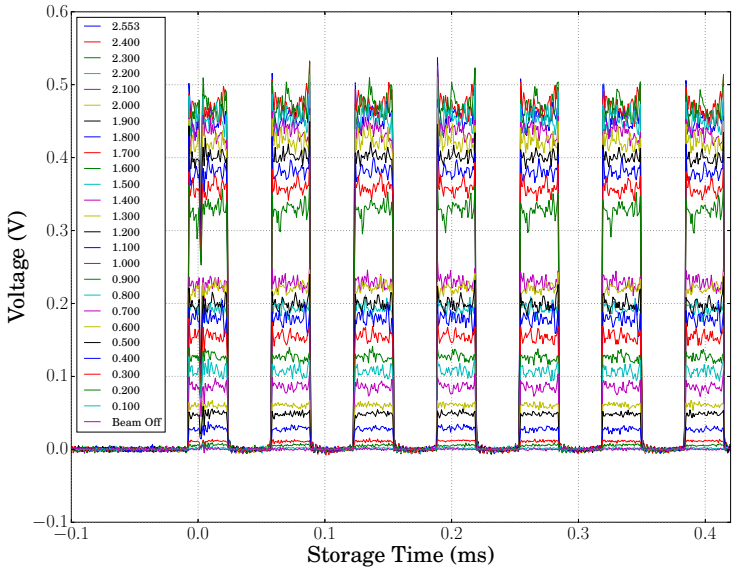

Figure 5.9: The measured current pick-up signal in time domain for different beam intensities (varied by the variable aperture openings at the source shown in the legend). The ion beam is an $^{40}Ar^{+}$ beam with 60 keV energy.

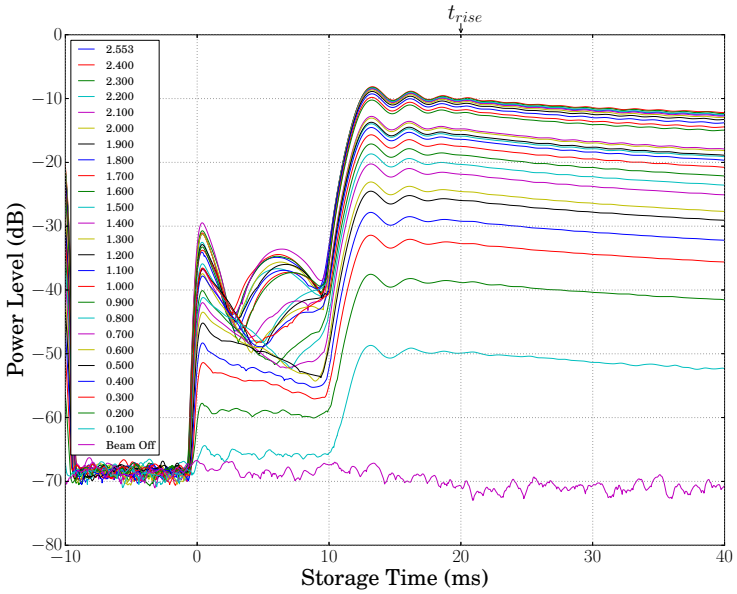

Figure 5.10: The measured current pick-up spectral power at f_{rf} during the bunching. Different aperture openings at the ion source are used, varying the beam intensities with the aperture openings shown in the legend. The ion beam is an $^{40}Ar^{+}$ beam with 60 keV energy.

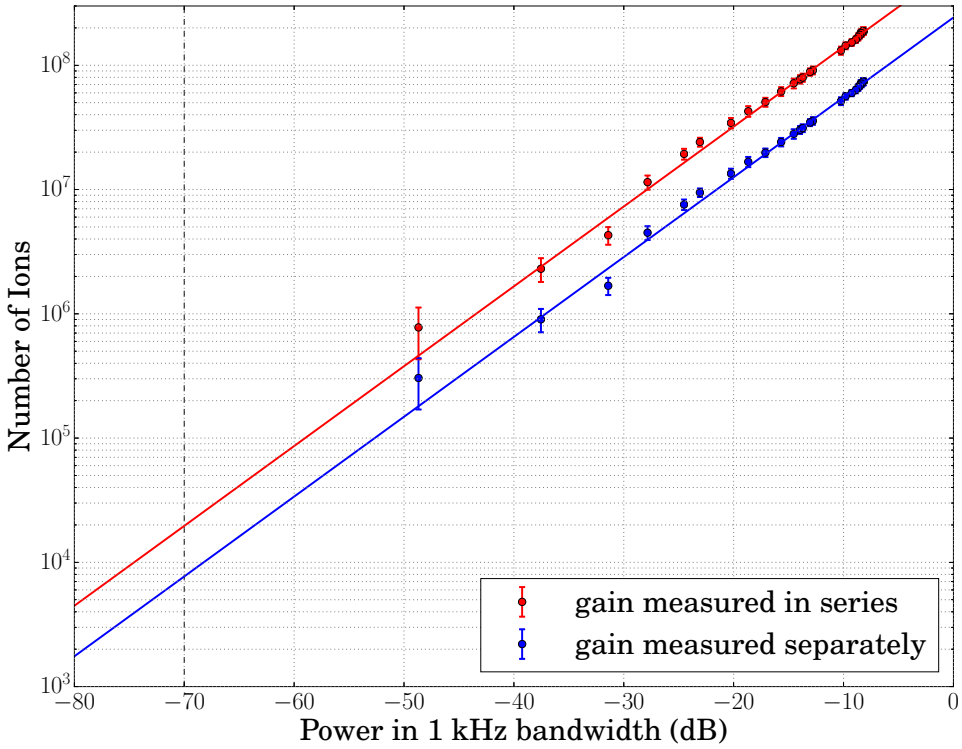

Figure 5.11: Measured number of ions versus the maximal power level in zero span mode of the bunched ion beam.

rises representing the bunched ion beam. The oscillations indicate a slight mismatch of the bunching frequency to the actual revolution frequency of the ion beam. The last spectrum shows a measurement with no ion beam representing the noise level at roughly −70 dB.

Integration of the second ion pulse in figure 5.9 and using equation (5.13) together with (red data) equation (5.3) and (blue data) equation (5.3), respectively, results in the number of initial stored ions as a function of the aperture opening. Figure 5.11 shows the determined ion number as a function of the measured maximal power level from the recorded spectra shown in figure 5.10. The black dashed vertical line represents the noise level.

Since the power level L is proportional to the logarithm of the number of ions N via $L \propto \log(U) \propto \log(N)$, the data can be fitted with exponential functions (note the logarithmic ordinate scaling) of the form $N \propto \exp(L) \propto \exp(\log(N))$. These are the red and blue straight lines. The intersection of both lines with the noise level marks

the sensitivity limit of the current pick-up at roughly 2×10^4 detectable ions (or below depending on the true gain of the amplification chain). The sensitivity could even be further increased by using the SCHOTTKY pick-up, since it has a larger ratio of electrode length to total capacity, compare equation (3.7), and since it can be operated resonantly, see section 3.6.6.

5.5 The ion beam position pick-up system

The ion beam position pick-up system consists of six position pick-ups distributed around the circumference of the storage ring, compare section 3.4, and it also relies on the rf bunching of the ion beam. Therefore for the commissioning of this system the ion beam has been bunched, as discussed in section 5.3 already, at the 15^{th} harmonic of the revolution frequency $f_{\text{rf}} = 229.826\,\text{kHz}$, a drift tube voltage of $\hat{U}_0 = 0.7\,\text{V}$ (corresponding to $\hat{U}_{\text{drift}} = 7.8\,\text{V}$) and a rise time of 20 ms. The timing is such that the ramp of the rf bunching voltage is started together with the ion beam injection. The injected ion beam $^{40}\text{Ar}^+$ with 60 keV has a pulse length of $\sim 95\,\%$ of the storage ring circumference.

Prior to the actual position measurements the capacitive diodes of the cryogenic amplifier have been adjusted manually (without ion beam) in order to compensate the capacity differences between the different pick-up electrodes. For this a calibration signal of a network analyzer (Bode 100, OMICRON Lab) has been coupled capacitively onto the input of the cryogenic amplifier. Since at the same time also the resonator coil is switched parallel to the amplifier, compare figure 3.19, the resonance frequencies could be measured and adjusted by changing the voltage at the capacitive diodes U_{cd} by some 100 mV (corresponding to a capacitive difference of only a few pF). In a later stage this capacitive adjustment procedure will be performed by the controlling software automatically.

The relays (switching between the different electrodes) are driven by voltage pulses with amplitudes of 5 V and pulse lengths of 30 ms. The data acquisition is started 100 ms after the relay switching pulse avoiding artifacts from the contact bouncing of the relays. Since for the compensation of the lifetime, compare section 3.4.5, in total three individual measurements have to be performed for one actual position measurement, the repetition time for the position measurement sums up to $\sim 0.5\,\text{s}$.

Figure 5.12 shows a screenshot of the position pick-up system software interface, where all of the individual position pick-ups can be monitored in real-time. For the determination of the actual ion beam position the software records the individual position pick-up signals with a fast ADC, derives the discrete FORUIER transforma-

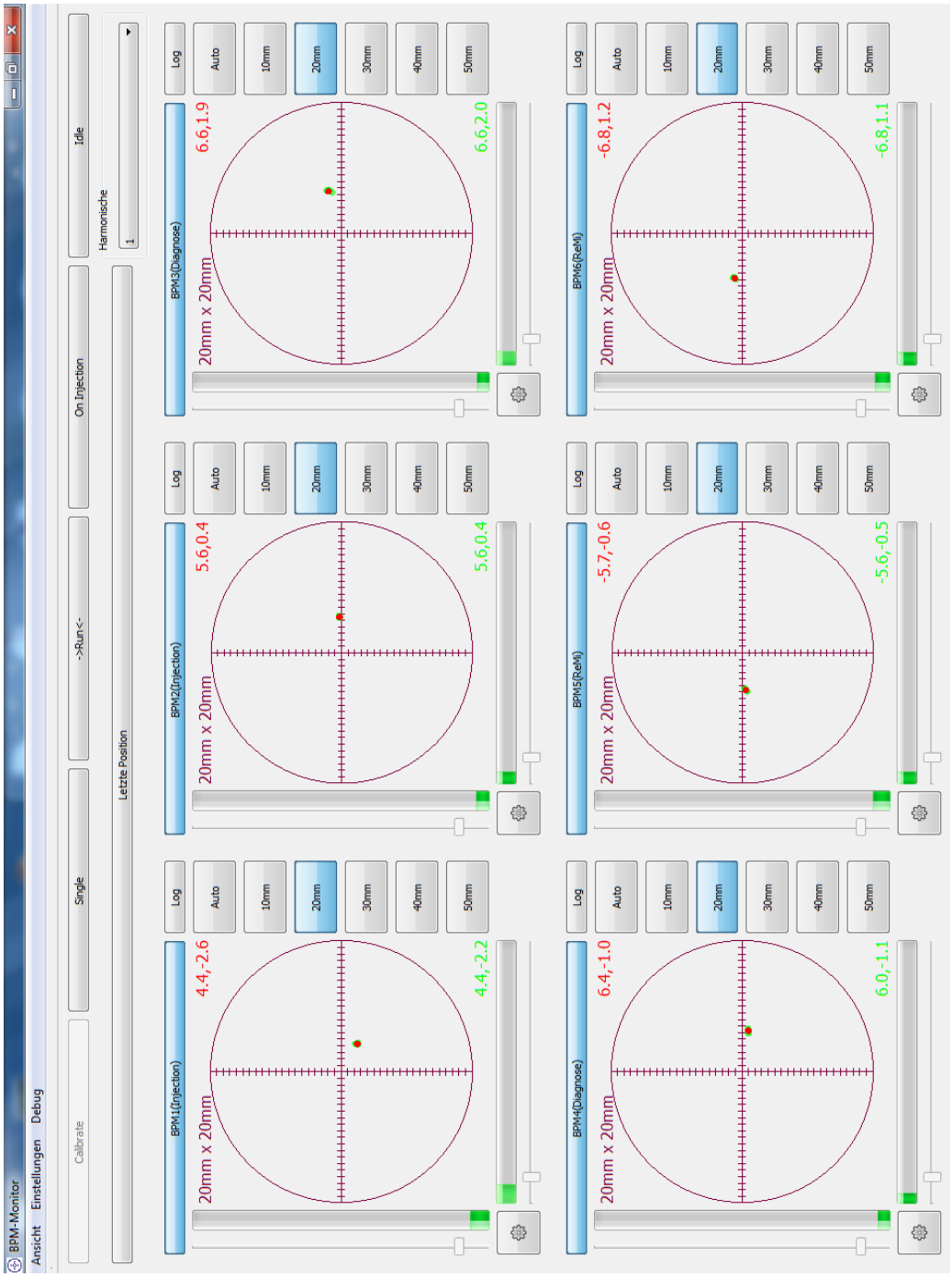

Figure 5.12: Screenshot of the ion beam position pick-up system software.

tion (DFT) and uses the spectral amplitudes at the bunching frequency f_{rf} (but also other harmonics can be chosen) together with the scaling factor (see section 3.4.4) for the position evaluation with equation (3.13).

The software shows each individual position measurement as a green marker (in the shown case 18 per position pick-up) and their average as a red marker. The depicted coordinate system has a scaling of 1 mm per tick. Thus, this measurement demonstrates that the ion beam orbit is stable within an estimated spread of $\sim$ 1 mm. From the dispersion measurements, which will be discussed in section 5.7.3, it can be concluded that the relative position measurement is reliable. However, the error in the absolute position can only be estimated as done in section 3.4.3. Nevertheless, there is a clear indication that the ion beam trajectory in this measurement has been not ideally symmetric, but somewhat horizontally elongated to the outside in section A and C of CSR and to the inside in section D and B, compare figure 2.6. In contrast the ion beam orbit in the vertical direction lies well within the horizontal plane and therefore no vertical steering was necessary. Hence, the position pick-up system showed safe operation and will be applicable for alignment of the stored ion beam in later beamtimes.

5.6 Detection of coasting ion beams via SCHOTTKY noise

In contrast to the active manipulation of the ion beam by rf bunching, as discussed in the previous sections, the ion beam can also be detected and analyzed when it is a coasting beam. For this purpose the SCHOTTKY noise of the coasting ion beam can be used. This detection is particularly important for the adjustment of the future electron cooler, since the cathode potential has to be fine tuned in order to achieve the velocity matching of electrons to the ions and therefore efficient cooling of the ions. Due to statistical density fluctuations of the ion beam, noise signals arise at harmonics of the revolution frequency. In addition to the obvious determination of the revolution frequency the signals also represent the velocity distribution and hereby the momentum spread of the stored ion beam. With the knowledge of the phase slip factor η at the actual working point and use of equation (2.19) the momentum spread of the ion beam can be deduced from the SCHOTTKY signals.

Figure 5.13 shows SCHOTTKY spectra observed with an $^{40}Ar^{+}$ ion beam with 60 keV energy. These were recorded with the SCHOTTKY pick-up connected to a spectrum analyzer (FSV, Rhode & Schwarz) at the 15^{th} harmonic of the revolution frequency and a resolution band width of 10 Hz. Each spectrum is the average of 100 single

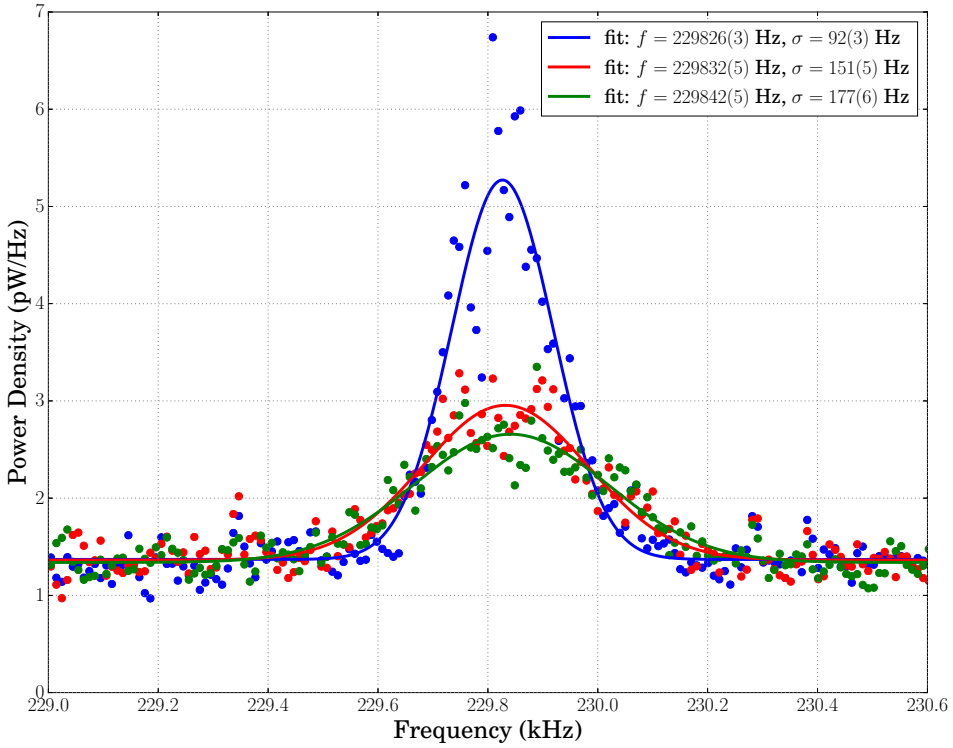

Figure 5.13: The spectral power density at the SCHOTTKY band of an $^{40}Ar^{+}$ ion beam with 60 keV energy as a function of time after injection (blue: 0−20 s, red: 20−40 s and green: 40 − 60 s) measured at the 15$^{\text{th}}$ harmonic of the revolution frequency with a resolution band width of 10 Hz. The spectra are fitted with GAUSSian peak functions (solid lines).

recorded frequency sweeps with a sweep time of 0.2 s. The spectra correspond to measurement intervals of 0 − 20 s (blue markers), 20 − 40 s (red markers) and 40 − 60 s (green markers), respectively. The denoted times are with respect to the ion beam injection. The first spectrum (blue markers) contains also the coherent contribution of the pulsed time structure of the initially injected ion beam. Therefore it is not considered to be a true SCHOTTKY spectrum. The 'debunching' (the loss of any time structure) of the ion beam takes typically some few seconds. Thus, the last two spectra represent real SCHOTTKY spectra.

The spectra are fitted with GAUSSian peak curves (solid lines) of the form

$$P(f) = \frac{A}{\sqrt{2\pi\sigma^2}} \exp\left(-\frac{(f - f_{\text{peak}})^2}{2\sigma^2}\right) \tag{5.18}$$

with the integral area A, the peak center frequency f_{peak} and the standard deviation σ. From the fitted parameters the measured phase slip factor $\eta = 0.674(4)$ at the corresponding working point, which has been experimentally determined as will be discussed in section 5.7.4, and with equation (2.19) the standard deviation of the momentum spread $\Delta p/p_0$ can be calculated. The true SCHOTTKY spectra for the time intervals of $20 - 40\,\mathrm{s}$ and $40 - 60\,\mathrm{s}$ yield standard deviations of $9.8(3) \times 10^{-4}$ and $11.4(4) \times 10^{-4}$, respectively for the momentum spread.

From the noise level of the background in the observed spectra, the input related spectral voltage noise density of the cryogenic amplifier of the SCHOTTKY pick-up can be estimated. The input related spectral voltage noise density is defined by

$$e_n = \frac{U_{\mathrm{in}}}{\sqrt{f_{\mathrm{rbw}}}} = \frac{1}{G}\frac{U_{\mathrm{out}}}{\sqrt{f_{\mathrm{rbw}}}} = \frac{\sqrt{p_{\mathrm{out}}\,50\,\Omega}}{G}, \tag{5.19}$$

where U_{in} and U_{out} are the voltage at the input and output of the amplifier chain, respectively, f_{rbw} is the measurement resolution band width, and G is the total amplification. The voltage amplification of the SCHOTTKY pick-up can be estimated from laboratory measurements[2] to be 8200^{+740}_{-5300} (at a frequency of $\sim 230\,\mathrm{kHz}$), the measured spectral power density of the noise level at $50\,\Omega$ is $p_{\mathrm{output}} = 1.3(1)\,\mathrm{pW/Hz}$ with the resolution band width $f_{\mathrm{rbw}} = 10\,\mathrm{Hz}$. This results in an input related spectral voltage noise density of the SCHOTTKY pick-up ULNA of $e_n = 1.0^{+1.8}_{-0.1}\,\mathrm{nV}/\sqrt{\mathrm{Hz}}$, which is in agreement with the values discussed in section 3.6.1.

The input related noise density of the amplifier also defines the sensitivity limit of the SCHOTTKY pick-up. The SCHOTTKY spectrum is visible, if the averaged SCHOTTKY noise power of N statistical homogenous distributed ions $P(h)$, given by equation 3.38, is greater than the input related noise density of the amplifier e_n times the width of the SCHOTTKY band $\Delta f_{\mathrm{Schottky}}$, which increases linearly with the harmonic number:

$$P(h) = \hat{U}_i^2(h)\,\frac{N}{2} > e_n^2\,\Delta f_{\mathrm{Schottky}} \tag{5.20}$$

Solving this equation for N and using the above deduced value for e_n and the voltage drop of a singly charged ion of $\hat{U}_i(h \lesssim 25) \approx 7\,\mathrm{pV}$, derived in figure 3.14, results in a minimal detectable ion number for the SCHOTTKY pick-up of:

$$N_{\mathrm{min,\ Schottky}} \gtrsim 4.1 \times 10^4\,\Delta f_{\mathrm{Schottky}}[\mathrm{Hz}] \tag{5.21}$$

Thus, the higher the harmonic number the more ions are needed to create a visible SCHOTTKY band, i.e. for optimal sensitivity as small as possible harmonics should

[2]The gain of the amplifiers has been measured individually, since there is no option for direct gain calibration for the SCHOTTKY pick-up foreseen at present. The value given is the multiplication of the individual measurements. The upper error is the uncertainty of these measurements and the lower error assumes a similar gain loss (by roughly a factor of 2.5) as observed for the current pick-up, see section 5.2.

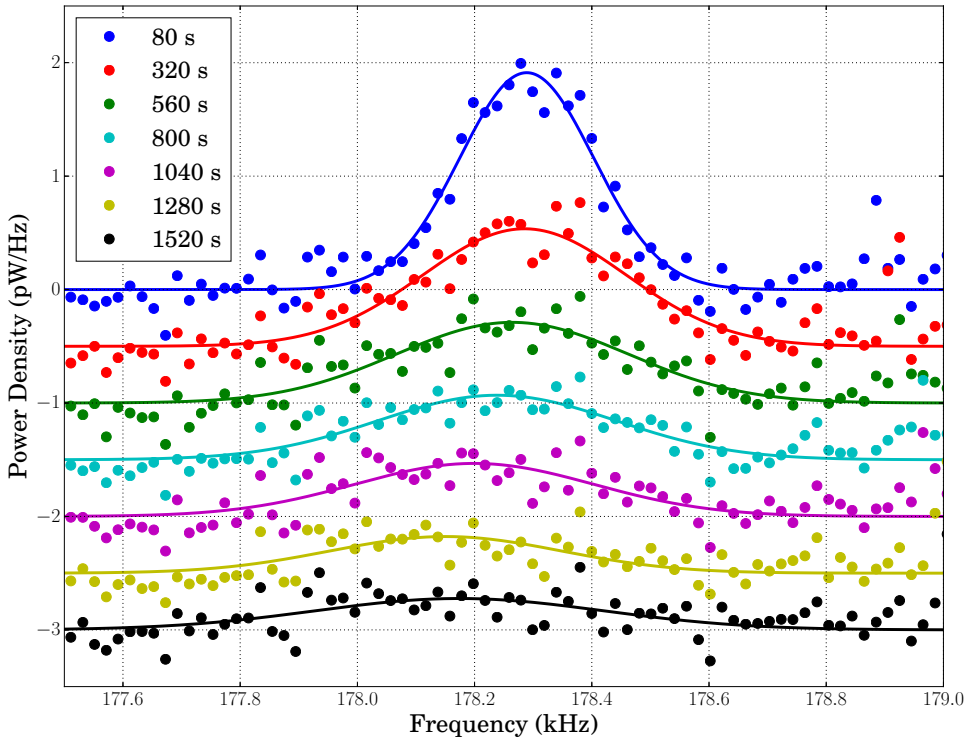

Figure 5.14: Background subtracted spectral power density of the SCHOTTKY band of a Co_2^- ion beam with 60 keV energy as a function of time after injection measured at the 20$^{\text{th}}$ harmonic of the revolution frequency with a resolution band width of 10 Hz. The spectra are shifted by −0.5 pW/Hz each and are fitted with GAUSSian peak functions (solid lines).

be used for the measurement of the SCHOTTKY spectra. Even higher sensitivity can be expected with resonant detection. The beamtimes that were possible so far did not allow the resonant detection system to be operated.

Since the SCHOTTKY power scales linearly with the number of stored ions, the SCHOTTKY spectra can also be used for the determination of the ion beam lifetime. Figure 5.14 shows some SCHOTTKY spectra from a Co_2^- ion beam with a total atomic mass of 118 and with 60 keV energy as a function of time after the ion beam injection. The spectra are recorded with a spectrum analyzer at the 20$^{\text{th}}$ harmonic of the revolution frequency and a resolution band width of 10 Hz. Each depicted spectrum is the average of 600 consecutive frequency sweeps with a sweep time of 0.2 s each. The times given in the legend of the figure denote the average of the respective measurement intervals, which are ±60 s. The spectra are already

background subtracted with a spectrum recorded without any ion beam. They are shifted by $-0.5\,\mathrm{pW/Hz}$ each for better graphical representation and fitted with GAUSSian peak curves according to equation (5.18).

The resulting fitting parameters (A, f_{peak}, σ) of all measured spectra are depicted in figure 5.15 as a function of storage time. The denoted error bars correspond to the standard deviation of the averaging (ordinate) and the time bin size (abscissa), respectively. The peak area (a) is the SCHOTTKY power and scales with the number of ions. A single exponential decay function (red line) is fitted to the data and reveals an ion beam lifetime of $\tau = 1115(33)\,\mathrm{s}$. Here it has to be mentioned that the data of the first 20 s are omitted in the analysis for the reason discussed earlier in this section.

Furthermore, both the peak center frequency corresponding to the revolution frequency (b) and the fitted standard deviation (c) representing the momentum spread of the ion beam are changing with storage time. Both the decrease of the revolution frequency and the increase of the momentum spread might be caused by external noise sources, which couple onto the ion optical deflector and focusing electrodes. The high voltage power supplies have been directly connected to the respective electrodes without any filtering of high frequency noise. Thus, statistically distributed noise on the signal lines could lead to a diffusion of the stored ions, which are thereby lost at the acceptance limits of the storage ring. More detailed studies of this are planned for the next beamtimes of CSR. It is also planned to equip the ion optical deflecting and focusing elements with low pass filters.

The measured ion beam lifetime can be compared to measurements performed with the installed single-particle detectors. Since the residual rest gas pressure in the experimental vacuum of CSR has been extremely low, no signal could be measured that originated from the neutralization of the stored cobalt dimer Co_2^- in a collision with a residual gas molecule X

$$Co_2^- + X \rightarrow Co_2 + X^-. \tag{5.22}$$

In order to create still some measurable neutralization events the merged laser beam setup, which has been installed for the commissioning phase of CSR in the section B (see figure 2.6), has been used to photo-detach the electron of the cobalt dimer

$$Co_2^- + \gamma \rightarrow Co_2 + e^-. \tag{5.23}$$

The electron affinity of the cobalt dimer is $\sim 1.1\,\mathrm{eV}$ [119] with the result that a standard HeNe laser diode ($\sim 1.9\,\mathrm{eV}$) is sufficient for the photodetachment. The neutralized products are detected with the COMPACT detector (label (11) in figure 2.6), which for this purpose has been positioned in the neutral line following the merged laser beam setup.

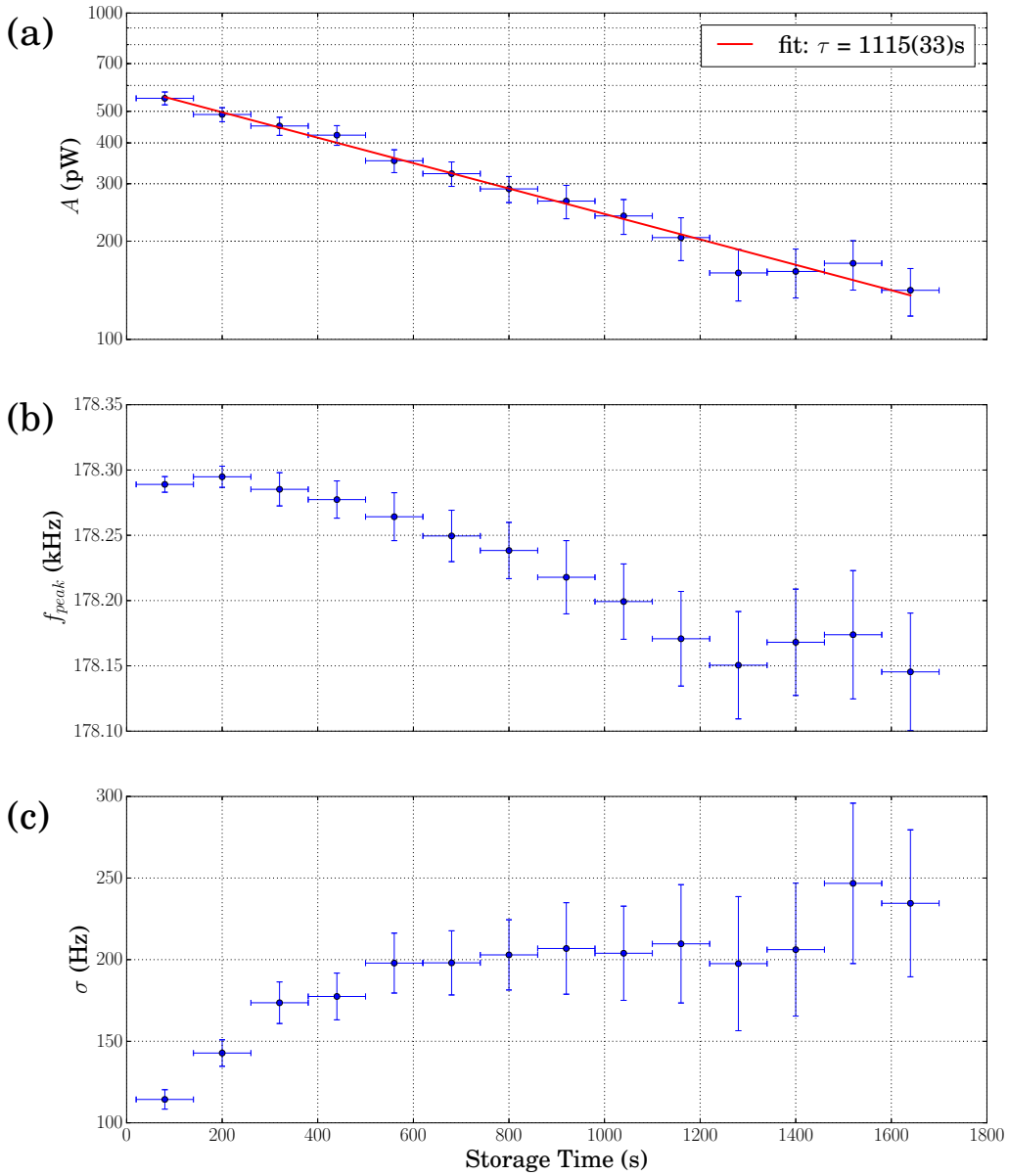

Figure 5.15: Fitting parameters of the SCHOTTKY spectra of a Co_2^- ion beam with 60 keV energy as a function of time after injection. Shown are the (a) integral area A, (b) peak center frequency f_{peak} and (c) standard deviation σ of a GAUSSian peak curve according to equation (5.21).

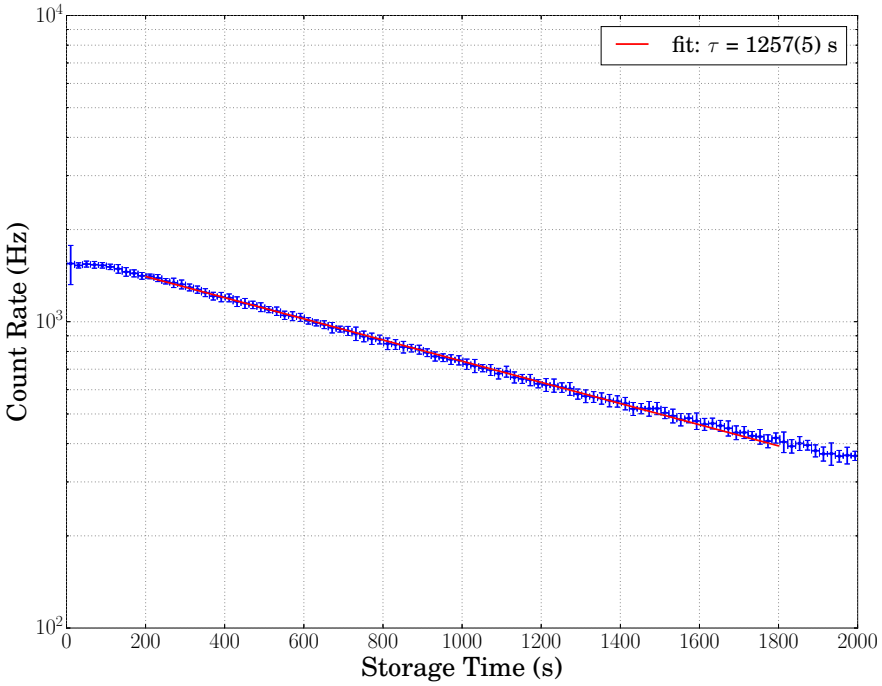

Figure 5.16: Neutralization rate measurement with the COMPACT 3.2 detector of the reaction $Co_2^- + \gamma \rightarrow Co_2 + e^-$.

Simultaneously with the measurement of the SCHOTTKY spectra discussed above the detector measured the count rate of the neutralization of a single ion beam injection.

Figure 5.16 shows the measured count rate as a function of the storage time together with a single exponential decay fit (red line) of the data performed in the same fitting range ($200 - 1800$ s), which is used for the SCHOTTKY lifetime measurement. The fitted lifetime of $\tau = 1257(5)$ s is almost in agreement to the beam lifetime deduced from the SCHOTTKY spectra. The deviation cannot be explained by the denoted statistical errors, but a systematical error of $\sim 10\,\%$ may be a reasonable assumption. The non exponential behaviour in the first 200 s indicates a saturation effect of the COMPACT detector and sets a limit for the maximal count rate at ~ 1 kHz. In the figure the excellent dark count rate of this detector, which is below 1 Hz, is not shown. Correspondingly, a clear neutralization signal of ~ 10 Hz could still be measured after a storage time of 7000 s.

Both lifetime determination methods have their advantages and disadvantages. For the detector measurement the ion beam has to be manipulated by a laser beam

in order to create a measurable signal. The SCHOTTKY pick-up does not need any ion beam manipulation. In addition, the photodetachment method only works for negative ion species and the photodetachment cross sections even may depend on internal excitations falsifying the measured lifetime. Nevertheless, also charged reaction products can be detected, if their charge-to-mass ratio differs from the parent ion beam. The advantage of the detector method is the sensitivity but also the clear data, which do not have to be further processed. Especially the GAUSSian fitting of the SCHOTTKY spectra of small signals becomes problematic. However, as demonstrated in this section, the SCHOTTKY pick-up is a powerful tool for the long-time detection and investigation of stored ion beams.

5.7 Characterization of the machine parameters

As discussed in section 5.1 the working point of a storage ring has to be chosen with care since it defines the ion beam dynamics. For this reason measurements of important machine parameters have been performed at various working points during the commissioning. Especially two of these investigated working points will be characterized in the following. Since the intended working point of CSR is near to the condition of $Q_x \approx Q_y$ (see figure 2.2) and the exact tune determination in this region has been difficult, as will be shown in the following section, we started the characterization of the beam parameters at a different working point close by. This is denoted in the following as the 'first working point'. Finally, with the gained knowledge we then came back to the vicinity of the intended working point denoted in the following as the 'second working point'.

Figure 5.17 shows the working diagram with resonances up to the fourth order (lines). The black marker indicates the first working point. The blue square indicates the experimentally determined region wherein the second working point has been, which will be discussed below. The red marker corresponds to the intended working point of CSR. The hereafter denoted quadrupole strengths are calculated with equation (5.1) from the measured revolution frequency (and from the storage ring circumference, see equation (5.9)) and the applied quadrupole voltages.

5.7.1 The tune

The tune denotes the number of betatron oscillations per revolution and is typically a non-integer number. Because experimentally only the non-integer part of the tune is accessible, it is convenient to split the tune $Q_{x,y}$ in an integer part $m_{x,y}$ and a

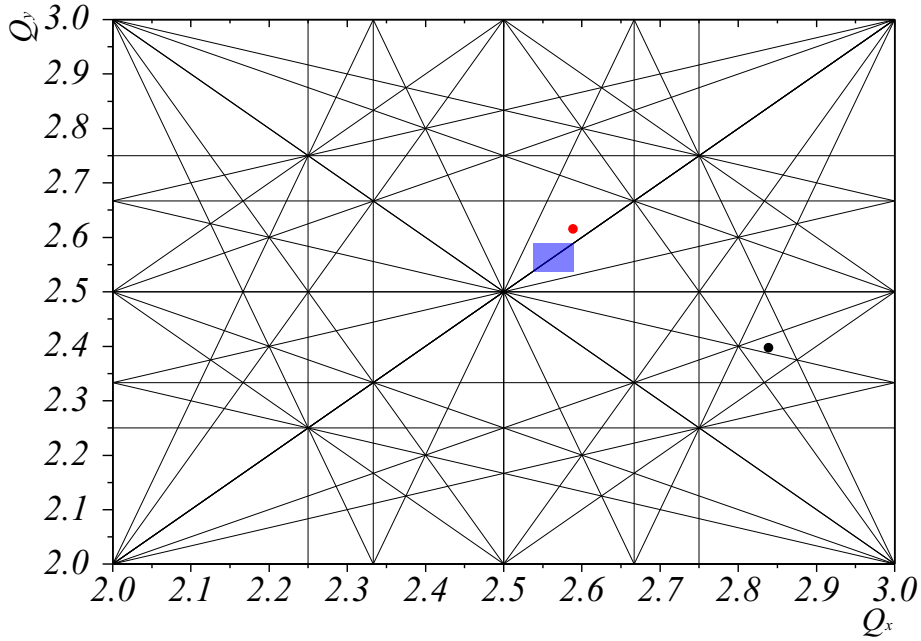

Figure 5.17: Working diagram of CSR. The markers are the first (black) and the for electron cooling intended (red) working point. The blue square indicates the experimentally determined region, where the second working point lies in. Due to the coupling of the transverse betatron oscillations the true value cannot be determined, which will be discussed later in this section.

fractional part $q_{x,y}$

$$Q_{x,y} = m_{x,y} \pm q_{x,y}. \tag{5.24}$$

The latter can be measured by a number of different methods, which have all in common that the betatron oscillations of the ion beam are excited by some method and some response of the beam is measured. The betatron oscillations appear as sidebands around the harmonics of the revolution frequencies f_{rev}, which can be expressed by the following formulas

$$f_x = (m_x \pm q_x)\ f_{\mathrm{rev}}, \tag{5.25}$$

$$f_y = (m_y \pm q_y)\ f_{\mathrm{rev}}. \tag{5.26}$$

Nevertheless, the sign of $q_{x,y}$ cannot be measured at a single working point alone, but must be determined by using the results from various working points in its vicinity by detuning the strength of one of the quadrupole families. By observing the movement of the sidebands in a measurement series the true fractional tune part can be deduced. A stronger focusing meaning higher quadrupole strength leads to an increased tune value and vice versa. The integer part of the tune has to be derived from simulations.

For the first tune measurement method used, the betatron oscillations were excited directly by detuning the injection quadrupole of the transfer beam line, thus, injecting with some angle and offset in x and y. The observation of the response of the ion beam has been measured at the position pick-up 3 located in the diagnostic section (see figure 2.6). The induced signals at one of the electrodes of the horizontal or the vertical pick-up, respectively, were recorded with a spectrum analyzer (FSV, Rhode & Schwarz).

The first working point

Figure 5.18 illustrates two exemplary measurement series using the above described method. The data acquisition was started a few ms after injection and with a sweep time of 0.5 s (corresponding to the $\sim$ 7500 revolutions of the ion beam). Each spectrum is the average of five consecutive injections.

In the upper panel the quadrupole family 1 has been varied starting from the first working point ($K_1 = 5.43(8)\,\mathrm{m}^{-2}$, $K_2 = -6.44(9)\,\mathrm{m}^{-2}$) and the horizontal response is shown. In the lower panel quadrupole family 2 has been varied and the vertical response is shown. The frequency range corresponds to the second and third harmonic of the revolution frequency $f_{\mathrm{rev}} = 15328(5)\,\mathrm{Hz}$ for a $^{40}\mathrm{Ar}^{+}$ beam with 60.0(8) keV energy. The arrows mark the betatron sidebands.

Calculating the fractional tune part from the betatron sideband frequencies using the equations (5.25) and (5.26) and deducing the correct signs from the sideband shift leads to figure 5.19. Here the calculated fractional tune parts q_x (blue) and q_y (red) are plotted as functions of the quadrupole strengths of family 1 (left column) and 2 (right column). Each data point was averaged from the calculated fractional tune values of four betatron sidebands. In most cases the statistical error is smaller than the data point. The linear fits (red lines) through the data are used for determining the betatron function, which will be discussed in following section 5.7.2.

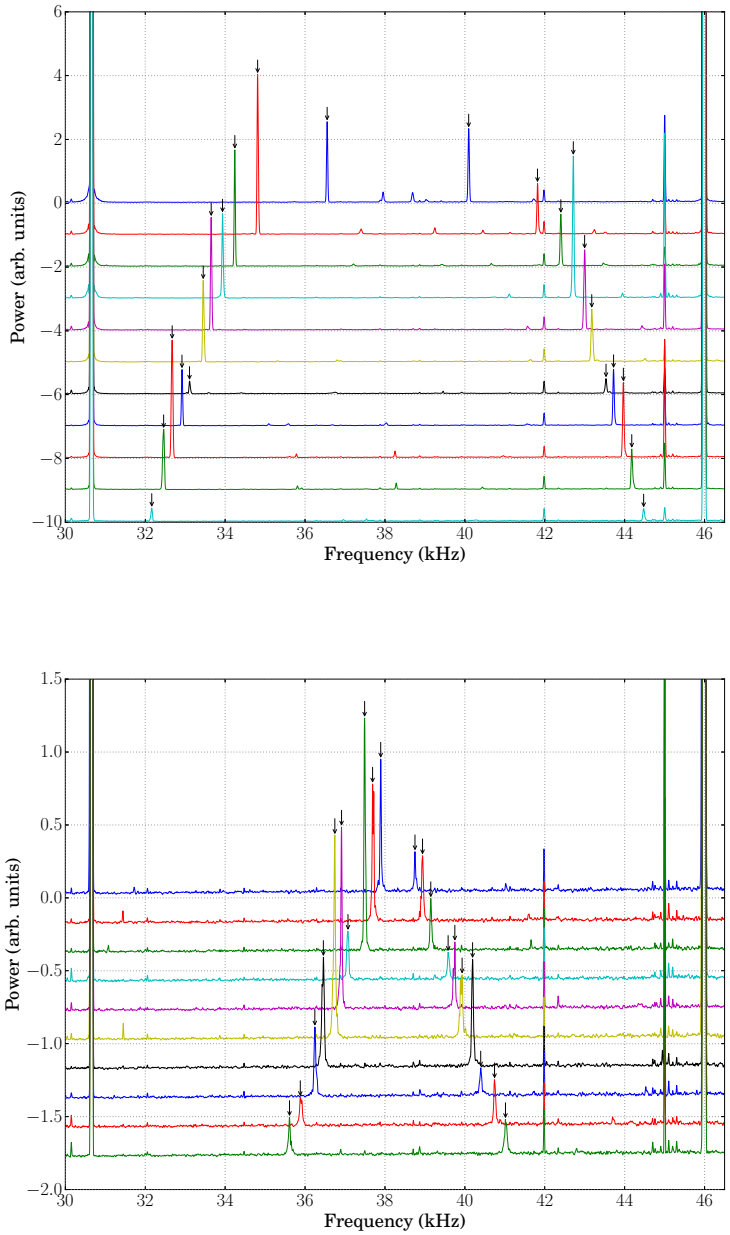

Figure 5.18: Horizontal (upper panel) and vertical (lower panel) tune measurements for $K_2 = -6.44(9)\,\mathrm{m}^{-2}$ and $K_1 = 5.43(8)\,\mathrm{m}^{-2}$, respectively. In the upper panel the quadrupole strengths of family 1 are varied between $K_1 = 5.25(7)$ and $5.48(8)\,\mathrm{m}^{-2}$ (from top to bottom) and in the lower panel the quadrupole strengths of family 2 are varied between $K_2 = -6.53(9)$ and $-6.36(9)\,\mathrm{m}^{-2}$ (from top to bottom). Arrows mark the betatron sidebands. The ion beam is a $^{40}\mathrm{Ar}^{+}$ beam with $60.0(8)\,\mathrm{keV}$ energy. The measurement resolution bandwidth is 20 Hz.

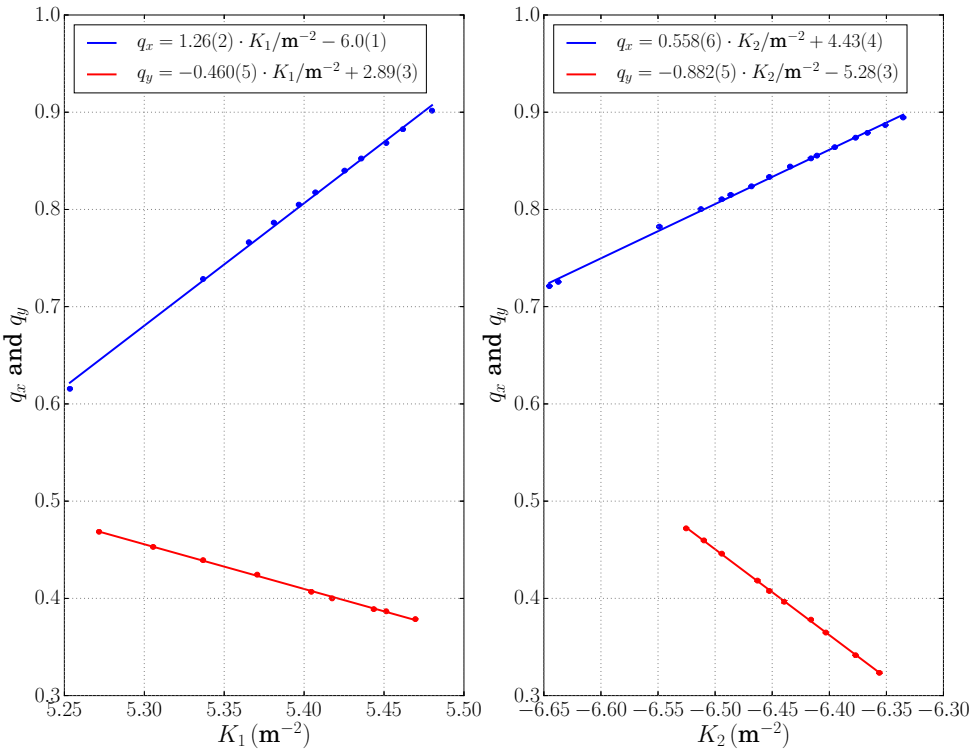

Figure 5.19: Measured fractional tune values q_x (blue) and q_y (red) as functions of the quadrupole strengths of family 1 (left column) with $K_2 = -6.44(9)\,\mathrm{m}^{-2}$ and 2 (right column) with $K_1 = 5.43(8)\,\mathrm{m}^{-2}$ at the first working point.

Determination of the effective quadrupole length

The derived tune at the first working point is $q_x = 0.840(1)$ and $q_y = 0.397(1)$. From MAD8 simulations it is known that the integer tune parts are $m_x = m_y = 2$. By additional simulations with MAD8 (setting the simulated effective quadrupole length equal to the geometrical length of 0.2 m) the corresponding quadrupole strengths K^{MAD} to the tune values of $Q_x = 2.840(1)$ and $Q_y = 2.397(1)$ have been found to be $K_1^{\mathrm{MAD}} = 5.6236(19)\,\mathrm{m}^{-2}$ and $K_2^{\mathrm{MAD}} = -6.7229(23)\,\mathrm{m}^{-2}$.

Since in linear approximation[3] the product of quadrupole strength and effective length defines the focusing properties of the quadrupole, see [30, eq. 5.52], an

[3]This is justified for reasonable short effective lengths and quadrupole strengths, and if the geometrical and effective lengths are comparable to each other.

experimental effective length can be defined by

$$L_{\text{eff}}^{\text{exp}} = L_0 \frac{K^{\text{MAD}}}{K}. \tag{5.27}$$

Using this approximation and equation (5.1) together with the set value voltages of the first working point $U_1 = 813.80(31)\,\text{V}$ and $U_2 = -965.92(31)\,\text{V}$, the aperture radius $R_0 = 50.0(1)\,\text{mm}$, the measured ion beam energy $E_0 = 60.0(8)\,\text{keV}$ with charge state $z = 1$ yields for the experimentally determined effective quadrupole lengths

$$L_{\text{eff, QP1}}^{\text{exp}} = 0.2073(38)\,\text{m}, \tag{5.28}$$

$$L_{\text{eff, QP2}}^{\text{exp}} = 0.2088(38)\,\text{m}. \tag{5.29}$$

These values are almost equal to each other and the small difference could be explained by field deviations, by misalignment or by imperfection compared to the assumed ideal fields of the electrostatic elements. A finite element analysis with the software package Opera-3D [34] yields a value of $L_{\text{eff}}^{\text{sim}} = 0.212\,\text{m}$ [35] for the effective length of the quadrupoles. This value also corresponds well to the values found here experimentally.

The second working point

As already discussed in the section 5.1 for successful electron cooling a working point far away from strong resonances is necessary. As can be seen from figure 5.17 the first working point (black marker) does not satisfy this criterion, but the intended working point (red marker) does. With the knowledge of the determined tune dependency on the quadrupole strengths at the first working point, see figure 5.19, the 'second' working point could be estimated aiming to the intended working point. However, as the below discussed measurement will demonstrate, the intended working point has not been hit exactly, but a working point in its close vicinity indicated as a blue area. At this second working point the tunes have again been measured as functions of the quadrupole strengths in order to deduce also the betatron function. The tune has been measured with the so-called *rf knock-out* method.

Here the excitation of the betatron oscillations is done by applying a rf signal on horizontal and vertical steering electrodes within the storage ring, respectively. By sweeping the frequency f_{exc} of this rf signal the betatron sidebands can be found. For horizontal excitation the inner electrodes of a 6° deflector and for vertical excitation the bottom electrode of one of the vertical steering electrodes (situated within the quadrupoles) has been used (see figure 2.6). The rf signal has been applied only for some ms (typically $50 - 200\,\text{ms}$) by using a gate/delay generator. The response

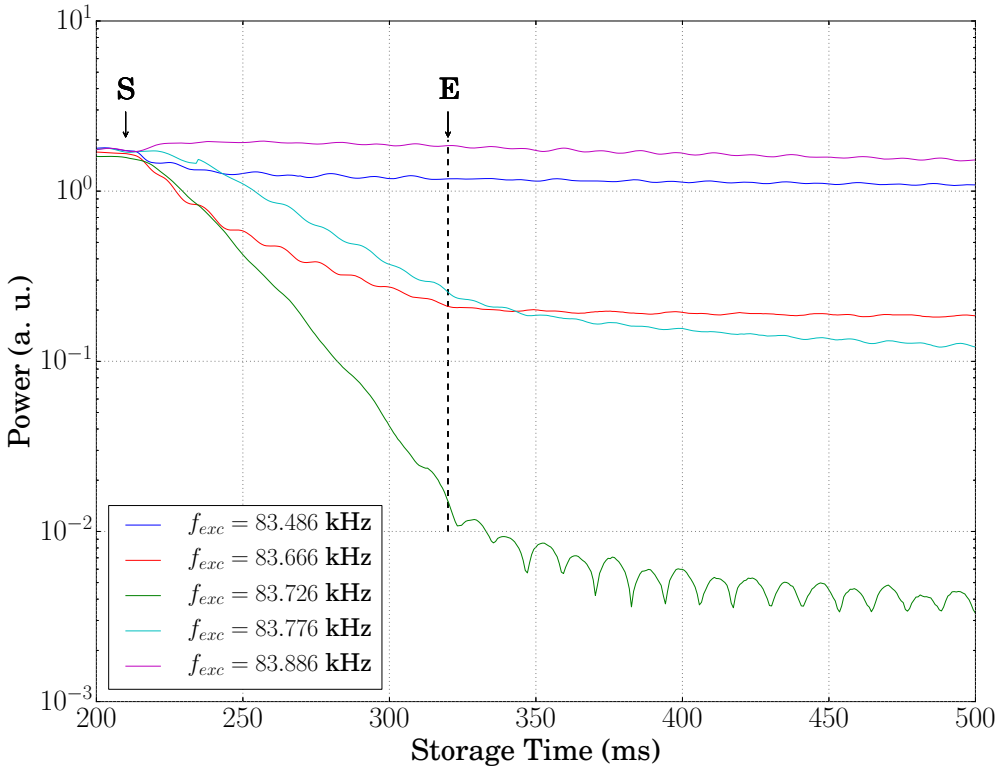

Figure 5.20: Bunched beam signals during rf knock-out measurements. 'S' and 'E' mark the start and end time of the excitation, respectively. The green line corresponds to the strongest particle loss.

of the beam is observed by using the SCHOTTKY pick-up, which is connected for this purpose to a spectrum analyzer set to a fixed frequency. In addition, the beam was bunched using the rf system with a second rf signal at $f_\mathrm{b} = 153.246\,\mathrm{kHz}$ corresponding to the 10^{th} harmonic. The spectrum analyzer is set to the same frequency as the rf bunching frequency f_b at a resolution bandwidth of 1 kHz. This way the SCHOTTKY pick-up signal measures the intensity of the stored bunched beam.

A typical rf knock-out measurement is shown in figure 5.20. When hitting the frequency of the betatron oscillation the decrease of the observed signal is strongest (green line), corresponding to maximal beam loss due to the excitation f_exc. 'S' and 'E' mark the start and end time of the excitation, respectively.

In figure 5.21 the fractional tune values determined from the respective frequencies $(f_\mathrm{exc})_\mathrm{max}$ for maximal beam loss are plotted versus the variation of the quadrupole

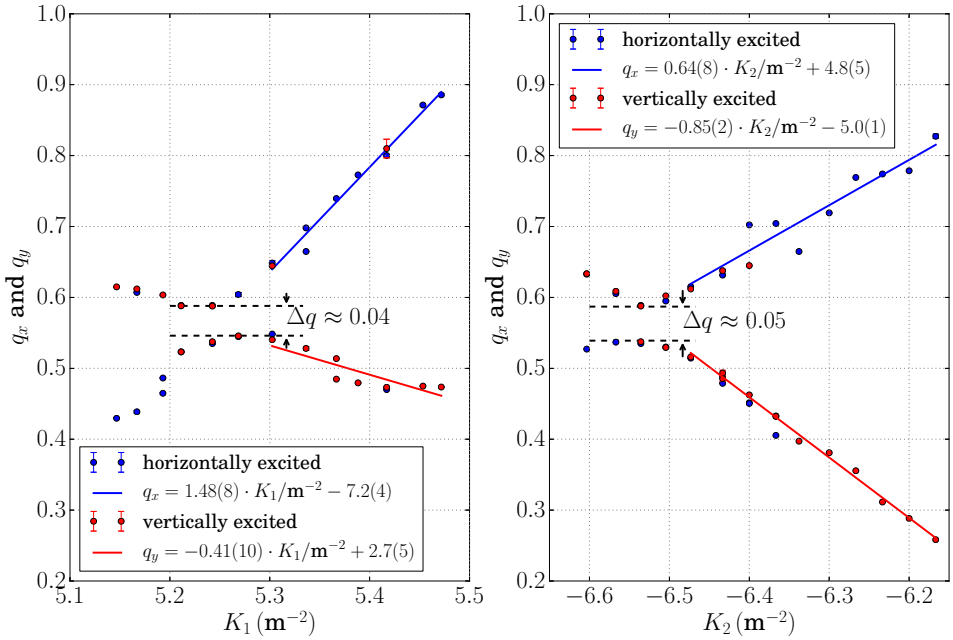

Figure 5.21: Measured fractional tune values q_x and q_y as functions of the quadrupole strengths of family 1 and 2 at the second working point. In the left plot is $K_2 = -6.54(9)\,\mathrm{m}^{-2}$ and in the right plot $K_1 = 5.24(7)\,\mathrm{m}^{-2}$.

strengths of family 1 and 2, respectively. Each data point averages the observations of two different betatron sidebands and the given statistical error is in most cases smaller than the data point. The blue data points are those of horizontal excitation (6° deflector), whereas the red data points are those of vertical excitation.

As indicated by the dashed lines a splitting $\Delta q \approx 0.045(5)$ of the tune values occurs near the second working point ($K_1 = 5.24(7)\,\mathrm{m}^{-2}$, $K_2 = -6.54(9)\,\mathrm{m}^{-2}$). For this reason the region can be only constrained in which the working point lies, indicated in figure 5.17 as a blue area. In fact, the intended working point (red marker) has not been hit exactly, but only minor adjustments will be necessary in the future to do so.

The reason for this splitting is a coupling between the horizontal and vertical betatron oscillations. This is surprising because there is no optical element causing that. For example a longitudinally oriented magnetic solenoid would cause such a coupling, as it will be the case for the implemented electron cooler. A simulation with the particle tracking software G4beamline [37] taking also the earth magnetic field into account could not explain this splitting [39]. However, a possible explanation could be one or more rotated quadrupoles (around their longitudinal axes),

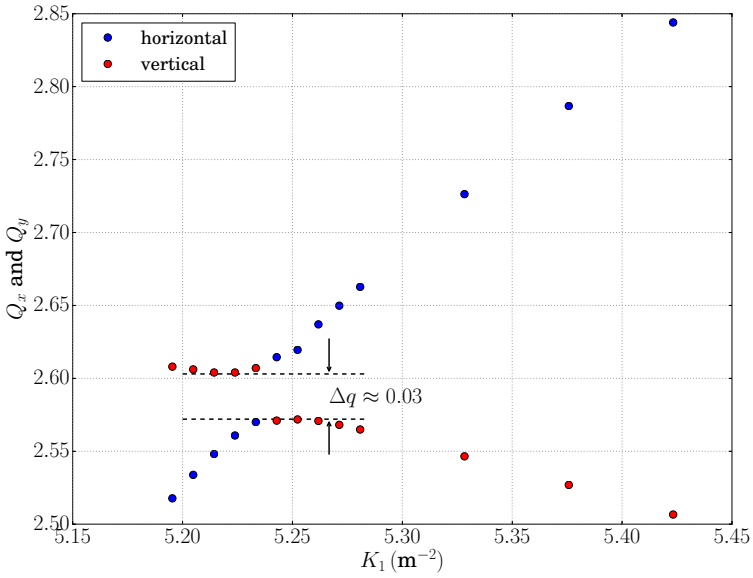

Figure 5.22: MAD8 simulation of the tune values Q_x and Q_y as a function of the quadrupole strength of family 1. In the simulation one of the quadrupole is rotated by 1° around the s-axis.

which would cause a coupling of the transverse coordinates. Results for the tune values from a MAD8 simulation where a single quadrupole dublet is rotated by 1° around the s-axis are shown in figure 5.22. The observed splitting is $\Delta q \approx 0.03$. An additional simulation with a single rotation of 0.5° gives a splitting of $\Delta q \approx 0.02$. For larger rotation angles the simulation showed no stable orbits. However, the simulated value for 1° rotation almost agrees with the measured splitting.

Most likely in reality there is a more complicated situation, where all of the quadrupoles could be rotated by some angle, which could add up to a larger splitting than simulated for a single rotated quadrupole. During the alignment of the optical elements at room temperature conditions solely the longitudinal angle and their height could be assured with telescopes and targets [82]. The rotation could not be guaranteed by this method. Another effect which has to be considered is the possible asymmetric shrinkage of the quadrupole support structure during the cryogenic cooldown.

The future electron cooler will complicate the situation even further. MAD8 simulations [39] with a 1 m long solenoid with a magnetic induction of 125 G (but without any rotated quadrupoles) reveal a splitting which is for a 300 keV proton beam $\Delta q \approx 0.03$. For a 300 keV HD^+ beam it is $\Delta q \approx 0.02$. Ion species with higher masses have a higher rigidity and are consequently less affected. Thus, the main

influence for most ion beams will be caused by the rotated quadrupoles.

5.7.2 The betatron function

The betatron function $\beta(s)$ is the central function for the description of the beam dynamics in a storage ring. It is linked to a variety of beam parameters as partly discussed in section 2.1.1. Therefore its knowledge is crucial for understanding and controlling a storage ring. The measurement series of the previous section gives the possibility of determining the betatron function, albeit not as a function of s, but at least at the position of the quadrupoles.

The following formula [30, eq. 7.19] describes the tune shift ΔQ depending on a change ΔK of the quadrupole strength distributed over the storage ring (gradient errors)

$$\Delta Q = \frac{1}{4\pi} \int_0^{C_0} \beta(s)\, \Delta K(s)\, \mathrm{d}s. \tag{5.30}$$

We assume that we change the focusing strengths of all quadrupoles in a family. The integration over the circumference C_0 of the storage ring then yields for the 8 quadrupole singlets per family

$$\Delta Q = \frac{8}{4\pi} \langle\beta\rangle\ L_{\mathrm{eff}}\, \Delta K, \tag{5.31}$$

where $\langle\beta\rangle$ is the average betatron function over the various quadrupole positions. Solving for the average betatron function yields

$$\langle\beta\rangle = \frac{\pi}{2} \frac{1}{L_{\mathrm{eff}}} \frac{\Delta Q}{\Delta K}. \tag{5.32}$$

For the effective lengths the experimentally determined values are used (see equations (5.28) and (5.29)) and the last quotient $\Delta Q/\Delta K$ corresponds to the slopes of the linear fits to the experimental data shown in the figures 5.19 and 5.21.

Thus, the averaged betatron functions for the first working point are

$$\begin{aligned}
\langle\beta_{x,\mathrm{QP1}}\rangle &= 9.55(23)\,\mathrm{m} \\
\langle\beta_{x,\mathrm{QP2}}\rangle &= 4.20(9)\,\mathrm{m} \\
\langle\beta_{y,\mathrm{QP1}}\rangle &= 3.49(7)\,\mathrm{m} \\
\langle\beta_{y,\mathrm{QP2}}\rangle &= 6.64(13)\,\mathrm{m}
\end{aligned}$$

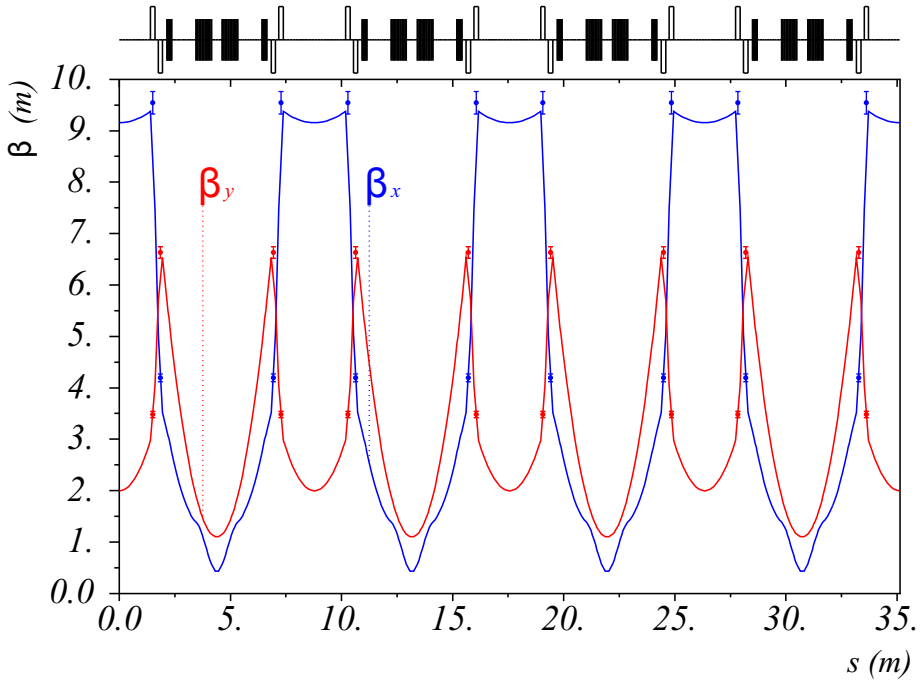

Figure 5.23: Comparison of the experimentally determined betatron functions (markers) with MAD8 simulations (lines) at the first working point.

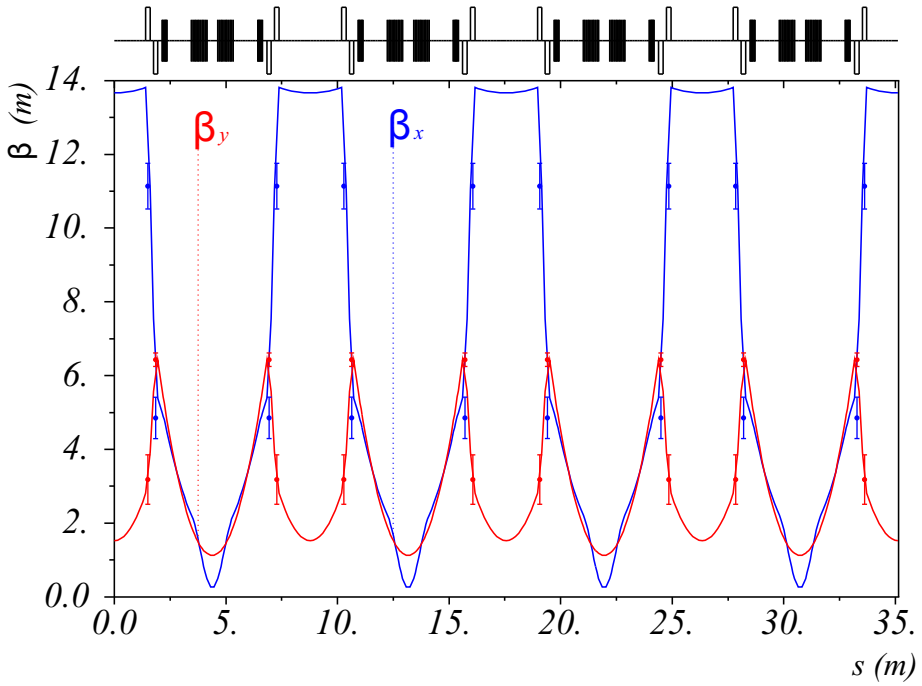

Figure 5.24: Comparison of the experimentally determined betatron functions (markers) with MAD8 simulations (lines) at the second working point.

and for the second working point are

$$\begin{aligned}\langle\beta_{x,\mathrm{QP1}}\rangle &= 11.21(64)\,\mathrm{m}\\ \langle\beta_{x,\mathrm{QP2}}\rangle &= 4.81(61)\,\mathrm{m}\\ \langle\beta_{y,\mathrm{QP1}}\rangle &= 3.11(76)\,\mathrm{m}\\ \langle\beta_{y,\mathrm{QP2}}\rangle &= 6.39(19)\,\mathrm{m}\end{aligned}$$

In figure 5.23 and 5.24 the determined averaged betatron functions are shown together with the corresponding MAD8 simulations of the betatron functions $\beta_{x,y}(s)$. The blue and red lines are the simulated horizontal and vertical betatron functions, respectively. Except for some measurements the experimental data (markers) are in reasonable agreement with the computed values. It should be taken into account that the measurement gives only averaged betatron functions.

5.7.3 The dispersion

The dispersion (see equation 2.16) is particularly important for electron cooling since it defines the ion beam movement during the cooling process, when the momentum deviation $\Delta p/p_0$ of the ion beam is changed. In order to ensure the overlap of ion and electron beam over a wide range of momentum deviations the dispersion should be as small as possible in the interaction region. For this reason it has been measured at the second working point as will be discussed below.

Equation 2.16 with the relation $\Delta E/E_0 = 2\,\Delta p/p_0$ leads to

$$x_D(s) = \frac{D(s)}{2}\,\frac{\Delta E}{E_0}. \tag{5.33}$$

The closed orbit can be shifted by changing the electrical potentials, but this has the inverse effect as compared to changing the energy of the ion beam (see appendix A.3)

$$\frac{\Delta U}{U_0} = -\frac{\Delta E}{E_0}. \tag{5.34}$$

From this equation (5.33) yields

$$x_D(s) = -\frac{D(s)}{2}\,\frac{\Delta U}{U_0}. \tag{5.35}$$

Thus, by scaling the electrical potentials of all electrostatic ion beam optics of the storage ring and by measuring the position of the stored ion beam, it is possible to determine the dispersion function at the location of the position measurement.

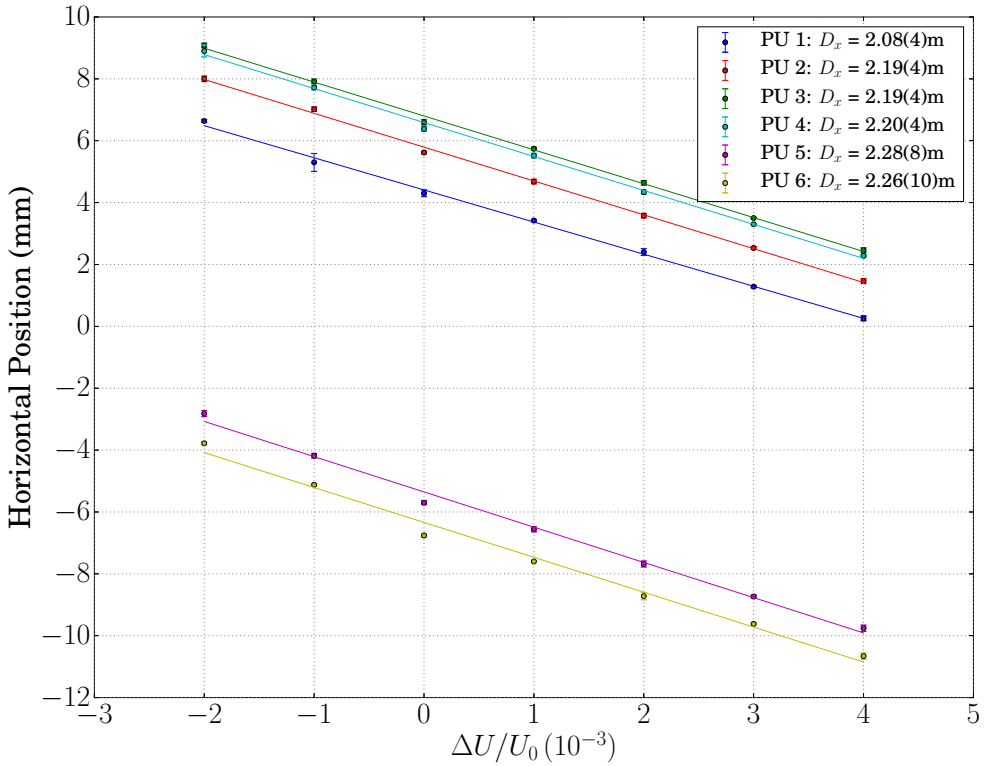

Figure 5.25: Measured horizontal ion beam position as a function of the variation of all CSR bending and focusing electrical potentials $\Delta U/U_0$.

The position of the stored ion beam can be measured by using the ion beam position pick-up system, which has been discussed in detail in section 5.5. For this measurement the ion beam was bunched with the rf system using a rf frequency of $f_{\mathrm{rf}} = 229.268\,\mathrm{kHz}$, which corresponds to the 15^{th} harmonic of a $^{40}\mathrm{Ar}^{+}$ beam with 60 keV energy.

In figure 5.25 the measured beam positions are shown as functions of the relative electrical potential changes. Each data point corresponds to the average of the beam position of five consecutive injections. The denoted error is the standard deviation between these five injections. For each injection the position of the ion beam has been measured each 0.5 s for 9 s and these results were averaged as well. The measured ion beam positions had an estimated variation of less than $< 1\,\mathrm{mm}$.

As already discussed in section 5.5, the ion beam trajectory at this working point had an elongated shape. This is also visible in the different absolute position in figure 5.25. In principle the shape of the ion beam orbit can be corrected by detuning the

deflection fields of the storage ring, but this has not been done for this measurement.

From the slopes of the linear fits through the data the dispersion at each position pick-up can be calculated using equation (5.35) as shown in the legend. Due to the symmetry of the storage ring the dispersion should be identical at each position pick-up. Nevertheless there are small deviations, which could indicate a misalignment or field errors of the ion optics. The average value of the dispersion is $\bar{D}_x = 2.20(7)\,\mathrm{m}$. A MAD8 simulation gives for the dispersion $D_x^{\mathrm{MAD}} = 2.05\,\mathrm{m}$ and a G4beamline tracking simulation $D_x^{\mathrm{G4}} = 2.14\,\mathrm{m}$, which are in good agreement with the experimentally determined average.

5.7.4 The phase slip and momentum compaction factors

For determining the momentum spread of an ion beam from the measurable revolution frequency distribution the knowledge of the phase slip factor is necessary.

As derived in section 2.1.1 for an electrostatic storage ring the phase slip factor η and the compaction factor α_{p} are linked with each other, see equation (2.27), via

$$\eta = 1 - 2\alpha_{\mathrm{p}}. \tag{5.36}$$

The momentum compaction factor can be measured experimentally, as derived in appendix A.4, by scaling all electrical potentials of the ion beam optics and measuring the change in the revolution frequencies:

$$\frac{\Delta f}{f_0} = \alpha_{\mathrm{p}} \frac{\Delta U}{U_0} \tag{5.37}$$

This method has been used to measure the momentum compaction at the second working point. Figure 5.26 shows the measured revolution frequency as a function of the variation of the electrical potentials. The revolution frequencies correspond to the 10^{th} harmonic of a $^{40}Ar^{+}$ beam with 60 keV energy. The revolution frequencies were measured with the SCHOTTKY pick-up connected to a spectrum analyzer (FSV, Rhode & Schwarz) triggered a few ms after injection and with a sweep time of 0.5 s (corresponding to the first ~ 7500 revolutions of the ion beam). The denoted errors in determining the center of the revolution frequency distribution are estimated as $\pm 10\,\mathrm{Hz}$.

A linear fit through the data is shown as a red straight line. From its slope the momentum compaction can be extracted using equation (5.37). With the relation to η and α_{p} from equation (5.36) the values at the second working point can be

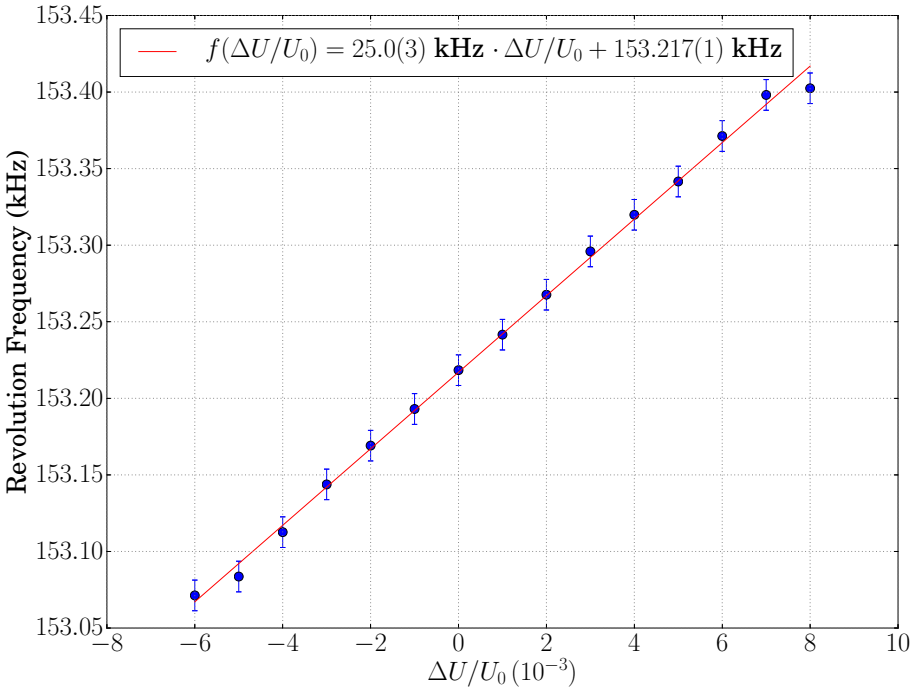

Figure 5.26: Measured revolution frequency at 10^{th} harmonic as a function of the variation of all CSR bending and focusing electrical potentials $\Delta U/U_0$.

given:

$$\alpha_p = 0.163(2) \tag{5.38}$$

$$\eta = 0.674(4) \tag{5.39}$$

A MAD8 simulation at this working point gives $\eta^{\text{MAD}} = 0.679$, which is in good agreement with the experimentally determined value.

Characterization of different working points

In order to investigate the ion beam storage at all islands of stability, which are predicted by the MAD simulations summarized in figure 5.1, different working points were studied. At each of these islands storage could be demonstrated in several cases or at least in a single case. Since simulations predicted an unusual dependency of the phase slip factor η on the horizontal tune Q_x, both have been measured at various working points, combining the method discussed above for η and the methods discussed in section 5.7.1 for Q_x.

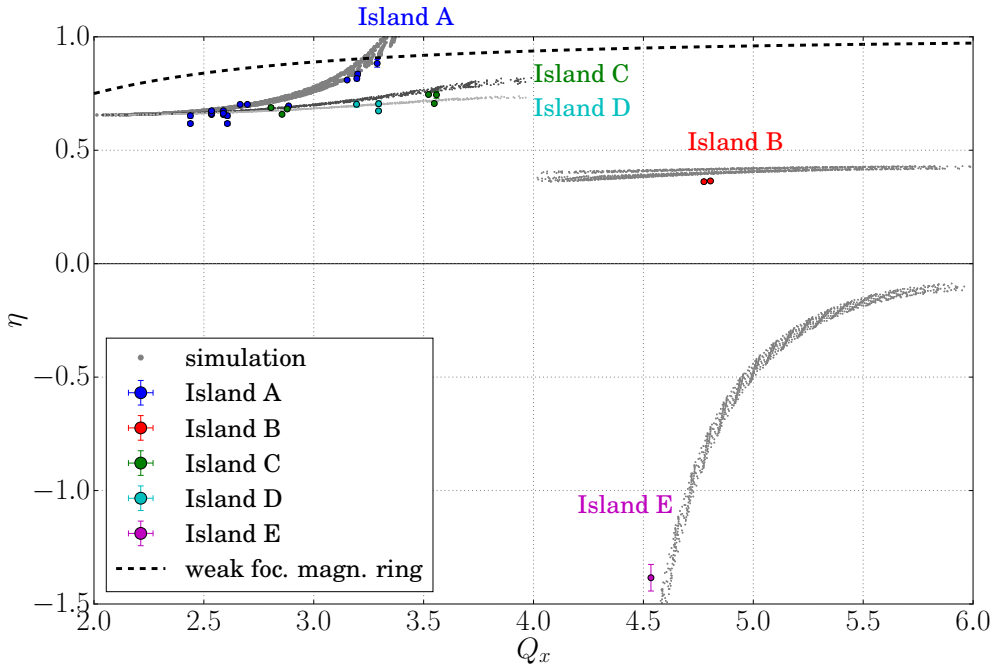

Figure 5.27: The measured (markers with error bars) and simulated (gray markers) phase slip factors as a function of the measured and simulated horizontal tune Q_x, respectively. The black dashed line corresponds to the case of a weak focusing magnetic storage ring, where $\eta_{\mathrm{magn}} = 1 - Q_x^{-2}$.

Figure 5.27 shows the phase slip factor η as a function of the horizontal tune. Simulations (gray markers) predict a functional relation $\eta = f(Q_x)$ which is different for the different islands of stability (also compare figure 5.1). The coloured markers correspond to independent measurements of η and the tune at various working points within different islands of stability. The denoted statistical errors in η are propagated from the fitting errors, whereas the errors in Q_x are too small to be visible.

Although there are a few deviations between the experimental data and the simulations, the overall agreement is good and the functional relation $\eta = f(Q_x)$ predicted from the simulations is experimentally verified. However, the fundamental reason for the variation of η and Q_x is not yet identified and it is unclear at this point if this is an unique property of CSR or of electrostatic storage rings in general.

As a comparison a black dashed line illustrates the case of a magnetic constant gradient synchrotron with weak focusing, such as a betatron [29]. For this it can be shown that the functional dependency is $\eta_{\mathrm{magn}} = 1 - Q_x^{-2}$ [30, eq. 6.76]. Also for a magnetic alternating gradient (AG) synchrotron with strong focusing the same is

almost true, i.e. $\eta_{\mathrm{AG}} \approx 1 - Q_x^{-2}$ [30, eq. 6.77]. For example for the TSR at MPIK the phase slip factor was practically $\eta_{\mathrm{TSR}} = 1 - Q_x^{-2}$ [120].

5.8 Summary of the CSR commissioning

The commissioning of CSR has been successful. The first steps in the characterization of this new facility have been done and various properties have been studied.

The current pick-up has been characterized and calibrated in operation and is ready for upcoming experiments where the initial ion beam intensity has to be known. Inconsistency of the gain measurements cannot be explained at this point and therefore must be further studied in the future. For this reason the determined ion number is afflicted with a relatively large systematic uncertainty. The sensitivity of the current pick-up can be increased by rf bunching and lies in the range of 10^4 detectable particles of single elementary charge. A possible further enhancement by resonant detection has been implemented, but not yet tested in practical operation. Also, the functionality of the ion beam position pick-up system has been demonstrated, with which the ion beam orbit can be monitored in real time and manipulation of the ion beam trajectory via the optical steering elements becomes possible. This meets the requirements of the upcoming experiments with merged neutral or laser beams.

The most powerful tool of the diagnostic system is the SCHOTTKY pick-up, which will be indispensable for the electron cooler, since it allows the detection of stored coasting ion beams and can measure important parameters of those. It will also be the tool for proving a successful phase space cooling once the electron cooler is in operation. The analysis of the SCHOTTKY spectra allows the measurement of the momentum spread of the ion beam, but can also be used for the determination of the ion beam lifetime. This provides a tool complementary to the ion beam lifetime determination via the single-particle detectors, which need a physical reaction of the ion beam with some target. The target can either be a laser beam, as was the case in the commissioning experiments, or a neutral or electron beam as will be possible in the near future.

Most important and fundamental is the study of possible working points of the new machine as represented in the stability diagram of figure 5.1. At each island of stability ion beam storage could be demonstrated and both the tune and phase slip factor have been measured at various working points (summarized in figure 5.27). As a result the predicted functional relation $\eta(Q_x)$, which results from simulations and is different for the different islands of stability, has been experimentally verified. This behaviour of the phase slip factor is in clear contrast to magnetic storage rings, where $\eta_{\mathrm{magn}} \cong 1 - Q_x^{-2}$.

For the upcoming electron cooler the working point of the storage ring has to be chosen with care. It should provide sufficient distance from storage ring resonances and lead to small betatron amplitudes as well as a small dispersion. Also, in that

direction first steps have been done, which will be continued once the electron cooler is installed. The search for a suitable working point was hampered by a coupling between the transverse coordinates. The coupling is attributed to a possible misalignment or a small tilting caused by the thermal shrinkage of the quadrupole modules of the storage ring. A similar effect is expected for the coupling caused by the solenoidal interaction coil of the future electron cooler. Both the betatron function and dispersion have been measured experimentally and compared to simulations at a working point in the vicinity of that considered suitable for electron cooling. In future only minor adjustments will be necessary in order to further optimize the working point.

With the storage ring properly adjusted by means of the diagnostic system, photodetachment experiments on a variety of ion species have been performed during the CSR commissioning phase, which are not in the scope of this work. The most outstanding of these experiments are the thermometry experiments on OH^- and CH^+ which are presently being analyzed and will be published soon. A preliminary result is that after minutes of storage in CSR at least $\sim 95\,\%$ [121] of the ions in an OH^- beam and (after somewhat shorter times of storage) at least $\sim 63\,\%$ [122] of ions in a CH^+ beam reached their rovibrational ground state. This demonstrates the powerful capabilities of this cryogenic electrostatic storage ring and will enables a variety of possibilities for atomic and molecular physical studies.

Chapter 6

Conclusion and outlook

In this work the non-destructive ion beam diagnostic system of the electrostatic cryogenic storage ring (CSR) has been developed and realized. Together with the CSR it has been taken into operation successfully. The diagnostic system was and will be indispensable for the operation of the storage ring and for upcoming experiments. The second part of this work concerned the development of the final design of the electron cooler setup for CSR, which will increase the ion beam performance for other experiments, and will allow studies on electron-ion collisions under cryogenic conditions.

The realized diagnostic system is based on capacitive pick-up electrodes and their respective amplification systems. The diagnostic system – consisting of a current-sensitive pickup for bunched beams, a distributed beam-position pickup system, and a Schottky noise electronics for coasting beams – was used successfully in the first cryogenic operation of the CSR storage ring. A practical solution has been found regarding the amplification chain which meets the requirement of low heat conductivity towards the cold part of the vacuum cryostat. The system consists of cryogenic pre-amplifiers and room temperature main amplifiers, and uses cryogenic electrical relays for the signal connections between the pre-amplifiers and the pick-up electrodes.

The beam diagnostic system operated correctly at an ambient temperature of the system of 6 K. Not only did it deliver important beam parameters in the commissioning beamtime like, e.g., beam current, position and momentum spread, it will also be an essential tool in upcoming CSR experimental runs. During the commissioning beamtime of CSR different storage ring working points and their machine parameters have been investigated, in particular with respect to their suitability for the future electron cooler operation. Two working points have been characterized

in detail by measuring their respective betatron oscillations (tune), betatron and dispersion functions, as well as the phase slip factors. Also other working points were explored and successful beam storage has been demonstrated. A interesting peculiarity of the phase slip factor has been experimentally verified, which former simulations predicted. In contrast to magnetic storage rings the phase slip factor of CSR does not follow the approximate dependency on the horizontal tune ($\eta \cong 1 - Q_x^{-2}$) known from magnetic storage rings. It has different functional dependencies which vary for the different islands of stability. During these studies also a slight coupling of both transverse betatron oscillations has been identified, which is attributed to a small rotation of quadrupoles within the mechanical alignment that could be performed. At least for light ion species, a similar effect is expected as soon as the electron cooler is implemented due to its solenoidal coil in the electron and ion beam interaction region. However, in future only small adjustments of the quadrupole strengths will be necessary to optimize the characterized working point for the electron cooler operation.

The electron cooler will be the first significant hardware upgrade of the CSR storage ring, enhancing the brilliance of stored ion beams beyond that of any other cryogenic facility for stored molecular ions. On the basis of previous work, the electron cooler has been fully designed during this work, and most mechanical subgroups of the cooler have already been manufactured. With the diagnostic system, SCHOTTKY spectra that will constitute the main diagnostic tool for observing phase space cooling have already been observed. The SCHOTTKY spectra showed very long beam storage lifetimes of $\sim 1000\,\mathrm{s}$ decay constants.

Most of the superconducting magnets of the cryogenic magnetic guiding field region of the electron cooler have been assembled and tested successfully for their functionality. The non-cryogenic parts of the magnetic electron guiding structure outside of the CSR cryostat have been simulated with finite element analysis software, designed, and set up completely. First electron beams from a photocathode source have been created. These were magnetically guided over one third of the total projected electron trajectory. The magnetic field of this section has been measured and compared to simulations, finding that it fulfills the requirements of an adiabatic electron transport.

With the planned implementation of the electron cooler setup into CSR in spring 2016, the storage ring will reach its design capabilities. First benchmark experiments are the dissociative recombination (DR) of HD^+ or HeH^+. For phase space cooling these ions with relatively low masses will need still moderate cooling energies of 54 eV and 33 eV (for 300 keV ion energy), respectively. Due to their dipole moment they are expected to cool rotationally and populate only few rotational levels close to their rovibrational ground state. Theoretically calculations [123, 124] predict

for both molecules a significantly different DR spectrum versus energy in a 10 K radiation environment compared to the measurements performed so far only at room temperature conditions. Understanding these benchmark reactions will serve as the base for measurements on more complex molecular ions in the future.

For successful realization and interpretation of recombination experiments, the effective electron beam temperature needs to be known. This temperature defines the phase-space cooling times as well as the energy resolution in the experiments. The electron temperature will primarily be measured by observing the recombination rate as a function of the electron acceleration voltage. Similar studies were done for the electron target of the magnetic cooler ring TSR [125, 126] and should be performed with the new electron cooler setup.

For absolute collisional cross section measurements it is crucial to determine the ion beam intensity at any time of ion beam storage. Up to now there is no direct current measurement for coasting beams (like current transformers) realized in CSR. In some cases, the relative current can be determined from a proxy signal, i.e., a reaction rate at fixed conditions (energy) which is proportional to the ion beam intensity. There may be issues, however, due to the varying internal excitation of the stored ions, leading to additional variations of their cross section. Here an option could be to use the diagnostic system to periodically bunch the ion beam for short time periods and to measure the ion beam intensity with the current pick-up of CSR, which gives a signal proportional to the number of ions. Another option which has been demonstrated in this work could be the lifetime determination using the Schottky noise power. By calibration against absolute current measurements during the storage time, this allows to derive the beam intensity as function of time.

With the Schottky pick-up also multiple ion species of different masses stored at the same energy might be separately identified as individual components in the Schottky spectra. Especially for massive and complex ion species the mass-selective production cannot always be achieved. Depending on the momentum spread of the ion beam the Schottky spectra can help identifying different masses and optimizing the ion source or transfer beamline parameters. In principle also the separation of multiple stored masses by mass-selective acceleration in CSR is conceivable, as was previously demonstrated at the TSR [127].

Appendices

A.1 Thermal conductivities of selected materials

The thermal conductivities can be described by one of the two following equations:

$$\lambda(T) = 10^{(A+C\,T^{0.5}+E\,T+G\,T^{1.5}+I\,T^2)/(1+B\,T^{0.5}+D\,T+F\,T^{1.5}+H\,T^2)} \tag{A.1}$$

or

$$\lambda(T) = 10^{A+B(\log T)+C(\log T)^2+D(\log T)^3+E(\log T)^4+F(\log T)^5+G(\log T)^6+H(\log T)^7+I(\log T)^8}, \tag{A.2}$$

where $\log T = \log_{10} T$ is the common logarithm. The values $A - I$ are summarized in table A.1 for some selected materials.

Table A.1: List of constants for the thermal conductivities of selected materials, taken from [100].

Material	**Copper (RRR50)**	**Titanium (Ti-6Al-4V)**	**stainless steel 316**	**PTFE**
A	1.8743	-5107.8774	-1.4087	2.7380
B	-0.41538	19240.422	1.3982	-30.677
C	-0.6018	-30789.064	0.2543	89.430
D	0.13294	27134.756	-0.6260	-136.99
E	0.26426	-14226.379	0.2334	124.69
F	-0.0219	4438.2154	0.4256	-69.556
G	-0.051276	-763.07767	-0.4658	23.320
H	0.0014871	55.796592	0.1650	-4.3135
I	0.003723	0	-0.0199	0.33829
Equation	(A.1)	(A.2)	(A.2)	(A.2)
Units	W m^{-1} K^{-1}	W m^{-1} K^{-1}	W m^{-1} K^{-1}	W m^{-1} K^{-1}
Validity Range	4 K – 300 K	20 K – 300 K	1 K – 300 K	4 K – 300 K

The data for the thermal conductivity of silver has been taken from [128].

A.2 Layout of the room temperature amplifier

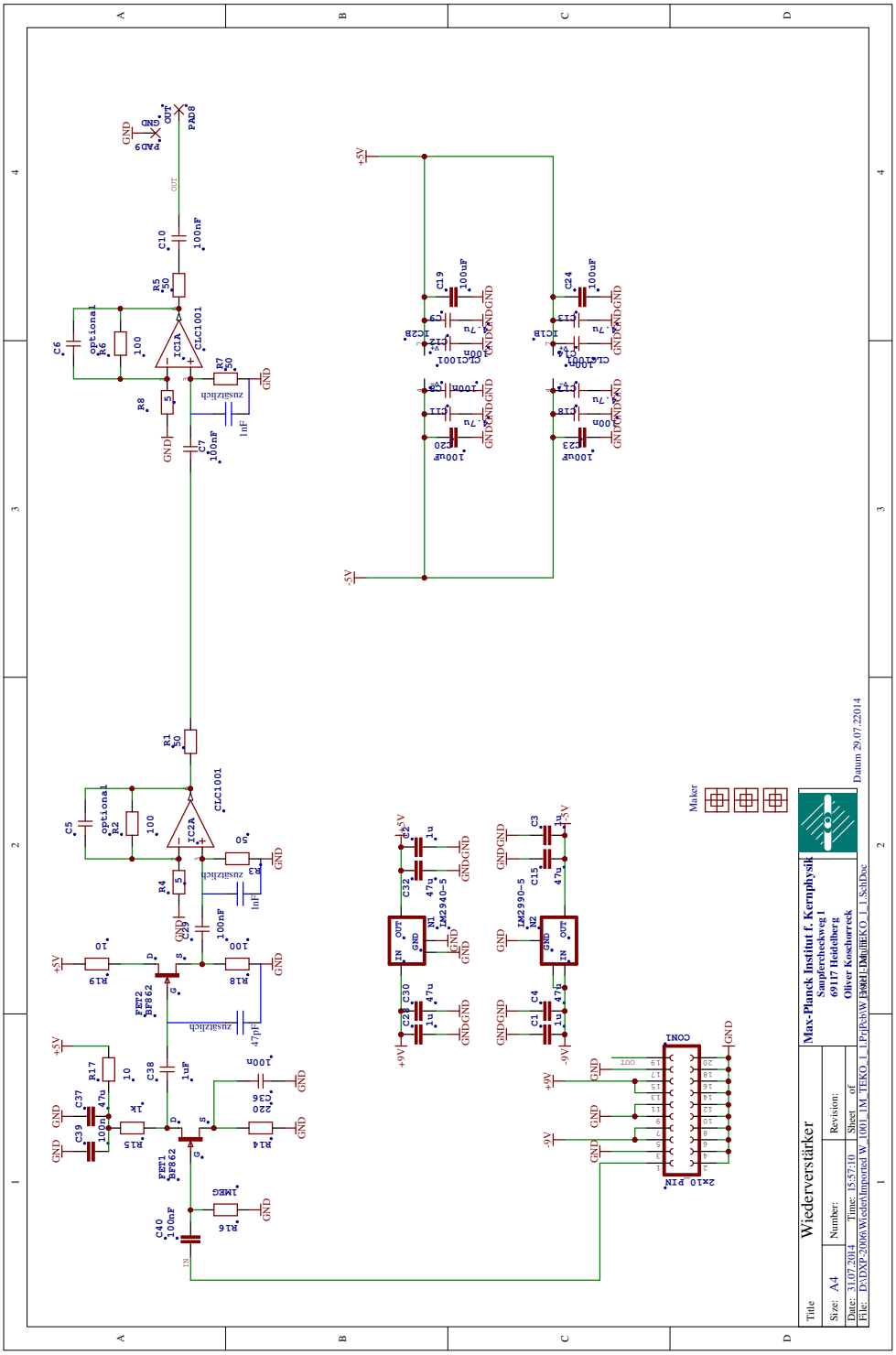

A.3 Closed orbit shift by electrical potential scaling

The equation of motion of a particle with mass m and charge $z\,e$ in an electrical field is:

$$m\frac{\mathrm{d}^2\vec{r}(s)}{\mathrm{d}t^2} = z\,e\,\vec{E}(\vec{r}(s)) \tag{A.3}$$

By substituting the ion path coordinate $s = v\,t$ and using for the electrical field $\vec{E}(\vec{r}(s)) = -\nabla\phi(\vec{r}(s))$ one gets:

$$mv^2\frac{\mathrm{d}^2\vec{r}}{\mathrm{d}s^2} = -z\,e\,\nabla\phi(\vec{r}(s)) \tag{A.4}$$

The energy of the particle is:

$$E_0 = \frac{m}{2}v^2 + z\,e\,\phi(\vec{r}(s)) \tag{A.5}$$

Inserting equation (A.5) in (A.4) results in:

$$\left(\frac{E_0}{z\,e} - \phi(\vec{r}(s))\right)\frac{\mathrm{d}^2\vec{r}}{\mathrm{d}s^2} = -\frac{1}{2}\nabla\phi(\vec{r}(s)) \tag{A.6}$$

Consider an ion trajectory with some small ($\alpha \approx 1$) ion energy deviation $E_0 \to \alpha E_0$:

$$\left(\frac{\alpha E_0}{z\,e} - \phi(\vec{r}(s))\right)\frac{\mathrm{d}^2\vec{r}}{\mathrm{d}s^2} = -\frac{1}{2}\nabla\phi(\vec{r}(s)) \tag{A.7}$$

and an ion trajectory with some small ($\beta \approx 1$) potential deviation $\phi \to \beta\phi$:

$$\left(\frac{E_0}{z\,e\beta} - \phi(\vec{r}(s))\right)\frac{\mathrm{d}^2\vec{r}}{\mathrm{d}s^2} = -\frac{1}{2}\nabla\phi(\vec{r}(s)) \tag{A.8}$$

These two ion trajectories are the same, if

$$\frac{\alpha E_0}{z\,e} - \phi(\vec{r}(s)) = \frac{E_0}{z\,e\,\beta} - \phi(\vec{r}(s)) \tag{A.9}$$

Consequently it is:

$$\alpha = \frac{1}{\beta} \tag{A.10}$$

This means, that small changes of the potential by β have the inverse effect on the closed orbit as small changes of the ion energy by α.

$$\frac{\Delta U}{U_0} = -\frac{\Delta E}{E_0} \tag{A.11}$$

A.4 Measurement of the momentum compaction

The ideal particle on the closed orbit with mass m, charge $z\,e$ and energy $E = E_0$ moves in the electrical fields with the velocity given by equation (2.24):

$$v(s) = v_0 \left(1 - \frac{x(s)}{\rho(s)}\right) \tag{A.12}$$

The revolution time of the ideal particle is:

$$T = \int_0^{C_0} \frac{1}{v(s)} \mathrm{d}s \tag{A.13}$$

The integration can be performed by substitution of the ion path s with the closed orbit path s_0:

$$\mathrm{d}s = \left(1 + \frac{x(s_0)}{\rho(s_0)}\right) \mathrm{d}s_0 \tag{A.14}$$

Inserting equation (A.14) and (A.12) in equation (A.13) and considering for the integrand only contributions up to first order results in:

$$T = \frac{1}{v_0} \int_0^{C_0} \left(1 + \frac{2x(s_0)}{\rho(s_0)}\right) \mathrm{d}s_0 \tag{A.15}$$

From this follows with the definitions of the dispersion (equation (2.16)) and the momentum compaction factor (equation (2.18)) as well as with $\Delta p/p_0 = \Delta E/2E_0$:

$$T = T_0 \left(1 + \alpha_\mathrm{p} \frac{\Delta E}{E_0}\right) \tag{A.16}$$

Finally it gives with equation (A.11) and $\Delta T/T_0 = -\Delta f/f_0$:

$$\frac{\Delta f}{f_0} = \alpha_\mathrm{p} \frac{\Delta U}{U_0} \tag{A.17}$$

Thus, the momentum compaction α_p can be measured by changing all of the electrical potentials of the ion optics and measuring the change in the revolution frequency.

Bibliography

[1] J. J. Thomson, *Cathode Rays,* Philos. Mag., **44**, 269, 393–316, (1897). (page 1).

[2] E. Rutherford, *The scattering of α and β particles by matter and the structure of the atom,* Philos. Mag., **21**, 125, 669–688, (1911). (page 1).

[3] E. Herbst, *The chemistry of interstellar space,* Chem. Soc. Rev., **30**, 168–176, (2001). (page 2).

[4] D. McElroy, C. Walsh, A. J. Markwick, M. A. Cordiner, K. Smith, and T. J. Millar, *The UMIST database for astrochemistry 2012,* A&A, **550**, A36, (2013). (page 2).

[5] R. A. Phaneuf, C. C. Havener, G. H. Dunn, and A. Müller, *Merged-beams experiments in atomic and molecular physics,* Rep. Prog. Phys., **62**, 1143–1180, (1999). (page 2).

[6] E. M. McMillan, *The Synchrotron – A Proposed High Energy Particle Accerlerator,* Phys. Rev., **68**, 143–144, (1945). (page 2).

[7] M. L. Oliphant, J. S. Gooden, and G. S. Hide, *The acceleration of charged particles to very high energies,* Proc. Phys. Soc., **59**, 4, 666–677, (1947). (page 2).

[8] D. Möhl, G. Petrucci, L. Thorndahl, and S. van der Meer, *Physics and technique of stochastic cooling,* Phys. Rep., **58**, 2, 73–102, (1980). (page 2).

[9] W. Petrich, M. Grieser, R. Grimm, A. Gruber, D. Habs, H.-J. Miesner, D. Schwalm, B. Wanner, H. Wernøe, A. Wolf, R. Grieser, G. Huber, R. Klein, T. Kühl, R. Neumann, and S. Schröder, *Laser cooling of stored high-velocity ions by means of the spontaneous force,* Phys. Rev. A, **48**, 3, 2127–2144, (1993). (page 3).

[10] G. I. Budker, *An effective method of damping particle oscillations in proton and antiproton storage rings,* Soviet Atomic Energy, **22**, 5, 438–440, (1967). (page 3).

[11] G. I. Budker, Y. S. Derbenev, N. S. Dikansky, V. I. Kudelainen, I. N. Meshkov, V. V. Parkhomchuk, D. V. Pestrikov, B. N. Sukhina, and A. N. Skrinsky, *Experiments on Electron Cooling,* IEEE Transactions on Nuclear Science, **22**, 5, 2093–2097, (1975). (page 3).

[12] P. Baumann, M. Blum, A. Friedrich, C. Geyer, M. Grieser, B. Holzer, E. Jaeschke, D. Krämer, C. Martin, K. Matl, R. Mayer, W. Ott, B. Povh, R. Repnow, M. Steck, E. Steffens, and W. Arnold, *The Heidelberg Heavy Ion Test Storage Ring TSR,* Nucl. Instrum. Methods A, **268**, 531–537, (1988). (page 3).

[13] M. Grieser, Y. Litvinov, R. Raabe, K. Blaum, Y. Blumenfeld, P. Butler, F. Wenander, P. Woods, M. Aliotta, A. Andreyev, A. Artemyev, D. Atanasov, T. Aumann, D. Balabanski, A. Barzakh, L. Batist, A.-P. Bernardes, D. Bernhardt, J. Billowes, S. Bishop, M. Borge, I. Borzov, F. Bosch, A. Boston, C. Brandau, W. Catford, R. Catherall, J. Cederkäll, D. Cullen, T. Davinson, I. Dillmann, C. Dimopoulou, G. Dracoulis, C. Düllmann, P. Egelhof, A. Estrade, D. Fischer, K. Flanagan, L. Fraile, M. Fraser, S. Freeman, H. Geissel, J. Gerl, P. Greenlees, R. Grisenti, D. Habs, R. von Hahn, S. Hagmann, M. Hausmann, J. He, M. Heil, M. Huyse, D. Jenkins, A. Jokinen, B. Jonson, D. Joss, Y. Kadi, N. Kalantar-Nayestanaki, B. Kay, O. Kiselev, H.-J. Kluge, M. Kowalska, C. Kozhuharov, S. Kreim, T. Kröll, J. Kurcewicz, M. Labiche, R. Lemmon, M. Lestinsky, G. Lotay, X. Ma, M. Marta, J. Meng, D. Mücher, I. Mukha, A. Müller, A. J. Murphy, G. Neyens, T. Nilsson, C. Nociforo, W. Nörtershäuser, R. Page, M. Pasini, N. Petridis, N. Pietralla, M. Pfützner, Z. Podolyák, P. Regan, M. Reed, R. Reifarth, P. Reiter, R. Repnow, K. Riisager, B. Rubio, M. Sanjari, D. Savin, C. Scheidenberger, S. Schippers, D. Schneider, R. Schuch, D. Schwalm, L. Schweikhard, D. Shubina, E. Siesling, H. Simon, J. Simpson, J. Smith, K. Sonnabend, M. Steck, T. Stora, T. Stöhlker, B. Sun, A. Surzhykov, F. Suzaki, O. Tarasov, S. Trotsenko, X. Tu, P. Van Duppen, C. Volpe, D. Voulot, P. Walker, E. Wildner, N. Winckler, D. Winters, A. Wolf, H. Xu, A. Yakushev, T. Yamaguchi, Y. Yuan, Y. Zhang, and K. Zuber, *Storage ring at HIE-ISOLDE,* Eur. Phys. J. Spec. Topics, **207**, 1–117, (2012). (page 3).

[14] R. Stensgaard, *ASTRID – The Aarhus Storage Ring,* Physica Scripta, **1988**, T22, 315–317, (1988). (page 3).

[15] K. Abrahamsson, G. Andler, L. Bagge, E. Beebe, P. Carlé, H. Danared, S. Egnell, K. Ehrnstén, M. Engström, C. J. Herrlander, J. Hilke, J. Jeansson, A. Källberg, S. Leontein, L. Liljeby, A. Nilsson, A. Paal, K.-G. Rensfelt, U. Rosengård, A. Simonsson, A. Soltan, J. Starker, M. af Ugglas, and A. Filevich, *CRYRING – a synchrotron, cooler and storage ring,* Nucl. Instrum. Methods B, **79**, 269–272, (1993). (page 3).

[16] S. P. Møller, *ELISA, an electrostatic storage ring for atomic physics,* Nucl. Instrum. Methods A, **394**, 3, 281–286, (1997). (page 3).

[17] S. Jinno, T. Takao, Y. Omata, A. Satou, H. Tanuma, T. Azuma, H. Shiromaru, K. Okuno, N. Kobayashi, and I. Watanabe, *TMU electrostatic ion storage ring designed for operation at liquid nitrogen temperature,* Nucl. Instrum. Methods A, **532**, 1, 477–482, (2004). (page 3).

[18] M. O. A. El Ghazaly, S. M. Alshammari, C. P. Welsch, and H. H. Alharbi, *Design of a novel electrostatic ion storage ring at KACST,* Nucl. Instrum. Methods A, **709**, 76–84, (2013). (page 3).

[19] T. Tanabe, K. Chida, K. Noda, and I. Watanabe, *An electrostatic storage ring for atomic and molecular science,* Nucl. Instrum. Methods A, **482**, 3, 595–605, (2002). (page 3).

[20] T. Tanabe, K. Noda, and E. Syresin, *An electrostatic storage ring with a merging electron beam device at KEK,* Nucl. Instrum. Methods A, **532**, 1–2, 105–110, (2004). (page 3).

[21] J. Bernard, G. Montagne, R. Brédy, B. Terpend-Ordacière, A. Bourgey, M. Kerleroux, L. Chen, H. T. Schmidt, H. Cederquist, and S. Martin, *A "tabletop" electrostatic ion storage ring: Mini-Ring,* Rev. Sci. Instrum., **79**, 075109, (2008). (page 3).

[22] J. Matsumoto, K. Gouda, N. Kondo, and H. Shiromaru, *Present status of a table-top electrostatic ion storage ring,* 6th International Workshop on Electrostatic Storage Devices, P09, (2015). Tokyo, Japan. (page 3).

[23] K. E. Stiebing, V. Alexandrov, R. Dörner, S. Enz, N. Y. Kazarinov, T. Kruppi, A. Schempp, H. Schmidt Böckinga, M. Völp, P. Ziel, M. Dworaka, and W. Dilfer, *FLSR – The Frankfurt low energy storage ring,* Nucl. Instrum. Methods A, **614**, 10–16, (2010). (page 3).

[24] H. B. Pedersen, A. Svendsen, L. S. Harbo, H. V. Kiefer, H. Kjeldsen, L. Lammich, Y. Toker, and L. H. Andersen, *Characterization of a new electrostatic storage ring for photofragmentation experiments,* Rev. Sci. Instrum., **86**, 063107, (2015). (page 3).

[25] R. D. Thomas, H. T. Schmidt, G. Andler, M. Björkhage, M. Blom, L. Brännholm, E. Bäckström, H. Danared, S. Das, N. Haag, P. Halldén, F. Hellberg, A. I. S. Holm, H. A. B. Johansson, A. Källberg, G. Källersjö, M. Larsson, S. Leontein, L. Liljeby, P. Löfgren, B. Malm, S. Mannervik, M. Masuda, D. Misra, A. Orbán, A. Paál, P. Reinhed, K.-G. Rensfelt, S. Rosén,

K. Schmidt, F. Seitz, A. Simonsson, J. Weimer, H. Zettergren, and H. Cederquist, *The double electrostatic ion ring experiment: A unique cryogenic electrostatic storage ring for merged ion-beams studies,* Rev. Sci. Instrum., **82**, 065112, (2011). (page 3).

[26] H. T. Schmidt, *A survey of the field of electrostatic ion-beam storage,* 6th International Workshop on Electrostatic Storage Devices, Mo01, (2015). Tokyo, Japan. (page 3).

[27] Y. Nakano, W. Morimoto, T. Majima, J. Matsumoto, H. Tanuma, H. Shiromaru, and T. Azuma, *A cryogenic electrostatic storage ring project at RIKEN,* J. Phys. Conf. Ser., **388**, 142027, (2012). (page 3).

[28] R. von Hahn, F. Berg, K. Blaum, J. R. Crespo López-Urrutia, F. Fellenberger, M. Froese, M. Grieser, C. Krantz, K. K.-U., M. Lange, S. Menk, F. Laux, D. A. Orlov, R. Repnow, C. D. Schröter, A. Shornikov, T. Sieber, J. Ullrich, A. Wolf, M. Rappaport, and D. Zajfman, *The electrostatic Cryogenic Storage Ring CSR - Mechanical concept and realization,* Nucl. Instrum. Methods B, **269**, 24, 2871–2874, (2011). (pages 3, 21, and 25).

[29] D. W. Kerst, *The Acceleration of Electrons by Magnetic Induction,* Physical Review, **60**, 47–53, (1941). (pages 6, 7, and 160).

[30] F. Hinterberger, *Physik der Teilchenbeschleuniger und Ionenoptik.* Springer-Verlag Berlin Heidelberg New York, 2nd ed., (2008). (pages 6, 9, 10, 11, 12, 15, 120, 149, 154, 160, and 161).

[31] Cern Accelerator School reports, *General Accelerator Physics,* (1983-2015). (page 6).

[32] G. W. Hill, *On the part of the motion of the lunar perigee which is a function of the mean motions of the sun and moon,* Acta Mathematica, **8**, 1, 1–36, (1886). (page 7).

[33] E. D. Courant and H. Snnder, *Theory of the alternating-gradient synchrotron,* Annals of Physics, **3**, 1, 1–48, (1958). (pages 7 and 9).

[34] Cobham CTS Limited, *Opera 16R1,* (2013). (pages 10, 13, 79, 80, 105, and 150).

[35] H. Fadil, M. Grieser, R. von Hahn, and A. Wolf, *Finite Elements Calculations of the Lattice and Ring Acceptance of the Heidelberg CSR,* Proc. EPAC06, 1960–1962, (2006). Edingburg, Scotland. (pages 10, 31, 120, 122, and 150).

[36] H. Grote and F. C. Iselin, *The MAD Program (Methodical Accelerator Design), Version 8.51/15, CERN-SL-90-14,* (1990). (pages 13 and 120).

[37] T. Roberts, *G4beamline User's Guide 2.16,* (2013). (pages 13 and 152).

[38] A. Dahl, David, *SIMION for the personal computer in reflection,* Int. J. Mass Spectrom., **200**, 3–25, (2000). (page 13).

[39] M. Grieser, *private communications,* (2012-2015). (pages 13, 152, and 153).

[40] G. I. Budker and Skrinskiĭ, *Electron cooling and new possibilities in elementary particle physics,* Sov. Phys. Usp., **21**, 277–296, (1978). (page 15).

[41] H. Poth, *Electron cooling: Theory, experiment, application,* Physics Reports, **196**, 3-4, 135–297, (1990). (pages 15, 17, and 76).

[42] L. Spitzer, *Physics of Fully Ionized Gases.* Wiley, New York, 2nd ed., (1962). (pages 16, 18, and 20).

[43] A. Shornikov, *An electron cooler for ultra-low energy cryogenic operation.* PhD thesis, Ruperto-Carola University of Heidelberg, Germany, (2012). (pages 16, 20, 77, 79, 87, 88, 90, 93, 97, 98, 103, 108, and 109).

[44] A. Wolf, *Wechselwirkung zwischen hochgeladenen Ionen und freien Elektronen in einem Ionenspeicherring: dynamische Reibung und Rekombination.* Professorial Dissertation, University of Heidelberg, (1992). (page 17).

[45] S. Pastuszka, U. Schramm, M. Grieser, C. Broude, R. Grimm, D. Habs, J. Kenntner, H.-J. Miesner, T. Schüßler, D. Schwalm, and A. Wolf, *Electron cooling and recombination experiments with an adiabatically expanded electron beam,* Nucl. Instrum. Methods Phys. Res., Sect. A, **369**, 11–22, (1996). (page 18).

[46] H. Danared, *Fast electron cooling with a magnetically expanded electron beam,* Nucl. Instrum. Methods A, **335**, 3, 397–401, (1993). (page 18).

[47] H. Danared, G. Andler, L. Bagge, C. J. Herrlander, J. Hilke, J. Jeansson, A. Källberg, A. Nilsson, A. Paál, K. G. Rensfelt, U. Rosengård, J. Starker, and M. af Ugglas, *Electron Cooling with an Ultracold Electron Beam,* Phys. Rev. Lett., **72**, 24, 3775–3778, (1994). (page 18).

[48] T. M. O'Neil and P. G. Hjorth, *Collisional dynamics of a strongly magnetized pure electron plasma,* Phys. Fluids, **28**, 11, 3241–3252, (1985). (page 18).

[49] G. H. Jansen, *Coulomb interactions in particle beams.* Acadameic Press, Boston, (1990). (pages 18 and 19).

[50] D. A. Orlov, H. Fadil, M. Grieser, and A. Wolf, *Cold Photocathode Electron Sources and Perspectives for Low-Energy Magnetically Guided Electron Beams,* AIP Conf. Proc., **862**, 274–280, (2006). (page 19).

[51] N. S. Dikansky, V. I. Kudelainen, V. A. Lebedev, I. N. Meshkov, V. V. Parkhomchuk, A. A. Sery, A. N. Skrinsky, and B. N. Sukhina, Ultimate Possibilities of Electron Cooling. Preprint 88-61, Budker Institute of Nuclear Physics, Novosibirsk, (1988). (page 19).

[52] F. Sprenger, *Production of cold electron beams for collision experiments with stored ions.* PhD thesis, Ruperto-Carola University of Heidelberg, Germany, (2003). (pages 90, 115, and 116).

[53] M. Lestinsky, *High-Resolution Electron Collision Spectroscopy with Multicharged Ions in Merged Beams.* PhD thesis, Ruperto-Carola University of Heidelberg, Germany, (2007). (pages 19 and 76).

[54] D. A. Orlov, U. Weigel, D. Schwalm, A. S. Terekhov, and A. Wolf, *Ultra-cold electron source with a GaAs-photocathode,* Nucl. Instrum. Methods A, **532**, 1-2, 418–421, (2004). (pages 19 and 76).

[55] C. Krantz, *Intense Electron Beams from GaAs Photocathodes as a Tool for Molecular and Atomic Physics.* PhD thesis, Ruperto-Carola University of Heidelberg, Germany, (2009). (pages 19, 20, 76, 79, and 115).

[56] A. Shornikov, D. A. Orlov, C. Krantz, A. S. Jaroshevich, and A. Wolf, *Maximum intensity, transmission limited cold electron beams from GaAs photocathode in the eV and sub-eV kinetic energy range,* Phys. Rev. ST Accel. Beams, **17**, 042802, (2014). (pages 20 and 77).

[57] C. Rubbia, *On the formation of intense electron beams with small transverse velocities for (anti)-proton cooling,* CERN EP International Report, **77-2**, 19, (1997). (page 20).

[58] C. Krantz, F. Berg, K. Blaum, F. Fellenberger, M. Froese, M. Grieser, R. von Hahn, M. Lange, F. Laux, S. Menk, R. Repnow, A. Shornikov, and A. Wolf, *The Cryogenic Storage Ring and its application to molecular ion recombination physics,* J. Phys. Conf. Ser., **300**, 012010, (2011). (page 21).

[59] A. Becker, *to be published.* PhD thesis, Ruperto-Carola University of Heidelberg, Germany, (2016). (pages 23 and 28).

[60] K. Spruck, *Dielectronic recombination experiments with tungsten ions at the test storage ring and development of a single-particle detector at the cryogenic storage ring.* PhD thesis, Justus-Liebig-Universität Gießen, (2015). (pages 23 and 28).

[61] K. Spruck, A. Becker, F. Fellenberger, M. Grieser, R. von Hahn, V. Klinkhamer, O. Novotný, S. Schippers, S. Vogel, A. Wolf, and C. Krantz, *An*

efficient, movable single-particle detector for use in cryogenic ultra-high vacuum environments, Rev. Sci. Instrum., **86**, 023303, (2015). (pages 23 and 28).

[62] F. Grussie, *to be published.* PhD thesis, Ruperto-Carola University of Heidelberg, Germany, (2016). (pages 23 and 71).

[63] K.-U. Kuehnel, M. Putignano, C. D. Schroeter, J. Ullrich, and C. P. Welsch, *A Novel Beam Profile Monitor Based on a Supersonic Gas Jet,* Proc. EPAC08, 1182–1184, (2008). Genoa, Italy. (page 23).

[64] M. Lange, M. Froese, S. Menk, J. Varju, R. Bastert, K. Blaum, J. R. Crespo López-Urrutia, F. Fellenberger, M. Grieser, R. von Hahn, O. Heber, K.-U. Kühnel, F. Laux, D. A. Orlov, M. L. Rappaport, R. Repnow, C. D. Schröter, D. Schwalm, A. Shornikov, T. Sieber, Y. Toker, J. Ullrich, A. Wolf, and D. Zajfman, *A cryogenic electrostatic trap for long-time storage of keV ion beams,* Rev. Sci. Instrum., **81**, 5, 055105, (2010). (page 24).

[65] RUAG Space GmbH, *Technical Data Sheet: COOLCAT 2 NW,* (2012). (pages 25, 70, and 103).

[66] Q. S. Shu, R. W. Fast, and H. L. Hart, *Heat flux from 277 to 77 K through a few layers of multilayer insulation,* Cryogenics, **26**, 671–677, (1986). (page 25).

[67] R. von Hahn, K. Blaum, J. R. Crespo López-Urrutia, M. W. Froese, M. Grieser, M. Lange, F. Laux, S. Menk, D. Orlov, R. Repnow, C. D. Schröter, D. Schwalm, T. Sieber, J. Ullrich, J. Varju, A. Wolf, H. Quack, M. Rappaport, D. Zajfman, and X. Urbain, *The Cryogenic Storage Ring Project at Heidelberg,* Proc. EPAC08, 394–396, (2008). Genoa, Italy. (page 25).

[68] M. Froese, K. Blaum, J. R. Crespo López-Urrutia, F. Fellenberger, M. Grieser, D. Kaiser, M. Lange, F. Laux, S. Menk, D. A. Orlov, R. Repnow, C. D. Schröter, D. Schwalm, A. Shornikov, T. Sieber, J. Ullrich, J. Varju, R. von Hahn, A. Wolf, O. Heber, M. Rappaport, J. Toker, and D. Zajfman, *Cryogenic ion beam storage,* Proc. PAC09, 4860–4821, (2009). Vancouver, BC, Canada. (page 25).

[69] W. Schottky, *Über spontane Stromschwankungen in verschiedenen Elektrizitätsleitern,* Annalen der Physik, **382**, 23, 541–567, (1918). (pages 27 and 47).

[70] D. Boussard, *Schottky noise and beam transfer function diagnostics,* Cern Accelerator School, Advanced Accelerator Physics, Oxford, England, **II**, 749–782, (1985). (pages 27 and 47).

[71] I. K. Harvey, *A Precise Low Temperature dc Ratio Transformer,* Rev. Sci. Instrum., **43**, 1626–1629, (1972). (page 28).

[72] A. Peters, V. Dürr, H. Reeg, C. Schröder, H. Koch, R. Neubert, W. Vodel, and H. Mühlig, *A Cryogenic Current Comparator for Nondestructive Beam Intensity Measurements,* Proc. EPAC94, 290–292, (1994). London, UK. No citations.

[73] A. Peters, W. Vodel, H. Koch, R. Neubert, H. Reeg, and C. H. Schroeder, *A Cryogenic Current Comparator for the Absolute Measurement of nA Beams,* Proc. BIW98, 163–180, (1998). Stanford, UK. No citations.

[74] A. Peters, H. Reeg, P. Forck, W. Vodel, and R. Neubert, *Recent Improvements of a Cryogenic Current Comparator for nA Ion Beams with High Intensity Dynamics,* Proc DIPAC99, 109–111, (1999). Chester, UK. (page 28).

[75] F. Laux, *Entwicklung von kapazitiven Positions-, Strom- und Schottkysignal-Messsystemen für den kryogenen Speicherring CSR.* PhD thesis, Ruperto-Carola University of Heidelberg, Germany, (2011). (pages 28, 35, 39, 41, 43, 45, 50, 53, 54, 55, 56, 58, 64, and 67).

[76] M. Grieser, *Space Charge Limitation of an electron-cooled proton beam,* (2004). https://www-alt.gsi.de/documents/DOC-2010-Jan-200.html. (page 30).

[77] N. Corporation, *SA-220F5 Specifications sheet,* (2007). (page 38).

[78] P. Forck, Lecture Notes on Beam Instrumentation and Diagnostics, in *Joint University Accelerator School*, Gesellschaft für Schwerionenforschung (GSI), Darmstadt, Germany, 2011. (page 39).

[79] R. E. Shafer, *Beam position monitoring,* AIP Conf. Proc., **212**, 26–58, (1990). (page 39).

[80] J. H. Cupérus, *Edge effect in beam monitors,* Nucl. Instr. Meth., **145**, 2, 233–243, (1977). (page 41).

[81] J. W. Ekin, *Experimental Techniques for Low-Temperature Measurements: Cryostat Design, Material Properties and Superconductor Critical Current Testing.* Oxford University Press Inc., New York, (2006). (pages 42, 67, 70, 99, 102, and 111).

[82] F. Fellenberger, *Aufbau und Charakterisierung der ersten Ecke des kryogenen elektrostatischen Speicherrings CSR.* PhD thesis, Ruperto-Carola University of Heidelberg, Germany, (2012). (pages 43 and 153).

[83] T. A. Hahn, *Thermal Expansion of Copper from 20 to 800 K - Standard Reference Material 736,* Journal of Applied Physics, **41**, 13, 5096–5101, (1970). (page 45).

[84] F. Schmitz. Schottky Diagnostics at the Heavy Ion Cooler Storage Ring TSR,. Bachelor's thesis, Ruperto-Carola University of Heidelberg, Germany, (2010). (page 47).

[85] A. Hofmann, *Dynamics of beam diagnostics,* Cern Accelerator School, Beam Diagnostics, Dourdan France, **V**, 65–139, (2008). (page 50).

[86] S. Sturm, *The g-factor of the electron bound in* $^{28}Si^{13+}$*: The most stringent test of bound-state equilibrium electrodynamics.* PhD thesis, Universität Mainz, (2011). (pages 53, 54, and 55).

[87] J. M. Miller, *Dependence of the input impedance of a three electrode vacuum tube upon the load in the plate circuit,* Scientific Papers of the Bureau of Standards, **15**, 367–385, (1920). (page 53).

[88] D. V. Camin, G. Pessina, and E. Previtali, *Cryogenic Semiconductor Electronics,* Jpn. J. Appl. Phys., **37**, 52–56, (1998). (page 54).

[89] C.-E. Roux, *High-Resolution Mass Spectrometry: The Trap Design and Detection System of PENTATRAP and New Q-Values for Neutrino Studies.* PhD thesis, Ruperto-Carola University of Heidelberg, Germany, (2012). (page 55).

[90] C. D. Motchenbacher and J. A. Connelly, *Low noise electronic system design.* Wiley-Interscience New York, (1993). (page 55).

[91] Teledyne Relays, *Specifications Sheet RF180,* (2008). (page 56).

[92] M/A-COM, *MA46H206 datasheet,* (2008). (pages 58 and 65).

[93] W. Macalpine, *Coaxial Resonators with Helical Inner Conductor,* Proc. IRE, **47**, 12, 2099–2105, (1959). (page 59).

[94] H. H. Meinke and F.-W. Gundlach, *Taschenbuch der Hochfrequenztechnik.* Springer-Verlag Berlin Heidelberg GmbH, 5th ed., (1992). (pages 59 and 63).

[95] J. D. Jackson, *Classical Electrodynamics.* Wiley, New York, 3rd ed., (1975). (page 59).

[96] W. Demtröder, *Experimentalphysik 2: Elektrizität und Optik.* Springer-Verlag Berlin Heidelberg New York, 4th ed., (2006). (page 63).

[97] C. Bowick, J. Blyler, and C. Ajluni, *RF Circuit Design.* Newnes/Elsevier, 2nd ed., (2008). (page 63).

[98] H. H. Meinke and F.-W. Gundlach, *Taschenbuch der Hochfrequenztechnik.* Springer-Verlag Berlin Heidelberg GmbH, 3rd ed., (1968). (page 63).

[99] H. Kracke, Entwicklung der kryogenen Nachweis-Elektronik zur Bestimmung der axialen Frequenz des Protons in einer Penning-Falle, Diploma's thesis, Johannes Gutenberg-Universität Mainz, (2007). (pages 63 and 64).

[100] National Institute for Standards and Technology, *Cryogenic Material Properties,* (2015). Online; accessed 08. September 2015, http://cryogenics.nist.gov/MPropsMAY/material%20properties.htm. (pages 70, 102, and 169).

[101] N. J. Simon, E. S. Drexler, and R. P. Reed, *Properties of Copper and Copper Alloys at Cryogenic Temperature,* NIST Monograph, **177**, 7–23, (1992). (page 70).

[102] T. M. Flynn, *Cryogenic Engineering.* Marcel Dekker Inc., New York, (1997). (page 70).

[103] D. Habs, J. Kramp, P. Krause, K. Matl, R. Neumann, and D. Schwalm, *Ultracold Ordered Electron Beam,* Physica Scripta, **T22**, 269–276, (1988). (page 76).

[104] J. J. Scheer and J. van Laar, *GaAs-Cs: A new type of photoemitter,* Solid State Commun., **3**, 8, 189–193, (1965). (page 76).

[105] U. Weigel, *Cold Intense Electron Beams from Gallium Arsenide Photocathodes.* PhD thesis, Ruperto-Carola University of Heidelberg, Germany, (2003). (pages 76, 85, and 116).

[106] H. Fadil, D. A. Orlov, M. Grieser, and A. Wolf, *Design of a Low Energy Electron Cooler for the Heidelberg CSR,* Proc. EPAC06, 1630–1632, (2006). Edingburg, Scotland. (page 77).

[107] S. Lohmann, to be published, Master's thesis, Ruperto-Carola University of Heidelberg, Germany, (2015). (pages 91 and 106).

[108] C. Krantz, CSR/eCool: Pumpsystem. Internal report, (2012). (page 93).

[109] A. Shornikov, C. Krantz, and A. Wolf, *Low cryogen inventory, forced flow Ne cooling system with room temperature compression stage and heat recuperation,* Cryogenics, **59**, 7–11, (2014). (page 97).

[110] J. Lion. Das mit Flüssigneon gekühlte supraleitende Magnetsystem des Elektronenkühlers am kryogenen Ionen-Speicherring CSR,. Bachelor's thesis, Ruperto-Carola University of Heidelberg, Germany, (2015). (page 97).

[111] R. A. Matula, *Electrical Resistivity of Copper, Gold, Palladium, and Silver,* J. Phys. Chem. Ref. Data, **8**, 1147–1298, (1979). (page 99).

[112] RUAG Space GmbH, *Technical Data Sheet: COOLCAT 2 LOX,* (2012). (page 102).

[113] RUAG Space GmbH, *Technical Data Sheet: COOLCAT 2 NF,* (2012). (page 102).

[114] I. E. Sumner, *Degradation of a Multilayer Insulation due to a Seam and a Penetration,* NASA, **TN-D-8229**, 1–34, (1976). (page 103).

[115] M. Lange, Die CSR-Strahlungsschilde. Internal report, (2013). (page 103).

[116] AMSC, *Amperium Copper Laminated Type 8501 and 8502 Wire data sheet,* (2014). (page 110).

[117] AMSC, *Guidelines for Hand-Assembled Splicing of Amperium Wire,* (2012). (page 111).

[118] R. L. Powell and A. A. Aboud, *Electrical Contact Resistance of Copper-Copper Junctions at Low Temperatures,* Rev. Sci. Instrum., **29**, 248–249, (1958). (page 111).

[119] S.-R. Liu, H.-J. Zhai, and L.-S. Wang, *Electronic and structural evolution of Co_n clusters ($n = 1 - 108$) by photoelectron spectroscopy,* Phys. Rev. B, **64**, 153402, (2001). (page 142).

[120] M. Grieser, F. Albrecht, D. Habs, R. von Hahn, B. Hochadel, C.-M. Kleffner, J. Liebmann, R. Repnow, D. Schwalm, G. Bisoffi, and E. Jaeschke, *Operation of the TSR close to the Transition Energy,* Workshop on Beam Cooling and related Topics, 257–261, (1993). Montreux, Switzerland. (page 161).

[121] C. Meyer, *private communications,* (2015). (page 163).

[122] A. O'Connor, *private communications,* (2015). (page 163).

[123] F. O. Waffeu Tamo, H. Buhr, O. Motapon, S. Altevogt, V. M. Andrianarijaona, M. Grieser, L. Lammich, M. Lestinsky, M. Motsch, I. Nevo, S. Novotny, D. A. Orlov, H. B. Pedersen, D. Schwalm, F. Sprenger, X. Urbain, U. Weigel, A. Wolf, and I. F. Schneider, *Assignment of resonances in dissociative recombination of HD^+ ions: High-resolution measurements compared with accurate computations,* Phys. Rev. A, **84**, 022710, (2011). (page 166).

[124] D. J. Haxton and C. H. Greene, *Ab initio frame-transformation calculations of direct and indirect dissociative recombination rates of $HeH^+ + e^-$,* Phys. Rev. A, **79**, 022701, (2009). (page 166).

[125] M. Lestinsky, E. Lindroth, D. A. Orlov, E. W. Schmidt, S. Schippers, S. Böhm, C. Brandau, F. Sprenger, A. S. Terekhov, A. Müller, and A. Wolf, *Screened Radiative Corrections from Hyperfine-Split Dielectronic Resonances in Lithiumlike Scandium,* Phys. Rev. Lett., **100**, 033001, (2008). (page 167).

[126] J. Stützel, *Fragmentation of Small Multi-Electron Molecular Ions in Cold Electron Collisions.* PhD thesis, Ruperto-Carola University of Heidelberg, Germany, (2011). (page 167).

[127] M. Grieser, R. Bastert, K. Blaum, H. Buhr, R. von Hahn, M. B. Mendes, R. Repnow, and A. Wolf, *Acceleration, deceleration and bunching of stored and cooled ion beams at the TSR, Heidelberg,* Proc. HIAT09, 1–5, (2010). Venice, Italy. (page 167).

[128] R. W. Powell, C. Y. Ho, and P. E. Liley, *Thermal Conductivity of Selected Materials.* Washington : U. S. Dept. of Commerce, National Bureau of Standards, (1966). (page 169).

Danksagung

An dieser Stelle möchte ich verschiedenen Personen danken, die zum Gelingen dieser Arbeit beigetragen haben.

Allen voran möchte ich Andreas Wolf für die Möglichkeit danken an einem so spannenden Projekt mitarbeiten zu dürfen, für die Betreuung und Unterstützung bei verschiedenen Problemen und für die vielen Kommentare, Erklärungen und Korrekturen beim Anfertigen dieser Arbeit.

Auch möchte ich André Schöning für die freundliche Übernahme des zweiten Gutachtens danken.

Claude Krantz und Oldřich Novotný möchte ich nicht nur für die sehr hilfreichen Kommentare beim Schreiben dieser Arbeit danken, sondern vielmehr für die jahrelange Betreuung, Unterstützung und Aufmunterung, wenn es um meine Stimmung mal wieder nicht so gut aussah.

Auch Manfred Grieser ist entscheidend für mein Verständnis, welches ich über die Jahre erlangt habe. Er ist niemals müde geworden mir Dinge rund um die Speicherring Physik zu erklären und zu verdeutlichen. Er hat mir einen kleinen Teil seines enormen Wissens darüber weitergeben.

Den verschiedenen MPIK Einrichtungen möchte ich danken, die mir eine Menge Arbeit abgenommen haben: Die mechanische Werkstatt unter der Leitung von Thorsten Spranz und das Konstruktionsbüro unter der Leitung von ehemals Thomas Weber und nun Frank Müller. Aber auch der Beschleuniger-Werkstatt unter der Leitung von ehemals Karl Hahn und nun Max Falckenthal sowie der Truppe rund um Manfred König. Aber auch einzelnen Personen wie Dirk Kaiser, Oliver Koschorreck, Peter Werle, Rolf Epking und Volker Wieder.

Der ganzen Arbeitsgruppe und dem gesamten CSR Team möchte ich danken für die freundliche Aufnahme, die sehr gute Arbeitsatmosphäre und die spannende Zeit an diesem großartigen Projekt.

Kaija Spruck möchte ich danken für die gemeinsame Zeit und dafür, dass ich überhaupt von diesem Projekt erfahren habe.

Arno Becker und David Frickel danke ich für die Kommentare beim Schreiben, aber vielmehr für die Zeit neben der Arbeit.

Zuletzt möchte ich meiner Familie für die jahrelange, ausnahmslose Unterstützung danken und meiner Freundin Laura dafür, dass du meine Gefährtin bist.